Control of Temperature Uniformity for Exothermic Liquid Reaction in Structured Passages

A thesis

Submitted to the University of Sheffield for the degree of Doctor of Philosophy in the Faculty of Engineering

By

Mohammed H. Msaed

Department of Chemical and Biological Engineering

The University of Sheffield

United Kingdom

March 2021

Dedication

To my mother and my wife,

…… to my daughters,

…… to my brothers, and my sisters

…….and to the wonderful memory of my father and my uncle.

Mohammed Msaed

ACKNOWLEDGEMENTS

The utmost thanks and gratitude is for my God for the help, great graces, and conciliation;

"Taught man that which he knew not". *The Holy Quran Al-Alaq (5).*

Firstly, I would like to express my deep thanks my supervisors Doctor Jordan MacInnes for his outstanding guidance, supervision, and continuous support throughout my PhD, who was, persistently, advising, motivating, and directing me. I'm also very grateful to Professor Annette Taylor, for her help in part of my work (reaction part).

I am thankful to the technical staff of the departmental workshop that made a lot of effort to construct the custom designed equipment for the research requirements. I should also thank the technical staff of laboratories for their kind assistance.

I am also great thankful to the Ministry of Higher Education and Scientific Research/Iraq, Iraqi cultural attaché/London, and the University of Diyala for the financial support.

My exclusive appreciation goes to my parents. My gratitude to my wife, my daughters, for their continuous, unconditional support and endless patience. They always made my life delighted.

Abstract

The temperature non-uniformity produced by energetic liquid reactions can cause unwanted products or otherwise uncontrolled reactions. On the other hand, operating a reaction at the highest acceptable temperature maximises the reaction rate. This work was designed to establish the relationship between flow conditions and temperature non-uniformity for a given reaction system in a particular structured flow passage. The work studied the temperature non-uniformity experimentally and computationally of the two reacting systems (HCl-NaOH and $NaClO_2$- $K_2S_4O_6$) in an F-element Reactor under different flow and thermal conditions.

A mathematical model was developed to show the approximate dependence of temperature non-uniformity on the Damköhler number (Da), reaction Enthalpy number (H), Reynolds number (Re) and Prandtl number (Pr). These parameters are non-dimensional numbers and they consist of physical variables. These variables include the dimension of the flow passage, species concentration, species velocity, enthalpy of reaction, etc. Substituting the non-dimensional parameters in terms of the physical variables shows the dependence of temperature non-uniformity on these variables.

Three small scale different structured reactors, i.e., C, F and S element Reactors, were used to investigate the temperature non-uniformity in the structured passages. These geometries were designed to have the same residence time. The experiments were implemented using a non-reacting flow system: this was, firstly, to discover the physical and thermal properties of the system through simulating with CFD; and secondly, to investigate the effect of gravity on the flow pattern and temperature distribution through the flow passage. The experiments were also implemented in two exothermic reacting flow systems, HCl-NaOH and $NaClO_2$- $K_2S_4O_6$, to investigate the effect of flow conditions on the temperature non-uniformity in the reacting flow. These experiments were only implemented in the F-element Reactor due to noise appearing in the temperature measurements in the C and S element Reactors. The experiments in both flow systems included a wide range of flow rates (Re) and thermal conditions (Ri). Ri represents the effect of buoyancy on the flow pattern and temperature uniformity within the flow passage. This effect decreases when the passage width and temperature difference between the reagent stream inlet temperature and the fluid temperature

decrease and when the fluid velocity increases. The spatial temperature along the reactor domain was measured using the movable fine-wire thermocouple method.

A three-dimensional (3-D) computational model was used to study the temperature non-uniformity within the domain of flow passages. This model used numerical solutions for the flow, species and energy equations to reliably capture the flow and temperature field within the reactor domain.

The results showed that the agreement between the experimental data and the computational results was acceptable. The results also showed that buoyancy has a significant effect on the flow pattern and temperature profile in all geometries. This effect decreased with decreasing Ri and increasing fluid flow rate (Re) due to the decrease in the effect of gravity force. This effect can be ignored at $Re \geq 130$ at the $Ri \geq 0.4$, 0.3 and 0.4 for the C, F and S element Reactors respectively in the non-reacting flow and at the $Ri \geq 0.1$ for the F-element Reactor in the reacting system. Furthermore, the results showed that the fluid temperature decreased along the flow passage due to the effective dissipation of the heat into the walls and the effect of the cooling system. Moreover, the temperature non-uniformity is affected by the Ri and the inlet temperature of the reagent stream. Temperature non-uniformity decreased with decreasing Ri. When the stream of reagent entering the reactor is cold, the temperature non-uniformity is higher than when it is hot. In addition, the temperature non-uniformity is also affected by the flow rate of fluid (Re): it decreased with an increasing fluid flow rate due to the enhancing of the dissipation of heat and a decrease in the effect of buoyancy. Finally, the temperature non-uniformity decreased with the decreasing enthalpy of reaction. The standard deviation of temperature for the HCl-NaOH reacting system was (1.9 ^{o}C) less than the $NaClO_2$- $K_2S_4O_6$ reacting system (2.2 ^{o}C) at the same Re and close Ri. This may be due to the large enthalpy of the $NaClO_2$- $K_2S_4O_6$ reacting system.

Generally, the experimental and computational works in this thesis demonstrate the potential for controlling the temperature non-uniformity within the flow passage using structured passages.

Table of contents

Table of Contents

Dedication i
ACKNOWLEDGEMENTS ii
Abstract iii
Table of contents v
List of figures ix
List of Tables xv
Nomenclature xvi
Greek Symbols xviii
Abbreviations xix
1. Introduction 1
1.1 Research objectives 2
1.2 Research hypotheses 3
1.3 Thesis structure 4
2. Literature Review 6
2.1. Properties of small scale passages 6
2.2. Optimum temperature of reaction 7
2.3. Thermal management in small scale passages 8
2.4. Influence of key parameters on thermal uniformity 9
2.4.1. Reynolds number 10
2.4.2. Damköhler number 11
2.4.3. Enthalpy of reaction 12
2.5. Mixing in small channels 13
2.5.1. Parallel lamination 13
2.5.2. Folding flow 14
2.5.3. Chaotic mixer 15
2.6 Temperature measurement in small scale reactors 17
2.6.1 Methods of temperature measurement in passages 18
2.6.2 Heat conduction error through thermocouple wire 19
2.7 The effect of wire coating on the accuracy of temperature measurement 22
2.8 The noise of the temperature measurement 23

2.9 Buoyancy effect on the flow pattern 24
2.10 Liquid-Liquid reaction system 27
2.10.1 Chlorite - tetrathionate ($NaClO_2$- $K_2S_4O_6$) reaction system 27
2.10.2 Hydrochloric acid-Sodium hydroxide (HCl-NaOH) reaction system 30
2.11 Effect of species diffusion (*D*) on the temperature uniformity 31
3. Mathematical model 34
3.1 Governing equations 34
3.2 Reaction mechanism 36
3.3 Non-Dimensional parameters 37
3.3.1 Flow 37
3.3.2 Species 39
3.3.3 Energy 40
3.4 Temperature non-uniformity 42
3.5 Reactor geometries 43
3.5.1 F-Element Reactor 43
3.5.2 S-Element Reactor 45
3.5.3 C-Element Reactor 46
3.6 Boundary Conditions 47
3.7 Physical properties 48
3.8 Measures of non-uniformity 50
3.9 Numerical Solution 50
3.9.1 Grid Dependence 51
3.10 Summary 55
4. The Experimental work 57
4.1 General apparatus 57
4.2 Thermal boundary conditions 61
4.2.1 Heat flux at top and bottom boundaries 62
4.2.2 Reagent inlet temperature 63
4.3 Spatial temperature measurement 64
4.3.1 Conduction error assessment 66
4.3.2 Conduction error measurement 70
4.3.3 Wire diameter 71
4.4 Gas bubbles 72

4.4.1 Removing gas initially 73
4.4.2 Bubble formation 73
4.5 Test procedures 77
4.5.1 Steady state 78
4.6 Summary 80
5. Results of the Non-Reacting Flow 82
5.1 The experimental conditions 82
5.2 Computed and measured temperature profiles 83
5.3 Richardson number effect 87
5.4 Effect of gravity on flow patterns 92
5.5 Temperature sections along the passages 96
5.6 Effect of inverting ΔT 103
5.7 Temperature statistics 115
5.7.1 Mean temperature change along the passages 115
5.7.2 Temperature non-uniformity change along the passages 117
5.8 Summary 121
6. Results of the Reacting Flow 123
6.1 The experimental conditions 123
6.2 Temperature measurement 124
6.2.1 Wire coating 124
6.3 Reaction parameters 126
6.3.1 Reaction kinetics 126
6.3.2 Heat released indication 128
6.4 Temperature profiles 130
6.4.1 Comparison with measured temperature profiles 130
6.5 Temperature statistics 135
6.5.1 Mean temperature change along the passages 135
6.5.2 Temperature non-uniformity change along the passages 137
6.6 Summary 143
7. The Conclusion and Future work 145
7.1 Conclusions 145
7.2 Recommendations for future work 147

References 149
Appendix A 158
Physical properties used in the computations 158
A.1 Determining the density and viscosity of solution 158
Appendix B 161
B.1 Determining Enthalpy of a Chemical Reactions 161
B.2 Testing procedure 161
B.3 Results and discussion 162
B.3.1 Minimum temperature of the reaction 162
B.3.2 Calculating the enthalpy of reaction 162
Appendix C 164
Assessment of the wire conduction error 164
C.1 Swirl element geometry 164
C.2 Flow System 166
C.3 Temperature measurement 166
Appendix D 167
Chemical Materials Used 167
D.1 Deionized water 167
D.2 Solutions A and B 167
D.3 Preparing the Solutions 167
D.3.1 HCl-NaOH Reacting System 167
D.3.2 $NaClO_2$- $K_2S_4O_6$ Reacting System 168
Appendix E 169
Reactor Design Details 169

List of figures

Figure 2. 1 Operating lines for minimum reactor size. XA is the conversion of reactant A. The curves represent the reaction rate which are increased with increasing the temperature (Levenspiel, 1999). 7

Figure 2. 2 Alkaline hydrolysis of 4-nitrophenyl acetate (Plouffe, et al., 2016). 10

Figure 2. 3 Computations showing species mixing of three Y mixers (Gobby, et al., 2001). 14

Figure 2. 4 Two consecutive elements of the specimen mixer considered computationally..... 15

Figure 3. 1 The four elements of the F-element Reactor 44

Figure 3. 2 The four elements of the S-element Reactor. 45

Figure 3. 3 The four elements of the C-element Reactor. 46

Figure 3. 4 Grid display on the walls of passages of S-element Reactor using uniform mesh at element size 0.0005 mm. 51

Figure 3. 5 Numerical solution dependence on the grid for C-elemen Reactor. The Z is zero in the meeting point of A and B species inlet (see Fig. 3.3 b) 53

Figure 3. 6 Numerical solution dependence on the grid for F-element Reactor. The Z is zero in the meeting point of A and B species inlet (see Fig. 3.1 b) 54

Figure 3. 7 Numerical solution dependence on the grid for S-element Reactor. The Z is zero in the meeting point of A and B species inlet (see Fig. 3.2 b) 55

Figure 4. 1 The experimental apparatus. 59

Figure 4. 2 Overall flow network of the apparatus. The blue lines are passages to transport the solutions. The red lines are the feed and outlet for the heat exchangers. The green lines are the surfactant passages..... 60

Figure 4. 3 Diagram showing the reactor..... 61

Figure 4. 4 Preheating system of F-Element Reactor 64

Figure 4. 5 Temperature measurement device. 65

Figure 4. 6 Thermocouple wire paths in domain of C, F and S element Reactor. 66

Figure 4. 7 Heat transfer for a thermocouple in a non-uniform temperature flow. 66

Figure 4. 8 Conducting rod in a sinusoidal temperature field..... 68

Figure 4. 9 Theoretical estimation of heat conduction error with effect of the wire diameter (d_R) and fluid flow rate (Re). 69

Figure 4. 10 Experimental estimation of heat conduction error at 125 μm wire diameter with effect of wire velocity. 71

Figure 4. 11 Experimental estimation of heat conduction error with effect of wire diameter..... 72

Figure 4. 12 Topside view of the F-element Reactor showing bubble formation within the passages. 75

Figure 4. 13 The relationship between bubbles formed and types of water. 75

Figure 4. 14 The relationship between bubbles formed and temperature of reactor plate. 76

Figure 4. 15 The effect of using the float on the number of bubbles formed. 77

Figure 4. 16 Reactor temperatures recorded at two different thermal conditions of heat exchanger. 80

Figure 5. 1 Reactor C: measured and computed temperature profiles along the rear path. Effect of Reynolds number and imposed temperature difference. The points represent the experimental data and the line represents the computational results. 85

Figure 5. 2 Reactor F: measured and computed temperature profiles along the rear path. Effect of Reynolds number and imposed temperature difference. The points represent the experimental data and the line represents the computational results. 86

Figure 5. 3 Reactor S: measured and computed temperature profiles along the rear path. Effect of Reynolds number and imposed temperature difference. The points represent the experimental data and the line represents the computational results. 87

Figure 5. 4 Reactor C: computed temperature profiles along the rear path at the two experimental values of Richardson number and with Ri = 0 (g = 0). 89

Figure 5. 5 Reactor F: computed temperature profiles along the rear path at the two experimental values of Richardson number and with Ri = 0 (g = 0). 90

Figure 5. 6 Reactor S: computed temperature profiles along the rear path at the two experimental values of Richardson number and with Ri = 0 (g = 0). 91

Figure 5. 7 Reactor C: computed pathlines of flow along the flow passage at Re = 32 and ΔT 20 ^{o}C. 93

Figure 5. 8 Reactor F: computed pathlines of flow along the flow passage at Re = 32 and ΔT 20 ^{o}C. 94

Figure 5. 9 Reactor S: computed pathlines of flow along the flow passage at Re = 32 and ΔT 20 ^{o}C. 95

Figure 5. 10 Location of the five passage sections used for contour and vector plots of temperature and flow fields in the computations. 96

Figure 5. 11 Reactor C: computed temperature contours over the five sections along the flow passage for each of the three Reynolds number values with ΔT = 20 ^{o}C. 97

Figure 5. 12 Reactor C: computed velocity vectors in the planes of the five sections along the flow passage for each of the two Reynolds number values with ΔT = 20 ^{o}C. .. 99

Figure 5. 13 Reactor F: computed temperature contours over the five sections along the flow passage for each of the three Reynolds number values with ΔT = 20 ^{o}C. 100

Figure 5. 14 Reactor F: computed velocity vectors in the planes of the five sections along the flow passage for each of the two Reynolds number values with ΔT = 20 ^{o}C. 101

Figure 5. 15 Reactor S: computed temperature contours over the five sections along the flow passage for each of the three Reynolds number values with $\Delta T = 20\ ^{o}C$..... 102

Figure 5. 16 Reactor S: computed velocity vectors in the planes of the five sections along the flow passage for each of the two Reynolds number values with $\Delta T = 20\ ^{o}C$..... 103

Figure 5. 17 Reactor C: measured temperature profiles along the rear path. Effect of inverting the temperature difference at the three different values of Reynolds number. 105

Figure 5. 18 Reactor F: measured temperature profiles along the rear path. Effect of inverting the temperature difference at the three different values of Reynolds number. 106

Figure 5. 19 Reactor S: measured temperature profiles along the rear path. Effect of inverting the temperature difference at the three different values of Reynolds number. 107

Figure 5. 20 Reactor C: measured and computed temperature profiles along the rear path. Effect of inverting temperature difference..... 108

Figure 5. 21 Reactor F: measured and computed temperature profiles along the rear path. Effect of inverting temperature difference..... 109

Figure 5. 22 Reactor S: measured and computed temperature profiles along the rear path. Effect of inverting temperature difference..... 110

Figure 5. 23 Reactor C: computed temperature contours over the five sections along the flow passage for each of the three Reynolds number values with $\Delta T = 20\ ^{o}C$ and $\Delta T = -20\ ^{o}C$..... 112

Figure 5. 24 Reactor F: computed temperature contours over the five sections along the flow passage for each of the three Reynolds number values with $\Delta T = 20\ ^{o}C$ and $\Delta T = -20\ ^{o}C$..... 113

Figure 5. 25 Reactor S: computed temperature contours over the five sections along the flow passage for each of the three Reynolds number values with $\Delta T = 20\ ^{o}C$ and $\Delta T = -20\ ^{o}C$..... 114

Figure 5. 26 C, F and S element Reactors: computed bulk temperature over the four elements along the flow passage for each of the three Reynolds number values..... 115

Figure 5. 27 C, F and S element Reactors: computed bulk temperature over the four elements along the flow passage at Re = 130..... 117

Figure 5. 28 Reactor C: computed standard deviation of temperature over the four elements along the flow passage for each of the three Reynolds number values. 118

Figure 5. 29 Reactor F: computed standard deviation of temperature over the four elements along the flow passage for each of the three Reynolds number values. 119

Figure 5. 30 Reactor S: computed standard deviation of temperature over the four elements along the flow passage for each of the three Reynolds number values. 120

Figure 6. 1 Temperature profile using uncoated thermocouple wire at the HCl-NaOH reaction system in F-element Reactor. 125

Figure 6. 2 Temperature profile using coated thermocouple wire at the HCl-NaOH reaction system in F-element Reactor. 126

Figure 6. 3 Effect of the pre-exponential factor (A) on the profile of average temperature along each element at Re 32 and Ri 3.4. 127

Figure 6. 4 Effect of the activation energy (E) on the average temperature along the wire path through each element computed using two different values of activation energy. Symbols are the corresponding values from the experiment. 128

Figure 6. 5 Temperature difference (ΔT_{max}.) between T_I and $T_{2\ max}$. in the HCl-NaOH and $NaClO_2$- $K_2S_4O_6$ reacting systems at different Re. The solid lines and dashed lines represent the computations and the experiments respectively. 130

Figure 6. 6 Measured and computed temperature profiles along the rear and front path at Re 32 in HCl-NaOH reaction system. Effect of imposed temperature difference..... 132

Figure 6. 7 Measured and computed temperature profiles along the rear and front path at Re 130 in HCl-NaOH reaction system. Effect of imposed temperature differences. 133

Figure 6. 8 Measured and computed temperature profiles along the rear and front path at Re 32 in the $NaClO_2$- $K_2S_4O_6$ reaction system. Effect of imposed temperature differences. 134

Figure 6. 9 Measured and computed temperature profiles along the rear and front path at Re 50 in the $NaClO_2$- $K_2S_4O_6$ reaction system. Effect of imposed temperature differences. 135

Figure 6. 10 Computed bulk temperature over the four elements along the flow passage for each of the two Reynolds number values of the HCl-NaOH reacting system. 136

Figure 6. 11 Computed bulk temperature over the four elements along the flow passage for each of the two Reynolds number values of the $NaClO_2$- $K_2S_4O_6$ reacting system.. 137

Figure 6. 12 Computed standard deviation of temperature over the four elements along the flow passage at Re 32 of the HCl-NaOH reacting system. 139

Figure 6. 13 Computed standard deviation of temperature over the four elements along the flow passage at Re 130 of the HCl-NaOH reacting system. 140

Figure 6. 14 Computed standard deviation of temperature over the four elements along the flow passage at Re 32 of the $NaClO_2$- $K_2S_4O_6$ reacting system. 141

Figure 6. 15 Computed standard deviation of temperature over the four elements along the flow passage at Re 50 of the $NaClO_2$- $K_2S_4O_6$ reacting system. 142

Figure 6. 16 Computed standard deviation of temperature over the four elements along the flow passage at Re = 32 in the HCl-NaOH and $NaClO_2$- $K_2S_4O_6$ reacting systems. 143

List of Tables

Table 2. 1 Properties of type-T and type-K thermocouples (Tarnopolsky, et al., 1999). . 21

Table 3. 1 The residence time of the reactors. 47

Table 3. 2 Physical properties used in the CFD model. 49

Table 3. 3 Grid specifications of reactors 52

Table 4. 1 Properties of convection boundary condition. 63

Table 4. 2 Constants of Eq. 4.5 for the circular cylinder in cross-flow. 68

Table 4. 3 Diameters of wires and inside sleeve diameters tested. 70

Table 5. 1 The boundary conditions used in the Non-Reacting flow tests. 83

Table 6. 1 The boundary conditions used in the HCl-NaOH reacting tests 124

Table 6. 2 The boundary conditions used in the $NaClO_2$-$K_2S_4O_6$ reaction tests. 124

Table 6. 3 The temperature difference (ΔT_{max}.) between T_I and $T_{2\ max}$. in the HCl-NaOH and $NaClO_2$-$K_2S_4O_6$ reacting system 129

Nomenclature

Symbol	Definition
A'	The pre-exponential factor
C_P	Specific heat capacity
C_j	Molar concentration of the species *j*
D	Mass diffusion coefficient of species
Da	Damköhler number (ratio of reaction rate to diffusion rate)
E	The activation energy of reaction
g	The gravitational acceleration
g_i	The gravity vector
g_i^*	Normalized the gravity vector
h	Heat transfer coefficient
k	Reaction rate constant
k'	Arrhenius rate
M	Mean molecular mass of species
OH*	Radical of hydroxyl
P	Pressure of the fluid
P^*	Normalized pressure
Pe	Péclet number (ratio of heat transfer by fluid motion to heat transfer by thermal conduction)
P_g	Outlet gage pressure
Pr	Prandtl number (ratio of momentum diffusivity to thermal diffusivity)
q	Convection heat transfer
Q	Volumetric flow rate of fluid
q^*	Heat generation rate from reaction
R	The gas constant
Re	Reynolds number (ratio of inertial force to viscous force)
Ri	Richardson number (ratio of natural convection to forced convection)
R_j	Reaction rate of species *j*
Sc	Schmidt number (ratio of momentum diffusivity to mass diffusivity)

T	Temperature
T^*	Normalized of temperature
T_B	Bulk temperature
T_B^*	Normalized bulk temperature
T_C	Temperature of the top and the bottom plates.
T_I	Temperature of reagent stream inlet
T_R	Temperature of copper reactor plate
T_o	Reference temperature
$\overline{T}$	Maximum temperature
u_i	Velocity of fluid in the flow direction
u_I	Velocity of inlet species
u_j	The velocity vector in the three directions (x, y, z)
u_j^*	Normalized velocity
V	Average velocity of fluid
V_R	The volume of reactor
W	Characteristic width of the flow passage
w	Width of flow channel
X_A	The conversion of reactant A
x_j^*	Normalized x direction
Y	Mass fraction of the species
$\dot{Y}$	Reaction rate
Y_o	Inlet mass fraction of species
Y^*	Normalized of mass fraction

Greek Symbols

Symbol	Definition
α	Thermal diffusivity of the fluid
ΔH	Enthalpy number of reaction
Δh_R	Enthalpy of reaction
μ	The fluid dynamic viscosity
λ	Thermal conductivity
τ_m	The relative measurement error of temperature
ξ	Normalized the glued length of the thermocouple
μV	Microvolt
ρ	Density
ρ_1	Fluid density at the temperature of inlet species
ρ_o	Reference density
ρ^*	Normalized density
ν_j	Stoichiometric coefficient of species *j*
δ_T	Characteristic thermal boundary layer thickness
τ	Residence time of reactor
σ_T	Standard deviation of temperature
$\overset{*}{\sigma}_T$	Normalized standard deviation of temperature

Abbreviations

Symbol	Definition
C, F and S	Types of reactors used in this work
CFD	Computational fluid dynamics
[BMIM]Br	1-butyl-3-methylimidazolum bromide
PQFP	The plastic quad flat pack
TBGA	The tape hall grid array
TCs	Thermocouples
AWG	American Wire Gage
A/D	Analogue to Digital Converter
CD	The drag force coefficient
BPB	Bromophenol blue
CR	Congo red
PDEs	Partial differential equations
PEEK	Polyether ether ketone
PFA	Per fluoro alkoxy

Chapter One

1. Introduction

Chemical processing commonly uses the liquid state for chemical reactions, whether for industrial production or for laboratory synthesis. This study aims to control the spatial variation of temperature produced by the heat of reaction, regardless of whether the reaction is exothermic or endothermic. The use of small sized passages with a geometry that encourages convection of heat to the passage walls will be explored in the research. Understanding the relationship between chemical kinetic parameters, flow parameters, fluid properties and the reaction process will be pursued using a combination of dimensional analysis, three-dimensional computation and experimentation.

Every reaction system has an upper limit of temperature, above which unwanted products form. Avoiding thermal runaway in a given reactor also requires the temperature to remain below a particular value. On the other hand, the highest possible temperature is needed to achieve a high reaction rate in order to have the smallest possible reactor size (Levenspiel, 1999).

Ideally, a given reaction would be carried out at precisely the highest temperature allowed since this maximizes the reaction rate for a successful reaction. In practice, since heat transfer between the reacting liquid and the surroundings requires a spatial temperature difference, there will always be variation in temperature within the reacting liquid. This variation means that when the highest temperature in the liquid is exactly at the value of the upper limit, all other elements of the liquid will not be reacting as rapidly as possible. The average reaction rate achieved will thus be lower than what could be achieved if the temperature were perfectly uniform and at the upper limit.

Approaching the upper limit of temperature requires reducing the temperature non-uniformity towards zero. This can be achieved using small passage size or a passage geometry that promotes convective heat transfer, both of which creates a smaller characteristic distance so the heat flux required to transfer the reaction heat release rate is achieved with a smaller characteristic difference in temperature.

Initial development of experimental and computational methodology will be based on a swirl element that has been developed previously in relation to species mixing in microfluidic devices.

Thermal mixing is far less difficult in liquids than species mixing, since the Prandtl number is typically much smaller than the Schmidt number for liquids. Thus, good species mixing should correspond to effective heat transfer. In the initial stage of reaction where the reactant streams mix, reaction occurs in thin mixing layers and the heat of reaction is able to spread easily to surrounding non-reacting liquid. Later in the reaction process, when the species are largely mixed, heat generation is more uniform throughout the liquid and heat transfer may be more critical to maintaining approximate thermal uniformity.

Typically, passage elements such as the swirl mixer can be connected together in series to form a long passage in which the reaction can progress, with the continuing mixing providing thermal regulation. This passage can be composed of different elements at the different stages of reaction. These element geometries can have different levels of mixing to suit the changing rate of reaction.

1.1 Research objectives

Control of spatial variation of temperature produced by the heat of reaction, whether the reaction is exothermic or endothermic, is crucial to avoid an uncontrolled reaction. This study aims to control heat reaction by enhancing the mass and heat transfer using small scale structured passages. The objectives of this study are to:

1. Use small scale passages to achieve a high level of thermal uniformity during the liquid phase reaction. Different passage geometries may be investigated to provide the range of thermal performance needed at different stages in a reaction with acceptable friction losses.

2. Establish a mathematical model for temperature non-uniformity within the flow passage in the small scale passages. This model demonstrates the main parameters that effect temperature non-uniformity such as the passage width, concentration of species, enthalpy of reaction and the species velocity.

3. Establish a (3-D) computational model for the geometries used in the study. This model can be used to predict the main features of the flow and temperature field in the passages of the geometries, such as flow direction and temperature non-uniformity along the flow passage. The physical and thermal properties of the system, such as heat transfer coefficient, heat capacity, density and viscosity of the fluid, will be discovered through CFD simulation with the experimental data of non-reacting flow.

4. Obtain measurements of the spatial variation of temperature within the passages of three different structured-passage geometries as the main objective of experimental work in the project. The spatial temperature will be measured using a fine-wire thermocouple to avoid disturbance of flow pattern and to achieve a high measurement accuracy. Using a small wire diameter could cause difficulty in controlling a location of temperature measurement; it may therefore be necessary to use a continuous and tensioned wire.

5. Investigate the effect of heat released from the reaction on the temperature non-uniformity in the flow passage in the geometries used.

6. Investigate the effect of buoyancy on flow direction and temperature non-uniformity in the flow passage in the geometries used.

7. Investigate the effect of the cooling system temperature on fluid temperature and temperature non-uniformity in the flow passage in the geometries used.

1.2 Research hypotheses

The current study investigates using the small scale structured passages to control the heat of reaction in the liquid phase exothermic reaction. Small scale passages allow for surface-to-volume ratios to be from 10000 to 50000 m^2/m^3. Consequently, a significant intensification of the mass and heat transfer and high yield of the desired product are achieved. Furthermore, using small size reactors could increase the process safety (Jovanovic, 2017).

Different passage geometries will be investigated to provide the range of thermal performance needed at different stages in a reaction. The geometries that will be used are

the simple channel, split-and-recombine and swirl geometries. The reactors will be designed to contain only four elements to reduce the cost and time required for the work. The first few elements will contain the largest concentrations of species and thereby the greatest challenge to thermal control occurs. The passage size will be relatively large to enable accurate measurement of the local temperature. In addition, the size is large enough allow to buoyancy to be significant. In spite of the smaller size passages allowing for significant thermal control, the importance of buoyancy will be reduced.

The experimental work focuses on measuring the spatial temperature within the domain of flow passage. Measuring the temperature required a fine-wire thermocouple to avoid disturbance of flow pattern and high accuracy of measurement. Two liquid phase exothermic reactions will be tested. The purpose of using two exothermic reactions is to investigate the effect of enthalpy of reaction on temperature non-uniformity. A computational model will be developed to simulate the experimental data for the temperature measurements. The physical and thermal properties of the system will be identified by implementing a non-reacting flow. This model will be used to predict the flow pattern and temperature distribution in the passages in the reacting flow. The buoyancy effect will be studied both experimentally and computationally. In addition, the computational model will be used to predict the standard deviation of temperature and flow direction along the flow passage. This will be used to establish the relationship between flow conditions and temperature non-uniformity for the reaction system in the structured flow passage.

1.3 Thesis structure

The structure of the thesis is organized in the following order:

Chapter **Two** includes the literature review of the previous work and the research related to the topic area of the current work is presented.

Chapter **Three** includes a description of how the mathematical model for the temperature non-uniformity in the reacting flow system was established. In addition, the geometry of three different reactors is described. Furthermore, a (3-D) computational model to simulate the temperature non-uniformity in reactors used is introduced. Also, the key

tools of this model are illustrated: these tools are boundary conditions, physical properties of the system, statistics and grid study.

In Chapter **Fou**r, the experimental apparatus used in this work and the temperature measurement procedure are described. Following this, three different geometries, F, C and S, which can be used as reactors are described. Subsequently, the measuring method for spatial temperature along the reactor is described and an experimental assessment of conduction error resulting from the measurement method used is presented. Finally, in this chapter, the methods used to reduce the number of air bubbles formed in the flow passage are described.

In Chapter **Five**, the experimental and computational results for non-reacting flow are presented. The chapter starts with the experimental conditions used and the agreement between the experiments and the computations. Then, the results that show the effect of Richardson number and gravity on the flow pattern and temperature distribution are presented. In addition, the effects of the Richardson number and Reynolds number on temperature non-uniformity are also presented.

Chapter **Six** is the last chapter describing results and focuses on the reacting flow. The chapter also starts with the experimental conditions used in this chapter. Then, the coating wire method and determination of the reaction parameters are described. Following this, the agreement between the experimental data and the computational results is examined. The effect of the Richardson number on the bulk temperature and temperature non-uniformity along the flow passage is shown.

Chapter Two

2. Literature Review

Recently, many studies have used small scale passages to try to increase the reaction rate by operating at the maximum allowable temperature uniformly throughout the reacting mixture. These passages are used to enhance the temperature uniformity by the increase in heat transfer coefficient associated with a smaller passage size. In a reacting system, temperature non-uniformity is affected by many parameters such as flow rate, reaction rate and heat of reaction. The effect of these on the temperature non-uniformity can be studied most effectively in terms of the dimensionless quantities Reynolds number, Damköhler number and non-dimensional enthalpy of reaction number.

2.1. Properties of small scale passages

A small scale passage, in the context of chemical reactors, is a structured channel which can be used to control mixing and heat transfer and typically refers to channels of size up to about a millimetre (Ehrfeld et al., 1999; Ehrfeld et al., 2000; Wegeng et al., 1996). Therefore, in comparison to traditional chemical reactors, the main feature of these structured reactors is the high surface area to volume ratio (Jäckel, 1996). Since the coefficient of heat transfer is inversely proportional to the channel diameter, the heat transfer rate in these channels can be significantly higher than for conventional heat exchangers (Schubert et al., 2001; Schubert et al., 1998). Therefore, within such channels, the reaction mixture can be cooled or heated with greater heat flux per reacting volume (Schubert et al., 1998; Lerou et al., 1996; Alépée et al., 2000). This case can lead to decreasing the accumulation of reaction heat and hot spots, and thus unwanted side reactions (Klaus et al., 2004). The result in many cases is a higher yield, selectivity and product purity. The structured channels are especially suited to strongly endothermic or exothermic chemical reactions.

In addition to heat transfer, small channels also improve mass transfer, so the species mixing time is shorter than for traditional reactors as diffusion time can be very short. Therefore, the impact of the mass transfer on the speed of the reaction rate can be decreased using small channels (Löwe et al., 2000).

The third important feature of small scale passages is the achievable hydrodynamic flow in the small sized channels. The flows are often laminar and highly symmetric (Gravesen et al., 1993; Branebjerg et al., 1996). These features are very important in modelling and simulating systems to develop the small scale engineering devices using rational design.

In reactions that occur in small size channels, the process parameters, for example flow rate, residence time, temperature and pressure, are easily controlled. In addition, the hazards of strongly explosive or strongly exothermic reactions can be largely reduced (Veser et al., 2000; Veser et al., 2001). Furthermore, the reactions that operate under high pressure or deal with toxic materials have been implemented more safely (Löwe et al., 2000; Ehrfeld et al., 2000).

Due to the above features, small scale channels can be helpfully used as process engineering tools for acquiring crucial information in a short time and safely (Klaus et al., 2004).

2.2. Optimum temperature of reaction

Levenspiel (1999) defines the optimum temperature of reaction as the temperature that makes the reactor size as small as possible for a given reactant conversion. This optimum could occur in an isothermal or a changing temperature system: in time for along the length of a plug flow reactor, a batch reactor or from stage to stage for a series of mixed flow reactors. Achieving this temperature is important because it represents the ideal so the real reaction system must try to approach it. It can also be useful to evaluate the extent to which the real reaction system departs from this ideal. In any type of reactor and at any composition, this optimum represents the temperature at which the rate of reaction is maximum. The locus of maximum rates is illustrated in Figure 2.1.

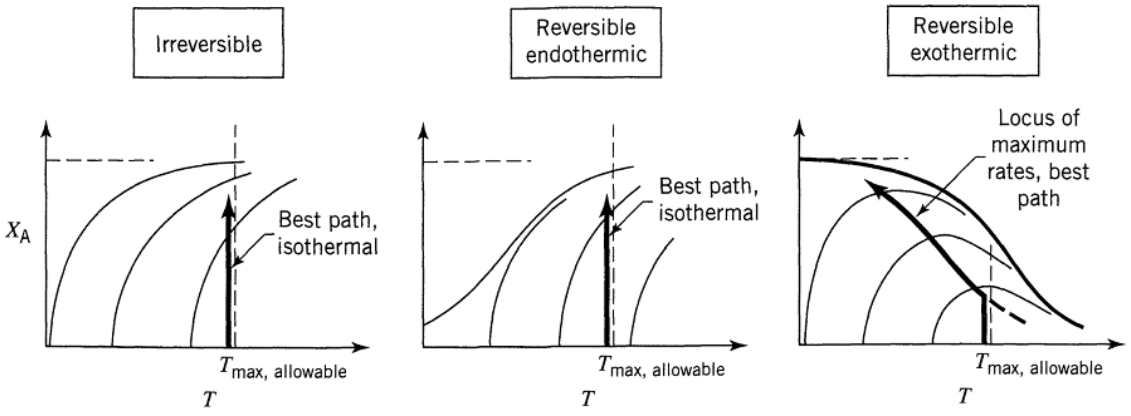

Figure 2. 1 Operating lines for minimum reactor size. XA is the conversion of reactant A. The curves represent the reaction rate which are increased with increasing the temperature (Levenspiel, 1999).

For irreversible reaction and at any composition, the rate of reaction always increases with increasing temperature. Therefore, the highest rate is achieved at the highest allowable temperature, in other words, at the optimum temperature of reaction: this is represented in Figure 2.1. by *T* max, allowable; the maximum conversion of reactant, which is represented by X_A, can be achieved, and then the maximum of the reaction rate. This temperature is crucial for design purposes and to prevent the possible occurrence of side reactions. For endothermic reversible reactions, the rate of reaction and the equilibrium conversion increase with increasing temperature. Therefore, as with irreversible reactions, the highest allowable temperature approach should be pursued. The situation is different with the reversible exothermic reaction. With increasing the temperature, both rates of forward and reverse reaction increase but the rate of reverse reaction increases more, so the maximum conversion of reactants decreases. Thus, in general, the maximum conversion in the reversible exothermic reaction decreases when the temperature is raised. This progression can be clearly seen in Figure 2.1. By linking the maxima of the different rate curves, the precise values of this progression are found, and this line can be called the locus of maximum rates.

2.3. Thermal management in small scale passages

Recently, in order to promote the production rate and purity of desired products through decreasing thermal non-uniformity, much research has shown using a small scale passage could lead to improvement of heat distribution within a specific reaction system. The diffusion length of the heat in small reaction passages is much smaller and this could lead to minimising hot spot formation and maximising heat dissipation through the walls of the passages. Because of their high heat transfer, small scale passages have wide application; for example, in the pharmaceutical industry production of specific chemicals and some biological reactions (Chen et al., 2012) can be implemented in such passages.

Hessel (2004) shows the advantages of using small reaction passages in chemical processes: this study explains some results of research related to using micro structured reactors in chemical reactions, some of which provide significant indicators regarding the probability of applying small scale channels with reactions, including homogeneous gas-gas and liquid-liquid reactions, gas-liquid reactions, halogenation reactions and catalytic reactions. On the other hand, there is little research referring to the ability of such mixers to enhance the isothermal reaction.

Waterkamp (2007) has studied the possibility of producing ionic liquids through using micro reactor technology which promotes the rate of synthesis. The study demonstrates the advantage of using a microstructured mixer in the alkylation step used in the production of an ionic liquid. This study used the strongly exothermic alkylation reaction to synthesise 1-butyl-3-methylimidazolum bromide, [BMIM]Br. In this reactor system, temperature was controlled which led to an increase in the reaction rates in a solvent-free process. The purity of product achieved was above 99% despite the temperature being as high as 85 ^{o}C. The increase of reactant conversion to product within a specific time clearly appeared in both the simulated and experimental results. The conversion of reactants increases with increasing rate of reaction, and the rate of reaction depends exponentially on the reaction temperature. Therefore, the conversion of reactants increases with increasing reaction temperature. The agreement between the simulated results and experimental results of the measured conversion data was good. This indicates the possibility of obtaining a reliable result for simulations of reaction at high temperature.

2.4. Influence of key parameters on thermal uniformity

The thermal uniformity within a reacting flow strongly depends on the heat released by the reaction and the surface area of heat diffusion. The quantity of heat released also depends on many parameters, such as the flow rate of reactants, reaction rate and the enthalpy of reaction. These parameters can be represented by dimensionless quantities, for example Reynolds number, Damköhler number and enthalpy of reaction number respectively. Therefore, the thermal uniformity and those dimensionless quantities are closely related. The Reynolds number, Re, is defined in fluid mechanics as a dimensionless quantity that describes the flow properties such as the pattern and rate of flow. The Reynolds number can be calculated as shown below:

$$\mathrm{Re} = \frac{\rho V W}{\mu} \qquad (2.1)$$

Where Re is the Reynolds number, ρ is the fluid density, V is the fluid velocity, W is the characteristic width of the flow channel and μ is the fluid dynamic viscosity. While, the Damköhler Number, Da, is defined in chemical engineering as a ratio of reaction rate to diffusion rate.

$$\mathrm{Da} = \frac{\text{Reaction rate}}{\text{Diffusion rate}} \qquad (2.2)$$

The Damkoler number can also be defined in terms of diffusion rate or convection rate. The value of Da can be used to indicate which is the faster reaction rate or diffusion rate, and also the conversion percentage of reactants. The reaction rate at Da>>1 is much greater than the diffusion rate and hence the conversion percentage of reactants is large. The diffusion rate at Da<<1 is much greater than reaction rate and hence the conversion percentage of reactants is small. The enthalpy number of reaction represents the heat content of reaction which is defined as the quantity of heat released or absorbed during the reaction at specific temperature and pressure.

2.4.1. Reynolds number

In most chemical processes, the channel geometry, flow velocity and fluid properties determine the flow regime and the extent of the contact area between the reactants. Increasing the contact area can enhance the reaction rate (Kockmann et al., 2013) and, thereby, change the enthalpy of the reaction within the domain of the reactor. Besides, the reaction rate strongly depends on the fluid flow rate and the residence time of the reaction; it decreases with increasing flow rate and decreasing residence time (Laudadio et al., 2017).

Plouffe et al. (2016) studied experimentally the effect of flow rate regimes on the conversion of reactants in two liquid-liquid systems. The study was implemented in five complex microreactors and focused on the hydrolysis of 4-nitrophenyl acetate using sodium hydroxide (NaOH) solution. The hydrolysis process was implemented in two different solvents: n-Butanol and toluene.

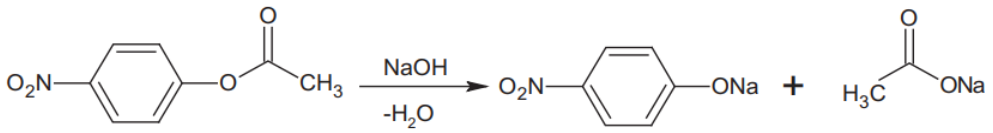

4-nitrophenyl acetate (4-NPA, org) Sodium 4-nitrophenolate (aq) Sodium acetate (aq)

Figure 2. 2 Alkaline hydrolysis of 4-nitrophenyl acetate (Plouffe, et al., 2016).

The results showed the same effect of flow rate regimes on the conversion of the reactant (4-nitrophenyl acetate) in all reactors used. The conversion of the reactant decreased with the increasing flow rate of reactant in the lower flow rate regime since the effect of the residence time is larger than the increase in the surface contact between reactants. The conversion

increased at higher flow rates, where the transition and the instabilities of the flow pattern occur. At the highest flow rates, a slight decrease of conversion was observed once the flow is fully dispersed.

Kockmann et al. (2013) studied the effect of the flow rate and residence time on the hydrolysis of the above reaction (hydrolysis of 4-nitrophenyl acetate), experimentally, in five new different microchannels. The results showed the consumption of reactant (NaOH) decreased as the flow rate increased and residence time decreased.

2.4.2. Damköhler number

The Damköhler number has a significant effect on thermal uniformity within the reacting system. Increasing the Damköhler number indicates an increased relative reaction rate and hence increasing heat released by the reaction. Therefore, it is hypothesized that thermal non-uniformity increases with an increasing Damköhler number, if the heat released from the reaction is uncontrolled. Waterkamp et al (2009) conducted a study to intensify the production process of ionic liquids by using microstructured channels. The study showed that the intensification of production can be enhanced by increasing the reaction rate, for the same flow conditions, by thermally controlling the heat of reaction and reducing the time required for the reaction. This was achieved by increasing the reaction temperature within small scale reaction channels which enhances controlling thermal non-uniformity through minimizing the distance of heat transfer to the wall. This study illustrated the capability of using continuously operating microstructured channels to produce 9.3 kg/day of 1-butyl-3-methylimidazolium bromide ([BMIM]Br), whilst the commonly used method is limited by ineffective batch procedures. This intensification occurred according to the Arrhenius rate law, that states the increasing reaction temperature leads to increasing the reaction rate. The Damköhler number has also increased due to increasing the reaction rate resulting from increasing reaction temperature.

Waterkamp (2009) showed that the reaction rate and quality of products are affected by the limitations in mass transfer and heat transfer, and hence the temperature non-uniformity. The study illustrated that these limitations have a negative effect on reaction rate and product quality. The results of the study showed how the temperature uniformity within the reacting system was affected by increasing the reaction temperature, and hence implied increase in the Damköhler number, through increasing the quantity of impurities in the final products. The increase in the reaction temperature leads to an increase in the reaction rate and hence the Damköhler number.

The increasing reaction rate with limitations in heat transfer can cause temperature non-uniformity within the reacting system and this is likely to lead to uncontrolled formation of hot spots. The hot spots can cause a side reaction and hence side products. The range of the Damköhler number did not appear explicitly in this study, which was reported without the kinetic parameter information for reaction. If the kinetic parameters of reaction and Damköhler number had been provided, the effect of the Damköhler number on the thermal uniformity and the product purity would have been clearly seen.

2.4.3. Enthalpy of reaction

In the reaction system, the non-dimensional enthalpy of reaction has a significant effect on the energy balance because it indicates the rate of the heat released from the reaction. It is expected the higher rate of heat released can lead to increasing the temperature non-uniformity through enhancing the hot spot formation. In order to determine and investigate the temperature non-uniformity in the reacting system, most research employs high exothermic reactions as they need a high thermal management. In this type of reaction, thermal non-uniformity will be clearly due to release enough heat to enhance the formation of hot spots. This case can cause thermal runaway and side reactions and consequently undesired products. Therefore, the low purity of desired products can indicate the occurrence of thermal non-uniformity within the reaction system. Using these exothermic reactions appears obviously in studies interested in achieving a thermal uniformity within liquid-liquid, gas-liquid and gas-gas reactions.

As mentioned, Waterkamp (2007) used a strongly exothermic alkylation reaction to study the intensification of ionic liquid synthesis in the microstructured channel under thermal controlled. Waterkamp showed, for the requirement of product purity and safety reasons, the bench top glassware is limited in most exothermic reaction system. Likewise, Löwe (2010) employed a highly exothermic reaction to synthesise a specific ionic liquid using a heat pipe-cooled microstructured reactor. Both studies refer to the fact that using the highly exothermic reaction, especially in synthesis of ionic liquids, can explain issues that relate to the thermal non-uniformity. Although both studies refer to the thermal uniformity within the reaction system decreasing with an increase in reaction heat magnitude, it is obvious that the motivation for the research is to increase the thermal uniformity within the reaction system.

2.5. Mixing in small channels

The mixing of reactants in small passages has increasing interest given the variety of relevant applications. These applications include production of pharmaceuticals, biological studies, medical testing and chemical materials. There are several mixer geometries and a diversity of techniques that have been studied to determine the advantages of utilizing each to obtain a high level of species mixing. Some of these are now reviewed to help identify those suitable for use later in the present study.

A number of papers (Hessel et al., 2005; Nguyen et al., 2005) have addressed some specific discussions on the subject of different mixer types. Most of these papers show a number of approaches to obtain a significant mixing in micro channels. However, a few of quantitative comparison between them is performed in most situations.

Hessel (2005) studied the mixing efficiency in micro scale channels within two types of liquid mixers. These mixers are classified as being either effective or ineffective mixers. Hessel identifies a variety of principles which have been used to motivate ineffective mixing in the channel: the mixing of species, which depends on liquid flow; physical restructure of the liquid elements; activation of a large interfacial region between reactants; and a large concentration gradient. These encourage the spreading of species through smaller scales and makes their contact more probable. Effective mixing depends on external factors which allow for liquids mixing through the exchange of momentum; for example, utilizing acoustic vibrations, electro kinetics or small scaled impellers. Achievement mixing in these techniques requires the application of external energy to the system. This energy is also in the ineffective mixers and is utilized to enhance the contact between liquids through increasing their interfacial region.

2.5.1. Parallel lamination

Parallel lamination of the inlet flows occurs in both "Y- Shaped" and "T-Shaped" mixers that employ the same principle for contacting elements incoming at separate inlets. In an explanation of the ineffective mixing principles, Hessel refers the employment of Y type micro scaled mixers for the mixing of liquids and gases. The mixing length required refers to the mixing efficiency for two gaseous species mixing in the Y mixer shape (Gobby et al., 2001). Computations illustrate the mixing length required around 2 mm for a channel width about 5 mm, a Peclét number of 8.08 and a flow rate of 0.3 m/s for both a -45° and +45° inlet orientation. When the distance of inlet streams reduces to 0.1 mm, the length of mixing required will

decrease to 0.5 mm with increasing the pressure drop in the required mixer. For these measurements, the comparison between this and other reports is not easy. Hessel also shows that for high turbulent flow of liquid systems, the times of mixing could be in milliseconds.

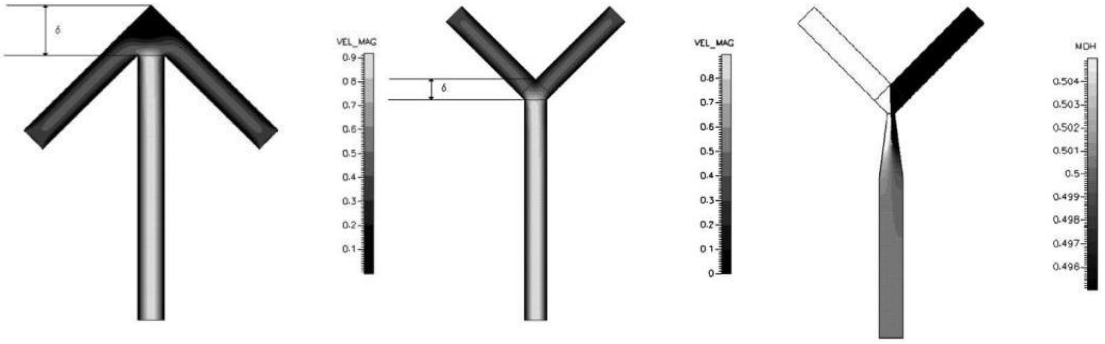

(a) (b) (c)

Figure 2. 3 Computations showing species mixing of three Y mixers (Gobby, et al., 2001).

Furthermore, he explains that there is little impact of the input channel angle on the efficiency of mixing. However, the change in flow passage scale could lead to the same impact by introducing a narrow bottleneck. In each situation, there is only one point of mixing through in the geometry and onc behind the first contacting area. This also indicates that the mixing depends only on species diffusion.

2.5.2. Folding flow

Folding mixer is an apparatus used to create a significant interfacial area between contacting liquids. This aspect allows the creation of a bigger contact area by dividing each liquid into a number of thin layers using split and reassemble mixers, thereby making the change of concentration gradient faster. The fast diffusion of species can occur when the thickness of layers of liquid are sufficiently small after enough splitting and recombining. This case increases the efficiency of mixing of materials. Hessel (2005) shows the split and recombine mixer requires three steps, which are flow splitting, flow recombining and flow rearrangement. The diffusion patterns of materials when increasing the Reynolds number might prevent determining of the success of the folding alone.

MacInnes (2007) discussed the features of folding flow mixers in the Stokes flow regime numerically through improving a scaling relationship. This relationship aids the prediction of the system uniformity and time of mixing. Most methodologies which discuss the

characterisation of mixers explain that the experimental methods using the estimating concentration to determine the mixing features are probably inaccurate. For perfect mixing, the deviation of species concentration preferable could be small enough. The measurement of such concentrations is, however, perhaps not easy. Therefore, this probably restricts the characterisation a micro mixer with high accuracy.

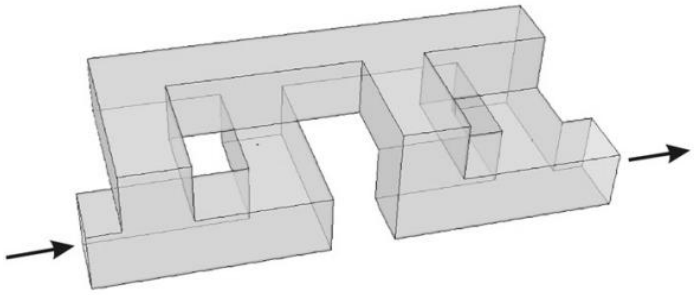

Figure 2. 4 Two consecutive elements of the specimen mixer considered computationally (MacInnes et al., 2007).

This research assumes the liquid flow mixing system consists of two liquid species. In this system, the mass flow rates and the volumes of these species are equal. This study used the F type of folding flow mixer to illustrate this mathematically, by using an equation describing the species transfer throughout the system of fluid. When using the dimensionless equations to characterize the species variation, the Peclét number considers a main dimensionless parameter to characterize the field of concentration. Subsequently, in addition to folding flow mixer features, such as split and recombine, the Peclét number represents the main parameter that affects the concentration deviation within a system of mixing. The Peclét number function is shown through the scaling relation. This function shows that the mixing elements number and constants link to the geometry used.

2.5.3. Chaotic mixer

Nguyen (2005) show that parallel lamination mixers, for example T type mixer, explained previously, could improve mixing performance by providing a rough surface or employing obstacles to allow chaotic advection to form throughout the flow. They clarified that obstacle insertion in the flow path probably aids the formation of the flow recirculation and swirl formation to enhance the perfect mixing. The review includes some examples which have been studied, such as Wang (2002), who showed the influence of obstacles in a T type mixer: a micro

channel of 100 μm, a Peclét number of about 200 and an obstacle diameter around 60 μm were all used. One result of this research explained that the obstacle did not enhance the recirculation formation at Reynolds number below 10 within the Stoke's flow regime. Therefore, a higher Reynolds number would be needed to make obstacles induce the chaotic advection. The suitable Reynolds numbers to achieve this case was above 100. Another study, undertaken by Lin (2003), shows practically the high effectiveness of obstacles in a micro mixer at Reynolds numbers above 200.

Mengeaud (2002) used a micro channel with a zig-zag shape for forming chaotic recirculating flow around the zig-zags' corners: Reynolds number were studied from 0.267 to 267 in a 100 μm channel with a 48 μm depth and at a fixed Peclét number of 267. Hessel (2005) showed the increasing of the degree of mixing could be obtained from additional recirculation at the larger Reynolds numbers, as well as through the lamination flow. This is a significant indicator which confirmed that perfect mixing can be obtained from lamination of flow with additional recirculation. Nguyen and Hessel showed that recirculation flow has a very small effect on the mixing efficiency at Reynolds numbers below 80/100. Consequently, the perfect design that includes any useful supporting of mixing should be at a Reynolds number higher than this scale.

Hessel and Nguyen referred to the induction of the recirculation flow which is developed by Stroock (2002) through the use of the staggered herringbone. Stroock shows the staggered herringbone mixer can work perfectly about 1-100 of Reynolds numbers. The research explains that the mixing length could be reduced approximately 100 times when using the herringbone mixer at Peclét numbers of 10^4 and 10^5 , when compared with a T shaped unstructured mixer. It was also mentioned that the mixing efficiency is highly dependent on the Peclét number, as MacInnes et al. (2007) found in folding flow mixers. In spite of the increase in efficiency of mixing in recirculation mixers, a large deviation of concentration might occur when the quiet dead zones, which contain a little mixing, are developed. Hessel found that the mixing efficiency is constant and dead zones are observed at low and moderate Re numbers below 100 if the Pe is kept fixed (Pe = 2600). These dead zones could be reduced through improvement of mixing using high Re numbers. This could be achieved by decreasing the lamellae width as a result of the reduced extension of the flow into the triangles; the impact of recirculation could also contribute to improving the mixing.

The continuous mixing could be tested despite more emphasis on encouraging chaotic flow. When chaotic mixing occurs throughout the structured internals of the reactor, the continuous dissipation of heat during the chaotic motion of liquids could be useful for a reacting system. However, undesired hot spots may be formed with the presence of quiescent zones.

Generally, it appears that there is some relationship between the properties of flow, for example, Peclét number and Reynolds number, which impact on mixing level and which can be achieved for a specific geometry. In addition, there was also a similar set of properties of flow which could help to obtain the appropriate level of deviation of temperature for a specific geometry.

2.6 Temperature measurement in small scale reactors

Measurement of temperature throughout various equipment is determined by several tools and different methods. However, some methods do not exactly match the requirements of measurement for such temperature or its gradation, where the application of the used tool may not fit. Thus, some of these methods need either modulation or replacement. Modulation could be difficult due to certain factors, such as the size of equipment, which is the most relevant factor influencing the measurement of temperature and its applied method and tools. The size of tools used in these methods also has other influences. Sometimes, any one of those influences can show a higher level due to the distribution of material inside, for example, large-size equipment; however, the influence may be smaller where the equipment is small (Sparrow, 1916). Accordingly, many methods employed to specify the temperature measurement in small-scale equipment such as the reactor passages.

Thermocouples have been shown to have several advantages for measuring temperature so they are commonly applied during thermal characterisation and testing of electronic equipment (Bailey, 1932). For example, thermocouples have been used to measure of the temperature of electronic components inside equipment (ASTM MNL 11, 1993). In addition to their simple application, thermocouples can be produced in a small size. Small scale thermocouples offer many benefits because of their ability to acquire data, as well as being more economic and widely obtainable. Nevertheless, small thermocouples are not fit for most electronic components due to the latter being too small. Generally, other similar components are not able to support holes or machine slots being drilled to accommodate thermocouples (Boelter et al., 1948).

Whatever the surface of a component, its temperature is typically measured by installing such thermocouples. A drawback of thermocouples can be seen when they are present on each component surface (Boelter et al., 1951). Local distortion of the temperature field represents this drawback and leads to errors in the taken readings from thermocouples. Almost all errors present are due to the following major causes which, according to Watson (1966) are:

1. The heat transfer by conduction between the wire of thermocouple and the component.
2. The created interface between the thermocouple measuring junction (bead) and the component shows specific resistances (Dutta, 1988).
3. The potential displacement of the effective junction of the thermocouple away from the intended surface to measure its temperature.

These causes enhance the tendency to find a proper technique to minimize errors with higher economic level (Watson, 1966). Therefore, the designed thermocouples must have important utilities that can by summarized by:

1. Good thermal contact with the component surface.
2. As small as possible.
3. Poor thermal conductivity of its manufactured material.

It is important that instructions for the installation of a thermocouple are followed precisely to minimize disturbance to the surface being measured and the surrounding environment (Kozarek, 1991). Moreover, many studies report the application, design, and adaptation of methods for testing and thermal characterisation of electronic packages (Joiner et al., 1996). Nevertheless, different problems occur during the measurement of temperature field in these studies.

2.6.1 Methods of temperature measurement in passages

This study has been devoted to investigating several cases: temperature measurement in passages is the most important case, especially in small scale passages. In this investigation, the design of the employed thermocouple is determined according to the specific concepts of the components used. Almost all of these concepts are based on previous designs or even applied methods. A description of important method can be shown in the following context.

Shaukatullah et al. (2003) reviewed the effect of thermocouple wire size and attachment method on the measurement of thermal characteristics of electronic packages. In this study, the measurement of surface temperature was achieved to determine the thermal characteristics of a plastic quad flat pack (PQFP) and tape hall grid array (TBGA) packages. This study includes the employment of various size ANSI type T thermocouples while the methods of attachment included thermally conductive epoxy, non-thermally conductive epoxy, aluminum tape, and polyimide tape. The outcomes of this study show that both thermocouple wire size and attachment method have significant effects on the parameters of thermal characterisation and the surface temperature measurement. In conclusion, Shaukatullah et al. (2003) demonstrate that the minimisation of error is obtained by both small size and low thermal conductivity thermocouple wires. Because of the better use of these designed thermocouples, the wires were able to transmit the amount of heat losses, otherwise, larger errors would have occurred due to the use of tapes and non-thermally conductive epoxy when attaching the thermocouples. Finally, as the wire size increases, the heat loss along with the wire increases.

The applied methods of temperature measurements in small scale passages are numerous and it would require considerable effort to include in this study. Therefore, only the important intended methods are reviewed, depending on specific limitations related to the design, attachment method, wire size, and error minimisation of the employed thermocouples. Some types of errors are classified as “heat conduction error”, and these are explored in the next section.

2.6.2 Heat conduction error through thermocouple wire

A contact-type temperature sensor is employed for measuring the temperature of non-isothermal fluid flows. In this test, heat conduction along the sensor body may cause a significant error known as “heat-conduction error”. A similar error can be estimated by a specific formula, derived when the fluid temperature is uniform, and which is determined as a specific condition. Differently, the heat-conduction error can be underestimated when a thermal field with a temperature gradient is measured using such a formula. Khine et al. (2013) accurately estimated the heat-conduction error by applying a universal physical model of a temperature-measurement system even when a temperature gradient occurred in the non-isothermal fluid flows. They succeeded in the derivation of a widely applicable estimation and/or evaluation formula of the heat-conduction error. Additionally, they experimentally verified their proposed formula and its

effectiveness in the two non-isothermal fields. These fields were a wake flow formed behind a heated cylinder and a candle flame. Whichever, the fluid-dynamical characteristics were quite different. Moreover, their results confirmed that the behaviours of the heat-conduction error are accurately experimentally represented by the proposed formula, even though this type of error is difficult to explain by the current formula. In their study, Khine et al. (2013) also undertook a theoretical analysis, which describes the effects of heat-conduction error on the fluctuating temperature measurement of a non-isothermal unsteady fluid flow. This analysis was conducted using the derivation of the frequency response of the temperature sensor. Their analysis showed a low-frequency range only caused the appearance of the heat-conduction error in the temperature-fluctuation measurement. Accordingly, the heat-conduction error can show no effect on the temperature-fluctuation measurement even by the temperature sensor accompanying the heat-conduction error in the mean-temperature measurements.

Khine et al. (2013) referred to the factors that affect the accuracy of temperature measurement, which are thermocouple-wire diameter, the thickness of an insulating layer of the wire, and type of thermocouple wire. For example, the increase in thermocouple-wire diameter will enlarge the time constant and slow the response speed of the thermocouple.

Another method for determining heat-conduction error is discussed in this section due to its important relationship to the temperature measurements in passages. A leaf temperature error from heat conduction along thermocouple wires is an investigation made by Tarnopolsky et al. (1999). Based on the idea of heat conduction through the wires can be specified as the one source of error in thermocouples (TC), they achieved their investigation. Since the leaf-to-air temperature difference is large and there is inadequate contact between TC and leaf, this error can potentially affect the leaf temperature measurement. While the problem (error) occurs, the best proper solution could be the selection of small-diameter TCs with low thermal conductivity, as well as good contact with the leaf. Hence, the researchers carried out a laboratory experiment to define the heat-conduction error as a function of TC-type, wire diameter, insulation, and the contact length between leaf and wire. They guaranteed repetitiveness through the use of a thin plastic plate as a leaf-substitute in most of their conducted tests. Moreover, they determined a correction factor during some measurements using vivo pepper and tomato leaves. During tests, good contact was ensured by glueing different lengths of the TC wires to the plate or leaf. In such tests, a thermo-electric cooler also establishes the controllable temperature differences.

When a length of about 22 mm of AWG 40 (0.08 mm diameter), Teflon-insulated type-T (copper-constantan) thermocouple was glued to a leaf, a conduction error, τ, about 1% which is relatively attributed to the leaf-to-air temperature difference was expected. This length reduced to 14 mm when the insulation was removed. Besides, the replacement of the insulated type-T thermocouple with another insulation of type-K (chromel-alumel) thermocouple of the same gage required about 10 mm for the same 1% error. A relationship was made between the relative measurement error, τ_m, and normalized glued length, ξ , as shown in the following equation, to introduce an approximate theoretical solution.

$$\tau_m = \exp(-\xi) \tag{2.3}$$

In summary, the conduction error of the popular type-T TCs can be reduced by (1) reducing the diameter of the wires; (2) improving contact between the wire and the substance to be measured (air, leaf); (3) stripping the insulation of the TC wires; and (4) switching from type-T to TCs with lower thermal conductivity, one possibility being the type-K (chromel ±alumel) TC, as shown in Table 2.1. (Tarnopolsky et al., 1999). Their attempt to quantify the conduction error associated with leaf temperature measurements, as a function of wire-type, diameter, insulation and contact length is shown below.

Table 2. 1 Properties of type-T and type-K thermocouples (Tarnopolsky, et al., 1999).

TC	Temperature range (°C)	Sensitivity μ V/K	Material	Thermal conductivity, kW/(m.K)	Conductivity sum for couple W/(m.K)
Type-T	-130 to +400	40	Copper Constantan	380 21	401
Type-K	-160 to +1260	40	Chromel Alumel	19 30	49

Heat transfer occurs through the thermocouple wires when exposed to an environment that has a temperature that differs from the object being measured. Such transfer disturbs this system, changes the thermocouple junction temperature and causes the error during measurement. Besides this, the electrical insulation of the thermocouple also has effects on the surface temperature measurement, according to Alwaaly et al. (2015), who investigated these effects through analytical, numerical and experimental analyses. Various surface temperatures were measured using a Type-K thermocouple with two diameters and different exposed wire lengths. To carry out the measurements, they employed thermocouples in three different cases

of direct contact, which were: 1) with the surface, 2) with vertical extended wires, and 3) exposure to natural convection. During their analyses, they confirmed three important points about the role of the wire diameter of the thermocouple and its impact on the temperature measurement. Ultimately, as a conclusion, a larger wire diameter means an increase in the cross-sectional area, which allows more heat to be conducted through the wires (Alwaaly et al., 2015).

Another theoretical investigation on the fluctuating temperature measurement using fine-wire of thermocouple was made by Tagawa et al. (2005). They performed a fine-wire thermocouple (temperature sensor) and cold wire for the theoretical analysis of their frequency response. Depending on the boundary condition of heat transport between the temperature-sensing part and its adjoining support, they rigorously derived a strict solution of the response with a single equation. Moreover, their theoretical results were employed as a platform for developing the technique of response-compensation, which are widely applicable to fine-wire thermocouple (sensors). The validation of the solution was examined through some experiments in which they successfully compared a 3.2 μm tungsten and a 0.63 μm platinum wire. In these experiments, they performed the technique of response-compensation to measure the fluctuating temperature using these two wires due to their common availability as some of the fastest temperature sensors (thermocouples) (Tagawa et al., 2005).

2.7 The effect of wire coating on the accuracy of temperature measurement

The insulation of thermocouple wires is particularly difficult and sometimes inflexible due to most insulation materials not having high-temperature resistance. Often, the insulation materials that show high-temperature resistance are fragile and inflexible or porous. For high-temperature applications, therefore, insulation of thermocouple wires will be difficult and the wires are not useful without such insulation.

Different inventions have been made for wires with ceramic insulation. These inventions relate to thermocouple wires and to thermocouples manufactured from these wires. Ragless et al. (1991) invented a specific wire that was insulated by a relatively thin ceramic coating to allow flexibility for use in thermocouples. They demonstrated the particular useful application of non-porous insulation for thermocouples made of this type of wire.

In their three confirmations of different analyses, Alwaaly et al. (2015) pointed out the effects of thermocouple electrical insulation on the measurement of surface temperature. The

first confirmation was obtained from the analytical results of the thermocouple wire with insulation. It specified that there is no determined critical radius and that there is a continuous increase of the rate of heat flux around the thermocouple wire with its specific diameter, even if it is larger than the critical radius. The second confirmation specified that during numerical analysis by COMSOL Multiphysics software, the electrical insulation shows a negligible thermal effect. The third confirmation specified that the temperature measurement was impacted by the thermocouple diameter during the experimental analysis.

Kato et al. (2007) developed a comprehensive fine-wire thermocouple probe to aid further theoretical analysis of the frequency response. In this development, the physical properties and insulation coating of two wires composing a butt-welded fine-wire thermocouple were investigated to evaluate their differences and influences. They demonstrated the complex behaviour of the frequency response of the copper-constantan (type-T) thermocouple through their developed solution. They also demonstrated the differences between the frequency responses of the thermocouple wire in air and water flows. It was uniform in the cross-section of the wire in the air, while it is remarkably nonuniform in water. Furthermore, the reliability of fluctuating temperature measurement in high-temperature turbulent flows was also improved. Particularly, both the physical properties and insulation coating have significant influences on the frequency response of a fine-wire thermocouple probe for fluctuating temperature measurement

2.8 The noise of the temperature measurement

As a product characterisation, temperature measurements represent an important part either in the development and verification of a design, or in the qualification of a product during production test. Almost all measurements are conducted within environments that have high levels of electrical noise. Sometimes, a noisy environment can be an obstacle in the taking of good measurements, especially, when the measured-required voltages are small, and when using thermocouples. Although thermocouples are rugged, inexpensive, and measure a wide range of temperatures, they also produce a millivolt range of voltages and microvolt changes per degree C temperature change. The complexity of measuring thermocouples can be hidden by the modern data logger, for example, Agilent loggers (Agilent, 2008). After the setting of the thermocouple type when it is typically connected to the data logger, the instrument shows the reading in degrees C. Due to the junction of the two-welded dissimilar metals of a thermocouple at one

end, a non-linear voltage with a low amount corresponding to the temperature is generated across the leads of the thermocouple. This generation of the voltage occurs because of the heating of that junction. For instance, the J-type thermocouple shows a very low voltage over 50 µV at 0 °C. This type of thermocouple displays the order of 5 µV per degree C in comparison with other types. Both small voltages and their small changes are measured and resolved by a proper measuring device, respectively. As a result, the measurement is largely impacted by a small amount of noise due to these very low-generated voltages.

The common sources of noise that influence the thermocouple measurements are mainly three sources:

1. Common mode noise generated from ground loops;
2. Normal mode noise generated from electromagnetic fields;
3. Electrostatic noise generated from rotating equipment.

The elimination or minimisation of each one of these common three sources can be described in several ways. For the common mode noise, their effect is minimised by avoiding the ground loops. The normal mode noise is minimised by 1) using twisted shielded pair which reduces the exposure to the magnetic field; 2) avoiding the fields; 3) using a filter; and 4) selecting the integration period of the A/D. Finally, the electrostatic noise must be coupled into the measurement via stray capacitance. Therefore, the minimisation of the capacitive coupling to the thermocouple is acquired by using shielded twisted pair and grounding one end to the shield (Agilent, 2008).

2.9 Buoyancy effect on the flow pattern

During the studies of flow and the characteristics of phases of materials inside small-scale equipment such as the reactor passages, some investigations have been performed to explore the effects of various operating and design parameters on flow dynamics and the quality of mixing. Such effects are qualitatively evaluated for the optimisation of mixing in these types of reactors. Most effects can be seen through the formation of vortices as one of the gravity influences on the flow dynamics and good mixing.

Soleyman et al. (2008) simulated a three-dimensional numerical investigation for the flow dynamics and mixing characteristics of liquids inside T-type micromixers to achieve the aforementioned purposes. As a result, good mixing was achieved by the development of vortices, which essentially influenced the performance of such mixing. Both flow rate and the geometrical parameters of the mixer, such as the aspect ratio, mixing angle, and throttle size, significantly impacted the occurrence and development of the vortices. It was experimentally proved that the new mixers provide a higher quality of mixing compared to that in the ordinary T-mixers.

Through their theoretical approach, using computational fluid dynamics and simple scaling, MacInnes et al. (2005) developed a quantitative understanding of the alternating flow method of mixing using a pressure-driven flow. In this approach, an alternating injection into a single microchannel of two or more solutions, to be mixed, is produced by using external flow control. Thus, the shear stress causes a thin striation that stretches the slugs of a solution, which is finally mixed. This mixing mostly encounters a specific condition, that is the approaching of the Reynolds number to zero and the negligibility of inertia effects. This condition is a common situation in microchannel flows where liquids of relatively high viscosity, such as ionic liquids, are employed. The core region of flow experiences much slower mixing, which is presented as Pe -1/2, after which it follows the initial time period of rapid mixing of fluid outside this core that is scaled as Pe -2/3. Both mixing cases are based on the scaling theory. They also developed an approximate correlation as a function of time for the deviation from the perfectly mixed state, where that the correlation is also valid for the Peclet number, slug length and solution mixture ratio . They conclude that the injection process forms the channel section, over which the initial uniformity of each solution causes the limitation of the produced mixture uniformity.

Another study on the numerical characterisation of folding flow in microchannel mixers and conducted by MacInnes et al. (2007) considered the circumstance of non-inertial flow, i.e. Stokes flow regime, for mixing different liquid streams. Due to the larger Schmidt number of liquids in such conditions, the diffusion of species remains weak, while the diffusion of momentum is dominant. In this regime, most mixers show a folding flow pattern, which approximates the baker's transformation. This scaling mixer is geometrically developed depending on the exact equation of transported species; however, the effectiveness of this scaling is examined through making the computations for a specimen mixer geometry. Moreover, the actual mixing characteristics of the specimen mixer over the whole range of Peclet number are

excellently represented by the relation of this developed scaling. They also developed the design relations based on the scaling relation in order to compute the Peclet number of operation, the number of mixing element, and the pressure drop incurred. All these computations are made to acquire a given mixture uniformity during a specified mixing time.

Liu et al. (2004) numerically conducted a further study in a microchannel for the mixing of two fluids, namely pure water and a solution of glycerol in water. They investigated the variation of mixing behaviour and the variation of the properties of the two fluids when the content of glycerol is varied; the properties were diffusivity, density and viscosity. They employed the following three micromixers: 1) a squarewave mixer, 2) a three-dimensional serpentine mixer, and 3) a staggered herringbone mixer, to test the mixing phenomena. Accordingly, their investigation includes the numerical solutions for the obtained equations of continuity, momentum, and solute mass fraction, respectively. As one proposition, a criterion index of mixing uniformity was made to evaluate the mixing performance. The averaged properties in this system led to Reynolds numbers about 1 and 10. These values show effective impacts on the performance of mixing. An inverse variation between the mass fraction of glycerol and the mixing performance was obtained for the value of 1 of the Reynolds number. This variation occurs due to the dominance of molecular diffusion. Consequently, inside the mixers, a significant reduction in the residence time of the fluid causes a deterioration in the mixing performance.

Another important parameter that can impact the flow and temperature distribution within the domain of the microreactor is the buoyancy of the formed bubble during the mixing of liquids. Bubbles behave as solid particles when a rigid surface and, consequently, no-slip boundary condition on their surface exist. When the bubble is generated within the domain of the microreactor, a drag force, consisting of pressure and friction parts, is created in the vertical direction. Due to the small Reynolds numbers, the friction dominates, although it originates from the viscous forces. Simultaneously, the higher velocities drive the flow to detach from the bubble and result in eddies. This detachment of flow leads the pressure part to become significantly effective. Hence, the drag force coefficient (C_D) makes the combination of both parts, i.e. friction and pressure parts. Furthermore, the buoyancy force, as shown in the following equation gives a vertical force balance (Hessel, 2015):

$$C_D \rho_l \frac{u^2}{2} A_b = (\rho_l - \rho_g) g \frac{d_b^3 \pi}{6} \quad (2.4)$$

where ρ_l and ρ_g are liquid and gas densities, u the liquid velocity, A_b the bubble surface normal to the flow, g the gravitational acceleration and d_b the bubble diameter. Ultimately, as a consequence of the reduced buoyancy forces, the generated bubbles move downward in a stabilizing position for the smaller bubbles case (Hessel, 2015).

2.10 Liquid-Liquid reaction system

Over the last decade, and due to their utilities, microreactors have begun to appear as an alternative reactor to conventional batch reactors. A microreacter provides a high surface-to-volume ratio, which could lead to a substantial increase in mass transfer inside the reactor. In addition, operating conditions such as flow pattern and small volumes could allow better control of a reaction compared to those of conventional reactors, thereby allowing safer process operating conditions; furthermore, higher yields of product are attainable in microreactors. Much research has been carried out on single phase and gas-liquid systems in microreactors; however few studies could be found in the literature on the liquid-liquid in such reactors. The chemical process, based on phase transfer analysis, is one of the chemical processes that could utilize the microreactor to a considerable extent. This chemical process is already widely applied in some chemical industries, such as in the pharmaceutical field and polymer industry (Jovanovic, 2017).

2.10.1 Chlorite - tetrathionate ($NaClO_2$- $K_2S_4O_6$) reaction system

During the last decade, many studies have used the reaction between the chlorite ions and tetrathionate, due to the reaction possessing important phenomena in connection with front propagation: excitation waves, spatial stability, 2D-front instability, 3D-front instability, pattern formation and oscillation. In spite of these wide uses, few studies have declared quantitative agreement between the model calculations and experiments. This is due to the lack of the key parameters, such as the rate coefficient, used in the partial differential equations of the model (Peintler et al., 2010). Peintler et al., (2010) showed that the stoichiometry of the chlorite consumption is given by:

$$2S_4O_6^{2-} + 7ClO_2^- + 6H_2O = 8SO_4^{2-} + 7Cl^- + 12H^+ \quad (2.5)$$

and the rate equation that described the initial rate of the reaction is

$$r = -\frac{1}{7}\frac{[ClO_2^-]}{dt} = k[H^+]^2[S_4O_6^{2-}][ClO_2^-] \quad (2.6)$$

where $k = 1.4x10^8$ $L^3.mol^{-3}.s^{-1}$. The authors mentioned that the partial order of H+ is almost three and the mechanism of the reaction is extremely complex. Tóth, et al. (1997) examined the modelling of front propagation using the same previous suggestion of kinetics and Eqs. 2.1 and 2.2. The equations were satisfactory but with $k = 7.28x10^4$ $L^3.mol^{-3}.s^{-1}$. Boissonade et al. (2001) have also used the same previous mechanism for their experiments and they found that $k = 5x10^6$ $L^3.mol^{-3}.s^{-1}$.

Jakab et al. (2002) studied experimentally the effect of temperature on the formation of cellular structures in the fronts of reaction-diffusion of chlorite–tetrathionate reaction. The reaction system was catalysed using acid catalysis. The experimental results were simulated using a simple model of reaction. A good agreement between the results and model was achieved yielding an estimated of activation energy ($E = 62.5 \pm 6.9$ kJ/mol) of the reaction system used.

A chemical model introduced by Peintler et al. (2010) has improved the quantitative description of the front propagation that occurs in the reaction of chlorite-tetrathionate. The stoichiometry of the reaction in this model facilitates the quantitative description for the front velocity as a function of the initial concentration of the reactants. Consequently, H+ as an autocatalyst in any front propagation study might be concerned with the obtained results from such a model.

Multiple effects due to hydrodynamic flows can affect an exothermal autocatalytic reaction. Buoyancy and the Marangoni convection are some of the exothermic reactions that experience these effects, which show a potential change in the structure and velocity of chemical waves. Thus, the production and consumption of chlorine dioxide in the reaction of chlorite-trithionate drive the induction and inhibition of Marangoni flow, respectively. This drive may

lead to different patterns of chemo-hydrodynamic (Liu et al., 2017). Liu et al. (2017) investigated the horizontal propagation of a reaction-diffusion-convection front with the upper surface open to the air. They showed that both Marangoni and heat convections have the same effect on the reaction. However, an oscillatory propagation of the front tip is observed under suitable conditions, only when the Marangoni effect is removed by the reaction of chlorine dioxide with the Congo red (CR) indicator. Thereafter, the floating is distinctly enhanced by replacing CR with bromophenol blue (BPB). This enhancement causes multiple vortexes as a result of the coexistence between BPB and chlorine dioxide. Additionally, the researchers employed several equations such as incompressible Navier-Stokes, reaction-diffusion, and heat conduction in this investigation. This employment of equations was to obtain numerical-experimental scenarios of front instability for the exothermic autocatalytic reaction coupled with buoyancy-driven convection and Marangoni convection.

Nagypál and Epstein (1986) studied the stoichiometry, kinetics, and mechanism of the chlorite-thiosulfate reaction. In their study, a variation in the time of reaction was irreproducible for identically prepared samples. They analysed the reaction time and its variation with temperature, volume, reactant concentrations, and stirring rate. This analysis led to the conclusion that the random fluctuations within the solution can induce the switch from net OH- production to net H+ generation.

Other important factors in the reaction of chlorite-tetrathionate have also been investigated (Horváth et al., 2003). Kinetics and mechanism are the factors that control the chlorine dioxide-tetrathionate reaction. Small deviations are initially present at high excess of chlorine dioxide with no chloride ions at the first step of the reaction. The presence of chloride influences the stoichiometry and accelerates the reaction too. The behaviour of the reaction is described clearly in a 14-step mechanism. Four known and two new proposed intermediates of those steps are used in this description.

Another study on the kinetics and mechanism has been achieved by Druschel et al., (2003) for the oxidation reaction of trithionate and tetrathionate at low pH by hydroxyl radicals. Unknown intermediate steps are tentatively assigned during the reaction of tetrathionate with OH*. The researchers proposed an outer-sphere electron transfer mechanism for this reaction to form $S_3O_4^{n-}$ based on the results of conducted experiments. They concluded that the rate

constant for the oxidation reaction of trithionate and tetrathionate with OH* is in excess of 108 $L.mol^{-1}.s^{-1}$ due to the kinetics of this reaction which include the Haber-Weiss mechanism.

In a series of investigations into the propagation front in the chlorite-tetrathionate reaction system, density fingering and its affected by chemical composition is experimentally investigated (Bánsági et al., 2004). For both upward and downward propagation fronts in such reactions, the observed region of convective instability increases with the increase of the concentration of reactants. Due to the domination of the pattern formation for certain chemical compositions by multicomponent convection, the increase of hydroxide ion concentration stabilizes and destabilizes the downward and upwards propagating fronts, respectively. This study includes the quantitative analysis for density fingering through the determination for dispersion values, whilst the initial evolution of the pattern formation is described by their characteristics.

Rica et al. (2013) investigated the tuning density fingering by changing the stoichiometry in the reaction of chlorite-tetrathionate. They showed that the variation of the ratio of the initial concentrations of the reactants can conveniently tune the buoyancy-driven spatiotemporal pattern formation. Moreover, the net density change during the reaction is reversed in its sign due to the increase in the stoichiometric excess of chlorite. However, a stabilization occurs to the originally unstable downward propagating reaction-diffusion fronts. In consequence, the density fingering coincides well with the observed behaviour of the reaction because of the quantitative characterizing for the diffusion curves obtained.

2.10.2 Hydrochloric acid-Sodium hydroxide (HCl-NaOH) reaction system

In every design of the reactor, the most important factors are the type of reaction, residence time, and the mechanisms of reaction. Mechanisms describe the chemical kinetics, which are determined to specify the basis for reactor design, the determining of activation energy, energy efficiency, steam production, and integrating the reactor outlet stream with the inlet.

Kralj (2018) examined a sensitivity method for the determination of concentration and activated energy using NaOH as a reactant, i.e. strong electrolytes, during titration. In this reaction, the estimation of the characteristics of the reaction is defined by the sensitivity parameter of the method. The defined parameter remains constant throughout the reaction where

the concentration of NaOH is determined by the sensitivity method according to the conductivity measurements. Kralj (2018) estimated the concentration of this electrolyte or even the product is proposed to be continuous.

David, (2004) suggested the activation energy for the HCl-NaOH reaction to be zero. This may be the reaction between strong acid and strong base is very fast.

2.11 Effect of species diffusion (*D*) on the temperature uniformity

A significant factor that shows effective influences on the flow of reactants, reaction rate, and temperature uniformity in the liquid phase reaction is the diffusion of species. Diffusion rate depends on the speed of species (kinetics) and temperature profile.

Phillips (2017) pointed out in his study the dramatic reduction of the heat and mass transfer due to the smaller hydraulic diameter of the channel allows much smaller diffusion distances of mass and heat. The swirl mixer for folding the flow using the inertial effects caused by a rotating motion at Reynolds numbers about 100 was used. This study shows slow mixing by diffusion across the interfaces between temperature or species gradients. For the enhancement of mixing, chaotic advection must be obtained. It was assumed, in this study, that both thermal and molecular diffusions are identical to directly apply the principles of species mixing to the heat transfer through a channel.

Mtsambiwa (2017) conducted an experimental investigation to assess the temperature measurement in a structured flow passage and quantify its performance as a new method. A swirl flow passage was employed to mix hot and cold deionized water at Reynolds numbers ranging from 20 to 80. This study indicates that microstructures promote a better level of thermal mixing, which enhances the distribution of heat within a reaction system (thermal diffusion). Small scales also reduce the required distance for heat transfer whilst such scales impressively increase the surface area to reactor volume ratio. Finally, the smaller volumes present higher heat exchange and mixing efficiency when the required distance for heat transfer is inversely proportional to the heat transfer coefficient.

2.12 Effect of bubbles formed on the temperature distribution

The generation of the bubble during the mixing of liquids within the domain of the microreactor, as mentioned in Section 2.10, enhances the challenges of investigations on the effects of such bubbles on the flow and temperature distribution in these microreactors.

Peela et al. (2012) fabricated a high-throughput microreactor and evaluated its performance for highly exothermic reactions. They implemented their design of such a reactor using COMSOL Multiphysics and a CFD package. During implementation, they investigated the effects of the distributor and channel position on flow uniformity. The total oxidation reaction of propane at low conversion was subsequently utilized in the fabrication and evaluation of their design. Comparably, the flow uniformity is significantly obtained as a result of the conical distributor used. This uniformity of flow is also influenced by the channel arrangement because of the removing of the central channel from the design. Both simulation and experiments show compatible results for flow uniformity. Furthermore, during experiments, the microreactor presents a reliable screening for catalysts and delivering kinetics. This behaviour of the reactor is attributed to the conversion deviation of propane between channels even when this deviation lies within the experimental error. Subsequently, the researchers completed propane oxidation by testing half a dozen catalysts during the application of such developed technology.

Al-Rawashdeh et al. (2014) proposed a design methodology for maintaining the non-uniformities of gas and liquid flow under the acceptable limit using a parallel micro/millichannels reactor. Maintaining the flow non-uniformities was achieved by the determination of the maximum allowed temperature deviation in each part of the reactor. A hydraulic resistive network model was utilized to quantify the effect of temperature deviation on flow distribution. Simultaneously, a one-dimensional energy balance model demonstrated the effect of flow rate on temperature deviation. The experiments were conducted using a barrier-based micro/millichannels reactor (BMMR). In the BMMR, hydraulic resistances (barrier channels) are placed in the gas and liquid manifolds to regulate the flow distribution. As a result, the flow nonuniformity is influenced in the barrier channels about 10 times more than in the reaction channels due to the temperature deviation. In consequence, above a certain critical liquid residence time, flow rate has no significant effect on the temperature deviation which depends on the liquid used, reactor material of construction, and its geometrical dimensions (Al-Rawashdeh et al., 2014).

Shah et al. (2012) developed a specific model for studying the effects of mixing, reaction rates, and stoichiometry on yield for mixing sensitive reactions. Since competitive-consecutive and competitive-parallel are the two classes of mixing sensitive reactions, the desired product

yields by these coupled reactions are based on the way of bringing the reactants rapidly. Furthermore, the stoichiometry of reactions influences the mixing as suggested by recent experimental data. All these aspects enhance their developed model of reaction-diffusion at the micromixing scale. The assumptions of mass concentration and mass diffusivities as constants lead to deriving PDEs on a mass fraction as the basis for these reactions. In addition, the analysis produces two dimensionless reaction rate ratios and a single general Damköhler number. Finally, the researcher have shown that the yield will be maximized when the striation thickness or the dimensionless rate ratio decreases. Also, the yield is affected considerably by the reaction stoichiometry, whereas the three variables all strongly interact.

In conclusion, bubble generation in microreactors has several effects, but it is impossible to restrict all these effects in this context. To avoid repetition and misunderstanding of the related factors, variables, and parameters that influence flow and temperature distributions, only the important effects have been reported from the previous studies. However, Hessel (2015) has specifically explored and explained all these effects of the bubble formation in liquids on the flow and temperature distributions in microreactors.

Chapter Three

3. Mathematical model

This chapter presents the 3-D computational model that is used in this study to complement the experimental work. The model uses the numerical solution for the flow, energy and species equations, with simplified representation of the dependence of reaction rate and the physical properties on temperature and composition. The model thus determines the 3-D fields of velocity, pressure, composition and temperature within the reactor. Thus the temperature non-uniformity in the passages can be determined by the model and, in comparison with temperature measurements, both model accuracy and reactor heat management performance can be assessed.

In this chapter, the governing equations are discussed in the first section. This is followed by the details of the geometry of reactors that will be used experimentally and for which computations will be made, and of the boundary conditions used to compute the reactors. Following this, the numerical solution approach is discussed and the relations used to represent the physical properties and to calculate statistics of the temperature field will be presented. This is followed by an assessment of the error associated with the finite grid size used in the numerical solution.

3.1 Governing equations

Reacting flow is governed by the equation for continuity, momentum, species and energy. The solution of these equations requires representation of the dependence of reaction rate and the physical properties on the local temperature and composition. These equations are solved to determine velocity, pressure, temperature and species concentrations.

This model is restricted by a steady laminar flow regime, Newtonian stress law, Fickian diffusion law and a second-order liquid phase reaction. In addition, the density and viscosity of the fluid were assumed to be non-uniform. The other physical properties of the fluid, such as thermal conductivity, diffusivity and heat capacity were assumed to be uniform. The governing equations are partial differential equations. The continuity equation represents the conservation of mass and the momentum equation represents the combination of Newtonian's second law of

motion; together with Stokes' stress law, these provide three momentum equations for velocity in the three directions. The equation for species represents the application of Fick's law of mass diffusion in the law of mass conservation. The energy equation represents the connection of the first law of thermodynamics with Fourier's law of heat conduction (Date, 2005). Using index notation, these equations can be stated as follows:

$$\frac{\partial \rho u_j}{\partial x_j} = 0 \tag{3.1}$$

$$\frac{\partial \rho u_j u_i}{\partial x_j} = -\frac{\partial p}{\partial x_i} + \frac{\partial}{\partial x_j}\left[\mu\left(\frac{\partial u_i}{\partial x_j} + \frac{\partial u_j}{\partial x_i}\right)\right] + (\rho - \rho_o) g_i \tag{3.2}$$

$$\frac{\partial \rho u_j Y_A}{\partial x_j} = \frac{\partial}{\partial x_j}\left(\rho D \frac{\partial Y_A}{\partial x_j}\right) + \rho \dot{Y}_A \tag{3.3}$$

$$\frac{\partial \rho u_j Y_B}{\partial x_j} = \frac{\partial}{\partial x_j}\left(\rho D \frac{\partial Y_B}{\partial x_j}\right) + \rho \dot{Y}_B \tag{3.4}$$

$$Y_C = 1 - (Y_A + Y_B) \tag{3.5}$$

$$\frac{\partial \rho u_j C_P T}{\partial x_j} = \frac{\partial}{\partial x_j}\left(\lambda \frac{\partial T}{\partial x_j}\right) - \rho \dot{Y}_C \Delta h_R \tag{3.6}$$

ρ, μ, C_P, λ and ρ_o are the physical properties of the fluid (density, viscosity, specific heat capacity, thermal conductivity and the reference density); g_i is the gravity vector; p is the pressure of the fluid; u_i is the velocity in the direction of the flow; u_j is the velocity vector in the three directions (*x, y, z*) in the Cartesian coordinates; D is the mass diffusion coefficient of species; Y_A and Y_B are the mass fractions of the species A and B respectively; $\dot{Y}_A$ and $\dot{Y}_B$ are the reaction rates; and, finally, Δh_R is the enthalpy of reaction.

The momentum equation shows the gravity term, which refers to buoyancy, and which could affect the flow pattern. The buoyancy depends on density difference (evident from the form of the term in Equation 3.2) and these differences arise from temperature variation in the flow and, in the case of reacting flow, also from concentration variation as reactants are consumed and products formed.

The flow regime was restricted by the steady laminar flow because that was the selected starting point to begin understanding the control of temperature, as it is easier to compute and measure. In addition, in the small size channels, it is likely that operation in the laminar regime would be practical.

3.2 Reaction mechanism

The chemical reaction applied in this model is an exothermic second-order irreversible liquid phase reaction as shown below:

$$A + B \rightarrow C$$

The reaction mechanism was assumed to be first order with respect to both A and B with the stoichiometric coefficient of each species equal to one:

$$R_j = \nu_j k' C_A C_B \tag{3.7}$$

R_j is the reaction rate of species *j*, ν_j is +1 for products and -1 for the reactants, C_A and C_B are the molar concentration of the reactants A and B respectively and k' is the Arrhenius rate.

$$k' = A' \exp(-\frac{E}{RT}) \tag{3.8}$$

A' is the pre-exponential factor, E is the activation energy for the reaction, R is the universal gas constant and T is the absolute temperature of the fluid. The reaction rate can be expressed in terms of mass fraction and as a mass rather than molar rate, using $C_j = \rho Y_j / M_j$, where C_j is the molar concentration of the species j, and M is the mean molecular mass of species. Thus, the rate terms in the species equations (Equations. 3.3 and 3.4) can be expressed:

$$\rho \dot{Y}_j = \nu_j \frac{\rho^2 M_j}{M_A M_B} k' Y_A Y_B \tag{3.9}$$

In terms of the enthalpies of formation per mass Δh_i , the heat generation rate from reaction is:

$$q^* = \rho \dot{Y}_A \Delta h_A + \rho \dot{Y}_B \Delta h_B - \rho \dot{Y}_C \Delta h_C \tag{3.10}$$

q^* is the heat generation rate from reaction. Δh_A , Δh_B and Δh_C are the enthalpy of formation of the species A, B and C respectively. Using the rate expression just developed, and defining the results in the expression for reaction enthalpy per mass of species C produced:

$$\Delta h_R = -\frac{M_A}{M_C} \Delta h_A - \frac{M_B}{M_C} \Delta h_B + \Delta h_C \tag{3.11}$$

The representation of reaction rate can be further simplified, without altering heat generation rate, by taking the mean molecular mass and formation enthalpy of the reactants to be equal. Noting that then $M_A = M_B = M_C / 2$ for simplification, the reaction rate and heat generation rate terms in the governing equations become:

$$\rho \dot{Y}_A = \rho \dot{Y}_B = -\rho k Y_A Y_B \tag{3.12}$$

$$\rho \dot{Y}_C = 2\rho k Y_A Y_B \tag{3.13}$$

where $k = A\exp(-\frac{E}{RT})$ and $A = \frac{\rho}{M_A} A'$.

and $$q^* = -2\rho k Y_A Y_B \Delta h_R \tag{3.14}$$

where $\Delta h_R = \Delta h_C$ if Δh_A and Δh_B are set zero.

3.3 Non-Dimensional parameters

In the reaction system developed, the flow, mass transfer and heat transfer depend on characteristic non-dimensional parameters. The above partial differential equations can be converted to non-dimensional forms in order to reveal these parameters. The following steps show how these conversions are made for each equation.

3.3.1 Flow

The flow equations involve some of the most important non-dimensional parameters. These scales are the average velocity of flow in the flow passage (*V*) and width of reactor passage (*W*). These scales can be used to obtain important parameters that can be used in the non-dimensionalising equations. These parameters can be described as the following:

$$u_j^* = \frac{u_j}{V} \tag{3.15}$$

$$\rho^* = \frac{\rho}{\rho_o} \tag{3.16}$$

$$x_j^* = \frac{x_j}{W} \tag{3.17}$$

The equation for conservation of mass can be non-dimensionalised by multiplying by $W / \rho_o V$:

$$\frac{\partial \rho^* u_j^*}{\partial x_j^*} = 0 \tag{3.18}$$

In order to non-dimensionalise the equation for momentum conservation, the definition of non-dimensional pressure and gravity vector use the same characteristic density and velocity as before and also the magnitude, *g*, of the gravity vector:

$$P^* = \frac{P}{\rho_o V^2} \tag{3.19}$$

$$g_i^* = \frac{g_i}{g} \tag{3.20}$$

when multiplying the equation for momentum conservation by $W / \rho_o V^2$, this equation can be converted to dimensionless form, and the Reynolds (Re) and Richardson numbers (Ri) appear.

$$\frac{\partial \rho u_j^* u_i^*}{\partial x_j^*} = -\frac{\partial p^*}{\partial x_i^*} + \frac{1}{\mathrm{Re}} \frac{\partial}{\partial x_j^*} \left(\frac{\partial u_i^*}{\partial x_j^*} + \frac{\partial u_j^*}{\partial x_i^*} \right) + \mathrm{Ri} \frac{(\rho^* - 1)}{(\rho_1^* - 1)} g_i^* \tag{3.21}$$

where $\mathrm{Re} = \dfrac{\rho_o V W}{\mu}$ and $\mathrm{Ri} = \dfrac{(\rho_1 - \rho_o) g W}{\rho_o V^2}$ (3.22)

and ρ_1 is the density of the fluid at the reagent stream inlet temperature.

The gravity term in the momentum equation (Equation 3.21) represents the effect of the gravity force (*g*), density difference $(\rho - \rho_o)$ and Richardson number on the flow pattern. The effect of gravity force increases with increasing density difference and increasing Ri. At high temperature, the fluid is less dense than ρ_o, the density difference $(\rho - \rho_o)$ is negative (-ve) and g_i in the *x*-direction is also negative (-ve) so the gravity term will be positive (+ve) and consequently the fluid tends to rise. In contrast, at low temperature, the fluid has a higher density than ρ_o, the density difference is positive (+ve) and g_i in the *x*-direction is negative (-ve) so the gravity term will be negative (-ve) and the fluid will fall. The effect of the gravity term can be neglected when the Ri and the density difference are very small. In other words, if there is no gravity force and the fluid density is uniform, the flow pattern is independent of the choice of the cooling and inlet temperatures. The density in the acceleration term, which is on the left hand side of the equation, has a minor effect on the flow field due to the small amount

of magnitude of density deference. The momentum equation also shows that the average velocity of fluid (*V*) has an effect on the flow field. This effect increases with a decreasing Re and decreases with an increase in it; this effect could appear clearly at the steady laminar flow. The steady laminar regime of the reactors used was at Re < 120. The flow regime was determined in the initial stage of this work using a swirl mixer (Appendix C describes this mixer).

3.3.2 Species

In order to convert the governing equation for species to non-dimensionless form, dimensionless parameters for the mass fraction of each species must be defined:

$$Y_A^* = \frac{Y_A}{Y_o} \tag{3.23}$$

$$Y_B^* = \frac{Y_B}{Y_o} \tag{3.24}$$

$$Y_C^* = \frac{Y_C}{Y_o} \tag{3.25}$$

where Y_o can be taken as the inlet mass fraction of one of the reagent species. Noting that the exponential term in the species reaction rate term, a suitable dimensionless temperature variable is

$$T^* = \frac{T}{T_o} \tag{3.26}$$

where T_o represents a reference temperature. The exponential term can then conveniently be expressed as:

$$\exp\left(\frac{-E}{RT}\right) = \exp\left(\frac{-E}{RT_o}\right)\exp\left(\frac{-E}{RT_o}\left[\frac{1}{T^*} - 1\right]\right) \tag{3.27}$$

The first exponential factor represents the characteristic level of the exponential contribution to the reaction rate, being that term evaluated at the reference temperature T_o. The second factor expresses the correction associated with the local temperature deviation from the reference temperature.

Using Equation 3.27 to express the exponential, multiplication of the species equation by $W / \rho_o V Y_o$ gives the non-dimensional forms of the species equations:

$$\frac{\partial \rho^* u_j^* Y_A^*}{\partial x_j^*} = \frac{\rho^*}{\mathrm{Re}\,\mathrm{Sc}} \frac{\partial^2 Y_A^*}{\partial x_j^{*2}} - \rho^{*2}\mathrm{Da} Y_A^* Y_B^* \exp\left(\frac{-E}{RT_o}\left[\frac{1}{T^*} - 1\right]\right) \quad (3.28)$$

$$\frac{\partial \rho^* u_j^* Y_B^*}{\partial x_j^*} = \frac{\rho^*}{\mathrm{Re}\,\mathrm{Sc}} \frac{\partial^2 Y_B^*}{\partial x_j^{*2}} - \rho^{*2}\mathrm{Da} Y_A^* Y_B^* \exp\left(\frac{-E}{RT_o}\left[\frac{1}{T^*} - 1\right]\right) \quad (3.29)$$

$$Y_C^* = 1 - (Y_A^* + Y_B^*) \quad (3.30)$$

The species equations, Equations 3.28 and 3.29, show that two new non-dimensional parameters have emerged. These parameters are the Damköhler number (Da), which indicate the importance of the reaction rate in relation to species convection, and the Schmidt number (Sc) that describes the diffusion of species within the reaction system. Equations 3.31 and 3.32 show the definitions of Da and Sc respectively.

$$\mathrm{Da} = \frac{\rho_o Y_o W A'}{VM} \exp\left(\frac{-E}{RT_o}\right) \quad (3.31)$$

$$\mathrm{Sc} = \frac{\mu}{\rho_o D} \quad (3.32)$$

The Damköhler number represents the effect of the reaction rate (exponential term) and the convection of species on the flow field. This effect increases with increasing the reaction rate and decreasing the convection of species.

The Schmidt number represents the effect of species diffusion, density and viscosity of fluid on the flow field. This effect increases with increasing the species diffusion and fluid density and decreasing the fluid viscosity. The Schmidt number influences flow through changes in reaction rate and hence heat release and the effect this has on density. The altered density variation then affects the flow through the gravity term in the momentum equation.

The effect of Da and Sc can be neglected at low reaction rates, low species diffusion and non-reacting flow where no reagents and no reaction occur.

3.3.3 Energy

Equation 3.6 represents the heat transfer within the reaction system. The non-dimensional form of the energy equation can be obtained by multiplying Equation 3.6 by $W / \rho_o V C_p T_o$,

and using the T^* definition (Equation 3.26) and exponential expression definition (Equation 3.27):

$$\frac{\partial \rho^* u_j^* T^*}{\partial x_j^*} = \frac{1}{\mathrm{Re}\,\mathrm{Pr}} \frac{\partial^2 T^*}{\partial x_j^{*2}} - 2\rho^{*2}\mathrm{Da}\Delta\mathrm{H} Y_A^* Y_B^* \exp\left(\frac{-E}{RT_o}\left[\frac{1}{T^*} - 1\right]\right) \quad (3.33)$$

Using the above equation, new dimensionless groups emerge: the Prandtl number (Pr) that describes the diffusion of heat within the reaction system and the enthalpy of reaction number (ΔH) that describes the heat of reaction.

$$\mathrm{Pr} = \frac{C_P \mu}{\lambda} \quad (3.34)$$

$$\Delta\mathrm{H} = \frac{\Delta h_R Y_\circ}{C_P T_\circ} \quad (3.35)$$

Together, Re Pr represent the thermal Pèclet number (Pe) of fluid. Pe represents the ratio of heat transfer by fluid motion to heat transfer by thermal conduction.

$$\mathrm{Pe} = \frac{VW}{\alpha} \quad \text{and} \quad \alpha = \frac{\lambda}{\rho_o C_p}$$

where α is the thermal diffusivity of the fluid. Pe represents the effect of the velocity and thermal conductivity of the fluid on the temperature profile in the flow system. This effect increases with the increase in fluid thermal conductivity and decrease in fluid velocity.

ΔH represents the effect of the enthalpy of reaction on the temperature field of the reacting system. This effect increases with the increase in the enthalpy of reaction.

The left-hand side term in the energy equation (Equation 3.33) represents the effect of flow on the temperature field. In this term, the flow carries the energy around. In other words, the flow pattern can affect the spatial distribution temperature in the flow. Therefore, the flow pattern is crucial for controlling the temperature non-uniformity within the flow passage. Since gravity has a significant effect on flow pattern (see Equation 3.21), it consequently has an effect on the temperature distribution within the flow passage (see Equation 3.33). The temperature distribution is also affected by the species diffusion and reaction rate (Equations. 3.28 and 3.29) which results in local heating by heat release.

3.4 Temperature non-uniformity

The mathematical model developed can be employed to identify the relationship between the magnitude of temperature non-uniformity deviation and the dimensionless groups on which the flow, species and energy fields depend. The heat generation rate has a characteristic magnitude:

$$\frac{\rho_o^2}{M} A' \exp\left(\frac{-E}{RT_o}\right) Y_o^2 \Delta h_R W^3 \tag{3.36}$$

The heat transfer rate to cooling surfaces by conduction within the system has magnitude:

$$\lambda \frac{\Delta T}{\delta_T} W^2 \qquad \text{with} \qquad \delta_T = \frac{W}{(\mathrm{Re}\,\mathrm{Pr})^{1/2}} \tag{3.37}$$

where δ_T: represents the characteristic thermal boundary layer thickness. For optimal performance (i.e. high conversion rates) of the microreactor, control of the concentration boundary layer is important. The inherently short distances lead to the potential for short residence times and fast heat and mass transfer compared to the macroscale. Minimization of the boundary layer thickness will create a steeper concentration gradient and thus drive a larger flux of reactants to the surface region. The thickness of the boundary layer could be minimized by increasing the fluid velocity across the flow passages. Equating these two heat rates and rearranging produces the following approximate relation for temperature non-uniformity:

$$\frac{\Delta T}{T_o} \alpha \frac{\rho_o^2 A' \exp\left(\frac{-E}{RT_o}\right) Y_o^2 \Delta h_R W \delta_T}{M \lambda T_o} \tag{3.38}$$

The above equation can be re-expressed in terms of the non-dimensional parameters:

$$\frac{\Delta T}{T_o} \alpha \mathrm{Da} \Delta \mathrm{H} (\mathrm{Re}\,\mathrm{Pr})^{1/2} \tag{3.39}$$

According to this result, the temperature non-uniformity (ΔT) is proportional to both reaction rate (Da) and enthalpy of reaction (ΔH) and depends on the square root of the Pèclet number, i.e. Re Pr (changing thickness of thermal boundary layer). Increasing the reaction rate and enthalpy of reaction increases the heat release and thereby the temperature non-uniformity within the reaction system.

The above relation also shows that $\Delta T \alpha W^{3/2} Y_o^2 V^{-1/2} \Delta h_R$. That is, the temperature non-uniformity can be reduced to any level required simply by using sufficiently small passage size (W), regardless of passage geometry. Besides, the temperature non-uniformity decreases with decreasing the concentration of the reagents (Y_o) and increasing the average velocity of them (V). Decreasing the concentration of the reagents could be lead to a decrease in reaction rate and thereby a decrease in the heat released. And, increasing the velocity of reagents could reduce the reaction rate by reducing the residence time (Kockmann *et al.*, 2013; Plouffe, et al., 2016; Laudadio *et al.*, 2017). The present study will investigate the effect of some of these non-dimensional parameters on the level of temperature deviation in a reacting liquid in three different structured reactors.

3.5 Reactor geometries

In this study, three types of reactors are considered: F, S and C element Reactors. These reactors have different geometries, the F-element reactor comprises geometric elements that are in the shape of the letter 'F'; the S represents 'swirl', which is used in that particular reactor; and the C-element Reactor uses simple channels. The reactors were designed as small scale structured reactors to enhance the temperature distribution within the reactor domain.

Each reactor involves a particular element geometry that can be linked in a series of elements to form a reactor. The element is repeated four times in each reactor. These geometries represent the exact geometries to be used in the experimental work. They also represent the domains over which the governing equations presented in this chapter are solved. In addition, the flow pattern is different in each reactor: each reactor has two inlets and one outlet. As mentioned above the naming of reactors is based on the flow pattern in each reactor, where the flow pattern is F-shaped in the F-element Reactor; a swirl pattern in the S-element Reactor; and a normal channel in the C-element Reactor. This difference in flow patterns causes a difference in the mixing pattern of species. The mixing is very weak in the C-element Reactor, compared to that in the F and S-element Reactors.

3.5.1 F-Element Reactor

Figure 3.1 shows the four elements of the F-element Reactor. The flow splits and re-joins again in each element to enhance the mixing of species and the heat. The mixing pattern is approximately the same in each element in the reactor. Repeat mixing four times can reinforce the transfer of species and heat. The flow passage includes two chambers: the upper chamber

and down chamber. Figure 3.1 b shows the coordinate system, passages dimensions and the geometry of the passages of F-element Reactor. The flow channel width (w) is 5.2 mm. The geometry is only dependent on this single dimension. For example, the channel height is equal to channel width (w) and the height of the reactor is double the channel width ($2w$). The characteristic width (W) of the flow passage is four times the cross-sectional area (A) of flow divided by the perimeter of that section (P), i.e. $W=4A/P$. For this Reactor, the characteristic width (W) is equal to the channel width (w). The average velocity of flow (V) is the flow rate (Q) through the channel cross-section, i.e. $V=Q/w^2$.

In the experiments, the elements of the reactor are structured within a solid heat-insulating body to ensure thermal isolation from the ambient temperature. Figure3.1c shows the overall computational domain (solid and flow passages) used for the F-element Reactor. The Reynolds number of the flow was calculated based on the average velocity (V) through the characteristic width (W) of the passage and the physical properties (density and viscosity) of the solution (Section 3.7 shows the details of density and viscosity of solutions used).

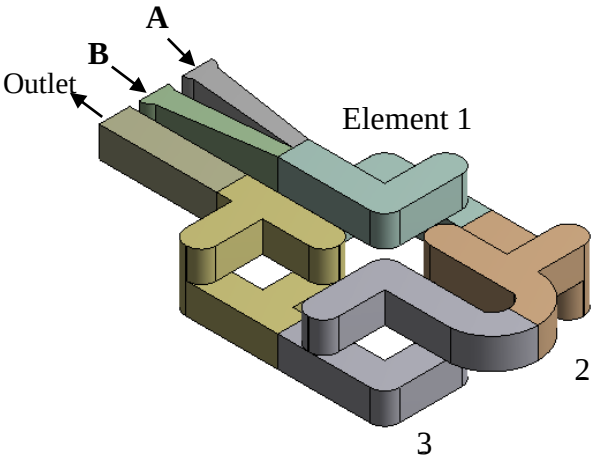

(a) Elements of F Reactor

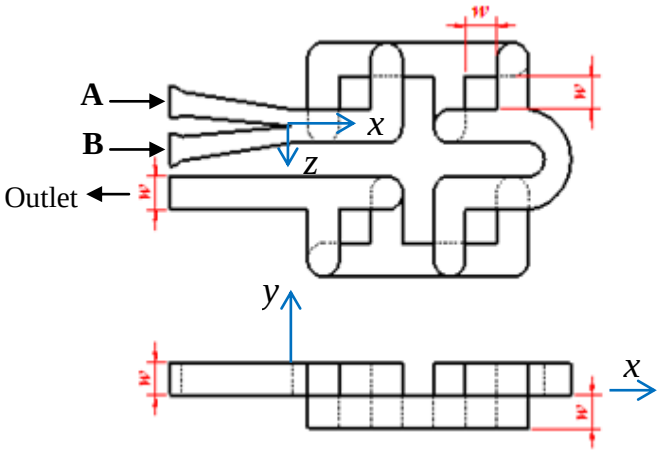

(b) Technical drawings of F Reactor

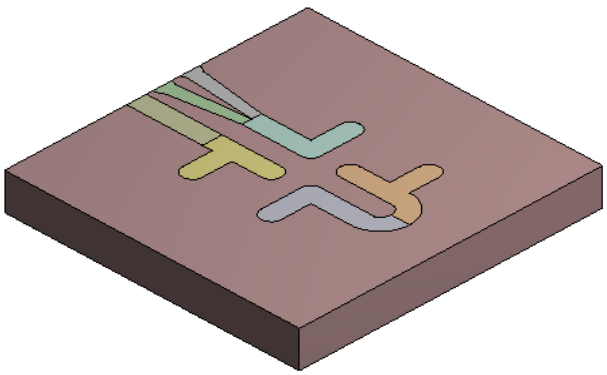

(c) Typical computational domain of F Reactor

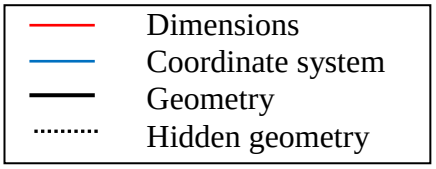

Figure 3. 1 The four elements of the F-element Reactor

3.5.2 S-Element Reactor

Figure 3.2 shows the four elements of the S-element Reactor. The mixing pattern repeats four times to reinforce the transfer of species and heat. The reactor includes two chambers; the upper chamber and down chamber. In each element, the upstream and downstream chambers are connected together by a central hole. The flow passes around the circumference of the first chamber and then through the narrow central hole. At a high enough Reynolds number, this results in fluid with a high angular momentum flowing through the central hole. In the narrow central hole, the solutions A and B are mixed closely, and this mixing should reinforce species and thermal mixing. After the narrow hole, the geometry expands and the emerging flow tends to move outward radially as a result of its angular velocity. This produces the toroidally circulating flow as the liquid travels towards the outlet of the second chamber.

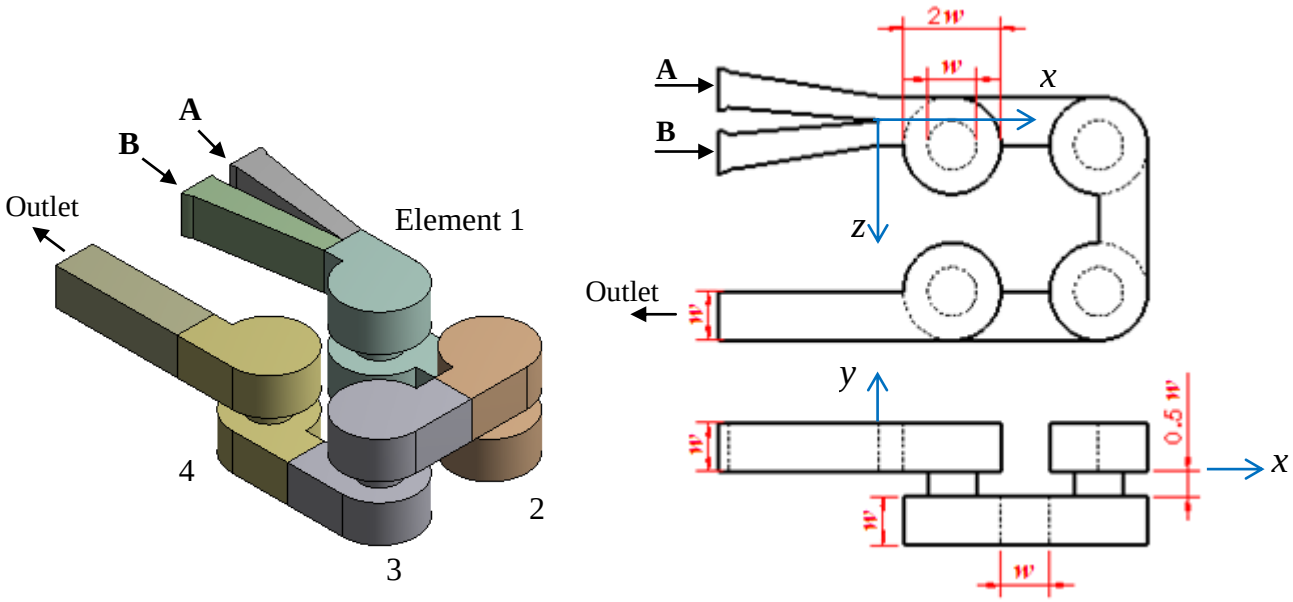

(a) Elements of S Reactor (b) Technical drawings of S Reactor

Figure 3. 2 The four elements of the S-element Reactor.

Figure 3.2 b describes the coordinate system, passages dimensions and geometry of the passages of the S-element Reactor. The flow channel width (w) is 6.06 mm. The geometry is only dependent on this single dimension where the channel height, reactor height, upstream diameter, downstream diameter and the central hole diameter are equal to w, 2.5w, 2w, 2w and w respectively (see Figure 3.2 b). The characteristic width (W) of the flow passage, according to the definition of characteristic width in the previous section, is equal to the channel width (w). The average velocity of flow (V) and the Reynolds number of the flow were calculated as

described in the previous section. The flow passages were structured within a solid heat-insulating body to isolate the reactor thermally from the ambient temperature.

3.5.3 C-Element Reactor

Figure 3.3 shows the four elements of the C-element Reactor. The flow passage in each element is a normal channel. There is a slight downward dip at the end of the channel to enhance the mixing of species and the heat. Each element includes one chamber only. The mixing pattern is approximately the same in each element in the reactor. Repeat mixing four times can reinforce the transfer of species and heat. Figure 3.2b displays the coordinate system and the passage dimensions of the geometry. The flow channel width (w) is 5.28 mm. The geometry is only dependent on this single dimension where the channel height and reactor height are equal to $2w$ and $2.5w$ respectively (see Figure 3.3 b). The characteristic width (W) of the flow passage, according to the definition of characteristic width in Section 3.5.1, is equal to ($4w/3$). The average velocity of flow (V) is ($Q/2w^2$). Reynolds number of the flow was calculated as described in Section 3.5.1. The elements of the reactor were covered with a solid heat-insulating body such as the F and S-element Reactor to ensure that it is thermally isolated from the ambient temperature.

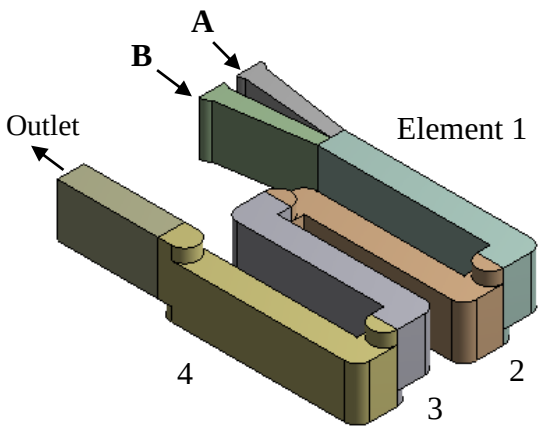

(a) Elements of C Reactor

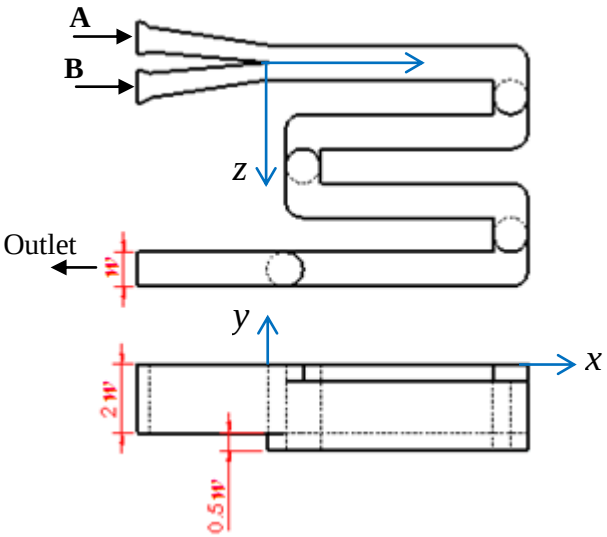

(b) Technical drawings of C Reactor

Figure 3. 3 The four elements of the C-element Reactor.

3.5.4 Mean residence time

The value of Characteristic width (W) for each reactor was set so that, at the same value of Reynolds number, each had the same mean residence time. This ensured that the time for

reaction to occur at a given value of Re would be the same for each reactor. Consequently, differences in performance between the reactors would only be due to the inherent differences. Table 3.1 shows the residence time of the reactors at Re 32, 65 and 130. The residence time was calculated according to the following:

$$\tau = \frac{V_R}{Q} \tag{3.40}$$

where τ represents the residence time of reactor, V_R is the volume of reactor and Q is the volumetric flow rate of fluid.

Table 3. 1 The residence time of the reactors.

Reactor	Re	V_R (m^3)	Q (m^3/s)	τ (s)
C	32	$9.42x10^{-6}$	$2.00x10^{-7}$	46.97
F	32	$6.19x10^{-6}$	$1.32x10^{-7}$	46.98
S	32	$7.21x10^{-6}$	$1.53x10^{-7}$	47.00
C	65	$9.42x10^{-6}$	$4.07x10^{-7}$	23.12
F	65	$6.19x10^{-6}$	$2.67x10^{-7}$	23.13
S	65	$7.21x10^{-6}$	$3.12x10^{-7}$	23.14
C	130	$9.42x10^{-6}$	$8.15x10^{-7}$	11.56
F	130	$6.19x10^{-6}$	$5.35x10^{-7}$	11.56
S	130	$7.21x10^{-6}$	$6.23x10^{-7}$	11.57

3.6 Boundary Conditions

The equations governing the experimental flow systems are now complete. These equations apply at every point in the domain of the flow passages and solid regions of the systems. However, solving these equations requires further conditions at the domain boundaries and these conditions are now presented. Four types of boundary condition are needed, those at the flow inlets, those at the flow outlets, those at the solid surfaces in contact with the flows (which are heating or cooling walls) and the external boundaries of the solid regions.

All of the solid wall boundaries are stationary, so the boundary condition for flow is zero velocity. Here, since no mass transfer occurs with the wall, the flux of species is zero and hence the normal component of gradient is zero. The thermal boundary conditions at the walls

divide into two types: zero heat flux at the side-walls and convective heat transfer in the top and bottom walls of the reactor.

$$u_i = 0 \text{ and } \frac{\partial Y_A}{\partial x_j} + \frac{\partial Y_B}{\partial x_j} = 0 \text{ at the wall boundaries} \quad (3.41)$$

$$\frac{\partial T}{\partial x_j} n_j = 0 \text{ at the side-wall boundaries} \quad (3.42)$$

$$q = h(T - T_C) \text{ at the top and the bottom wall boundaries} \quad (3.43)$$

where q, h, T and T_C are the convection heat transfer, heat transfer coefficient, the temperater of fluid inside reactor and the convection temperature of the top and bottom plate. The details of convection boundary condition at the top and bottom of reactor walls are shown in Equation 4.1 in Section 4.2.1.

For the flow system, the conditions of each inlet are velocity, temperature and mass fraction of one species (u_I, T_I and Y_o respectively). The pressure in the outlet is zero-gauge pressure.

$$u_i = u_I n_i \text{ , } T = T_I \text{ and } Y_o = 1 \text{ at the inlet boundaries} \quad (3.44)$$

$$P_g = 0 \text{ at the outlet boundaries} \quad (3.45)$$

The vector n_j is the unit normal to the surface at any given position on the boundary. P_g represents the gauge pressure at the outlet.

3.7 Physical properties

Solving the governing equations (Eqs. 3.1-3.6) using the boundary conditions requires inputting the parameters of the system. These parameters include physical properties of the solid body and fluid. The properties of the solid body such as density (ρ), heat capacity (C_P) and thermal conductivity (λ) are shown in Table 3.2. The main fluid properties are density (ρ) and viscosity (μ). These properties are a function of temperature and concentrations of solutions. Equations. 3.46-3.47 below represent the equation for density and viscosity of pure water respectively. These equations were obtained by drawing the data of density and viscosity of water with temperature (David, 2004) in Excel:

$$\rho(T) = 1.569x10^{-5}T^3 - 1.877x10^{-2}T^2 + 6.759T + 2.342x10^2 \quad (3.46)$$

$$\mu(T) = 3.323x10^{-11}T^4 - 4.555x10^{-8}T^3 + 2.345x10^{-5}T^2 - 5.379x10^{-3}T + 4.648x10^{-1} \quad (3.47)$$

Two reaction systems are used in the experiments: HCl-NaOH system and $NaClO_2$-$K_2S_4O_6$ system. The equation for density and viscosity of these systems were obtained experimentally according to the Poiseuille method (Walker, 2008). The detail of this method is described in Appendix A.1. The equation for density and viscosity for the reactant solutions are represented in Eqs. A.4 and A.5 and the factors of these equations are listed in Tables A.1, A.2, A.3 and A.4. The other properties of the fluid, such as heat capacity (C_P), thermal conductivity (λ) and diffusivity (D), were considered a constant where they change slightly with temperature. The values of these properties are shown in Table 3.2.

Table 3. 2 Physical properties used in the CFD model.

Solid Properties		
Density	1320	kg/m^3
Heat Capacity	1700	J/ (kg. K)
Thermal Conductivity	0.25	W/(m. K)
Fluid Properties		
Heat Capacity	4182	J/ (kg. K)
Thermal Conductivity	0.6	W/(m. K)
Diffusivity	1.00×10^{-9}	m^2/s

For the reacting systems, the enthalpy of reaction (Δh_R) used was -28438 J/kg for the HCl-NaOH reaction and -75276 J/kg for the $NaClO_2$-$K_2S_4O_6$ reaction. These enthalpies were measured experimentally (the details of measuring method is shown in Appendix B). The activation energy (E) of a $NaClO_2$-$K_2S_4O_6$ reaction is 60 kJ/mole approximately (Jakab, et al., 2002) and for the HCl-NaOH reaction, where the reaction is very fast, it was assumed to be zero (David, 2004).

According to these values, the value of the pre-exponential factor (A) for each reaction was adjusted computationally to match the experimental data. A good agreement with experimental data was obtained when A was 10^6 $L^3.mol^{-3}.s^{-1}$ of the $NaClO_2$-$K_2S_4O_6$ reaction and 0.00015 $L.mol^{-1}.s^{-1}$ of the HCl-NaOH reaction. Section 6.3.1 shows the matching of computational results with experimental data for the $NaClO_2$-$K_2S_4O_6$ reaction.

3.8 Measures of non-uniformity

The numerical solution of the governing equations allows important measures of the conditions within the reactor to be determined. These measures can be computed for a volume average at a flow surface and for area average over a solid surface. The measures include average temperature (T_B), maximum temperature ($\overline{T}$). Measuring these parameters experimentally is difficult. The parameters can be used to evaluate the non-uniformity of temperature accurately by calculating the standard deviation of temperature along the reactor. In this work, the non-uniformity of temperature was evaluated computationally by calculating the standard deviation of temperature (σ_T) in this way. The standard deviation of temperature was calculated as follows:

$$\sigma_T = \sqrt{\overline{T^2} - (T_B)^2} \tag{3.48}$$

The standard deviation of temperature was calculated over volumes and surfaces. The average temperature over volume and surface are calculated as follows:

$$T_B = \frac{1}{V}\int_V T dV \text{ , over volume} \tag{3.49}$$

$$T_B = \frac{1}{\dot{m}}\int_A \rho u_n T dA \text{, over surface} \tag{3.50}$$

3.9 Numerical Solution

The solution of the governing equations must be made numerically as the equations are non-linear, three dimensional and the domain geometry is complex. ANSYS/Fluent software (CFD model) was used to obtain the numerical solutions. This software can be applied to solve the partial differential equations (PDEs) accurately (Botti et al., 2018). The numerical solution in this software uses the finite volume method. This method divides the computational domain into small subdomains and forms a mesh of cells. This mesh distributes the nodes over the domain of the solution. At these nodes, the PDEs are approximated into algebraic equations which are solved to determine variable values at the node positions. A reliable solution to these equations can be obtained using a sufficiently large number of nodes. Therefore, a large number of algebraic equations are formed that are solved by iteration to reach a converged solution.

There are a number of important parameters in meshing that can affect the accuracy of the numerical solution. The most common parameters are the shape and size of the element. These parameters should be selected carefully. In this work, tetrahedral elements were used

(as shown in Figure 3.4) as these could adapt to the 3-dimensional geometry without severe distortion of the elements (Nelder. et al., 1965). A highly accurate solution can be achieved using a small element size but this can require an unacceptably long computation time in order to converge the solution.

The element size used in the final computations was 0.0005 mm for both the passages (as shown in Figure 3.4) and the solid body. The total number of elements were 5325488, 4492893 and 5778337 for the C, F and S element reactors respectively. The percentage of mesh size relative to the size of passage (*W*) was 9.5%, 9.6% 8.3% for the C, F and S element reactors respectively. The accuracy of the numerical solution also depends on the Reynolds number, as the spatial variation that must be captured by the grid increases with increasing Reynolds number. In addition, the buoyancy has an effect on the solution accuracy, as the high Richardson number requires a small element size to capture the temperature field carefully. Moreover, it is important to have sufficient iterations to solve the discrete numerical equations accurately. A grid study in which the average size of the mesh cells is progressively decreased must be carried out to identify the cell size needed to achieve a given accuracy. It is necessary to use double-precision arithmetic in these computations so the slight changes in calculated parameters can be resolved accurately.

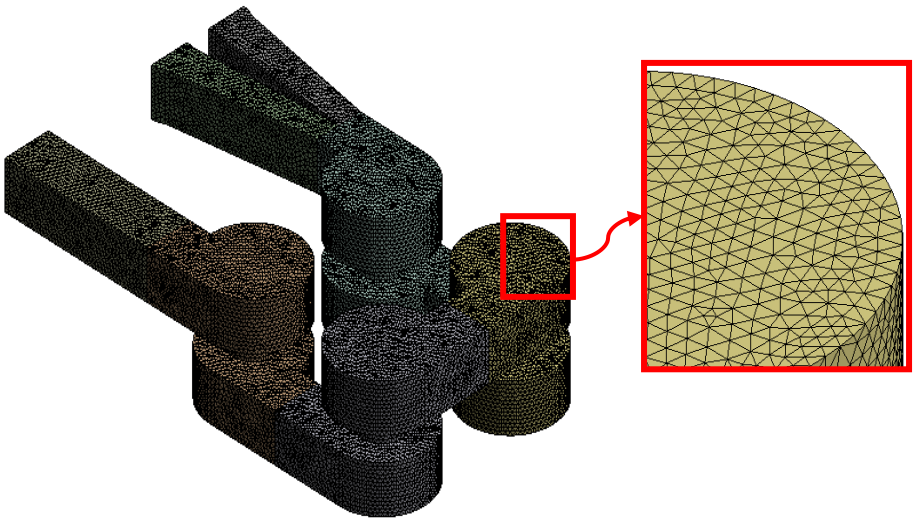

Figure 3. 4 Grid display on the walls of passages of S-element Reactor using uniform mesh at element size 0.0005 mm.

3.9.1 Grid Dependence

The accuracy of the numerical solution increases with the decreasing mesh size of the geometry. Beyond this size, this dependence becomes negligible. Therefore, the grid

dependence must be implemented carefully to determine the mesh size required to compute the numerical solution to a required accuracy. The grid study was tested directly by reducing the size of the elements, both in the solid body and in the passages, using the tetrahedral shape of element. The computational work here aims to simulate the extreme conditions, the upper limit of the Reynolds and Richardson numbers, used in the experiments. For example, using high Reynolds and Richardson numbers requires a very small element size to compute the velocity and temperature fields in such small elements. This approach can appear clearly in the S-element Reactor due to the increasing the angular momentum.

In the computations, the computed profile of temperature along particular lines through the domain space was used to judge the dependency of the solution on the grid size for the C, F and S element Reactors, using the non-reaction system. The mesh refinement process starts from an initial element size of 0.004 mm and is then reduced by a factor of 0.5. Table 3.3 shows the grid specifications of each reactor. Figs. 3.5-3.7 show the effect of the grid on the accuracy of numerical solutions for the C, F and S element Reactors through comparison between the computed and experimental results. The comparison used measurements from the experimental approach, described in detail in the next chapter. The figures show clearly that the grid has a significant effect on the solution accuracy. The figures show also a good agreement between experimental data and computation results using a sufficiently small grid size in the C and F element Reactors. In the S-element Reactor, there is good agreement between computations and experiment in the first element only. This may be due to disturbance of the flow after passing through the first connecting hole in that first element. The disturbance of flow affects flow in the downstream chambers (both inlet and outlet) of elements 2, 3 and 4. In addition, this also may be due to using an unsteady flow regime. Generally, the finest grid, which is 0.0005 mm, could be used to compute the solution reliably in this work.

Table 3. 3 Grid specifications of reactors

Mesh Size (mm)	C-Element Reactor		F-Element Reactor		S-Element Reactor	
	No. of Elements	Time (hr. : min)	No. of Elements	Time (hr. : min)	No. of Elements	Time (hr. : min)
0.004	12,129	00 : 06	12,2019	00 : 09	65,075	00 : 20
0.002	88,858	00 : 10	155,717	00 : 21	121,031	00 : 50
0.001	505,505	01 : 13	586,324	01 : 35	729,006	02 : 20
0.0005	5,325,488	03 : 55	4,492,893	04 : 18	5,778,337	05 : 34

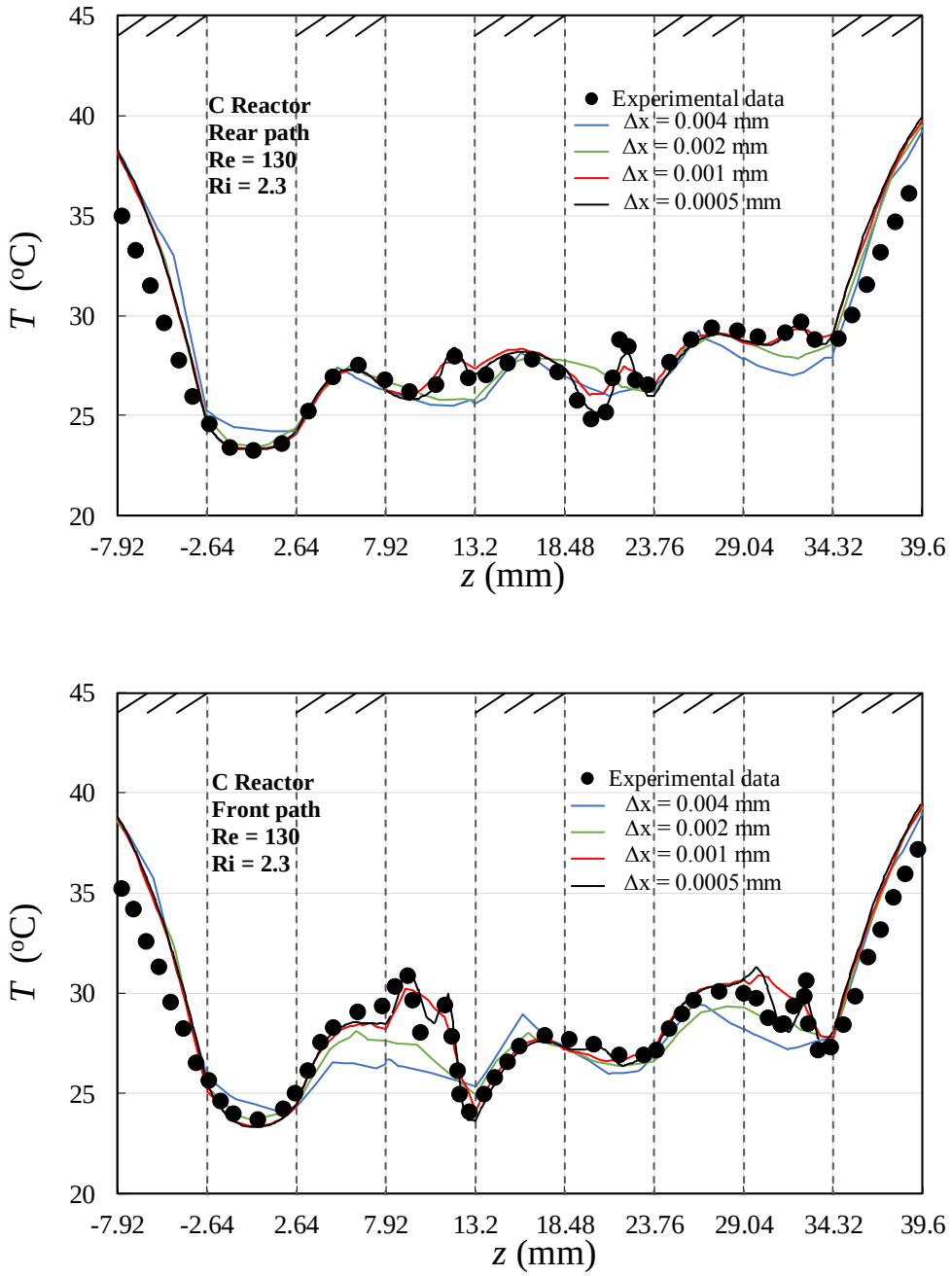

Figure 3. 5 Numerical solution dependence on the grid for C-elemen Reactor. The Z is zero in the meeting point of A and B species inlet (see Fig. 3.3 b)

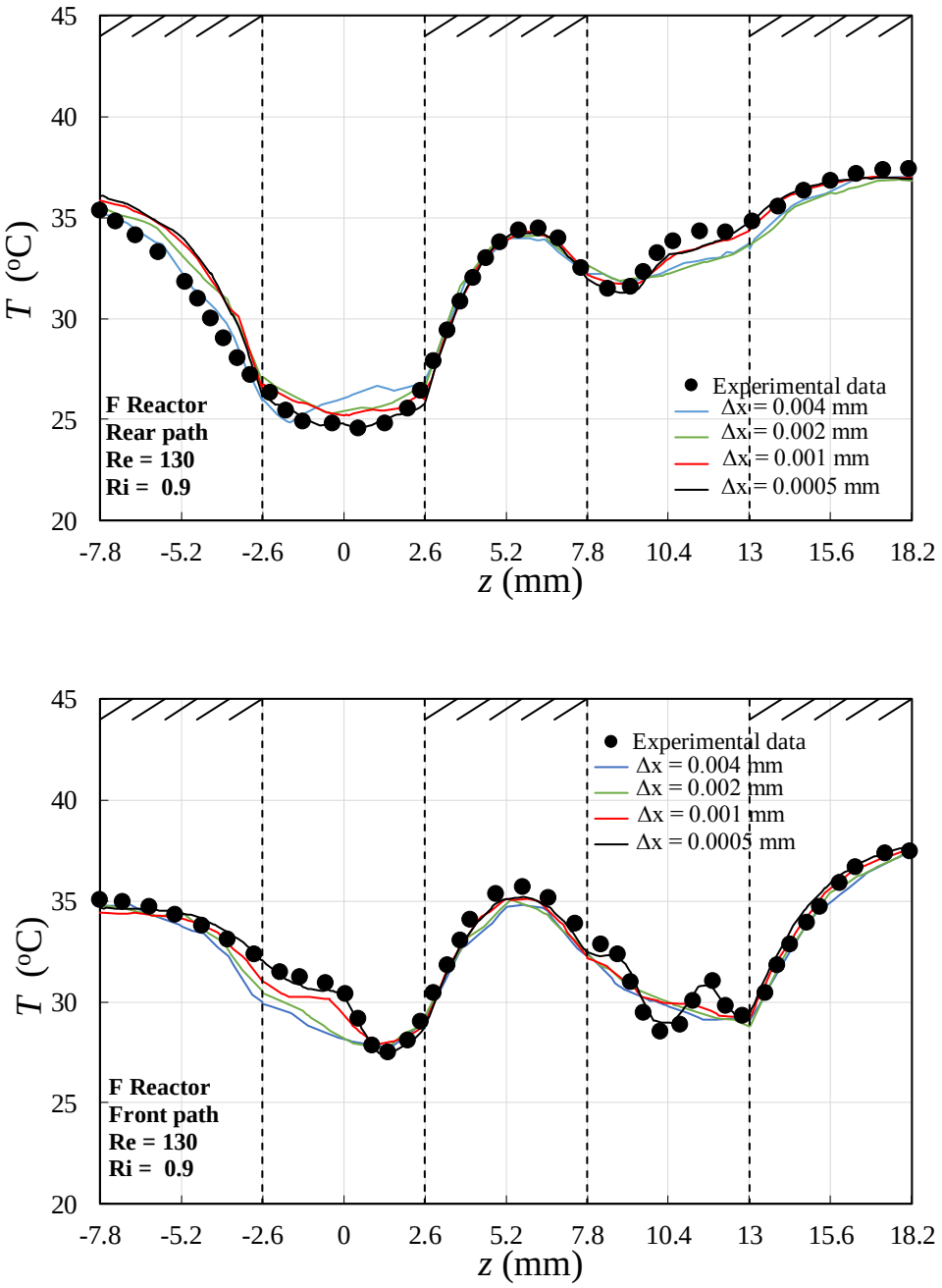

Figure 3. 6 Numerical solution dependence on the grid for F-element Reactor. The Z is zero in the meeting point of A and B species inlet (see Fig. 3.1 b)

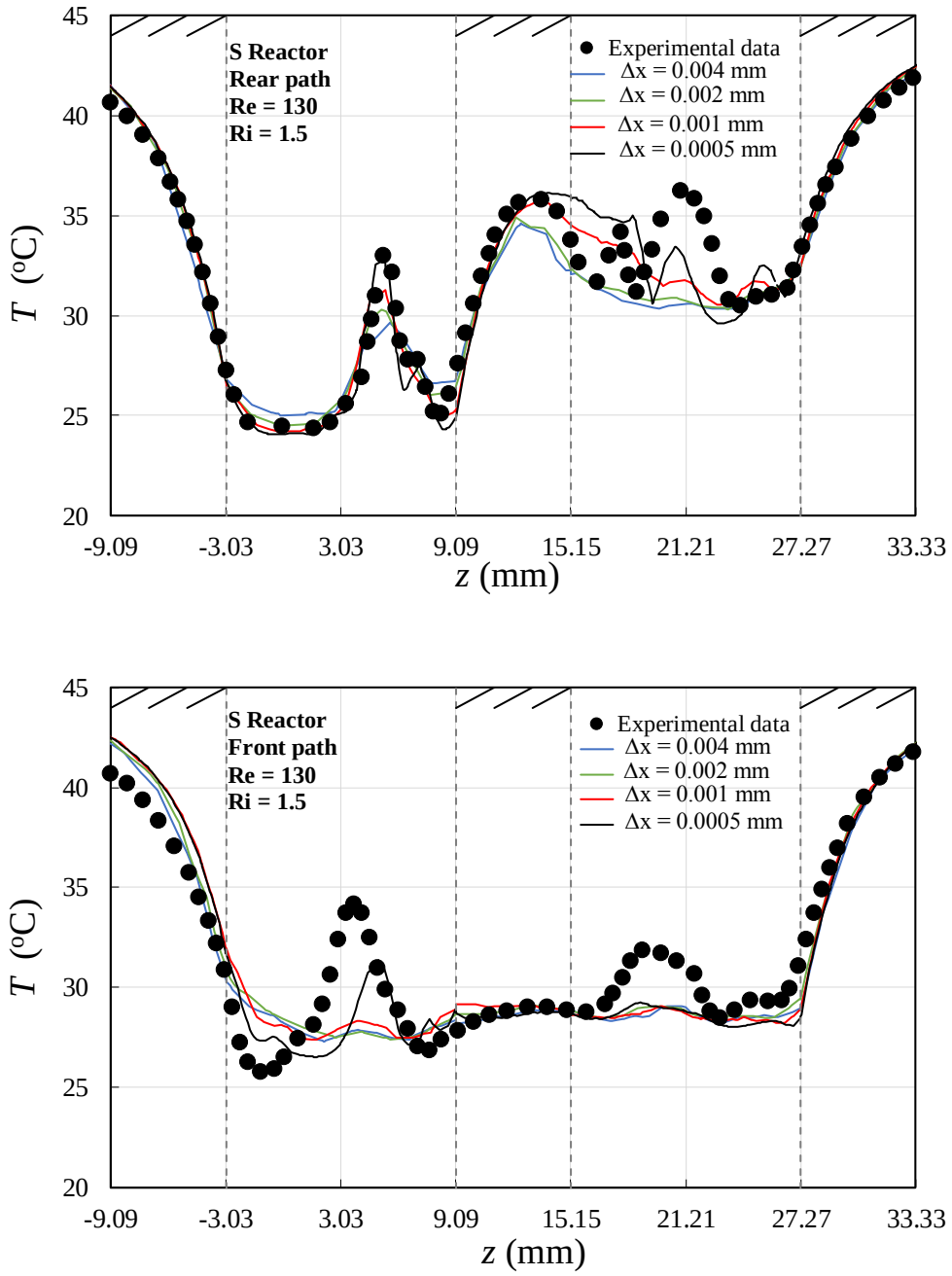

Figure 3. 7 Numerical solution dependence on the grid for S-element Reactor. The Z is zero in the meeting point of A and B species inlet (see Fig. 3.2 b)

3.10 Summary

This chapter introduced a 3-D dimension numerical model to simulate the temperature non-uniformity in three structured reactors, of type C, F and S, for two flow situations: non-reacting and reacting flow. In the chapter, a simple analysis demonstrated the approximate

dependence of temperature non-uniformity on the Pèclet and Damköhler numbers, and non-dimensional reaction enthalpy.

In addition, the geometries of the reactors used and boundary conditions were described in detail. The key aspects of the numerical solution, such as the physical properties and the statistics, were explained. At the end of this chapter, the dependence of the solution on the grid was determined. The main conclusion of this grid study is that the computations should be carried out with a mesh size of 0.0005 mm to achieve solution accuracy within the uncertainty of the experiments so that comparisons can be made.

Chapter Four

4. The Experimental work

Obtaining measurements of the spatial variation of temperature within the passages of three different structured-passage geometries was the main objective of experimental work in the project. This will supply both direct information about temperature uniformity and data with which to evaluate the effectiveness of the model prediction. An apparatus allowing liquid reaction by mixing of two reagent solution streams and independent control of inlet solution temperature and the temperature of the reactor cooling walls was designed and fabricated in the department specifically for this project. The reactor integrates the preheating of the reagent streams, thermal control of the reactor and spatial measurement capability; it also uses corrosion resistant materials to allow a wide range of reaction systems to be tested. This chapter provides a detailed description of this apparatus, along with analysis showing the basis for accurate local temperature measurement and special procedures associated with ensuring rapid achievement of steady state operation.

4.1 General apparatus

Figure 4.1 is an overall view of the apparatus with pressure tanks to the right for two reagent solutions supplying these through resistance tubing and valves to the reactor. Two continuous water heaters (ZIP InLine CEX-O), mounted on the wall at the upper left each supply a regulated flow of water at a steady temperature in the range from about 25 to 45 °C, one to a reagent preheat exchanger and the other to the cooling plates in the reactor. A flow diagram of the experiment is shown in Figure 4.2. The flow of each reagent solution is controlled by pressurising a 'pot' containing a beaker of the particular liquid. The two reagent solutions are supplied separately from Pots A and B. A dip tube conveys the liquid from the beaker and the value of applied pot pressure and the resistance of the tubing connection to the reactor determine the flow rate. Cover floats in each beaker reduce gas absorption into the liquid in the pressure pots. A third supply from Pot C is used for a surfactant solution to clear bubbles at the start of each test. Pot air pressure was measured with a 0-2.5 barg digital pressure gauge. By using a series connection from the pot to the reactor comprising a 1.5 m length of 0.762 mm internal diameter tubing and a 0.5 m length of 0.508 mm internal diameter tubing, the 2.5 barg maximum

pressure allowed Reynolds number values up to about 150 to be reached, i.e. the range of interest in this study. The surfactant tubes were 1/8" diameter.

Figure 4.2 shows further main aspects of the apparatus. The division of the reactor into a preheating section and the section containing the reactor passages is shown, with Heater 1 supplying heated water flow at one temperature to the preheat section and Heater 2 supplying water flow at a second temperature to the reactor passage region. This enables setting the reagent supply temperature independently of the reactor cooling surface temperature. Thermocouples positioned at each heater inlet allow the temperature imposed on each heating section to be known and to be monitored during the experiment. The heating sections, which are the preheat section and the reactor cooling surfaces section, have been fabricated from copper to make the temperature is uniform and approximately the same at each position of the section (see Section 4.2.1). The thermocouples are connected to a temperature data logger (TC08, Omega Engineering) to record the temperature online using computer software.

The reactor is formed from a sandwich comprising a series of plates clamped together. An exploded view of the design is given in Figure 4.3 (Appendix E shows the details of design of the apparatus). In the middle is a plate made from PEEK in which channels and holes associated with the preheating and reaction passages are milled. Above and below the pre-heat and reaction regions are corresponding copper plates with machined channels for the heated water flows. Thin stainless steel plates (1 mm) between the reactor plate and the copper heat exchanger plates close the pre-heat and reactor passages and also the adjoining side of the exchanger passages. The reactor side of these steel plates is coated with per fluoro alkoxy (PFA) for resistance to reagent corrosion. Two thin (1 mm) acetal plates between aluminium clamps and the remaining copper plate surfaces close the copper heat exchange passages. O-ring seals in grooves made in the copper plate and reactor plate surfaces prevent leakage from the preheater, reactor and copper heaters. The thickness of the outer Aluminium plates is sized to reduce deflection to within a few microns under 1 bar internal reactor pressure. (The leakage flow between different regions of the reactor passages associated with gaps of a few microns is negligible. At the relatively low flow rates required in this study, the reactor pressure has remained effectively atmospheric.)

Finally, in Figure 4.2, the system for spatial temperature measurement is schematically depicted. The key elements are a fine (75 μm diameter) butt-welded thermocouple wire with

leads that run around pulleys to connections on a linear motorised stage. This allows the thermocouple junction, where temperature is sensed, to be traversed along a predetermined line in space through the reactor passages.

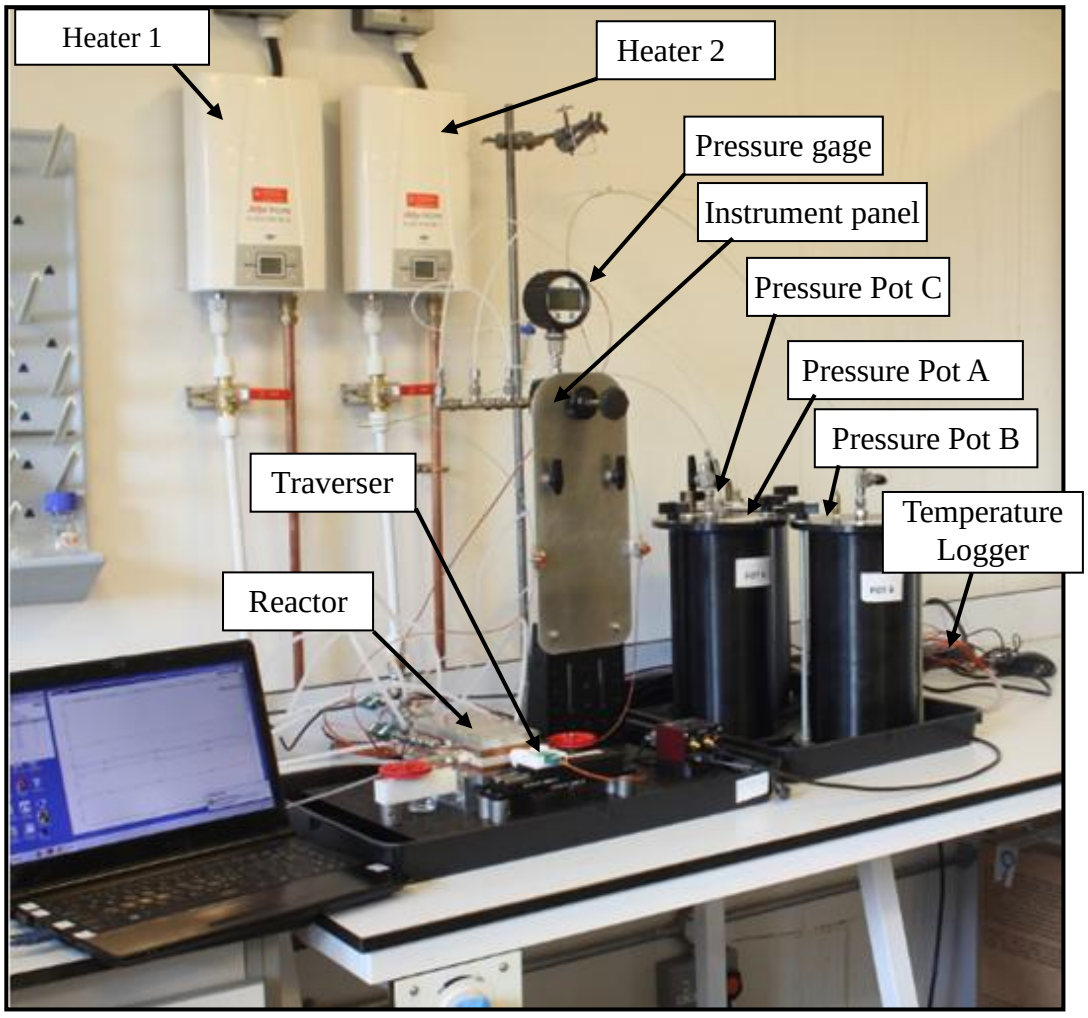

Figure 4. 1 The experimental apparatus.

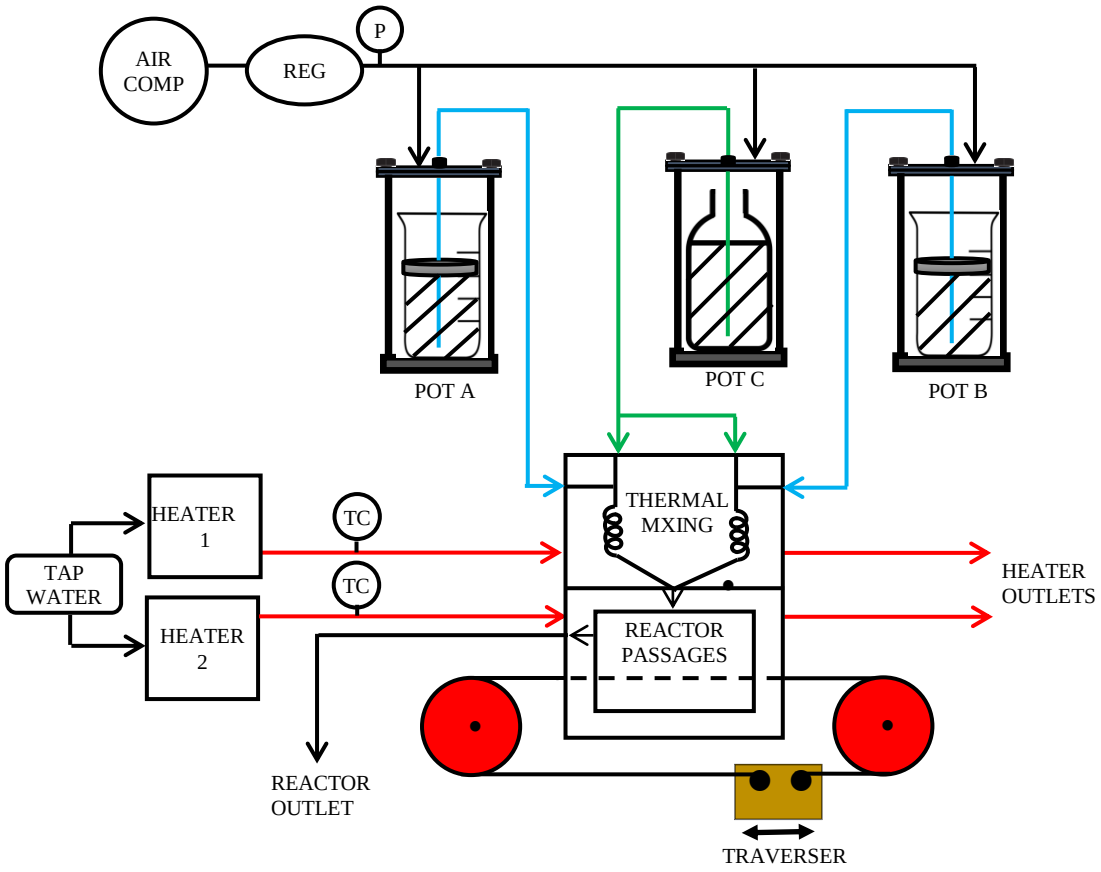

Figure 4. 2 Overall flow network of the apparatus. The blue lines are passages to transport the solutions. The red lines are the feed and outlet for the heat exchangers. The green lines are the surfactant passages.

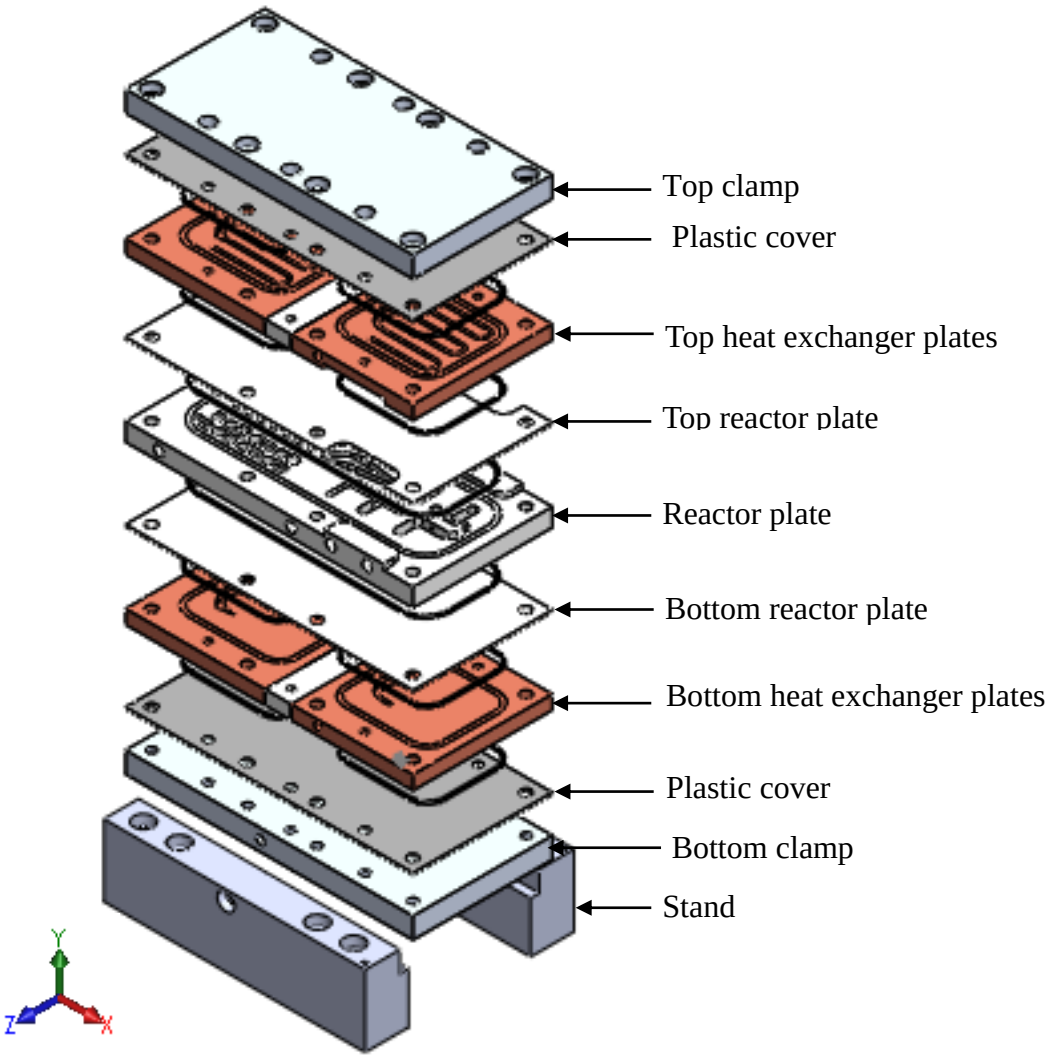

Figure 4. 3 Diagram showing the reactor.

4.2 Thermal boundary conditions

As far as possible the design of the reactor has aimed to facilitate convenient theoretical prediction of the processes in the reactor flow. This places especial emphasis on aspects affecting the thermal boundary conditions. Generally, the approach is to approximate zero flux conditions at the perimeter surfaces of the reactor plate so, with a computational domain only including the region of the reactor plate that includes the reaction passages, a zero-heat-flux boundary condition at the side surfaces of the domain is reasonable. The requirement of approximately zero flux at the side boundaries dictated the use of plastic (PEEK) to give low thermal conductivity. Two further important boundary conditions must be determined: the heat

flux over the top and bottom copper plate surfaces and the temperature at the reagent solution inlet. These topics are addressed in the next two sub-sections.

4.2.1 Heat flux at top and bottom boundaries

A highly uniform temperature is achieved in each copper heat exchanger plate as a result of the high thermal conductivity of copper in relation to that of the surrounding materials (stainless steel, PEEK, acetal and air) and a high flow rate of heater water passing through the copper passages. The approximately 5 L/min flow rate from each heater is divided between the top and bottom copper plate of each heat exchanger. This flow rate produces a temperature change from water inlet to outlet that is within 1% of the expected maximum adiabatic temperature rise from the reactions considered. With copper itself further acting to distribute heat the expected uniformity is yet smaller. (Since the resistances to flow through the top and bottom plates of each heat exchanger are equal, the flow rate will be the same and satisfactorily high in each.) Note that an insulating spacer (acetal) in the top and bottom layers of copper heat exchange plates (Figure 4.3) provides thermal separation so uniform preheat and uniform reactor plate temperatures can be set independently.

Thus, by measuring the temperature of the water at the inlets, the uniform temperature of the copper plates for each heat exchanger will be known and, in particular, the temperature at the surface of the copper plates in contact with the thin stainless steel plate, where a boundary condition is required, will be known. That boundary condition results from the approximation that the stainless steel cover plate thickness (δ_S) is small enough that heat transfer in the plane of the plate is negligible. Then, noting that the cover plate actually consists of two layers since it is coated with a thickness (δ_P) of PFA, the one-dimensional steady heat conduction results in a heat flux boundary condition based on a heat transfer coefficient that is simply dependent on the two-layer thicknesses and thermal conductivities:

$$q = h\left(T - T_C\right) \qquad \text{with} \qquad h = \left(\frac{\delta_S}{\lambda_S} + \frac{\delta_P}{\lambda_P}\right)^{-1} \tag{4.1}$$

Here, T_C is the uniform temperature of the copper plate and T is the local temperature at the PFA surface in contact with either the reactor plate solid or the liquid contained in the reactor passages; λ_S and λ_P are the thermal conductivities of the stainless steel and PFA layers respectively. Table 4.1 gives the values of the thicknesses and thermal conductivities of the

stainless steel and PFA layers. Eq. 4.1 and these values are used to impose the boundary condition at the top and bottom domain surfaces in the computations presented later.

Table 4. 1 Properties of convection boundary condition.

Property	Value
Thickness of the stainless steel plate (δ_S), mm	1
Thickness of the PFA layer (δ_P), mm	0.1
Thermal conductivity of the stainless steel plate (λ_S), W/(m. K)	15.0
Thermal conductivity of the PFA layer (λ_P), W/(m. K)	0.209
The heat transfer coefficient (h), W/(m^2.K)	1834

4.2.2 Reagent inlet temperature

The final boundary condition needed is that of the inlet reagent temperatures. This temperature depends on the copper preheater temperature, the reagent solution supply temperature and the reagent solution flow rates. Knowing that relationship allows the bulk inlet temperature to be determined for any combination of preheater inlet temperature, heater plate temperature and flow rate used in the experiment. Since it is most convenient if the preheater delivers liquid of uniform temperature and also is able to transfer heat effectively to the liquid as it passes through the preheater, each reagent solution stream is repeatedly mixed as it progresses through the preheater. Figure 4.4 shows the detail of the preheating passage for one of the reagent solution streams. The passage consists of 21 swirl mixer elements in series. Rough computations using the approach presented in Ch. 3 were applied to this mixing passage and established the high uniformity of temperature produced at any stage along the preheater passage. In addition, the outlet temperature may reach up to 80% and nearly 100% of the rise from preheater inlet temperature to that imposed by the copper preheater plates, depending on flow rate (over the range of flow rates used for the results reported here). According to these computations, the outlet temperature of the preheater that is used as the inlet temperature of the reactor in the computations of the reactor is estimated. This temperature may be slightly adjusted computationally to match the experimental data.

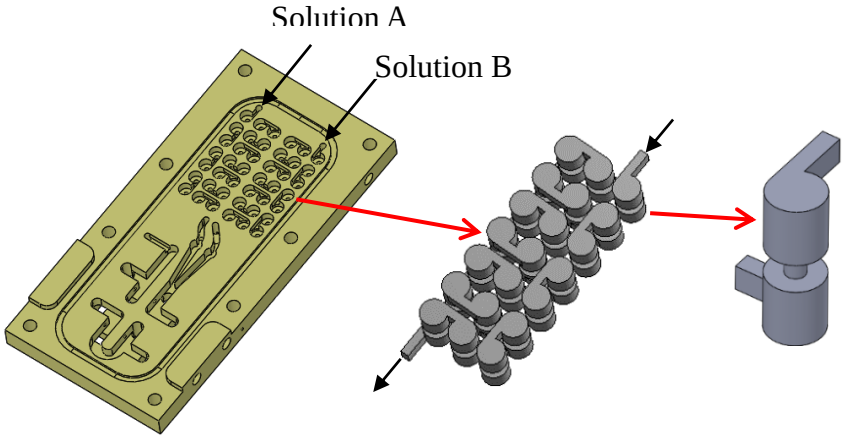

Figure 4. 4 Preheating system of F-element Reactor

4.3 Spatial temperature measurement

The spatial temperature was measured along a line within the reactor domain using a fine (75 μm diameter) butt-welded type K thermocouple wire. Using the fine wire requires tensioning the wire enough to control the location of the thermocouple junction that is sensing the temperature. The tension required was achieved as part of guiding the wire around pulleys (as shown in the Figure 4.5) to link it to a motorized traverser (as shown in the Figure 4.2). One of these pulleys uses a linear spring to maintain tension on the wire and keep the wire along the line of measurement. The free ends of thermocouple wire are connected to the thermocouple plug which is fixed in the motorized traverser (Figure 4.2). The traverse speed of the thermocouple wire depends on the motor speed which is controlled using computer software. The instructions of the software allow the wire to move at speeds up to 2.4 mm/s, while recording temperature with the logger. The wire speed used in the experiment is 0.3 mm/s as this is sufficiently slow for the junction to adapt fully to the local liquid temperature field.

The wire traverses the reactor domain, including the solid body and the flow passages, through two specific paths through each reactor with only a minor effect on the geometry of the passages. Figure 4.6 shows the front and rear wire paths along the domain of reactors C, F and S. These paths include 1/16″ diameter holes in the reactor block to pass the wire. The wire path runs through the middle of the upper level of passages in the F and S element reactors and through the middle of reactor C. The height of the wire path above the base plate is constant so the stand (Figure 4.3) is different for each reactor to accommodate the particular reactor thickness, height and distance back from the front edge of the wire paths. Therefore, a special

stand was used for each reactor in order to maintain the wire path along the fixed line of the traversing thermocouple. Also, each stand has two sets of holes for mounting securely to the base, one for the front wire path and one for the rear. Before beginning a test, the upper covers of the reactor are removed to determine the position of thermocouple junction along the measurement line that is the z-coordinate using a magnifying glass. Determining this junction position assists with determining the starting and ending points along the path for a temperature measurement traverse.

A number of 1/16" sleeves are inserted inside the wire path holes in the reactor body to avoid flow through these holes. The sleeves are inserted up to the passage such that the end of the sleeve is even with the passage wall. Sleeves are inserted within each individual solid section, including the intermediate wall sections, where the wire passes through, using a sleeve length equal to the wall thickness. Standard fittings and ferrules were used to eliminate liquid leakage through the outer sleeve. The sleeve inside diameter of 125 µm, however, does result in minor leakage, which is unavoidable if the wire is to traverse freely. The leakage rate was measured manually by collecting mass of leaked liquid in a specific time. Using the water density at the ambient temperature (White, 2008), the collected mass is converted to a volumetric flow rate. The leakage over the range of conditions used in the experiments was within 1 % of the total flow.

Using a small thermocouple wire is crucial for the registered temperature to accurately represent the local liquid temperature in the flow, as is demonstrated in the next section. A small wire diameter is also important to reduce the obstructing effect of the wire on the flow.

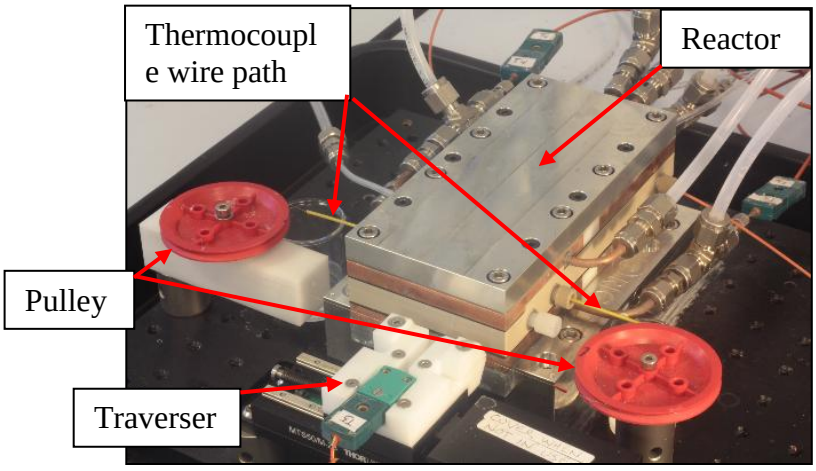

Figure 4. 5 Temperature measurement device.

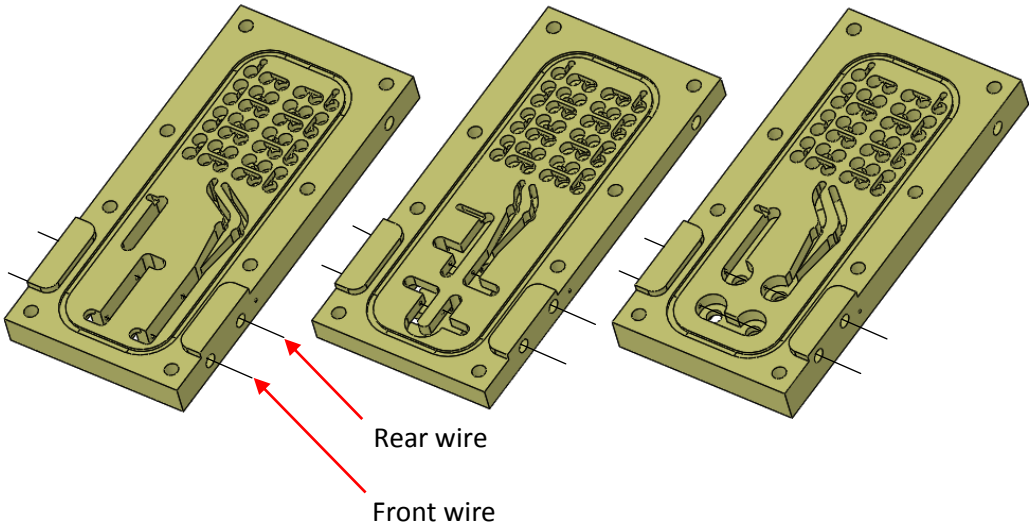

Figure 4. 6 Thermocouple wire paths in domain of C, F and S Reactor.

4.3.1 Conduction error assessment

The heat conduction error for a continuous thermocouple wire can be analysed theoretically by modelling the wire as a cylindrical rod within a uniform flow perpendicular to the wire and having a sinusoidally-varying temperature in the direction along the wire. Figure 4.7 shows the heat balance on a rod of diameter d_R placed in fluid flow at temperature $T_F(x)$ and velocity V.

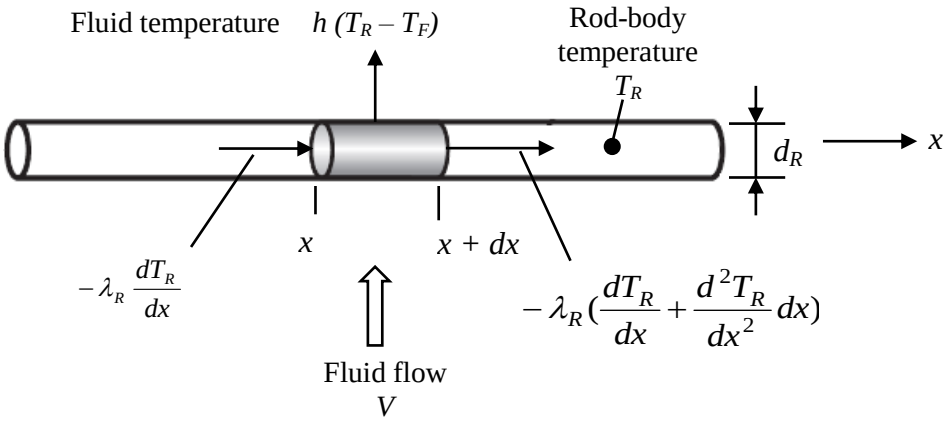

Figure 4. 7 Heat transfer for a thermocouple in a non-uniform temperature flow.

The analysis assumes a steady flow and constant fluid properties. The thermal energy balance can be expressed as the following equation:

$$-\lambda_R\left(\frac{dT_R}{dx}+\frac{d^2T_R}{dx^2}dx\right)\frac{\pi d_R{}^2}{4}+h(T_R-T_F)\pi d_R dx=-\lambda_R\frac{dT}{dx}\frac{\pi d_R{}^2}{4} \qquad (4.2)$$

T_R is the rod temperature; d_R and λ_R are the rod diameter and thermal conductivity; h and x are the liquid heat transfer coefficient and the coordinate along the rod axis. Eq. 4.2 can be expressed, after cancelling terms and dividing by dx, as follows:

$$\frac{d^2T_R}{dx^2}=\frac{4h}{\lambda_R d_R}(T_R-T_F) \qquad (4.3)$$

Imposing sinusoidal fluid temperature,

$$T_F=T_{F_0}+\frac{\Delta T}{2}\sin\frac{2\pi x}{\ell} \qquad (4.4)$$

where T_{F_o}, ℓ and ΔT are the average fluid temperature, length of the sinusoidal wave and the height of wave, respectively. Differentiating Eq. 4.4 twice and subtracting it from Eq. 4.3 leads to the final equation in terms of the wire-liquid temperature difference:

$$\frac{d^2}{dx^2}(T_R-T_F)=\frac{4h}{\lambda_R d_R}(T_R-T_F)+\frac{2\pi^2\Delta T}{\ell^2}\sin\frac{2\pi x}{\ell} \qquad (4.5)$$

which has solution:

$$T_R-T_F=A\sin\frac{2\pi x}{\ell} \qquad (4.6)$$

where A is a constant. Differentiating Eq. 4.6 twice and subtracting it from Eq. 4.5 leads to the following equation:

$$-\frac{4\pi^2}{\ell^2}A\sin\frac{2\pi x}{\ell}=\frac{4h}{\lambda_R d_R}A\sin\frac{2\pi x}{\ell}+\frac{2\pi^2\Delta T}{\ell^2}\sin\frac{2\pi x}{\ell} \qquad (4.7)$$

Simplifying Eq. 4.7:

$$A=-\frac{\Delta T/2}{1+\dfrac{h\ell^2}{\lambda_R\pi^2 d_R}} \qquad (4.8)$$

Substitution Eq. 4.8 in Eq. 4.6:

$$\frac{T_R - T_F}{\Delta T} = -\frac{\sin\frac{2\pi x}{\ell}}{2 + 2\frac{h\ell^2}{\lambda_R \pi^2 d_R}} = -\frac{\sin\frac{2\pi x}{\ell}}{2 + 2\frac{\mathrm{Nu}}{\pi^2}\left(\frac{\ell}{d_R}\right)^2 \frac{\lambda_F}{\lambda_R}} \tag{4.9}$$

where Nu and λ_F are the Nusselt number and thermal conductivity of the fluid respectively. Nu can be related to the flow condition using standard heat transfer relations for a cylinder in cross-flow (Incropera *et al.*, 2013).

$$\mathrm{Nu} = \frac{h\, d_R}{\lambda_F} = C\,\mathrm{Re}^m\,\mathrm{Pr}^{1/3} \tag{4.10}$$

where C and m are constants and they depend on the Reynolds number regime (Table 4.2).

Table 4. 2 Constants of Eq. 4.5 for the circular cylinder in cross-flow.

Re	C	m
0.4-4	0.989	0.330
4-40	0.911	0.385
40-4000	0.683	0.466
4000-40,000	0.193	0.618
40,000-400,000	0.027	0.805

The conduction error $(T_R\text{-}T_F)/\Delta T)$ will be zero when $(2\pi x/\ell) = 0$, at the resting position of the temperature wave, and a maximum when $\sin(2\pi x/\ell) = \pm 1$, at the peak and trough of the wave.

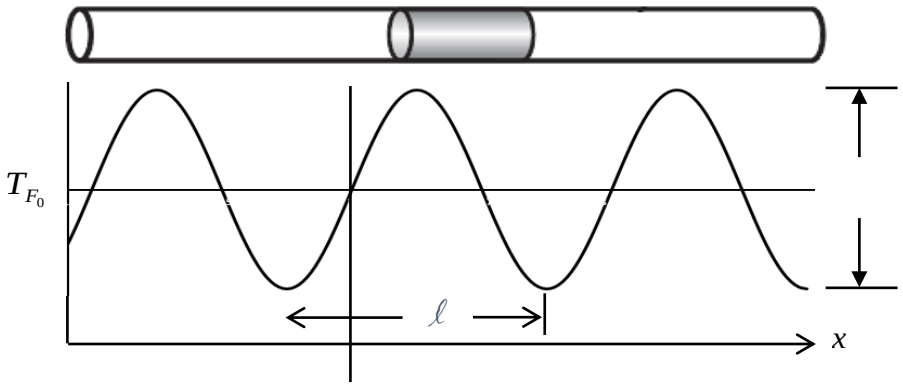

Figure 4. 8 Conducting rod in a sinusoidal temperature field.

Figure 4.9 represents the maximum theoretical estimation of the heat conduction error of the sensor rod, assuming the fluid is water and the wire material is steel. The conduction error was calculated for a range of Reynolds number and rod diameter using the physical properties of water (ρ_F , μ_F , Cp_F and λ_F) and steel (λ_R) at standard conditions. The velocity used (in Eq. 4.5) is the average velocity of flow through the top chamber where the wire passes through. The length of the sinusoidal wave (ℓ) was taken to be 0.01 m. The Figure shows that the heat conduction error decreases with decreasing wire diameter (Eq. 4.9). In other words, the wire becomes more spatially sensitive and the recorded temperature more accurate as the wire diameter decreases (Tarnopolsky and Seginer, 1999). This is because the heat lost along the wire decreases due to reducing the surface area for heat transfer with the liquid (Shaukatullah and Alan, 2003). In addition, the decrease in thermocouple-wire diameter will reduce the response time of the thermocouple (Minn Khine, Houra and Tagawa, 2013). It is also clear from the analysis for this 0.01 m wavelength that the conduction error is about 1% of the correct liquid temperature when the thermocouple diameter is less than 100 μm. If the characteristic wavelength is smaller than 0.01 m, the wire diameter must be further reduced to maintain the same accuracy. Similarly, for a lower Reynolds number (velocity), larger wire thermal conductivity or smaller fluid conductivity, a reduced wire diameter is required to maintain accuracy.

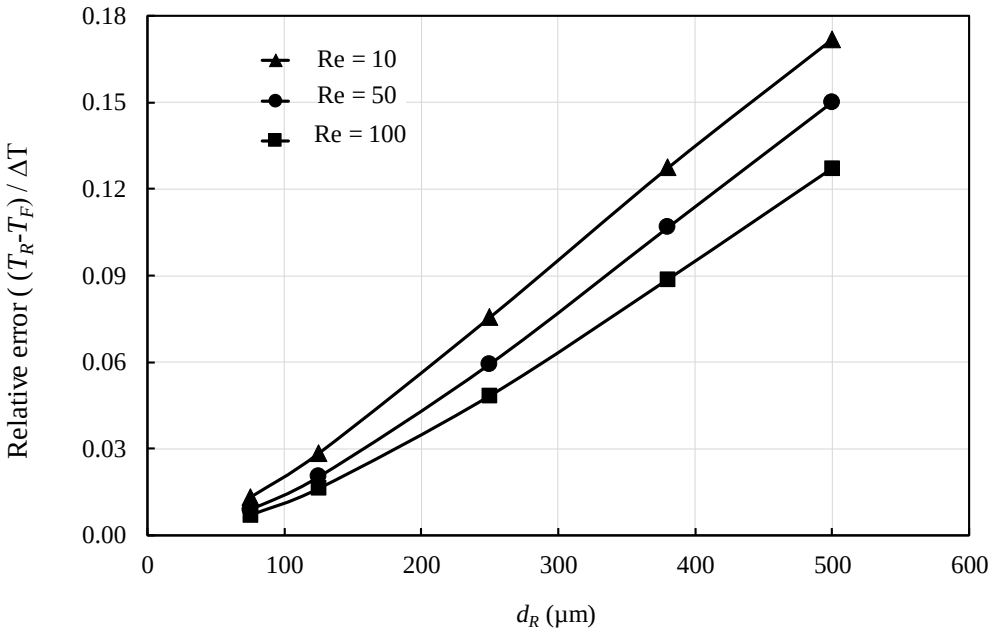

Figure 4. 9 Theoretical estimation of heat conduction error with effect of the wire diameter (d_R) and fluid flow rate (Re).

4.3.2 Conduction error measurement

An experimental study was undertaken to assess the heat conduction error directly. This study was carried out in an initial stage of the work using a small scale swirl element apparatus. The element had two separate inlets and one outlet. Appendix C gives further detail of the geometry of this element and the conditions of the tests. However, these focused on the effect of wire size and wire velocity on the temperature measurement error (Section 4.3 explains how the wire velocity is determined). Different wire diameters with suitable 1/16" sleeves were used.

Table 4. 3 Diameters of wires and inside sleeve diameters tested.

Wire diameter (μm)	The inside diameter of the sleeve (μm)
75	125
125	160
250	275
380	400

Figure 4.10 shows the effect of wire velocity (v_w) on the accuracy of temperature measurement at Re 60 and wire diameter 125 μm. One inlet stream was warm and the other inlet was cool to create the variation in temperature. The temperature was measured along a line across one of the chambers (diameter 24 mm) of the element. According to Fig. 4.10, the results vary considerably and erratically at the left side of the chamber (between -12 and -8 mm), except for speeds of 0.4 mm and lower. Whilst throughout the rest of the profile the results for speeds of 0.4 mm and lower remain more coincident than the higher speeds. There is one anomaly near to the central valley of temperature where the 0.4 mm deviates more considerably from the two lower speed results. It looks like using 0.4 mm/s or below is sufficiently slow to measure the temperature.

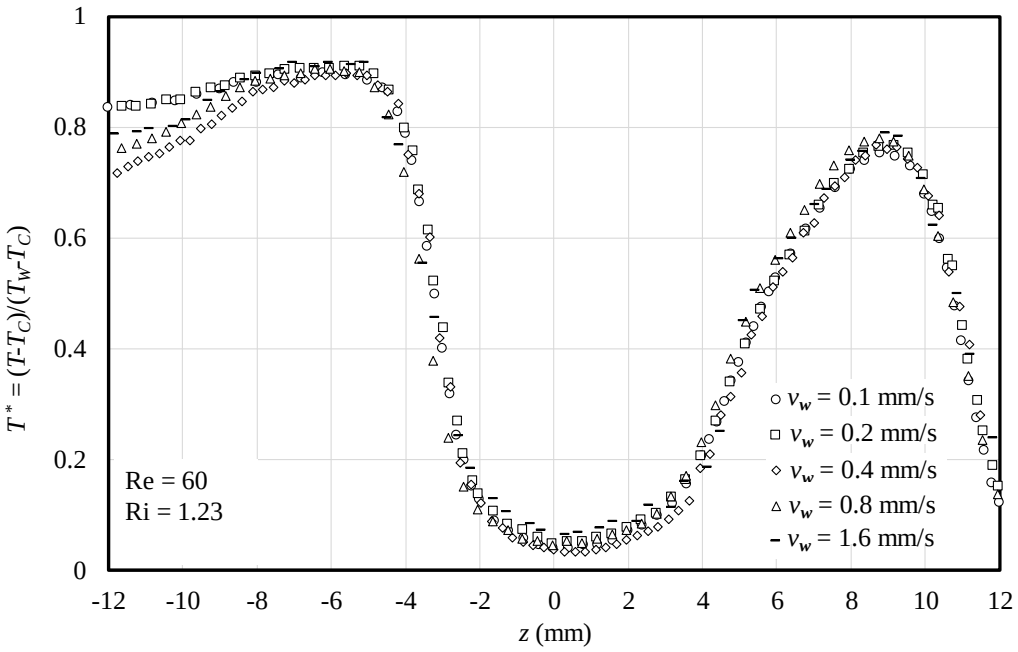

Figure 4. 10 Experimental estimation of heat conduction error at 125 µm wire diameter with effect of wire velocity (v_w).

4.3.3 Wire diameter

Figure 4.11 shows the effect of wire diameter (d_w) on the measured temperature profile at Re 60 using a wire speed of 0.1 mm/s in all cases. The figure shows that the wire size has a significant effect on the temperature profile, of course as a result of the corresponding conduction error. Eq. 4.9 showed that the greatest error is expected at the peaks and the troughs of temperature variation and that is certainly what is observed for the temperature peak at the right side of the profile. The temperature peak increases considerably as wire size is decreased. There is a clear convergence to a peak height with a decrease in the wire diameter that is dependent of wire conduction. On the left side of the temperature trough in the centre of the profile, however, a clear progression to a wire size independent profile is evident, with the difference in the profiles for the two smallest wire diameters nearly coinciding. Overall, for this flow condition and temperature distribution, the 75 µm wire appears to produce temperature measurement with an acceptably small conduction error.

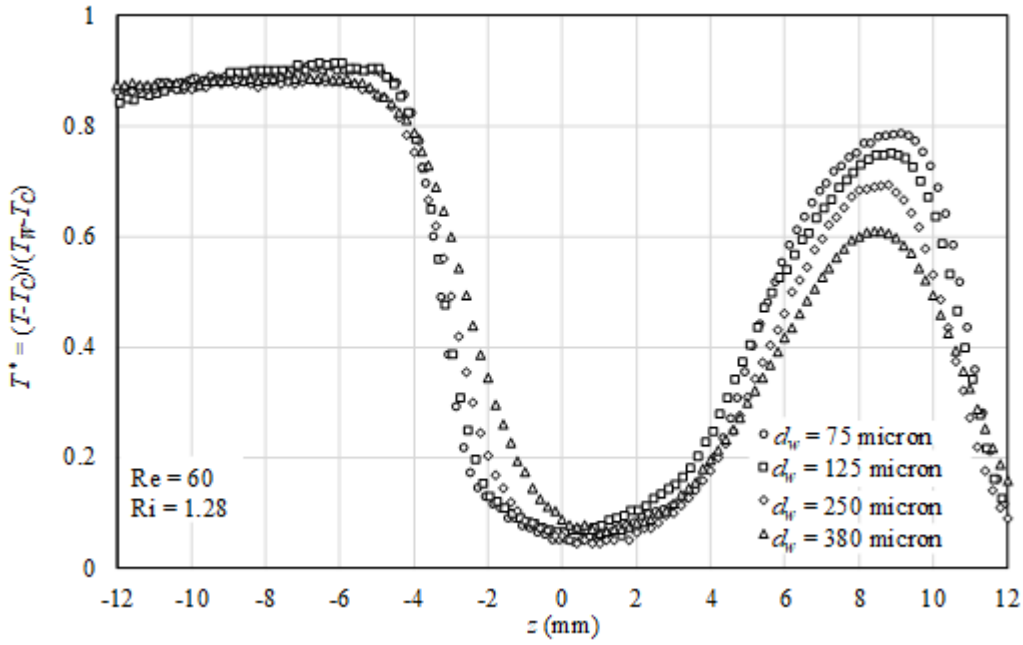

Figure 4. 11 Experimental estimation of heat conduction error with effect of wire diameter (d_w).

According to Figure 4.11, the length of the temperature wave is 0.01 m approximately at 75 µm wire diameter. The maximum conduction error calculated for this experiment is 1% (according to the Eq. 4.9) of the correct liquid temperature at the conditions used. On the other hand, Figure 4.11 shows the maximum conduction error, at the peak of the right-hand side where the curvature is greatest, of approximately 5%. That means the conduction error in the theoretical assessment (Figure 4.9) looks different to the conduction error in the experimental assessment (Figure 4.11). This may be because the theoretical model was based on uniform velocity, constant physical properties and cross-flow of wire rod. In addition, in the experiment, and due to the angular momentum of the flow, there is a velocity component (u_x) that is parallel to the wire which could affect the velocity component (u_y) perpendicular to the wire rod. Generally, the temperature can be measured reliably at these values of conduction error.

4.4 Gas bubbles

Removing pockets of gas at the beginning of each test and avoiding bubble formation during a test are necessary so the test is made with only liquid occupying the flow passages. Gas pockets fill the dry passages at the beginning of the test. But also, gas bubbles can form during the test as the flowing liquids experience suitable changes in temperature and pressure for dissolved gassed to come out of liquid solution (David, 2004). The pockets and bubbles must be

removed from the passages, or prevented from forming there, where they can affect the flow and, hence, the profile of temperature.

In the experiment, initial pockets of gas were removed by forcing a surfactant-water solution at high flow rate through the preheater and reactor passages just before beginning each test. Bubble formation during the tests was reduced by using deionized water, which has a low quantity of dissolved gases, in preparation of the reagent solutions and by avoiding excessive reactor temperature. In addition, a float was used to cover the reagent solutions in the pressure pots to reduce gas access to the liquid and consequently gas absorption taking place in the pressure pots. The details of the development of the strategies used to limit bubble formation during the tests are presented in the next two sub-sections.

4.4.1 Removing gas initially

Air bubbles were removed before each test by pumping surfactant at a high flow rate, 2.4 L/min, to remove the majority of any gas initially in the reactor. The surfactant was 0.2 mL/L of Fairy Liquid soap in deionized water. Section D.1 in Appendix D shows the details of DI water used. The surfactant assists in reducing the surface tension of the solution to facilitate the separation of bubbles from the walls of the passages. (Pot C, Figure 4.2, was used for surfactant without a cover float since the pumping period was only about 3 minutes and in any case the surfactant solution was immediately replaced by liquids from the covered beakers in Pots A and B). The surfactant was pumped in reagent streams individually at the beginning and then together to ensure the passages were completely clean. The process of clearing bubbles was studied by covering the top of the reactor with a transparent window that allowed observation of bubbles and gas pockets within the reactor passages. A camera was used to see the position of bubbles within the passages. It was noted that most bubbles were removed from the passages by pumping surfactant at high speed (2.4 L/min). However, it was also necessary to interrupt the flow by opening and closing the shutoff valves repeatedly during the surfactant solution flow to ensure dislodging and removal of all bubbles. At this stage, the reactor was ready to carry out a test.

4.4.2 Bubble formation

The equilibrium concentration of the dissolved gases in a liquid solution strongly depends on the pressure and temperature. The concentrations increase with increasing pressure and decreasing temperature (David, 2004; Kolev, 1991). The solutions that fill the beakers initially

at 1 bar and the ambient temperature are pumped to the reactor by exposing them to air at high pressure in the pots. This exposure increases the solubility of the main air gases, such as O_2 and N_2, in the solutions due to increasing pressure. These dissolved gases desorb from the solutions inside the reactor due to the drop in pressure between the pots and the reactor and the rise in temperature that takes place in the heated reactor and the heat released from the reaction.

Preliminary tests were made to investigate the factors affecting the formation of gas within the reactor passages during operation. In this study, the top heat exchangers and reactor cover plate were replaced by a transparent acrylic window and a camera was used to monitor the formation of bubbles for a period of 15 minutes from the start of flow into the prepared reactor. This study focused on three main factors: quality of water, reactor temperature and the air pressure inside the reagent pots. The effect of the water quality on bubble formation was tested using four different states of water: water saturated with O_2 and N_2 at 12 ^oC (tap water under pressure 3 bar and cooled up to 12 ^oC), saturated at 25 ^oC, and freshly deionised (DI) water and, finally, surfactant solution. The concentration of surfactant solution was described in the previous section. The three cases of water differ in the amount of dissolved oxygen and nitrogen. The effect of reactor temperature was tested at three different bottom reactor plate temperatures (35, 40 and 45 ^oC). The effect of the pressure inside the pressure pots was tested by operating with and without a float to cover the reagent solutions (Figure 4.2). Studying the formation of bubbles included the size of the bubble formed and the place of the bubble within the passages. The tests were implemented with no flow (Re = 0) in order to monitor the bubbles clearly and a photograph was taken at one-minute intervals. The pressure inside the reactor was 1 bara.

Figure 4.12 shows that the bubbles formed within the upper chamber passages of the F-element Reactor at a heat exchanger plate temperature of 45 ^oC using DI water. The bubbles can form and appear at any place within the passages, whether on the walls of the passages, within the liquid in the passages of flow, or around the thermocouple wire. These bubbles might cohere together to form one big bubble or move to another place due to buoyancy and the surface tension effect. The maximum diameter of bubbles formed was approximately 7% of the passage width – a size that might be acceptable to some extent.

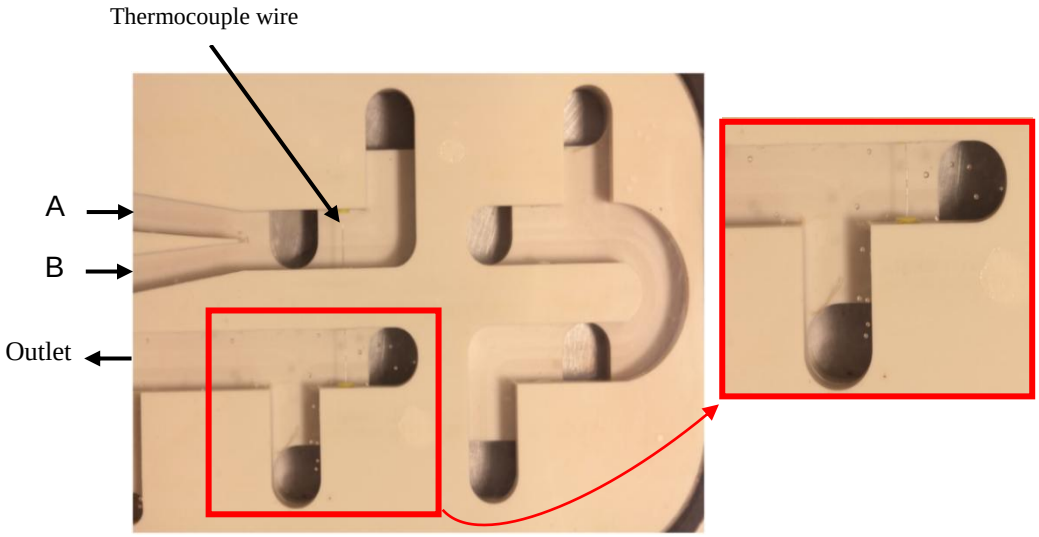

Figure 4. 12 Topside view of the F-element Reactor showing bubble formation within the passages.

Figure 4.13 represents the effect of water state on the number of bubbles recorded in photographs over the 15-minute test for a 45 ^{o}C reactor plate temperature. The figure shows that when using saturated water, the number of bubbles formed (N_B) when using 12 ^{o}C saturated water is higher than with the 25 ^{o}C saturated water. This is because the equilibrium concentration of gases is greater at the lower temperature.

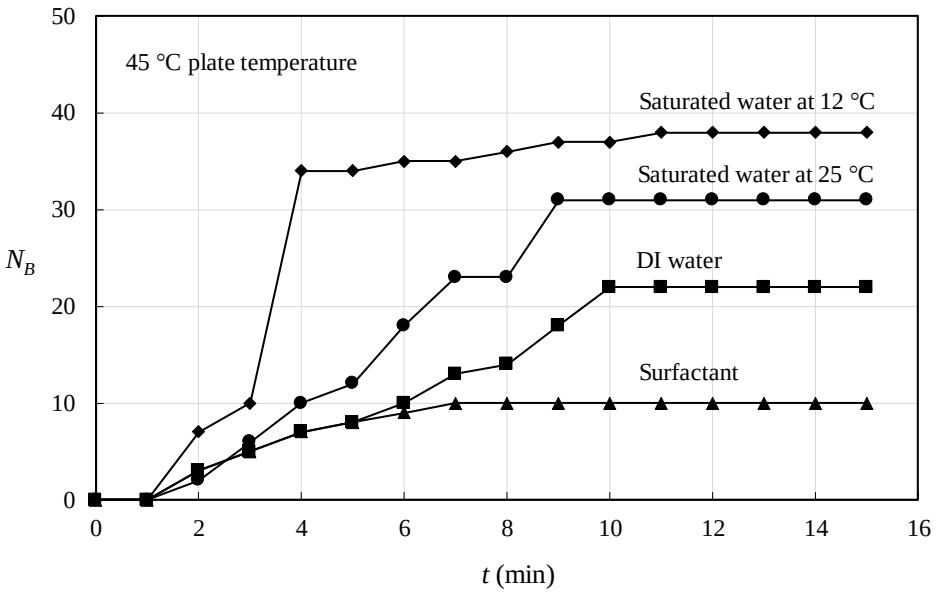

Figure 4. 13 The relationship between bubbles formed and types of water.

The figure also shows that the number of bubbles formed using saturated water at either temperature was higher than when fresh DI water, which is collect from water purification system directly, was used. This must be due to a smaller amount of oxygen and nitrogen in water from that source. In addition, the number of bubbles formed using surfactant is lower than when using DI water; this is because the surfactant reduces the surface tension of the liquids, thereby causing the air bubbles which stick to the surfaces of the reactor, to be removed.

Figure 4.14 shows the effect of the reactor temperature on the number of bubbles. The figure shows that the number of bubbles (N_B) formed increases as expected with increasing reactor plate temperature, since this will increase the temperature of the flowing liquid to some extent and hence lower the gas solubility.

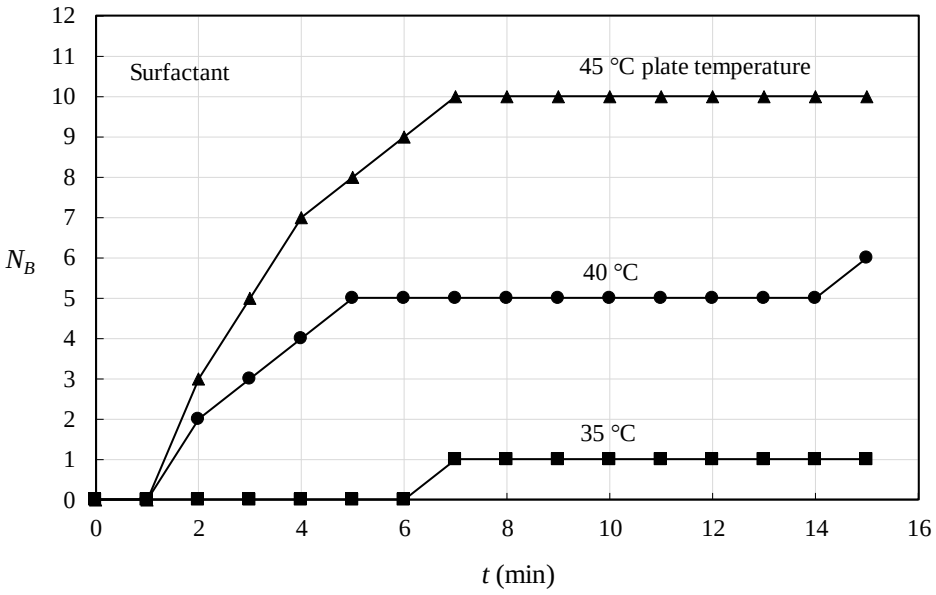

Figure 4. 14 The relationship between bubbles formed and temperature of reactor plate.

The effect of using the cover float is shown in Figure 4.15. The float greatly reduces the contact area between the air and solution in the pressure pot so it is not surprising that using the float reduces the number of bubbles considerably. Therefore, using the float in such experiments is essential to eliminate the bubbles formed.

Based on the results of the tests, it is important to use DI water when preparing the reagents solutions; this will minimise the number of bubbles formed, and their size, to an acceptable level. The reactor plate temperature must not exceed 45 ^{o}C to prevent the formation of extra bubbles.

Using floats to cover the reagent solutions A and B in the pressure pots is essential to reduce the bubbles formed.

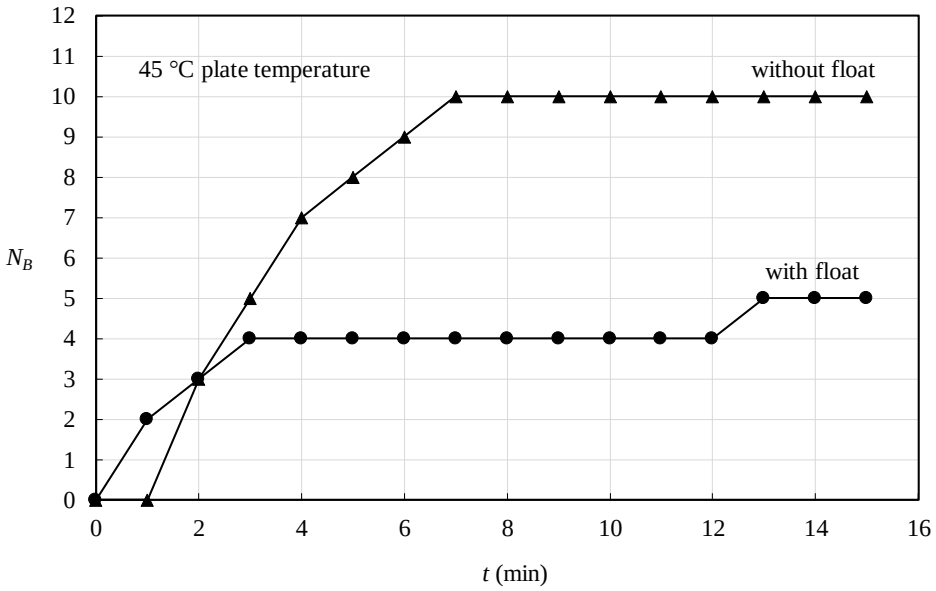

Figure 4. 15 The effect of using the float on the number of bubbles formed.

By following these precautions, the bubbles formed could slightly affect the flow pattern and temperature field within the flow passages. This means the agreement between the experimental data and the computational results of the temperature profile could be slightly affected.

4.5 Test procedures

At the beginning of the experiment, a surfactant was introduced to the reactor at a high flow rate to remove the air bubbles from the reactor passages at the ambient temperature (as described in Section 4.4.1). The flow rate of the surfactant was adjusted using a pressure regulator. After clearing bubbles, the surfactant flow was stopped and solutions A and B were introduced to the reactor at the required flow rate. The reagent solutions A and B had been prepared previously using DI water at a given concentration of A and B. Appendix D shows the details of the chemicals used in this study and the preparation procedures. The beakers of these solutions were covered with a float inside each pressure pot to reduce the solubility of the air gases in the solutions. The solutions were left for 15 minutes to rid of the heat of dilution before being introduced into the reactor.

For testing at a given Reynolds number, the required flow rate was obtained by setting the suitable pressure in the solution Pots. The flow rate was measured directly by collecting the outlet solution from the reactor at a specific time. The relative rms (root mean square) of the total flow rate was within 2 %. The flow of solutions continued for a period of time to reach the compositional steady-state. During this time, the remaining surfactant in the passages was replaced by solutions A and B. Following this, the required thermal conditions for the apparatus, reagent stream inlet temperature and reactor temperature were prepared by setting the temperature of the two heaters at the required conditions. This setting allows control of the temperatures of the copper preheating plates and copper reactor plates. It took 4 minutes for the system to reach the thermal steady state. The details of the compositional and thermal steady state are addressed in the next sub-section. After this, the temperature along a line within the reactor domain was measured using the movable continuous thermocouple wire. The position of the measurement line, starting and ending points of the measurement line, and the wire speed were determined using the traverser software. The starting and ending points of the temperature measurement line depend on the position of thermocouple junction along the measurement line that is determined before the test is started (see Section 4.3). The speed of the thermocouple wire was 0.3 mm/s and the wire diameter used was 75 μm. Recording data along the measurement line took 2.8 min.

4.5.1 Steady state

The temperature measurement along one of the paths through a reactor must be carried out after the system has reached the state of compositional and thermal stability. Otherwise, the temperature will be measured under transient conditions, in which the temperature distribution within the passages changes with time. The compositional steady-state includes removing residual surfactant remaining from the flushing process and producing the steady concentration fields of reagents A and B in the reactor for the flow and thermal steady state conditions of a test. The surfactant may affect the reaction mechanism and the heat distribution by affecting the composition of reagent solutions. Therefore, the temperature should be measured after reaching the compositional steady-state to exclude the possibility of the surfactant interfering with the chemical reaction. Pushing the reagents continued for 8 minutes, at least 10 times longer than the residence time of the reactor, before the experiment started to ensure removal of all the surfactant. This approach was carried out in all experiments.

As shown in Figure 4.2., two heaters are used to provide the thermal operating conditions for the preheater and reactor using tap water. These heaters have the ability to heat water instantaneously with significant control of water temperature. For each experiment, these heaters were set carefully to obtain the required temperatures for the heat exchangers of the preheater and reactor. These temperatures were measured using four thermocouples type K. A significant amount of heat coming from the heat exchangers transfers to the reactor. Furthermore, the heat released from the chemical reaction is additional heat that could be added to the heat of the reactor. These heats need a period of time to spread through the reactor and reach uniform temperature distribution. The temperature must be measured after this time and reach a thermal steady state. Achieving a steady thermal condition was obtained by controlling the temperature of the copper heat exchanger plates and the concentrations of chemical solutions used. The temperature was measured at a specific place in the solid body of the reactor using a continuous-wire thermocouple method. The temperature was read every second. This test was implemented at the thermal mixing system.

Figure 4.16 shows the typical smoothing of the reactor temperature with time for two different thermal conditions of copper heat exchangers: 37 ^{o}C and 41 ^{o}C. According to this figure, the temperature rises quickly when heating starts and reaches the steady-state after 4 minutes. After that, the apparatus will normally be ready to measure the temperature after t > 4 min.

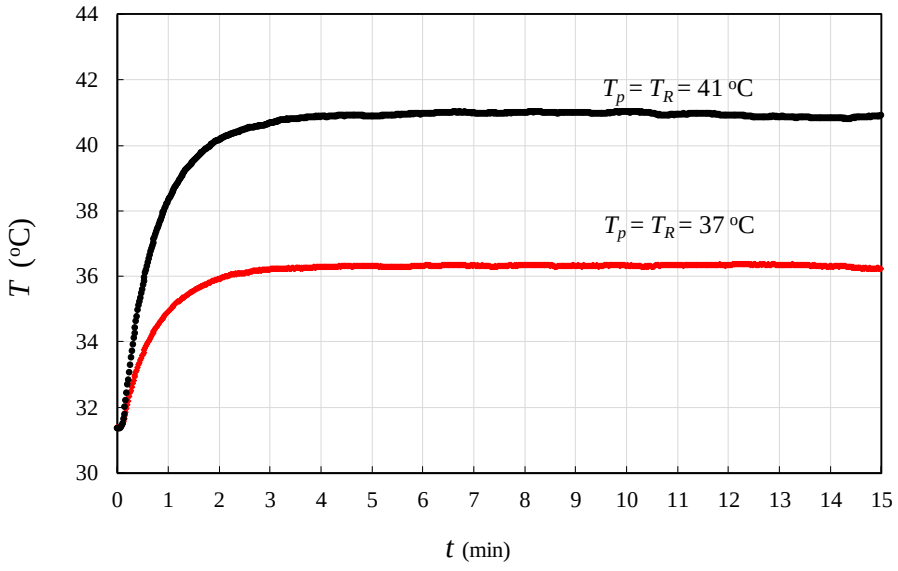

Figure 4. 16 Reactor temperatures recorded at two different thermal conditions of heat exchanger.

This non-fluctuating behaviour of the stabilized state indicates that the reactor has an acceptable control of the temperature at these thermal conditions. On the other hand, these 4 minutes are perhaps also sufficient to obtain the compositional steady state, specifically at high Re, where during this period of time a sufficient volume of flow through the reactor passes to replace the fluid in the reactor many times. Accordingly, the total time required to complete one test was approximately 7 minutes: 4 minutes to reach the steady state and 3 minutes to record the temperature along one of the paths through a reactor. This meant the test could be completed before the bubbles strongly affected the flow as the test was completed well within the 15-minute time period, during which the number of bubbles accumulated is acceptable (see Section 4.4.2).

4.6 Summary

This chapter described the apparatus used and the temperature measurement procedure followed in this work. The experimental apparatus used to obtain the data was described, including the flow network, the reactor and the heat exchangers. Three different geometries, which can be used as reactors, were described: F, C and S. Controlling the temperature of the reagent streams and the reactor using copper preheater plates and the copper reactor plates was explained. Inlet temperature to the reactor can be estimated according to the preheater computations depending on the copper preheater plates and flow rate of the reagents. This temperature may be adjusted slightly according to the reactor computations to match the experimental data. The measuring method of the spatial temperature along the reactor using a movable fine-wire thermocouple was described. This method can cause an error in heat conduction depending on the wire size and wire velocity. The heat conduction error increased with increasing the wire diameter and increasing the wire velocity. Reliable temperature measurement can be obtained experimentally at wire diameter 75 μm and wire velocity 0.4 m/s or below. The temperature measurement has the largest error at peaks or troughs in the temperature profile, and these may be up to around 5%. The leakage rate from thermocouple wire ports can be controlled using sleeves and ferrule fittings. The leakage was within 1 % of the total flow under a range of conditions. Air bubbles can form at any position of the flow passages as a result of desorption of the dissolved gases in the reagent solutions inside the reactor. The number of bubbles formed was reduced by pushing a surfactant at a high flow rate at the beginning of the test, using DI water in preparation of the reagent solutions A and B and covering the reagents solutions A and B inside the pressure pots with floats; nevertheless, some

bubbles still formed in the flow passages. These bubbles could alter both the flow field and the heat distribution within the reactor. This change can lead to a significant error in the profile of the temperature measured when the bubbles are formed close to the thermocouple paths. The procedure followed to implement the test and record the temperature was described. At the end of the chapter, the time required to reach the chemical and thermal steady-state of the apparatus was explained.

Chapter Five

5. Results of the Non-Reacting Flow

The results were generated as explained in preceding chapters (Ch. 3 and 4) using zero-heat-flux at all four side boundaries; uniform temperature and uniform velocity at the reagent inlets; and the top and bottom heat transfer coefficient represented in Eq. 4.1. This chapter includes the results of the non-reacting flow system tests only. The aim of using the non-reacting flow system first was to discover the physical and thermal properties of the system, such as heat transfer coefficient, heat capacity, density and viscosity through CFD simulation. A further aim was to investigate the effect of gravity on the flow pattern and temperature distribution through the flow passage. In this flow system, the solutions of the flow equations and energy equations are completely independent of the species equations where no reaction occurred.

This chapter is divided into four main sections. The first section presents the experimental conditions used in this chapter and the comparison between the experimental data and the computational results. This comparison aims to show the extent of agreement between the experimental data and the computational results. The comparison may indicate the possibility of using the model to reliably predict the spatial temperature distribution within the domain of the reactor. The second section presents the factors that affect the flow pattern and temperature distribution along the flow passage, such as the Richardson number and gravity. This section describes the characterizations of reactors used, such as the flow pattern and temperature field along the flow passage. The third section shows the effect of inverting the thermal boundary conditions on the temperature distribution within the reactor domain. This will assist in determining which boundary conditions can be used to reduce temperature non-uniformity. Finally, the chapter closes with the effect of Ri and Re on the mean temperature and temperature non-uniformity along the flow passages.

5.1 The experimental conditions

A non-reacting flow system was tested at different thermal boundary conditions. Table 5.1 shows the thermal boundary conditions used in this chapter. The thermal conditions depend on the temperature of the copper preheater plates (T_P) and the temperature of the

copper reactor plates (T_R). The geometry of the plates of the preheater and reactor was described in Section 4.1. The value of Richardson number (Ri) depends on the temperature differences (ΔT) between T_R and the temperature of the reagent stream inlet (Section 4.2.2 shows how the inlet temperature is determined). Reynolds number (Re) and Richardson number (Ri) were calculated according to Eq. 3.22. The reference density (ρ_o) represents the density of the liquid at T_R. The range of temperature differences (ΔT) between T_P and T_R gives a different value of Richardson number (Ri) for a given flow system and somewhat affects the temperature profile. The temperature differences (ΔT) in this chapter are 20 ^{o}C, 10 ^{o}C and -20 ^{o}C. The value of T_R was selected to ensure that the phase of flow remained liquid and hence a reliable measurement of temperature could be obtained. The experiments were implemented in the laminar regime flow, where the largest value of Re was near to the upper limit of the laminar regime for swirl element (Re < 120). Re was 32, 65 and 130.

Table 5. 1 The boundary conditions used in the Non-Reacting flow tests.

Re	T_P, ^{o}C	T_R, ^{o}C	ΔT, ^{o}C	C-Element Reactor	F-Element Reactor	S-Element Reactor
				Ri	Ri	Ri
32	45	25	20	-30.4	-15.5	-19.6
	40	30	10	-14.2	-6.6	-9.5
	25	45	-20	36.3	15.6	23.1
65	45	25	20	-6.7	-3.2	-4.6
	40	30	10	-2.8	-1.4	-2.1
	25	45	-20	9.3	3.6	6.0
130	45	25	20	-1.2	-0.6	-0.9
	40	30	10	-0.4	-0.3	-0.4
	25	45	-20	2.3	0.9	1.5

5.2 Computed and measured temperature profiles

This section shows the agreement between the experimental data and the computational results in the C, F and S element Reactors. The results represented in this section are only for the hot liquid inlet, when the copper preheater plates are hot, and cool copper reactor plates along the rear wire path only. The results for the other wire path, i.e. the front path which is not shown here, and for the cool liquid inlet, lead to identical conclusions in terms of agreement between the experimental data and computations. The

wire path in the C-element Reactor passes through four passage sections (see Fig. 4.6), whereas for F and S it only passes through two sections (see Fig. 4.6). The domains for measuring the temperature across the reactor include solid domain and flow passages along the z-direction. The value of z is zero at the meeting point of reagents A and B at the beginning of the first element (see Figs. 3.1-3.3). The shading along the top plot indicates the regions that are solid.

Figs. 5.1, 5.2 and 5.3 show that the computed results are impressively close to the experiment in all boundary conditions and in all geometries used, with the exception of the results for the S-element Reactor at the higher Re values. The computations reliably capture the features of the profiles. This agreement becomes weak at a high Re in the S-element Reactor: this may be due to the unsteady flow regime at high Re and the complexity of the process of liquids mixing. This complexity in mixing is due to the disturbance in flow when the liquids pass through the connection hole between the upper and down chambers in the first element. A very fine mesh size is required to capture reliably the differences between computations and experiments. Generally, the agreement between the experimental data and the computational results was acceptable, which allows the model to be used to reliably predict the characters and features of flow patterns and temperature within the domain of all three reactors.

The figures also show the effect of Re and Ri on the temperature profile, which is that the two factors interact with each other: a change in Re leads to a change in Ri and, consequently, a change in the flow pattern (Eq. 3.21) and temperature distribution (Eq. 3.21 3.33). The results include a large range of Ri due to changing Re and also temperature differences. The figures show the Ri has a clear effect on the temperature profile in all geometries. This effect increases with increasing Ri and decreases when it decreases.

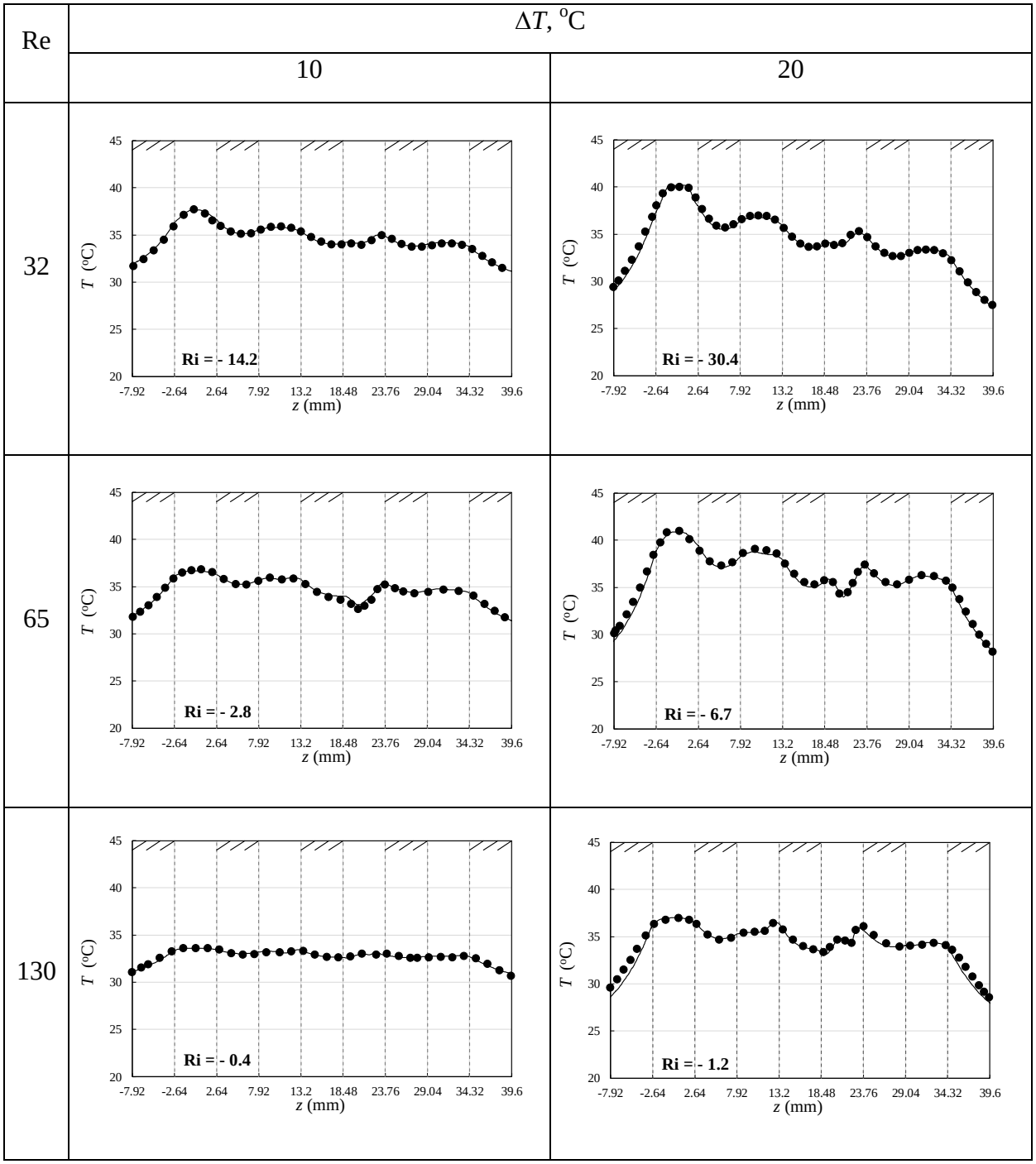

Figure 5. 1 Reactor C: measured and computed temperature profiles along the rear path. Effect of Reynolds number and imposed temperature difference. The points represent the experimental data and the line represents the computational results.

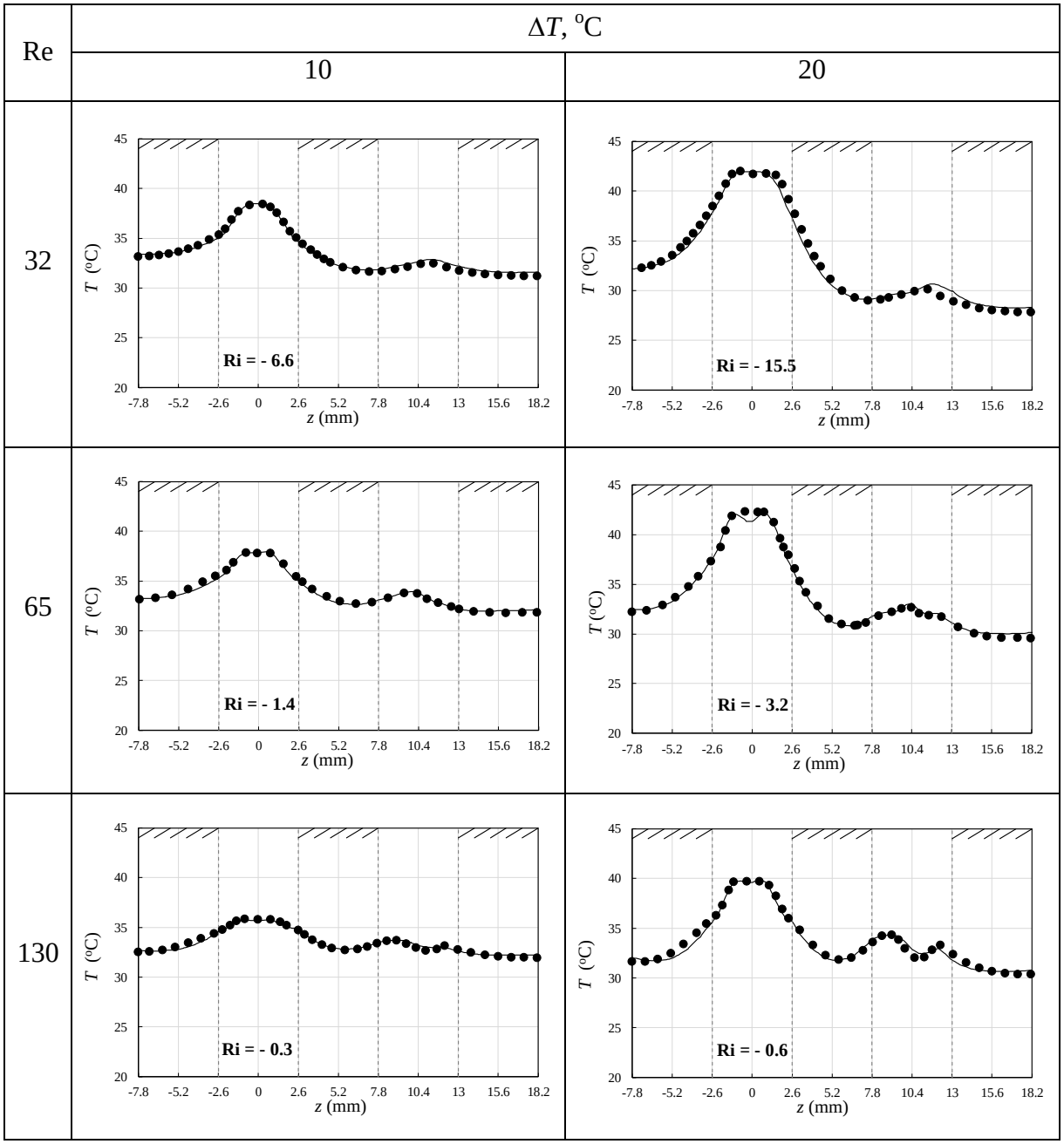

Figure 5. 2 Reactor F: measured and computed temperature profiles along the rear path. Effect of Reynolds number and imposed temperature difference. The points represent the experimental data and the line represents the computational results.

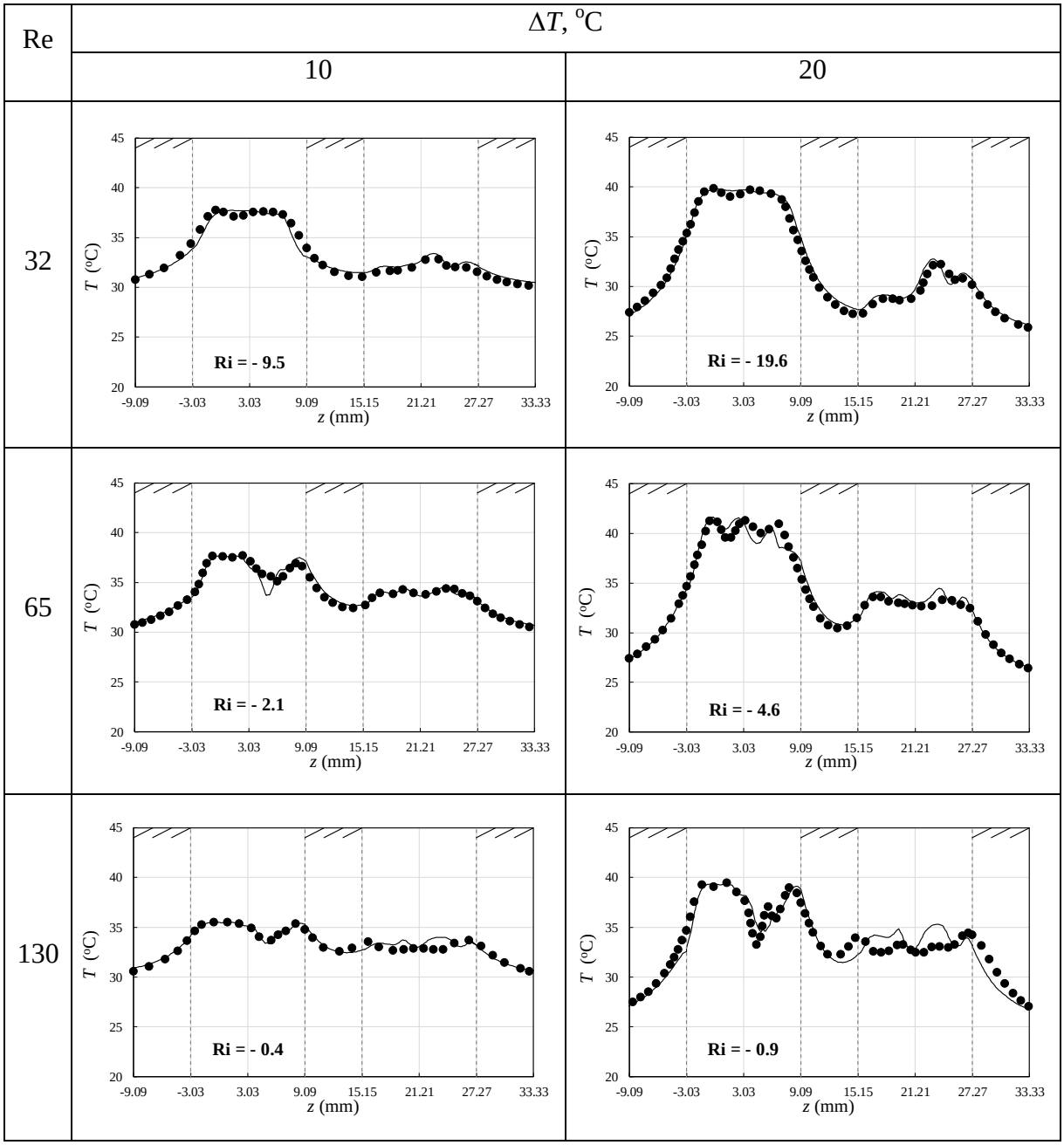

Figure 5. 3 Reactor S: measured and computed temperature profiles along the rear path. Effect of Reynolds number and imposed temperature difference. The points represent the experimental data and the line represents the computational results.

5.3 Richardson number effect

Figs. 5.4, 5.5 and 5.6 show the computational results of the temperature profile along the rear path of the C, F and S element Reactors respectively, at ΔT 20 ^{o}C, 10 ^{o}C and zero gravity (g = 0). Computations can be used to investigate the effect of gravity on the

temperature profiles; gravity can be set to zero in the computation to entirely eliminate that term in the equations. Using computed profiles allows the reliable capture of the temperature variations to gain insight into the buoyancy effect in the experimental cases considered so far in this chapter.

The temperature profile for each reactor includes Re 32, 65 and 130. In these figures (5.4, 5.5 and 5.6), normalised temperature is plotted so the range of temperature is similarly scaled. The normalized temperature ($\widetilde{T}$) is the temperature difference between the temperature and the copper reactor plate temperature $(T - T_R)$, divided by the temperature difference between the reagent stream inlet temperature and the copper reactor plate temperature $(T_I - T_R)$. The figures show there are deviations in temperature profiles in each plot with a changing Ri. The figures also show that Ri has a significant effect on the temperature profile especially at a low Reynolds number due to increasing the gravity force. This effect becomes weak with an increasing Re. In other words, the effect of buoyancy on the temperature profile increases with an increasing Richardson number (Eq. 3.21) and decreasing Re (Eq. 3.33). This effect in the S-element Reactor is larger than in the C and F element Reactors. The effect of buoyancy was minor at a low Ri where there is significant convergence between the temperature profiles. Therefore, the effect of buoyancy on the temperature profile is minor at the lowest Ri values shown in the plots. In other words, the cut-off values of Ri are 0.4, 0.3 and 0.4 for the C, F and S element Reactors respectively, where buoyancy has a strong effect on the temperature profile at the Ri ≥ cut-off value, and a minor effect at the Ri < cut-off value.

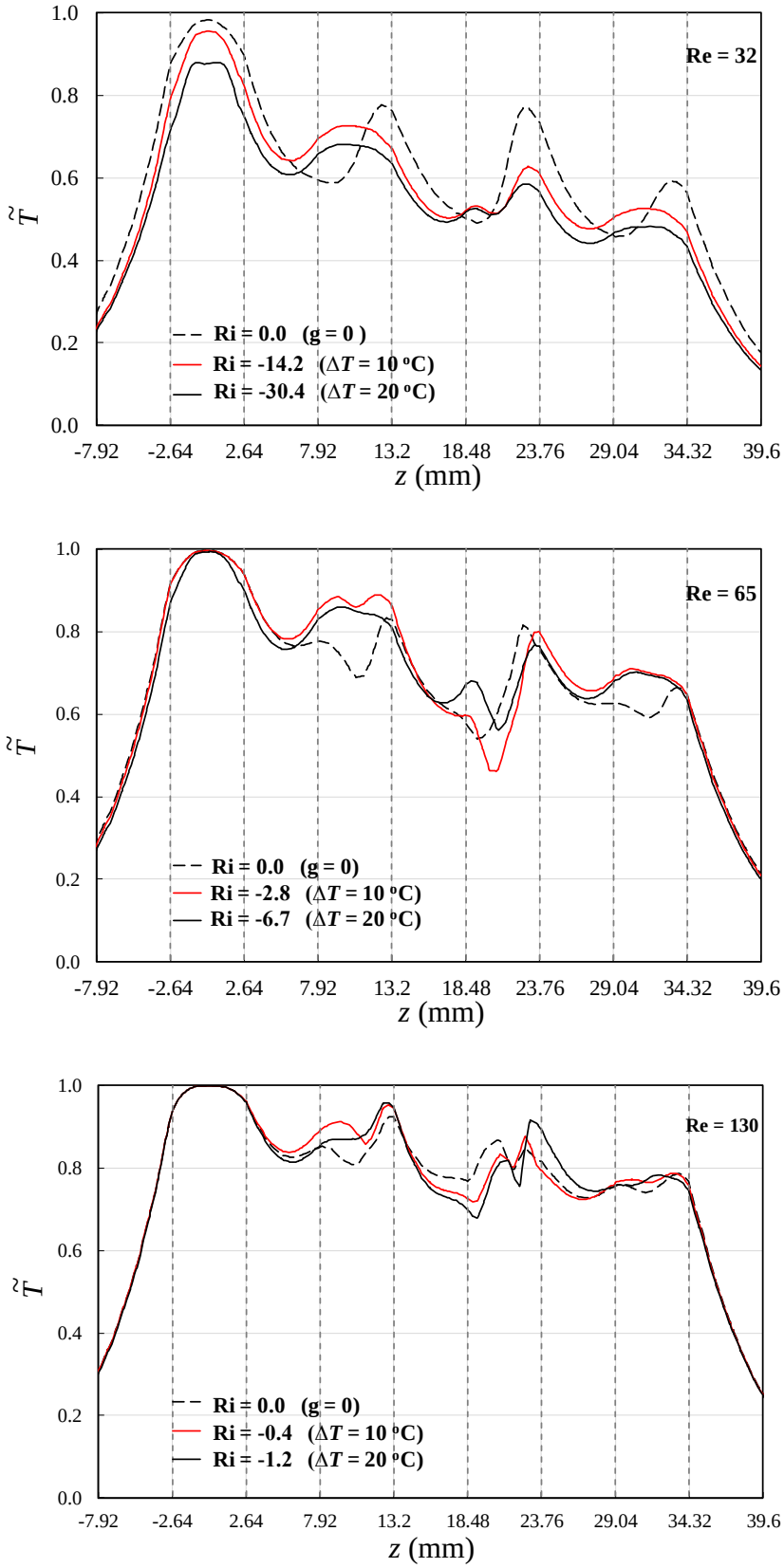

Figure 5. 4 Reactor C: computed temperature profiles along the rear path at the two experimental values of Richardson number and with Ri = 0 (g = 0).

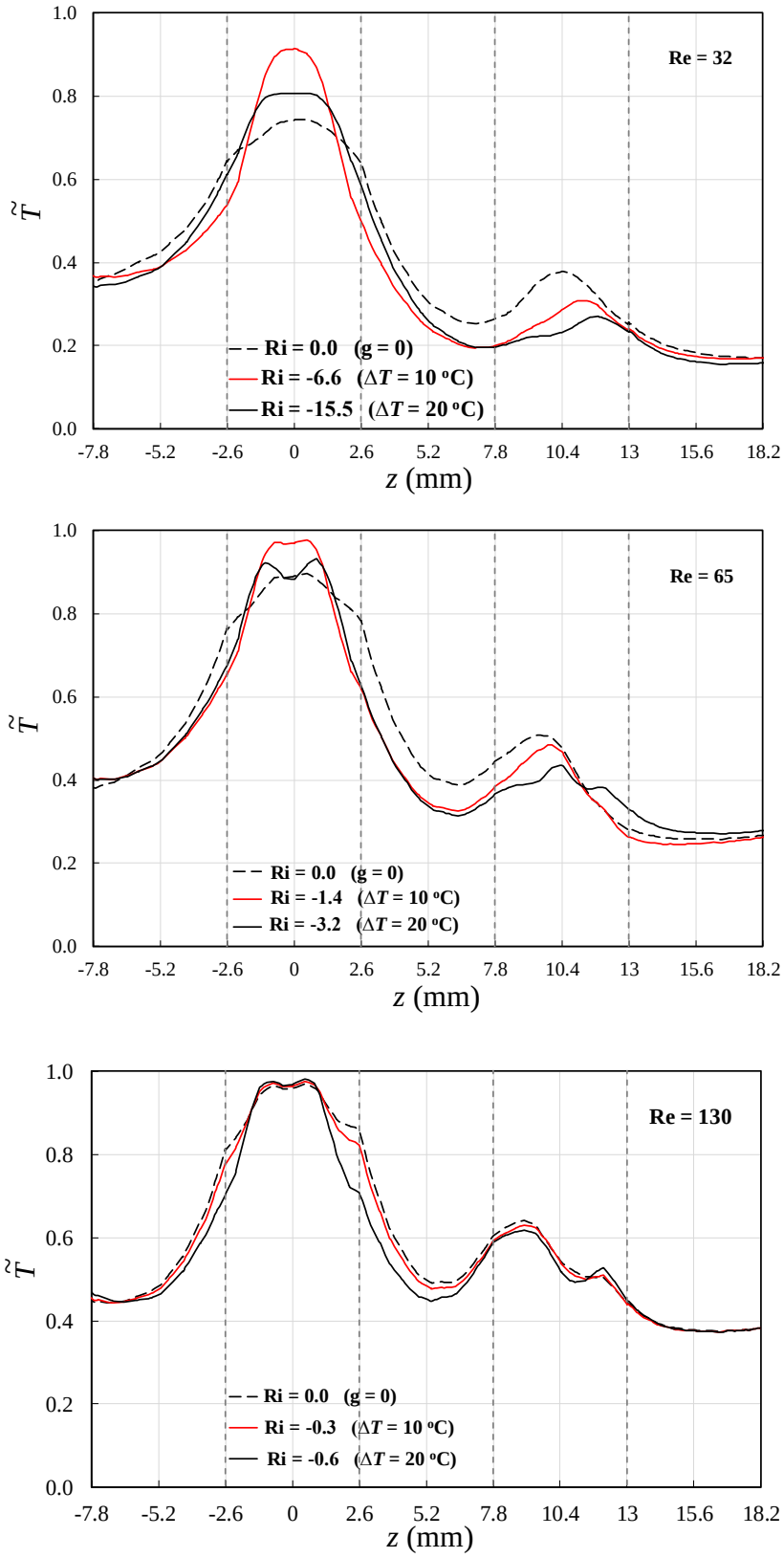

Figure 5. 5 Reactor F: computed temperature profiles along the rear path at the two experimental values of Richardson number and with Ri = 0 (g = 0).

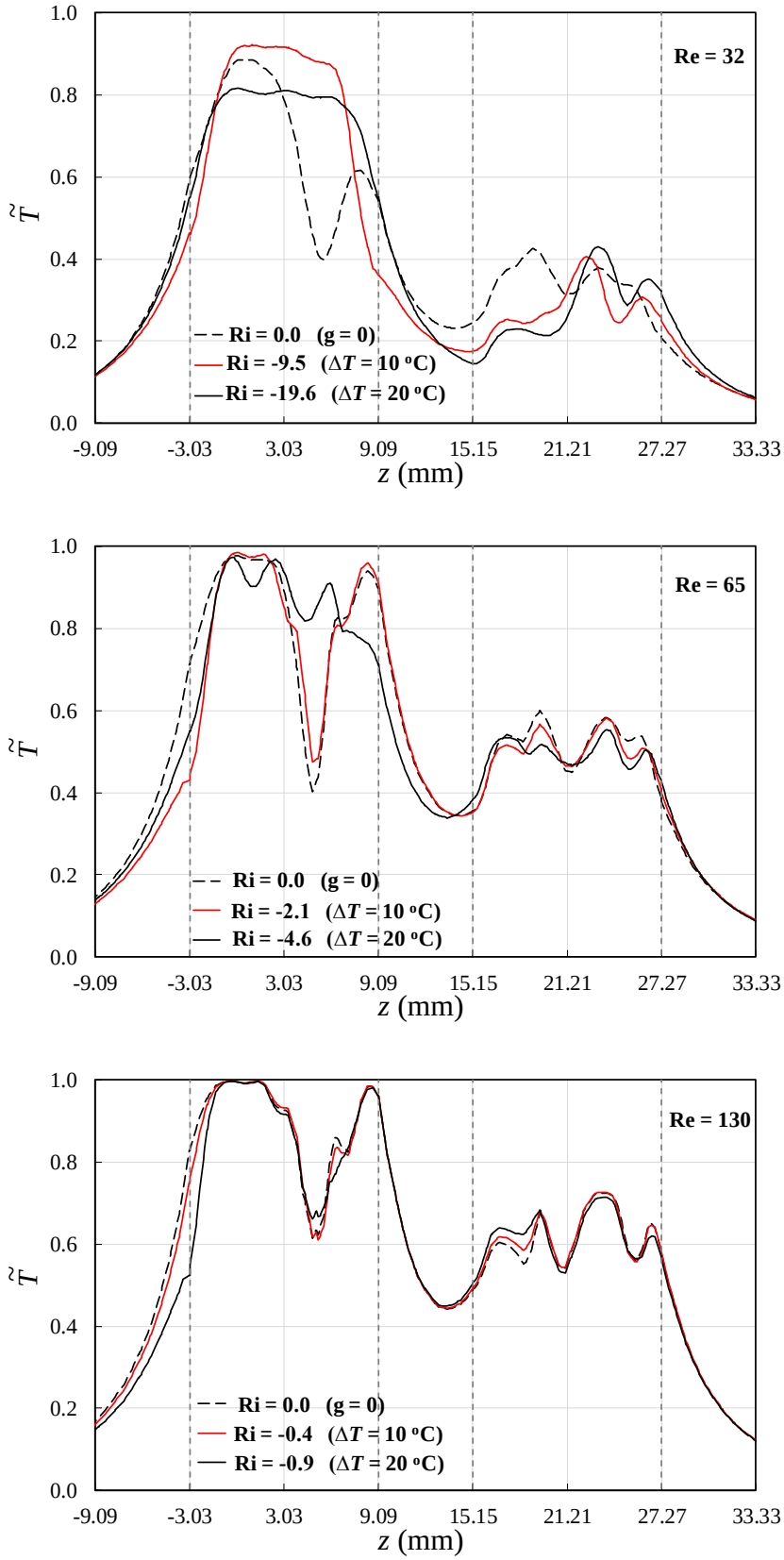

Figure 5. 6 Reactor S: computed temperature profiles along the rear path at the two experimental values of Richardson number and with Ri = 0 (g = 0).

5.4 Effect of gravity on flow patterns

Figs. 5.7, 5.8 and 5.9 show the effect of gravity on the flow pattern and the temperature distribution in the C, F and S element Reactors respectively. The pathlines in these figures are coloured by temperature: the maximum temperature is the reagent stream inlet temperature (T_I), and the minimum temperature is the copper reactor temperature (T_R). These pathlines were at Re 32 and ΔT 20 ^{o}C **(**see Table 5.1).

Fig. 5.7 shows the flow pattern and the temperature distribution in the C-element Reactor. In this reactor, the flow carries the fluid in a straight direction in the first element and then transfers it to the second element through a small downward dip at the bend. This type of flow repeats four times in the reactor to enhance the mixing of reagents. The fluid temperature along the flow passage might be affected by the temperature of the copper reactor plates. This effect could cause a change in the buoyancy of the fluid. As buoyancy becomes stronger the flow will be affected depending on the stability of the density layering.

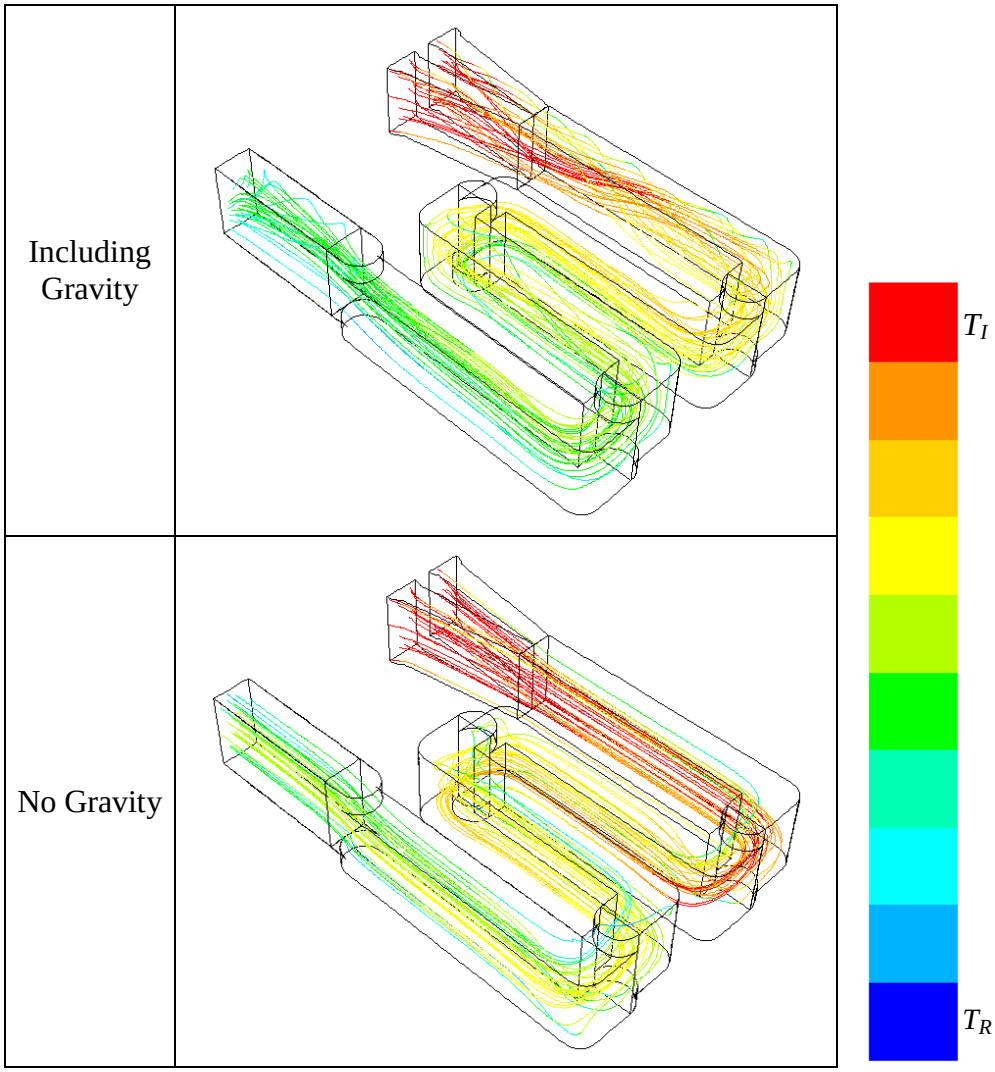

Figure 5. 7 Reactor C: computed pathlines of flow along the flow passage at Re = 32 and ΔT 20 ^{o}C.

Figure 5.8 shows the flow pattern and the temperature distribution in the F-element Reactor. The flow in this reactor divides into two branches in the first element. These branches fall downwards and recombine again. The fluid continues to be heated or cooled, according to the temperature of the copper reactor plates, in certain places and the fluid comes together with some parts having been heated or cooled. This type of flow repeats four times in the reactor to enhance both reagent and thermal mixing. The flow through each element might be affected by gravity depending on the reagent flow rate and thermal boundary conditions.

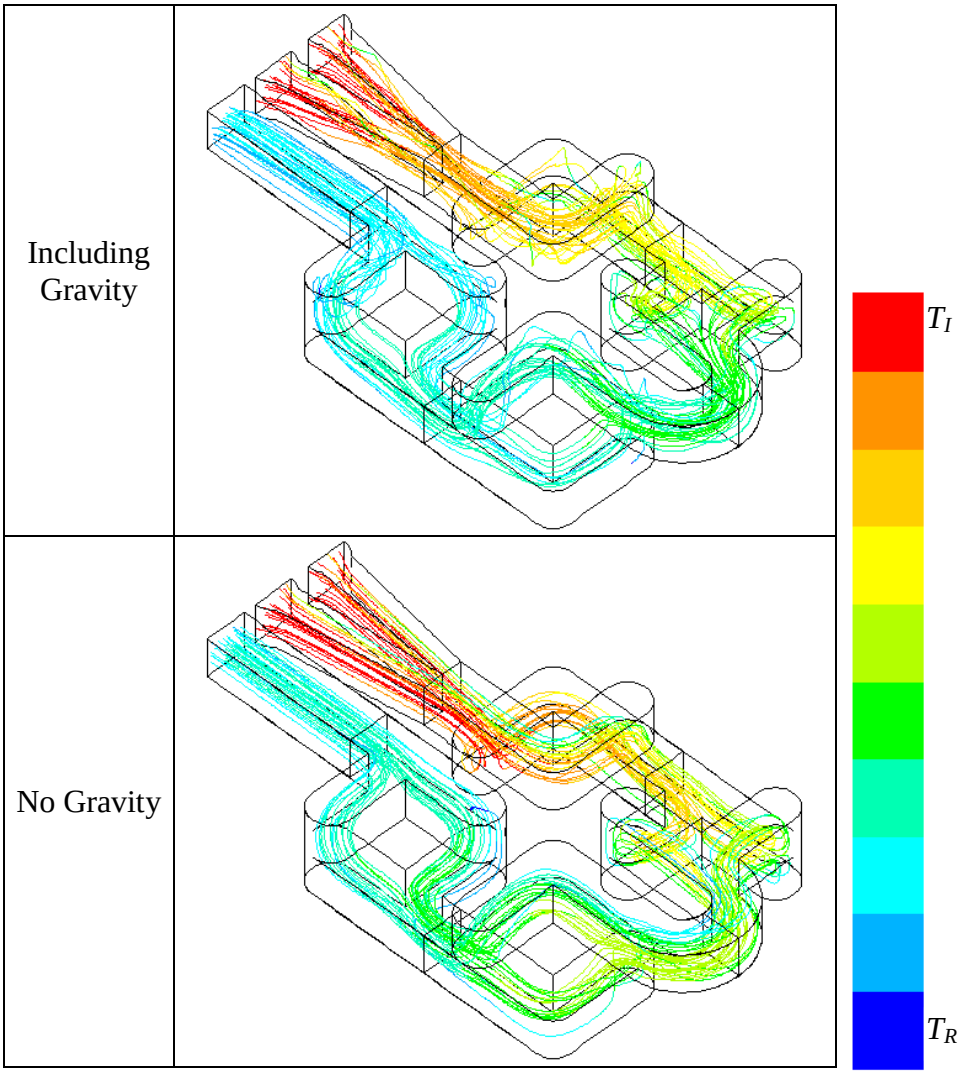

Figure 5. 8 Reactor F: computed pathlines of flow along the flow passage at Re = 32 and ΔT 20 ^{o}C.

Figure 5.9 shows the flow pattern and the temperature distribution in the S-element Reactor. The flow in this reactor passes through a circular hole which connects the upper chamber with the lower chamber in the first element. An angular momentum forms when the flow passes through the hole. This angular momentum causes a high tangential velocity due to the reduced radius of the circular passage. The high tangential velocity which passes through the hole results in strong radian movement and mixing. This type of flow, which is like a swirl flow, repeats four times in the reactor to enhance the mixing of reagents and thermal mixing.

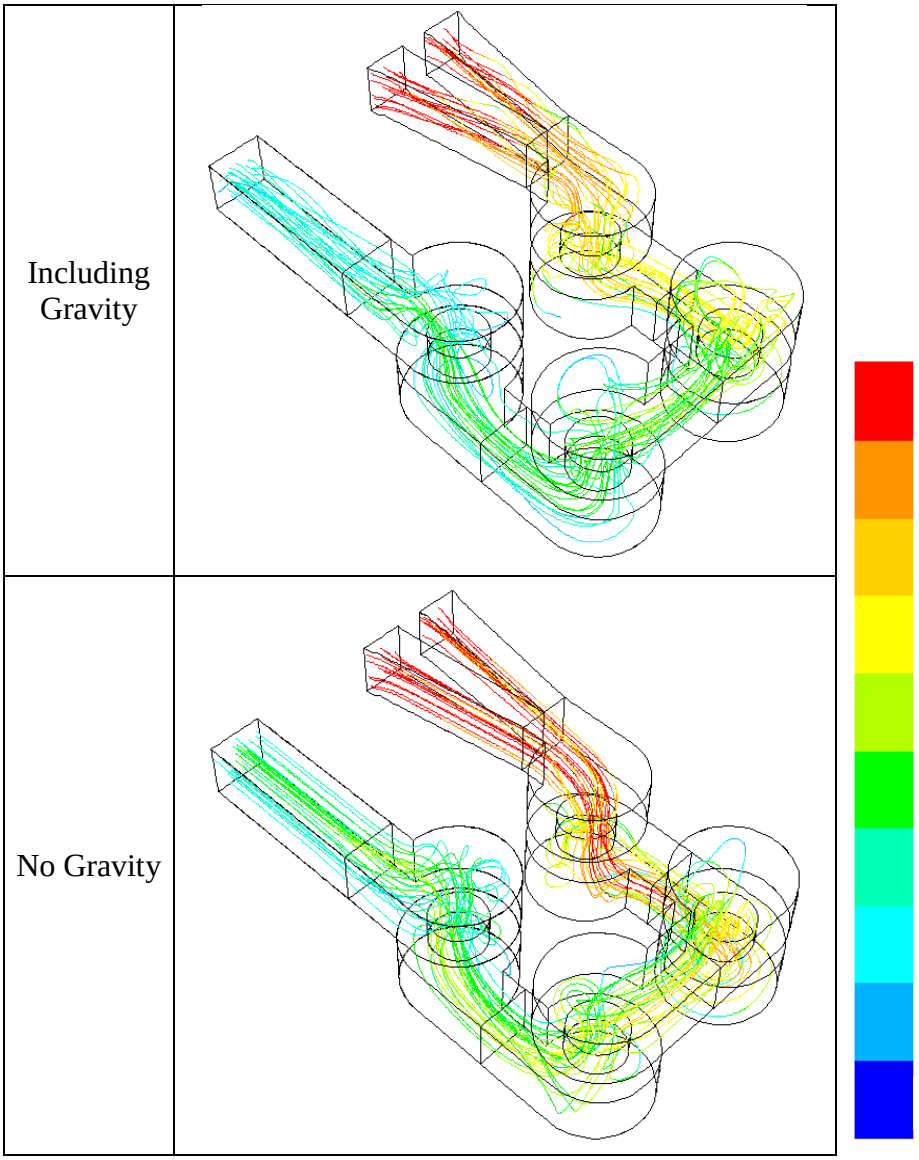

Figure 5. 9 Reactor S: computed pathlines of flow along the flow passage at Re = 32 and ΔT 20 ^{o}C.

Figs. 5.7, 5.8 and 5.9 show a clear difference in flow pattern along the first element and across the mixing sections with changing gravity to zero in the C, F and S element Reactors. At zero gravity, the flow is stable, smooth and straight, going directly in the direction of the channel, especially in the first element in each reactor. However, when the flow includes gravity, it becomes unstable in these positions. These differences occur due to the effect of buoyancy on the flow pattern and hence on the temperature distribution in the reactors.

The figures also show the resulting change from red towards blue as the flow progresses from the inlet to the outlet. This might indicate that the fluid temperature decreases along the flow passage due to the heat transfer from the fluid to the copper reactor plates. The F and S element Reactors show more blue (lower temperature) at the outlet compared to the C-element Reactor; this could be evidence of the mixing of energy being enhanced in the F and S-element Reactors, compared to the C-element Reactor. Since each reactor has the same mean residence time at a given value of Re, this difference cannot be due to greater residence time, only to increased heat transfer coefficient at the cooled walls. In addition, each mixer is improved at this low Re by the action of gravity (more blue colour at the outlet). Furthermore, with or without the gravity effect, the F-element Reactor appears to mix slightly more effectively than the S and these two much better than the C at this low Re.

5.5 Temperature sections along the passages

The planes which can be used to represent the features of the temperature and the flow, such as the temperature contours and velocity vector along the flow passage, are planes 0, 1, 2, 3 and 4. These planes are located at the meeting point of reagents A and B at the beginning of the first element, the end of the first element, the end of the second element, the end of the third element and the end of the fourth element respectively. Figure 5.10 shows the location of these planes in the domain of the C, F and S element Reactors.

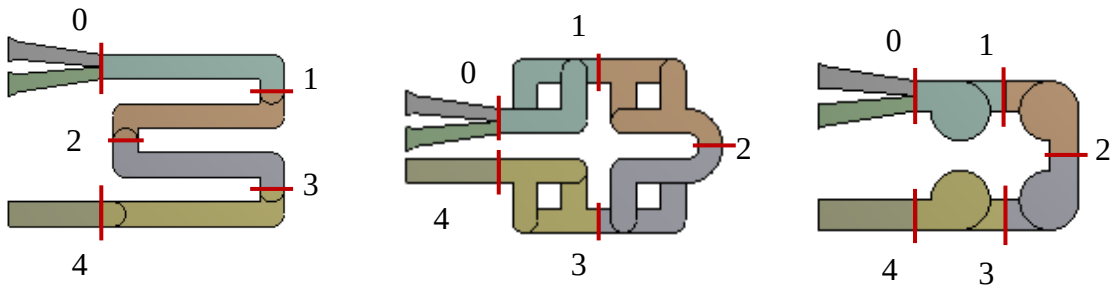

Figure 5. 10 Location of the five passage sections used for contour and vector plots of temperature and flow fields in the computations.

An additional investigation was undertaken to discover the effect of gravity on the temperature distribution in more detail in the C, F and S element Reactors. Fig. 5.11 shows the effect of the gravity on the temperature contours in the C-element Reactor at ΔT 20 ^{o}C and Re 32, 65 and 130. These contours are in the 0, 1, 2, 3 and 4 planes. In these contours, the

maximum temperature is the reagent stream inlet temperature, (T_I) and the minimum temperature is the copper reactor temperature, (T_R).

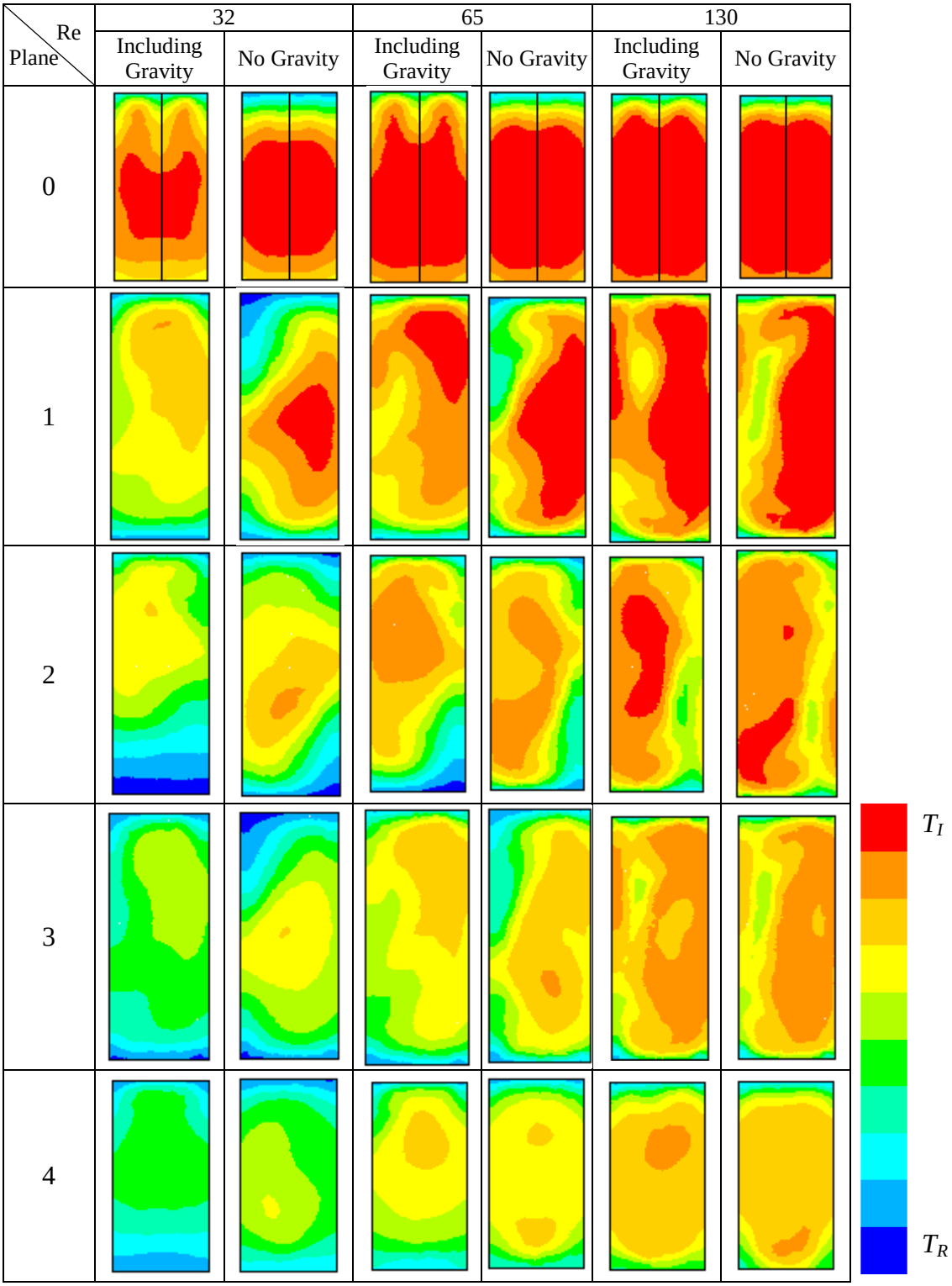

Figure 5. 11 Reactor C: computed temperature contours over the five sections along the flow passage for each of the three Reynolds number values with ΔT = 20 ^{o}C.

The figure shows that the temperature decreases along the flow passage. This might be due to the effect of the cooling system. This effect increases due to the increases in the contact area between fluid and cooling system and, consequently, enhances the heat transfer. This effect could increase with increasing Re due to the decreases in the thermal boundary layer thickness (Hermann, 1970). The figure also shows that gravity has a strong effect on the temperature contours along the flow passage. This effect is due to the effect of the gravity on the flow pattern (Eq. 3.21). This effect decreases with increasing Re due to the decreasing Ri. (Eq. 3.22).

Figure 5.12 shows the transverse components of the velocity of the fluid flow in the C-element Reactor at ΔT = 20 ^{o}C, including gravity and no gravity at Re 32 and 130. These transverse components are in the 0, 2 and 4 planes. The transverse components of velocity play a direct role in folding the layers of differing temperature. Therefore, plots of the velocity vector in the transverse sections through the passages might be helpful. The figure explains how gravity changes the flow direction within the flow passage. The figure shows that gravity has a strong effect on the flow direction along the flow passage, especially at low Re. This effect becomes weaker at high Re due to reducing of the Ri. The figure indicates that the effect of buoyancy on the flow direction, and consequently on the temperature distribution, can be ignored at Re $\geq$ 130.

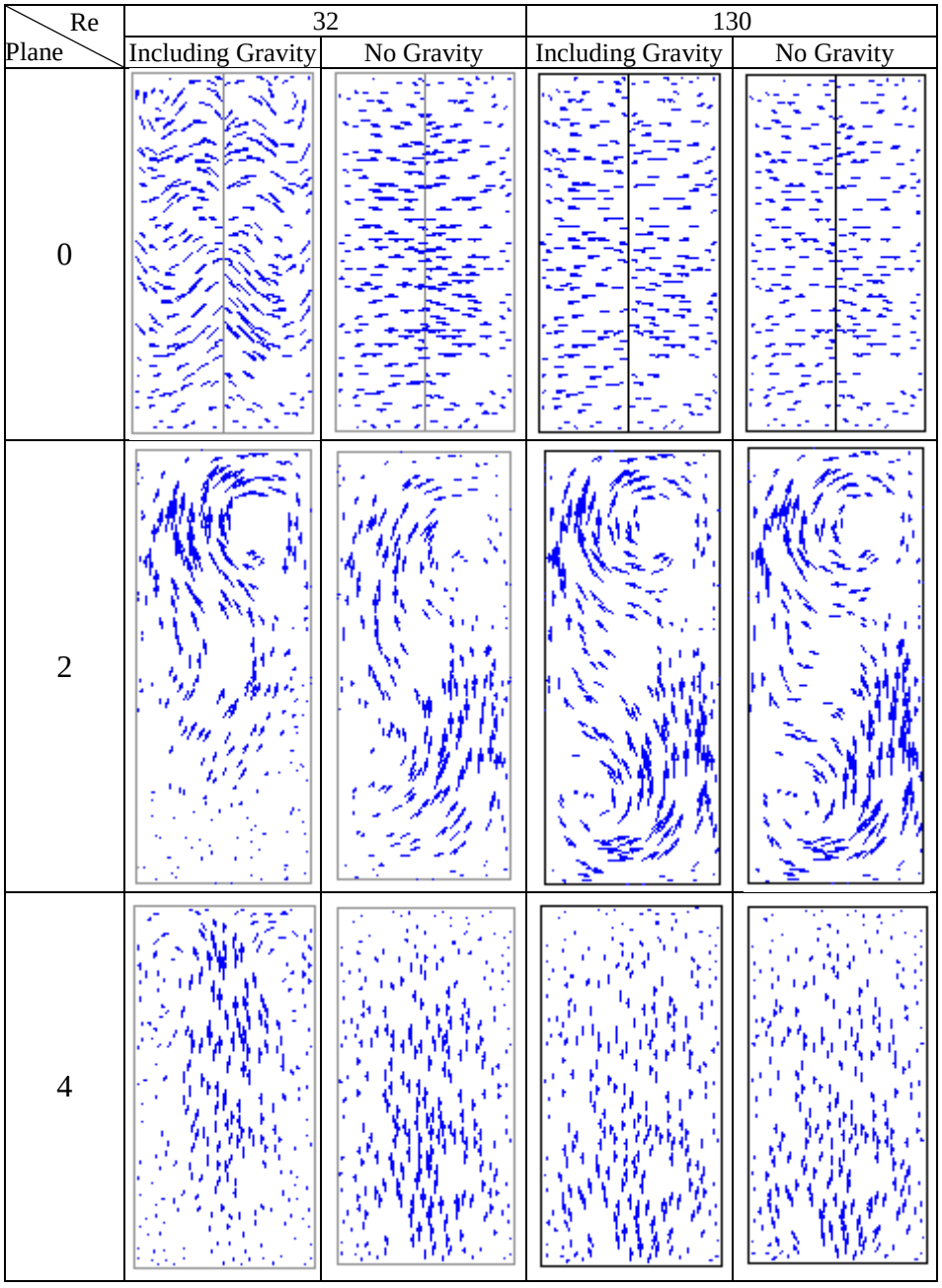

Figure 5. 12 Reactor C: computed velocity vectors in the planes of the five sections along the flow passage for each of the two Reynolds number values with $\Delta T = 20\ ^{o}C$.

Figs. 5.13 and 5.14 show the effect of gravity and Re on the temperature contours and flow direction in the F-element Reactor. These effects are the same as in the C-element Reactor. Fig. 5.13 shows the cooling rate in the F-element Reactor is better than in the C-element Reactor. In addition, the temperature in the F-element Reactor is more uniform than that in the C-element Reactor. This might be because the heat transfer area relative to the passage volume in the F-element Reactor is larger than in reactor C.

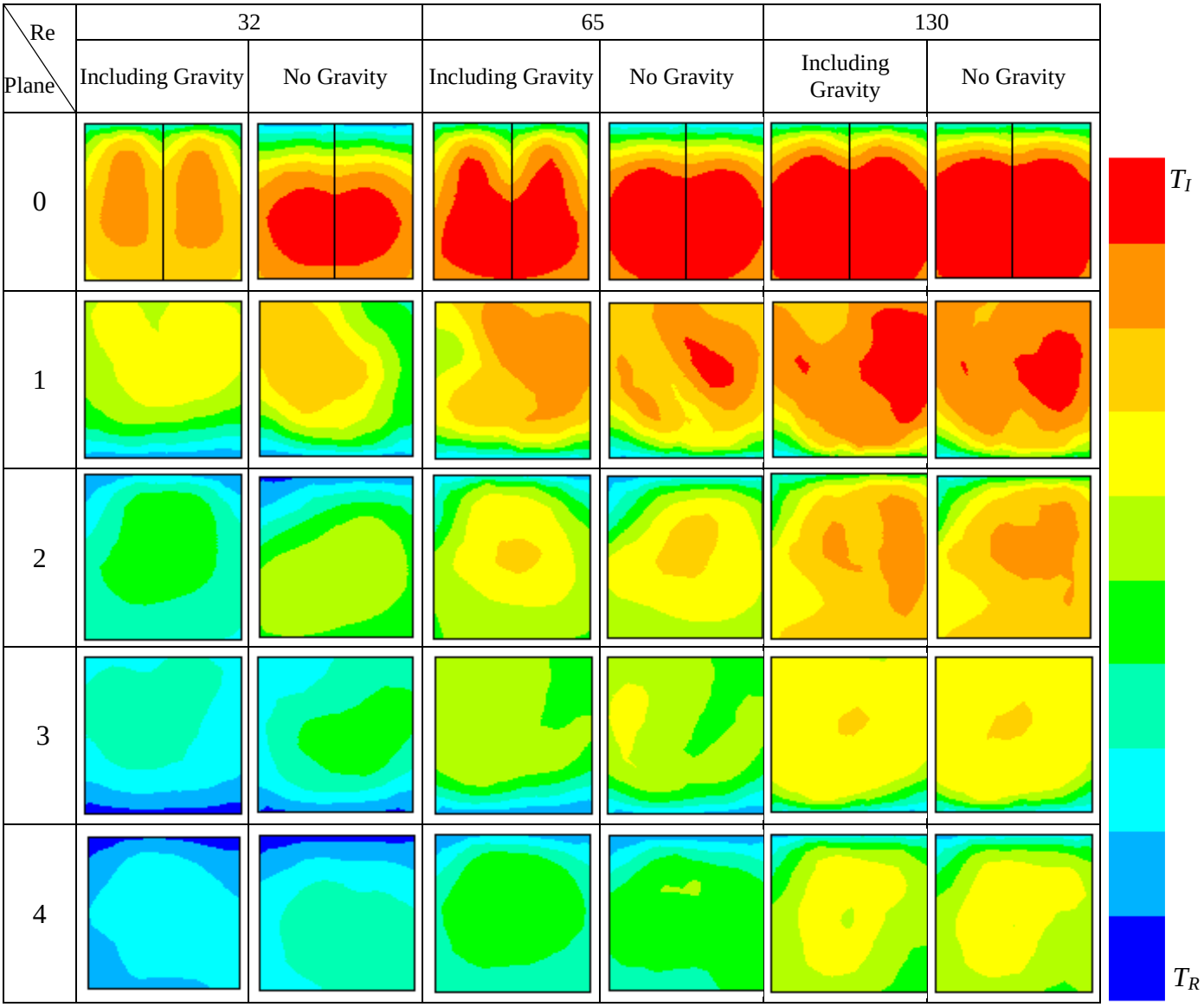

Figure 5. 13 Reactor F: computed temperature contours over the five sections along the flow passage for each of the three Reynolds number values with $\Delta T = 20\ ^{o}C$.

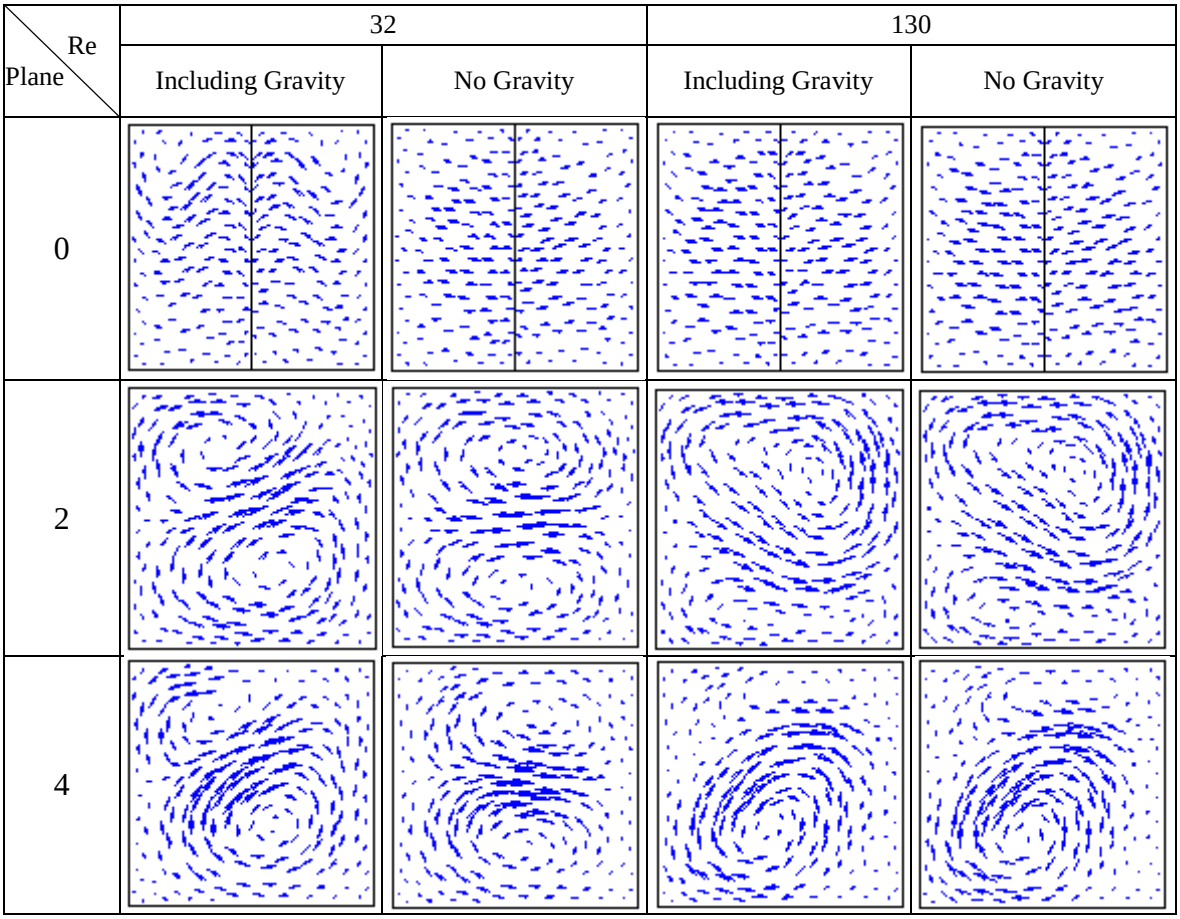

Figure 5. 14 Reactor F: computed velocity vectors in the planes of the five sections along the flow passage for each of the two Reynolds number values with $\Delta T = 20\ ^{o}C$.

Figs. 5.15 and 5.16 show the effect of gravity and Re on the temperature contours and flow direction in the S-element Reactor. These effects are approximately the same as in the F-element Reactor. Also, the cooling rate in the S-element Reactor is close to that in the F-element Reactor.

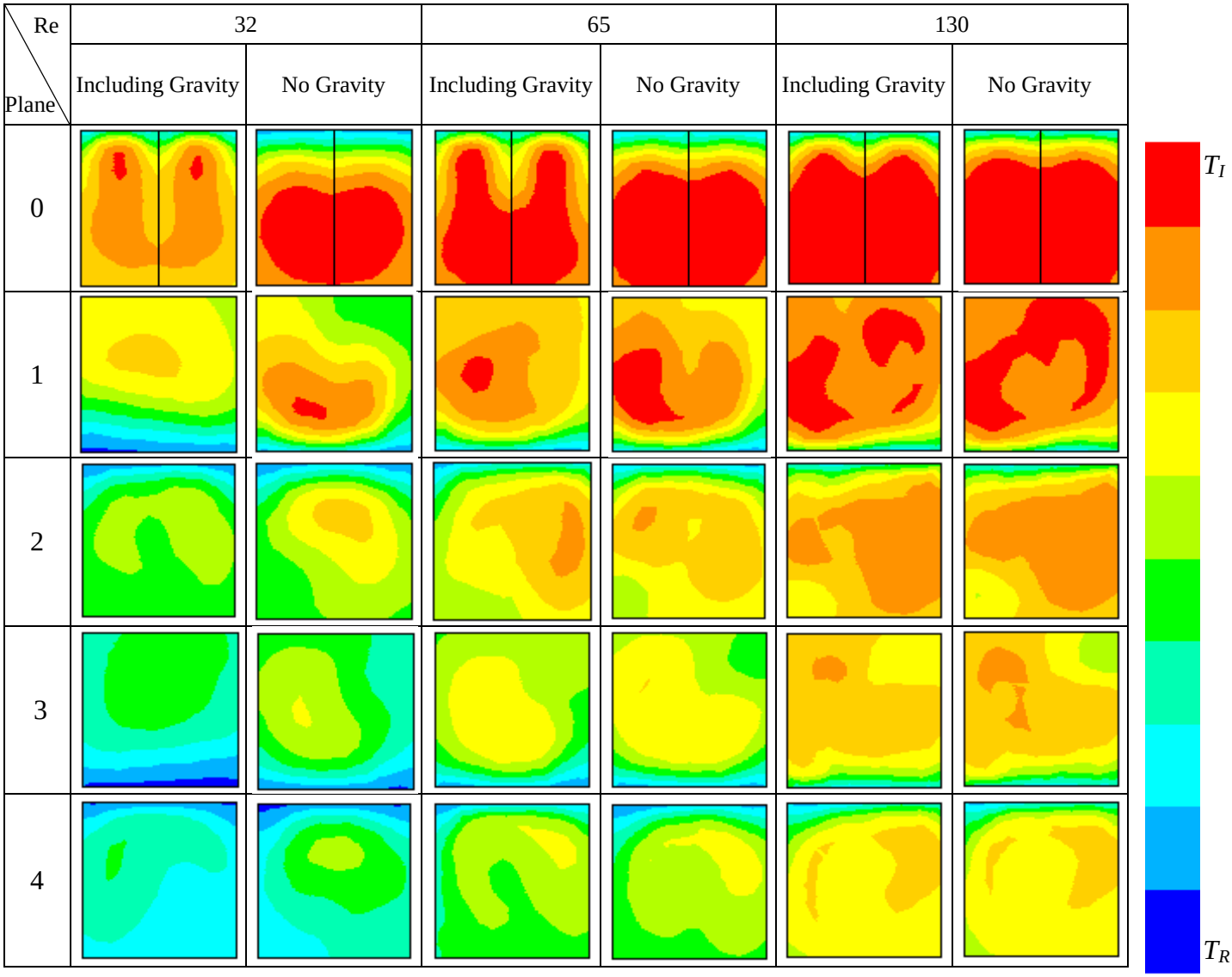

Figure 5. 15 Reactor S: computed temperature contours over the five sections along the flow passage for each of the three Reynolds number values with $\Delta T = 20\ ^{o}C$.

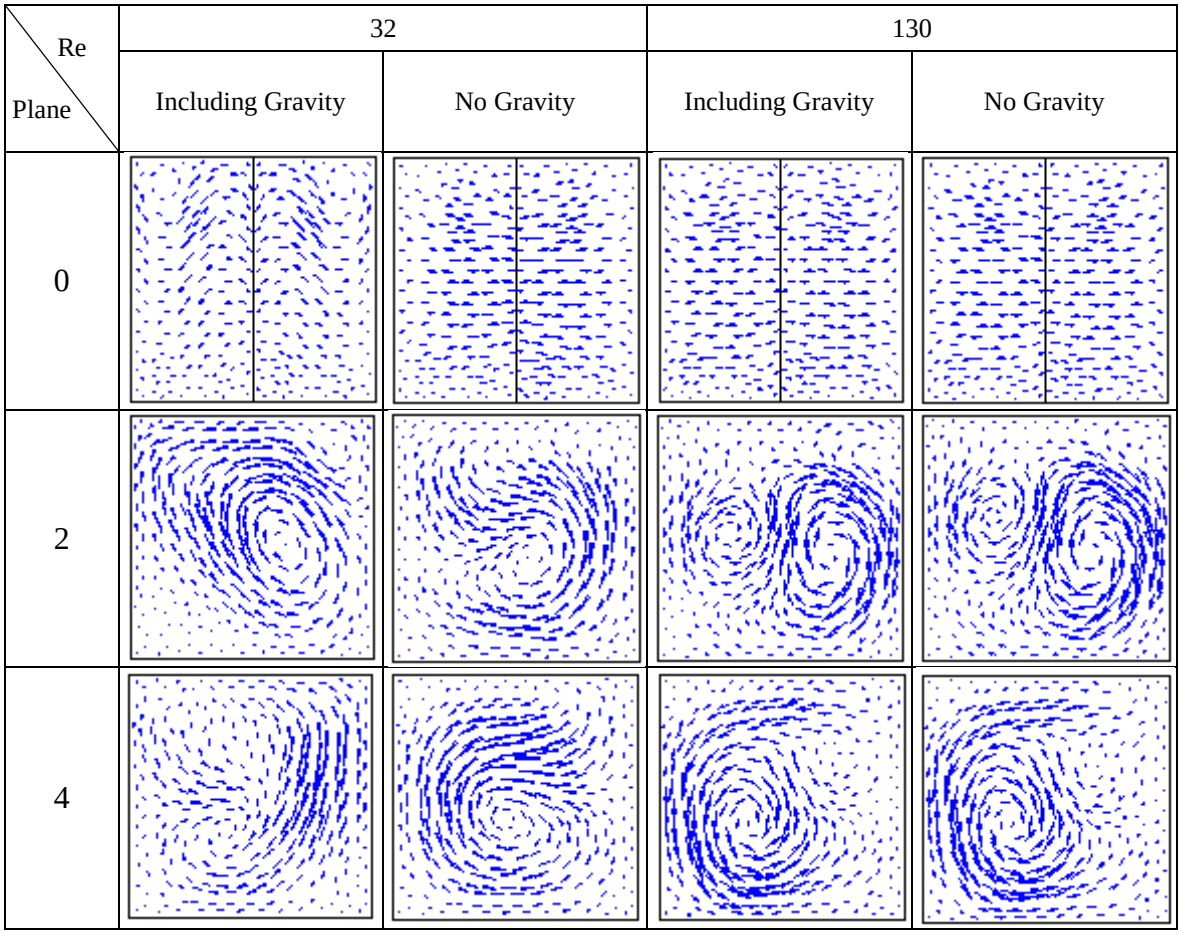

Figure 5. 16 Reactor S: computed velocity vectors in the planes of the five sections along the flow passage for each of the two Reynolds number values with $\Delta T = 20\ ^{o}C$.

5.6 Effect of inverting ΔT

A further investigation of the buoyancy effect on the flow pattern and temperature distribution can be undertaken by inverting the temperatures of the reagent stream inlet and the copper reactor plates. The results in this section relate to the inversion of the temperatures of the copper preheating plates, which control the reagent stream inlet temperature, from 45 ^{o}C to 25 ^{o}C, and the copper reactor plates from 25 ^{o}C to 45 ^{o}C. In this situation, cool water was introduced into the reactor and heated by the copper reactor plates. The temperature difference (ΔT) between copper preheating plates temperature and the copper reactor plates temperature is -20 ^{o}C. By inverting the temperature difference from 20 ^{o}C to -20 ^{o}C, the values of Richardson numbers of these two cases must be equal but in the opposite. However, the value of Richardson numbers, which are calculated depending on the reagent stream inlet

temperature, are slightly different here because there is a difference in the reagent stream inlet temperatures.

Inverting the temperature difference causes the stability of flow at each position along the passage to alter, if the buoyancy has a significant effect on the flow pattern (Section 3.3.1 Momentum equation). In other words, inverting the temperature difference, and hence the density difference, can cause an alteration in the stability of flow and a very different flow to before is expected. The alteration in the stability of flow depends on the buoyancy effect, such that a big alteration in the stability of flow can happen at the big effect of the buoyancy.

Figures 5.17, 5.18 and 5.19 show the experimental temperature profile along the rear path of the C, F and S element Reactors at ΔT 20 ^{o}C, -20 ^{o}C. The temperature profile for each reactor includes Re 32, 65 and 130. In these figures, the temperature has been normalized to enable precise monitoring of the differences between the temperature profiles. The figures show that inverting the temperature difference can cause a clear deviation in the temperature profiles in all geometries. This means that buoyancy has a significant effect on the temperature profiles, especially at low Re. The temperature profiles become more similar with increasing Re and decreasing Ri because the buoyancy is decreasing. The deviation in the temperature profiles was bigger in the S-element Reactor than the deviation in the F and C element Reactors, which means the buoyancy effect on the temperature profile in the S-element Reactor is larger than that effect in the F and C element Reactors.

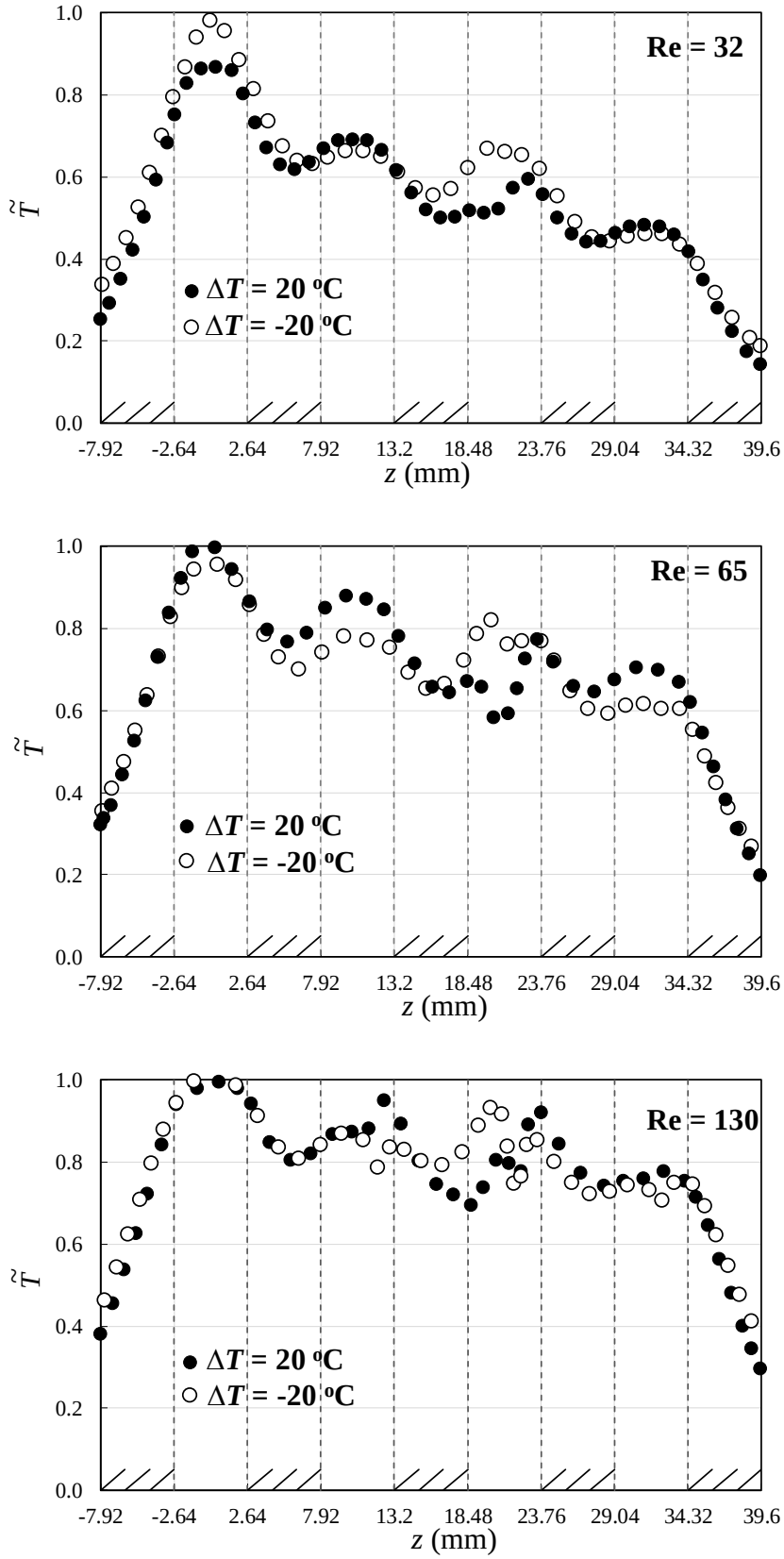

Figure 5. 17 Reactor C: measured temperature profiles along the rear path. Effect of inverting the temperature difference at the three different values of Reynolds number.

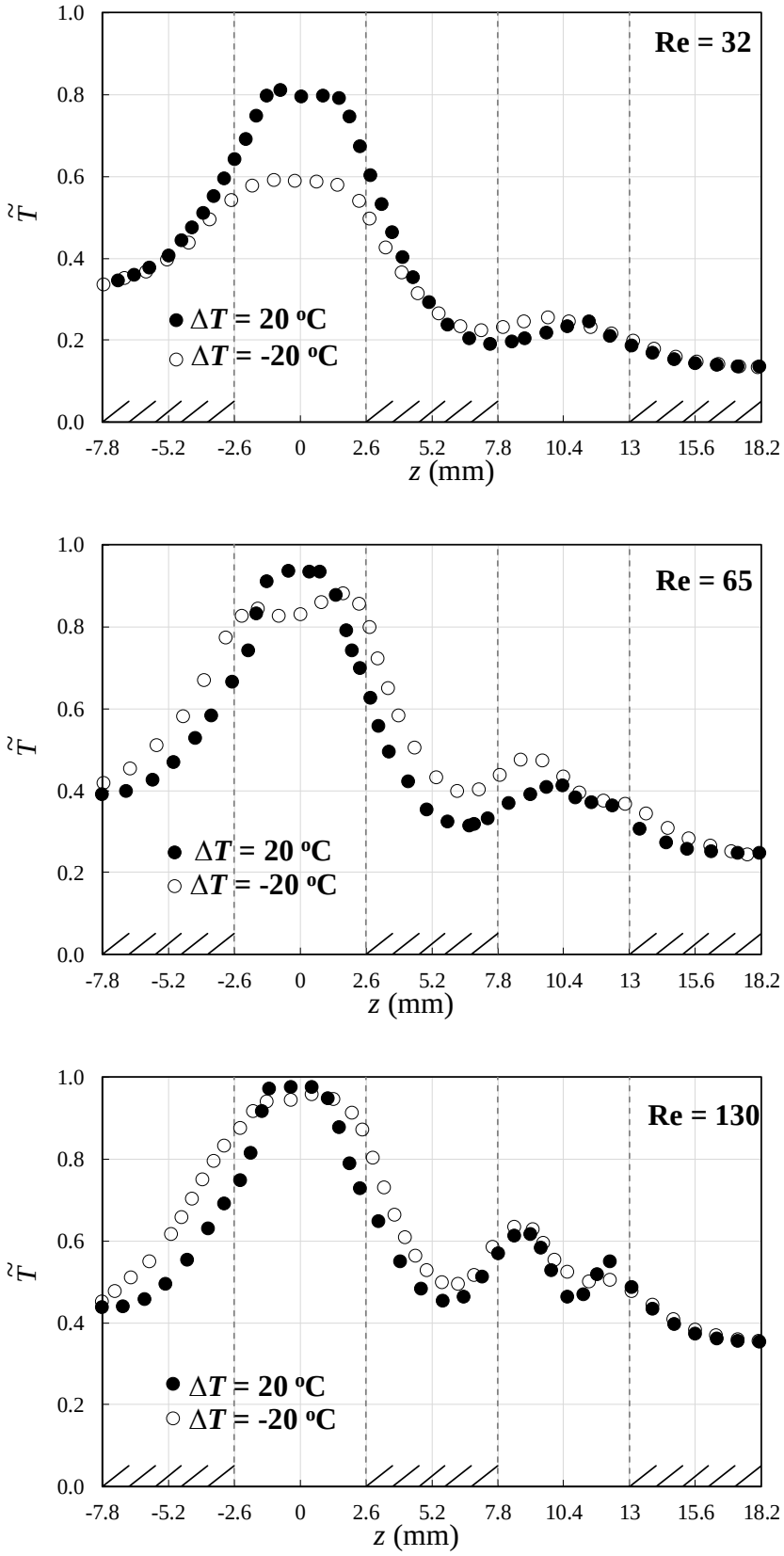

Figure 5. 18 Reactor F: measured temperature profiles along the rear path. Effect of inverting the temperature difference at the three different values of Reynolds number.

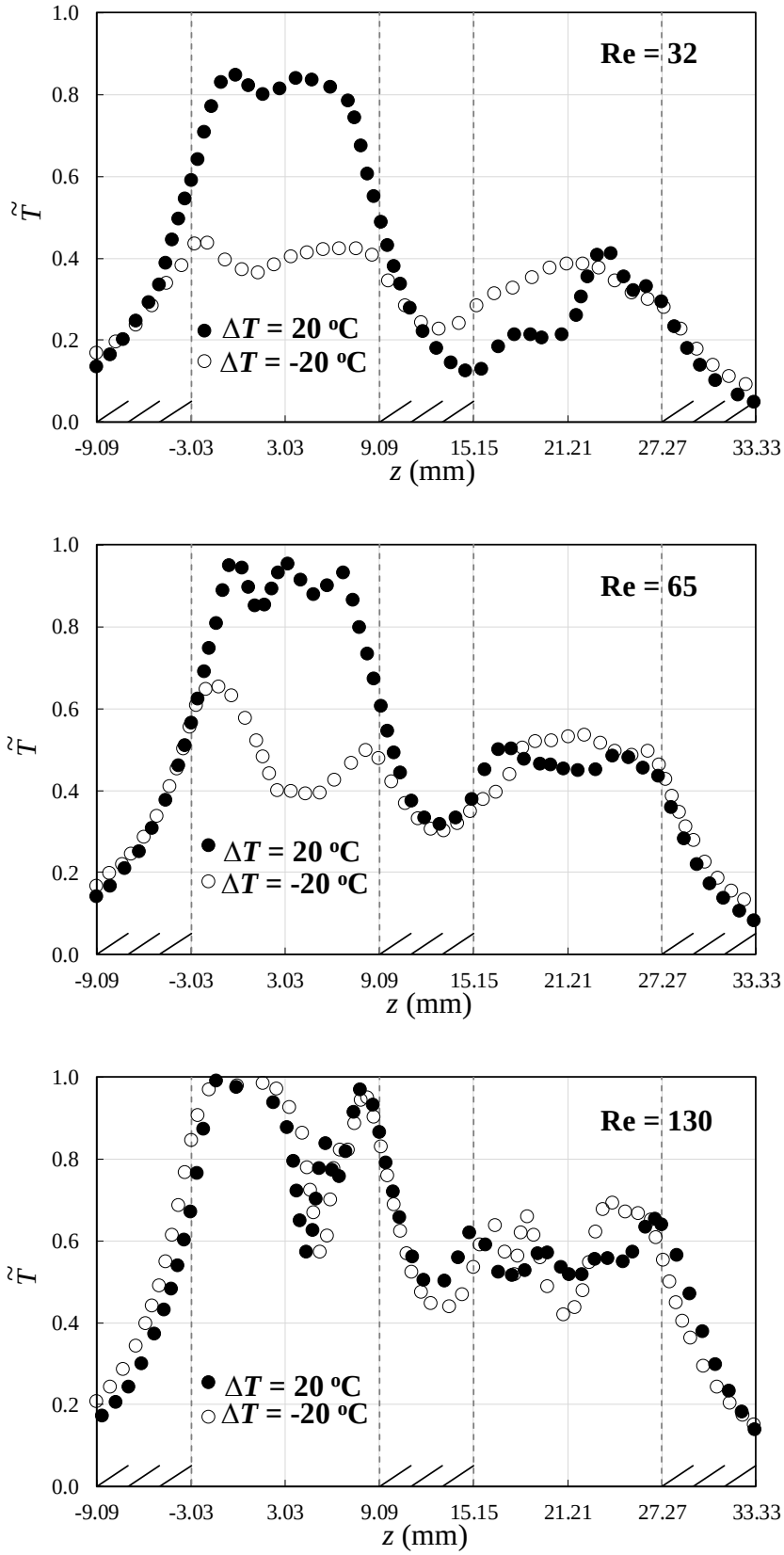

Figure 5. 19 Reactor S: measured temperature profiles along the rear path. Effect of inverting the temperature difference at the three different values of Reynolds number.

The experimental data for inverting the temperature difference were simulated computationally. The agreement between the experimental data and the computation results were acceptable. Figs. 5.20, 5.21 and 5.22 show this comparison.

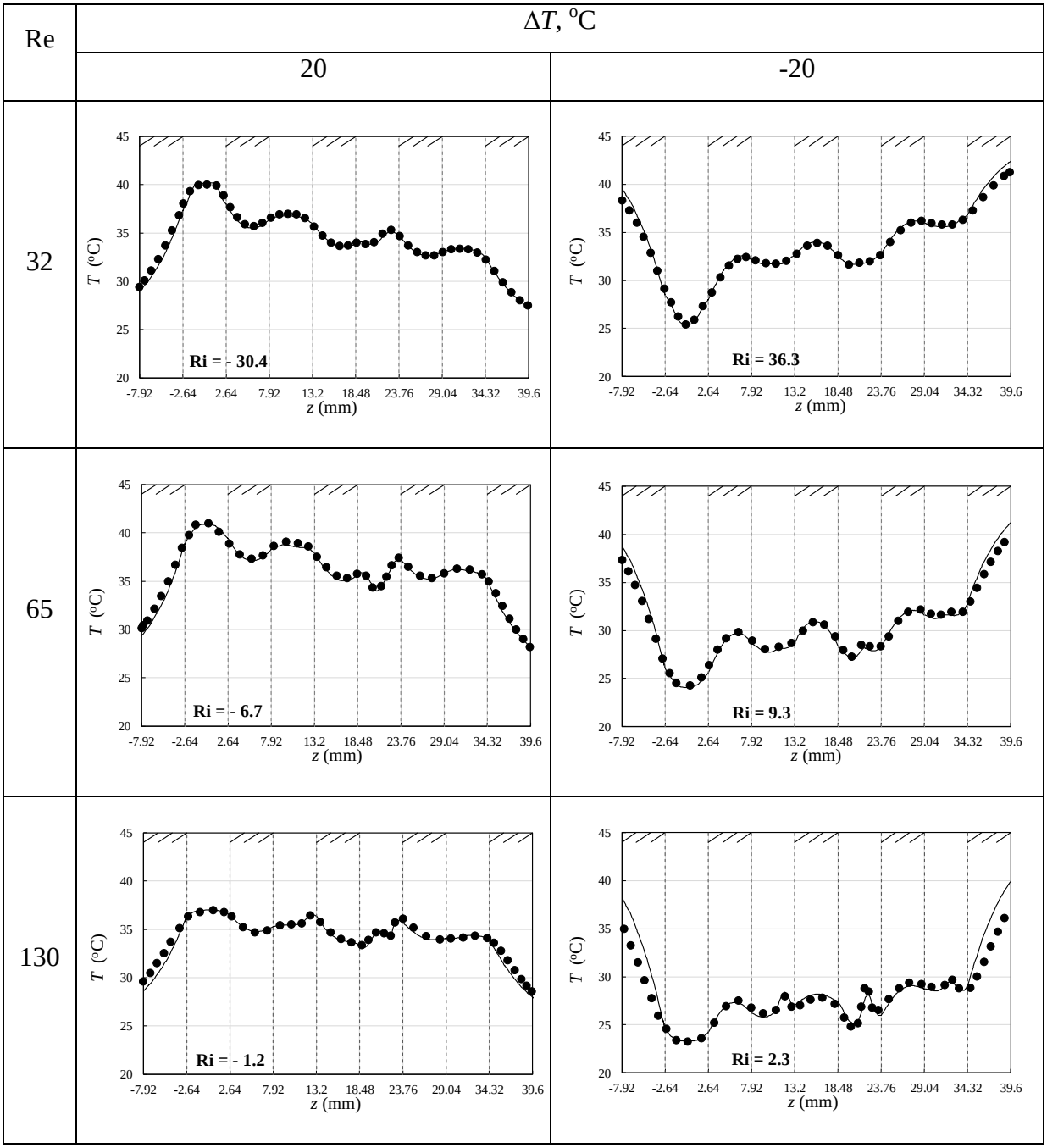

Figure 5. 20 Reactor C: measured and computed temperature profiles along the rear path. Effect of inverting temperature difference.

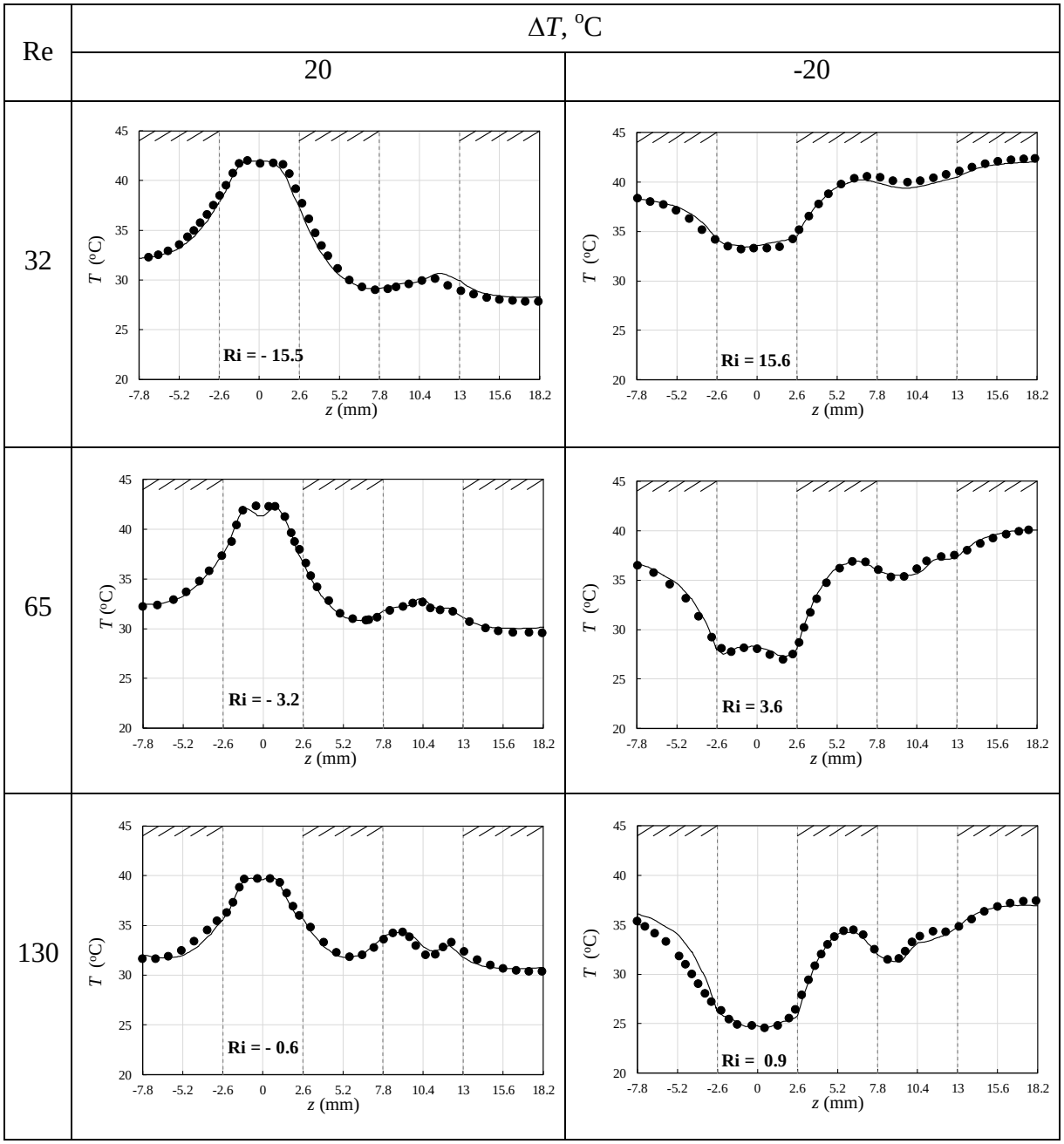

Figure 5. 21 Reactor F: measured and computed temperature profiles along the rear path. Effect of inverting temperature difference.

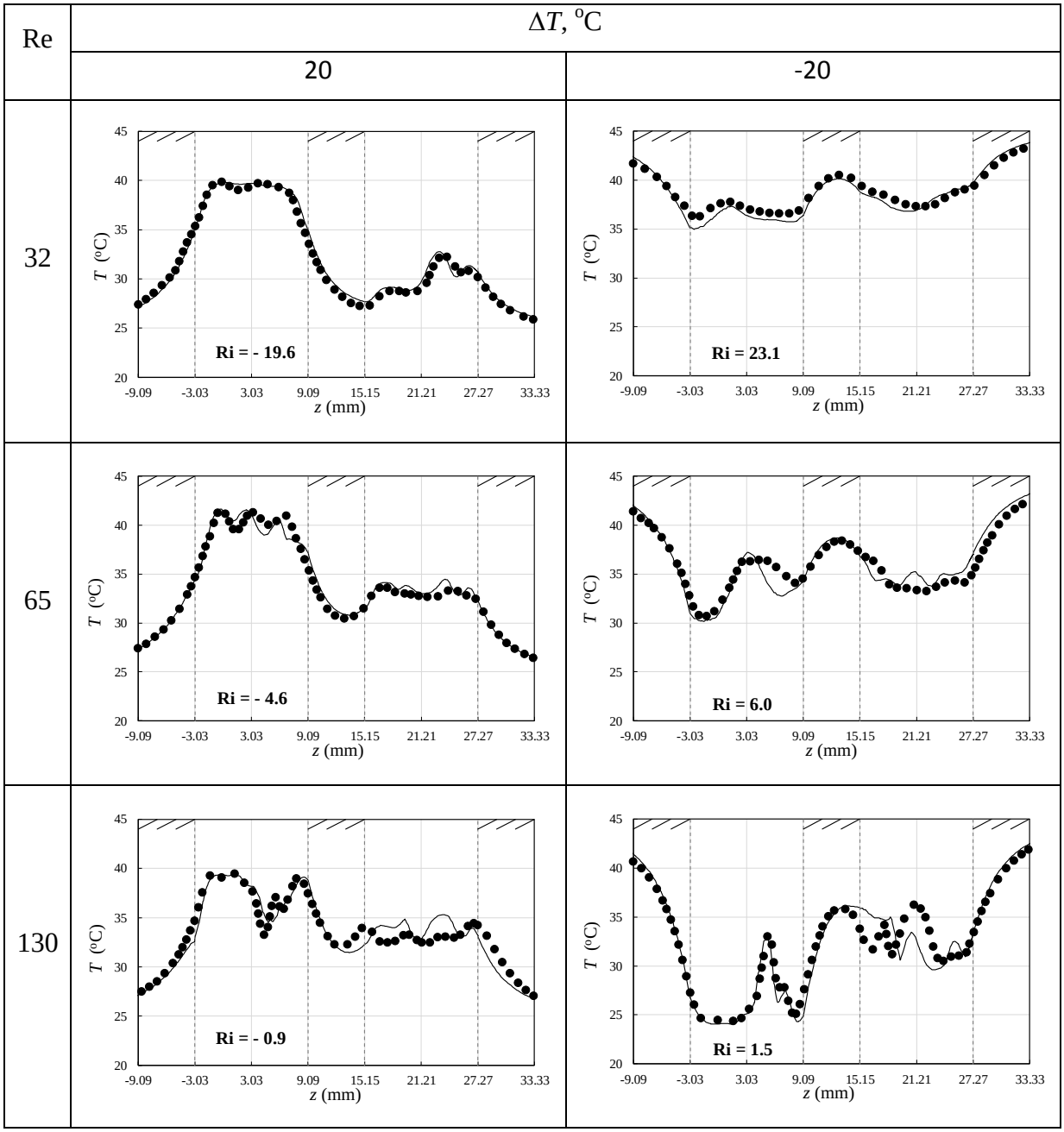

Figure 5. 22 Reactor S: measured and computed temperature profiles along the rear path. Effect of inverting temperature difference.

Figs. 5.23, 5.24 and 5.25 show the effect of inverting temperature difference (ΔT 20 ^{o}C and -20 ^{o}C) on the temperature contours along the flow passage in the C, F and S element Reactors respectively. These contours are in planes 0, 1, 2, 3 and 4. When ΔT = 20 ^{o}C, the maximum and minimum temperatures are T_I and T_R respectively, while when ΔT = -20 ^{o}C, the maximum and minimum temperatures are T_R and T_I respectively, where T_I is the reagent stream inlet temperature. The figure shows that inverting temperature difference (ΔT)

produces a strong effect on the character of the temperature field. This effect represents the effect of gravity. When the flow is warm and passing over a cool surface below, this will tend to supress the transverse motion since the cooling liquid is dense. Consequently, the warm liquid (hot spots) tends to rise due to the gravity effect, especially noticeable at low Re, since Ri is then large. In contrast, when the flow is cool and passing under a warm surface, the cool liquid (cooled spot) is forced down due to gravity. In other words, the temperature of the inlet flow strongly affects the features of the temperature field within the domain of the passage. This effect increased at Re = 32 and decreased at Re = 130. This means the gravity has a strong effect on the temperature distribution at Re 32 and decreases at Re 130.

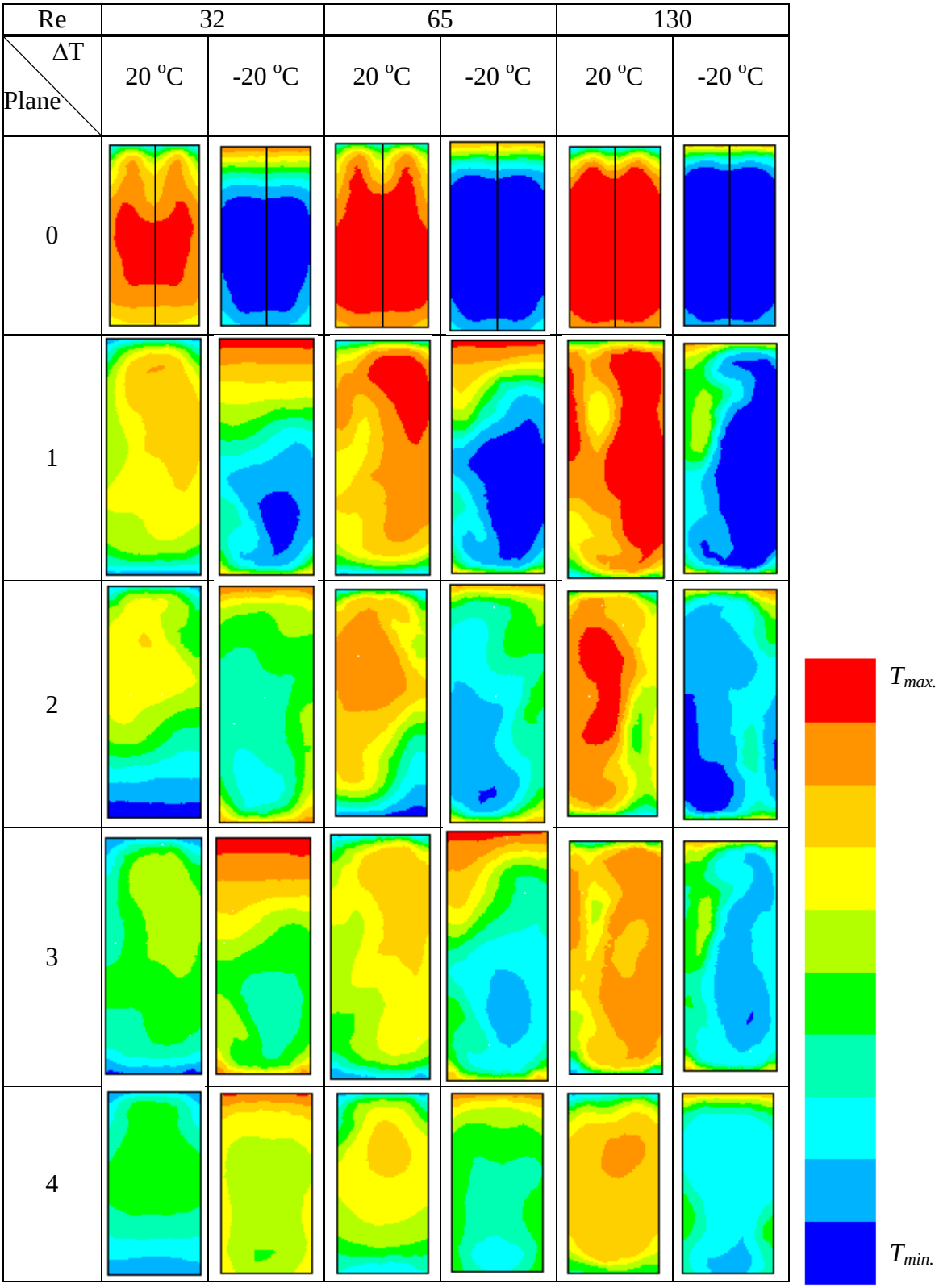

Figure 5. 23 Reactor C: computed temperature contours over the five sections along the flow passage for each of the three Reynolds number values with ΔT = 20 °C and ΔT = -20 °C.

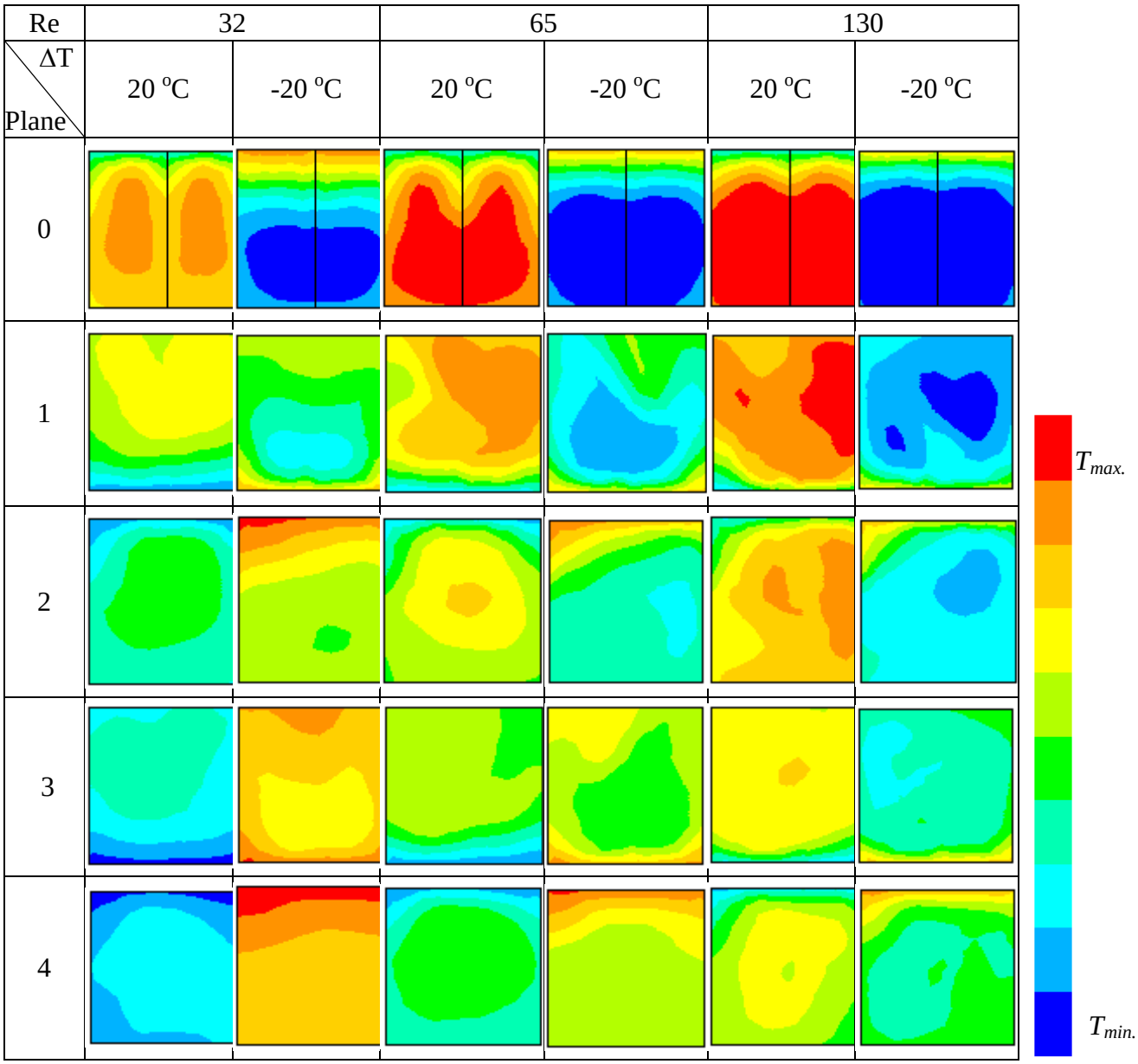

Figure 5. 24 Reactor F: computed temperature contours over the five sections along the flow passage for each of the three Reynolds number values with ΔT = 20 °C and ΔT = -20 °C.

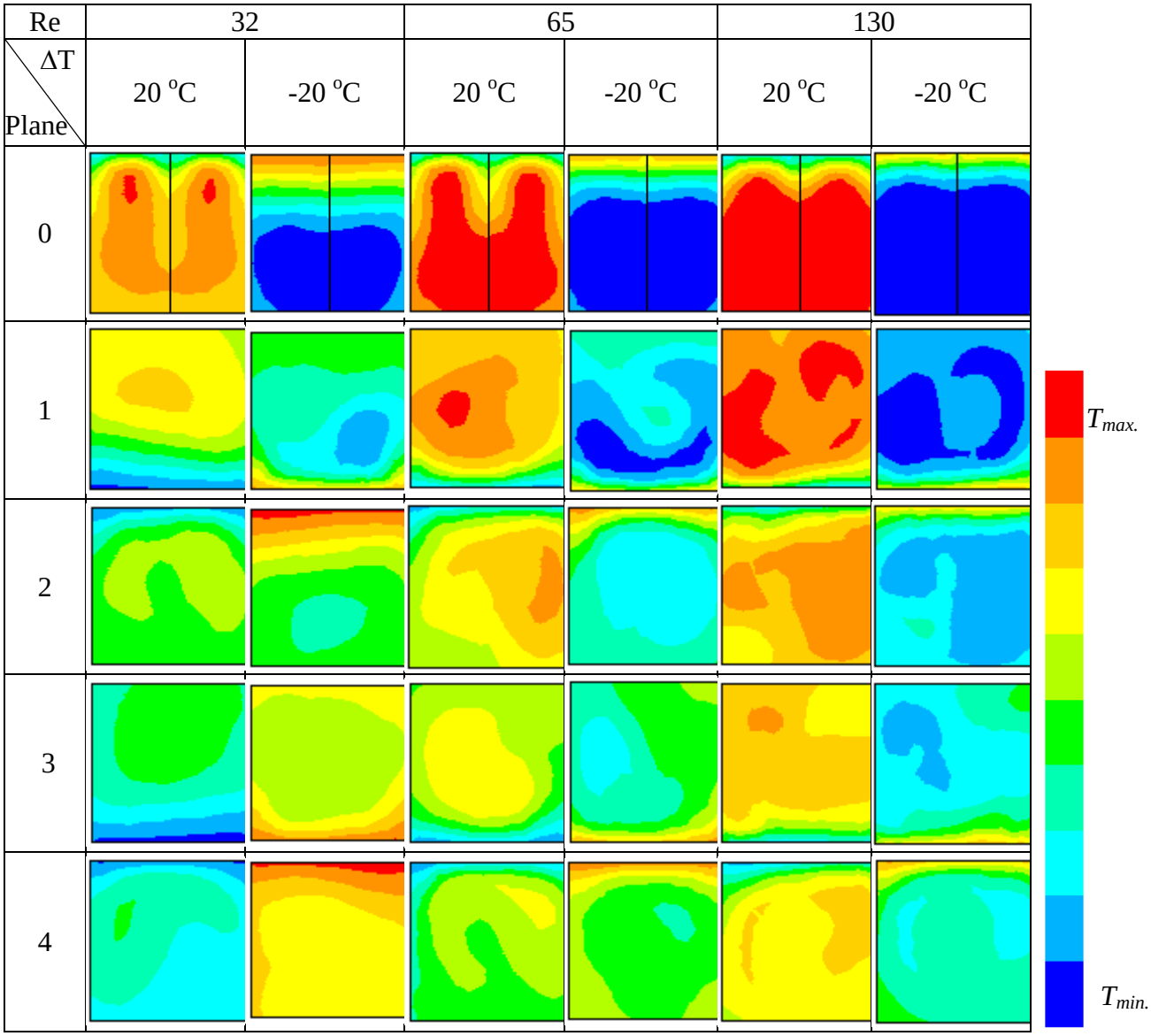

Figure 5. 25 Reactor S: computed temperature contours over the five sections along the flow passage for each of the three Reynolds number values with ΔT = 20 °C and ΔT = -20 °C.

5.7 Temperature statistics

5.7.1 Mean temperature change along the passages

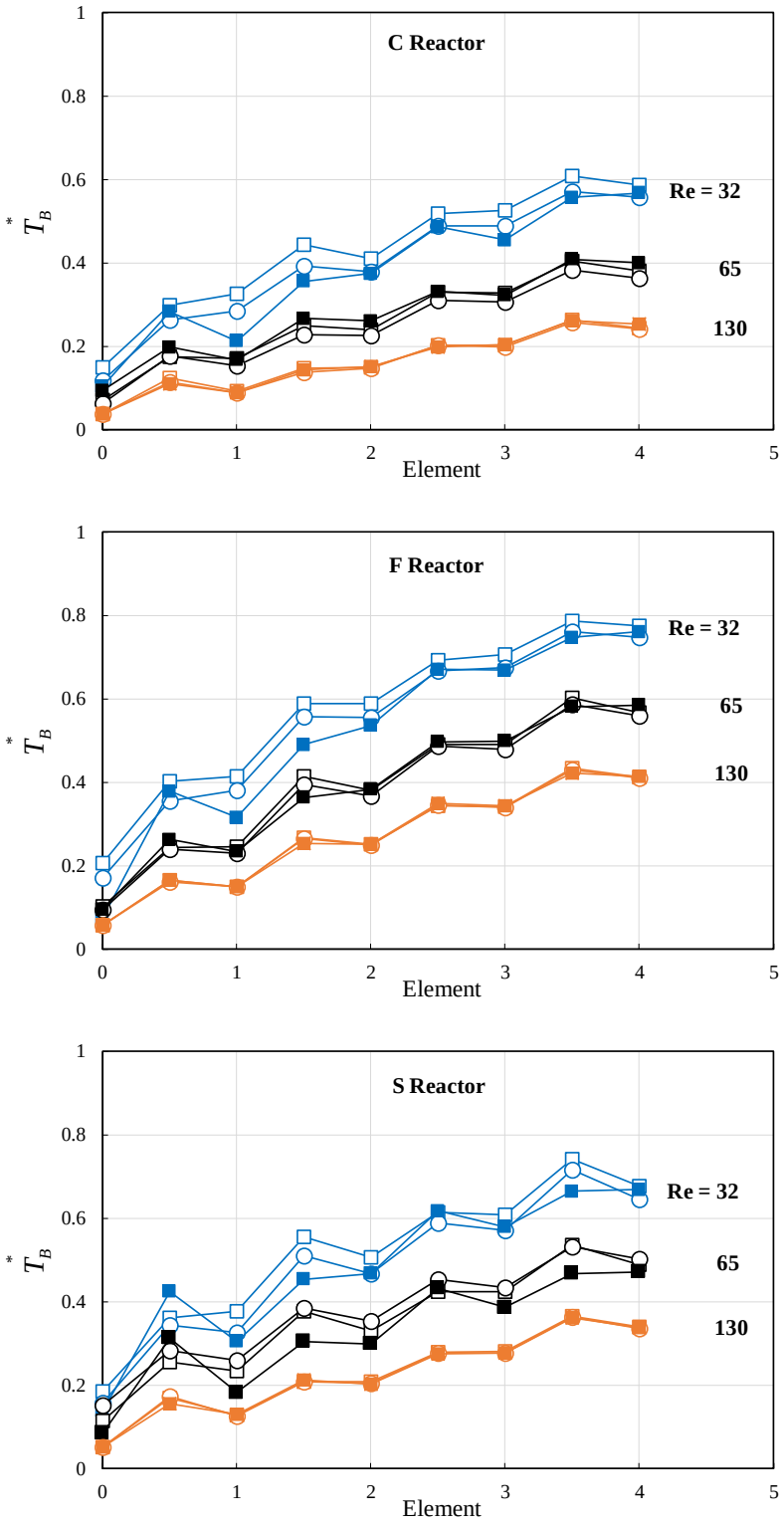

Figure 5. 26 C, F and S element Reactors: computed bulk temperature over the four elements along the flow passage for each of the three Reynolds number values.

Changing the fluid flow rate (Re) could affect the bulk temperature (see Eqs. 3.49 and 3.50), along the flow passage (Eq. 3.33). Fig. 5.26 shows the profile of the bulk temperature over the four elements along the flow passage for each of the three Reynolds number values in the C, F and S element Reactors. The temperature profile was presented at three different Ri at each Re (see Table 5.1). The fill marker and empty markers represent the temperature profiles at the cool and warm inlet temperatures respectively. Normalised bulk temperature is plotted so the range of temperature is similarly scaled. The normalized bulk temperature (T_B^*) is the difference between the bulk temperature and reagent stream inlet temperature ($T_B - T_I$), divided by the difference between the copper reactor plates temperature and reagent stream inlet temperature ($T_R - T_I$). The figure shows the temperature profile changes clearly when the flow rate of the fluid (Re) is changed. The bulk temperature increases with decreasing Re. The figure also shows that there are deviations in the temperature profile with changing Ri at the same Re in all geometries. These deviations decrease with increasing Re. This effect becomes very weak at Re 130 and the lower Ri used. In other words, the effect of buoyancy can be ignored at Re $\geq$130 and Ri $\geq$ 0.4, 0.3 and 0.4 for the C, F and S element Reactors respectively.

Fig. 5.27 shows the profile of bulk temperature at Re = 130 and cool inlet temperature in the C, F and S element Reactors. The figure shows that in the C-element Reactor the temperature adjusted to the reactor plate temperature very poorly. However, it adjusts better in the F-element Reactor compared to the C and S element Reactors. This may indicate that the fluid mixing in the F-element Reactor is better than in the C and S element Reactors. In addition, the cooling system in the F-element Reactor seems more efficient due to the enhancing of the fluid mixing.

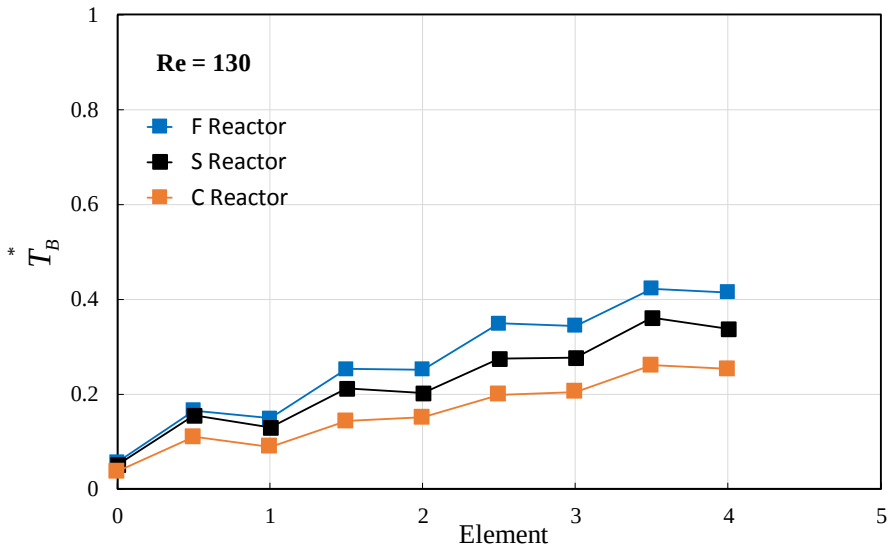

Figure 5. 27 C, F and S element Reactors: computed bulk temperature over the four elements along the flow passage at Re = 130.

5.7.2 Temperature non-uniformity change along the passages

Figs. 5.28, 5.29 and 5.30 show the standard deviation of the temperature along the flow passage in the C, F and S element Reactors respectively. The standard deviation of temperature (σ_T) within any part of the reactor, such as a surface or a volume, was calculated as described in Section 3.8. In these figures (5.28, 5.29 and 5.30), normalised standard deviation of temperature is plotted so the range of temperature is similarly scaled. The normalized standard deviation of temperature $(\overset{*}{\sigma}_T)$ is the standard deviation of temperature (σ_T), divided by absolute value of the temperature difference between the copper reactor plate temperature and the reagent stream inlet temperature $(T_R - T_I)$. The figures show that the standard deviation of temperature, which represents the temperature non-uniformity, decreases along the flow passage in all boundary conditions and all geometries. In other words, the structured reactor can be used to minimize the temperature non-uniformity in these geometries within the boundary conditions used. The figures also show the temperature of inlet reagent stream has a strong influence on the temperature uniformity, especially at a low Reynolds number. At the same Re, the temperature non-uniformity for the cool reagent stream inlet, positive Ri, is higher than the temperature non-uniformity for the hot reagent stream inlet. This behaviour seems clear at the beginning of the reactor: this may be due to the nature of the reactor geometry used. This behaviour of temperature non-uniformity

decreases with increasing Re. Furthermore, the figures show that the temperature non-uniformity is also affected by the Re and Ri. The temperature non-uniformity decreased with increasing flow rate of fluid (Re) and decreasing the buoyancy effect (Ri) in the same time (Eq. 3.39). This may be due to decreasing the effect of gravity on the flow pattern (Eq. 21) and temperature field (Eq. 33).

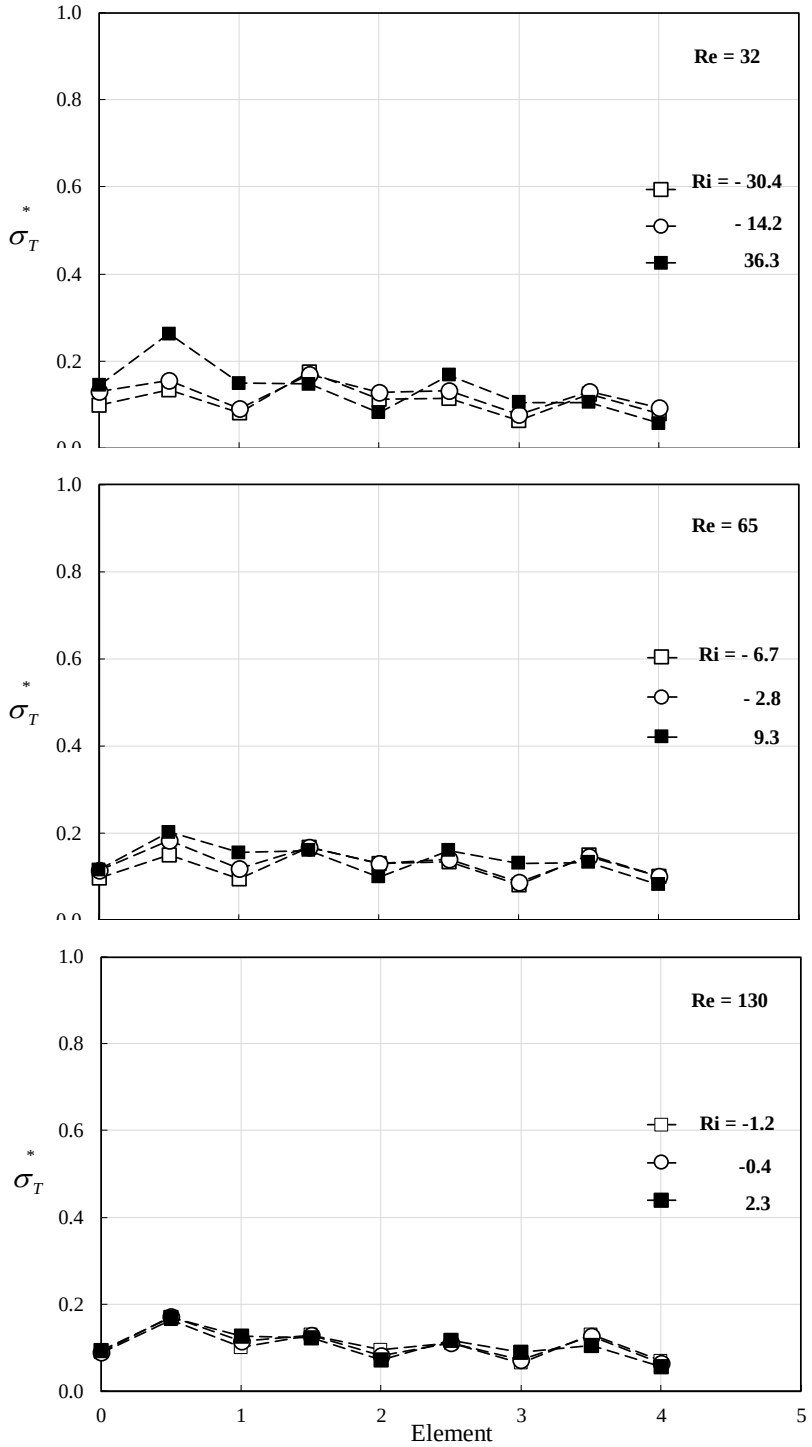

Figure 5. 28 Reactor C: computed standard deviation of temperature over the four elements along the flow passage for each of the three Reynolds number values.

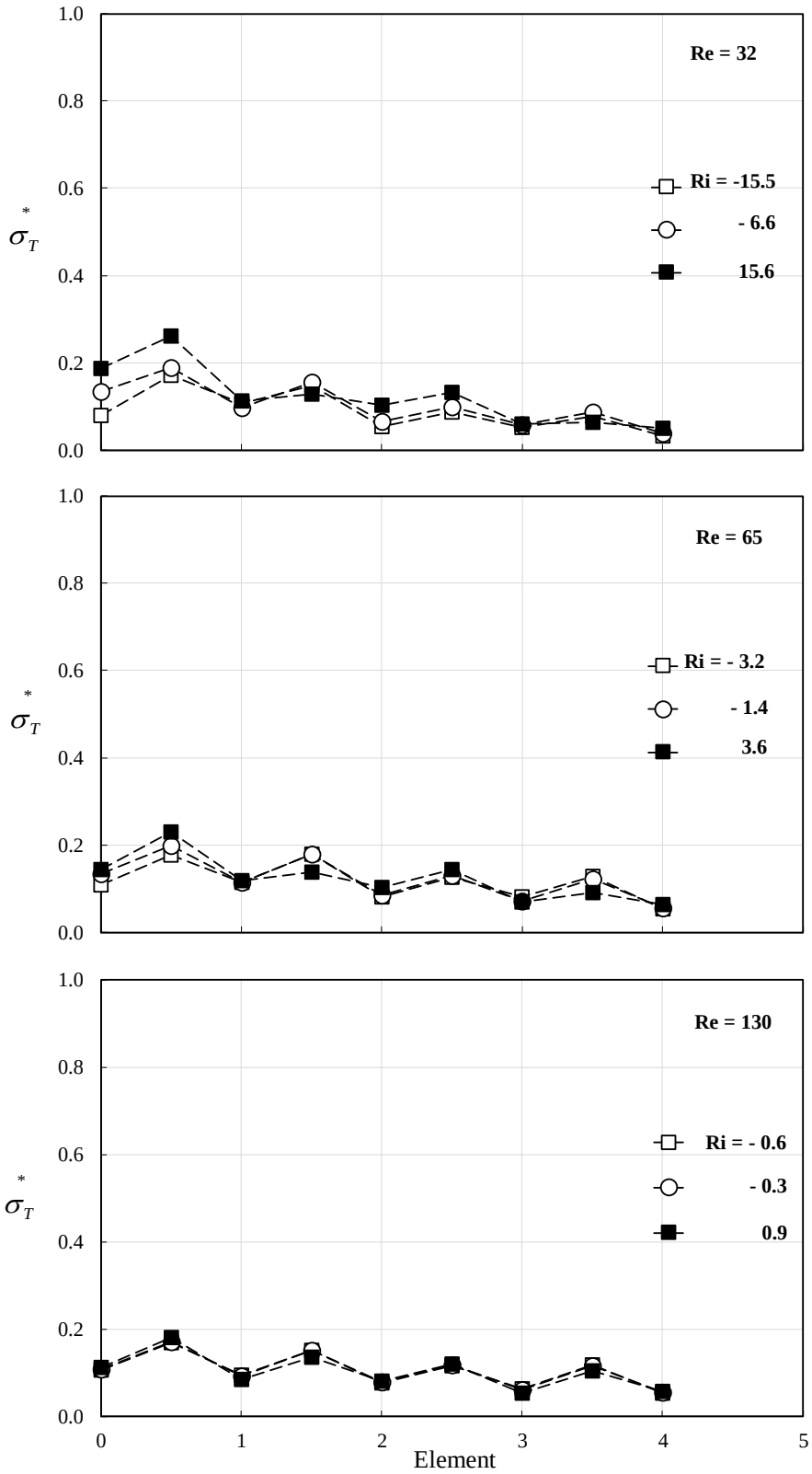

Figure 5. 29 Reactor F: computed standard deviation of temperature over the four elements along the flow passage for each of the three Reynolds number values.

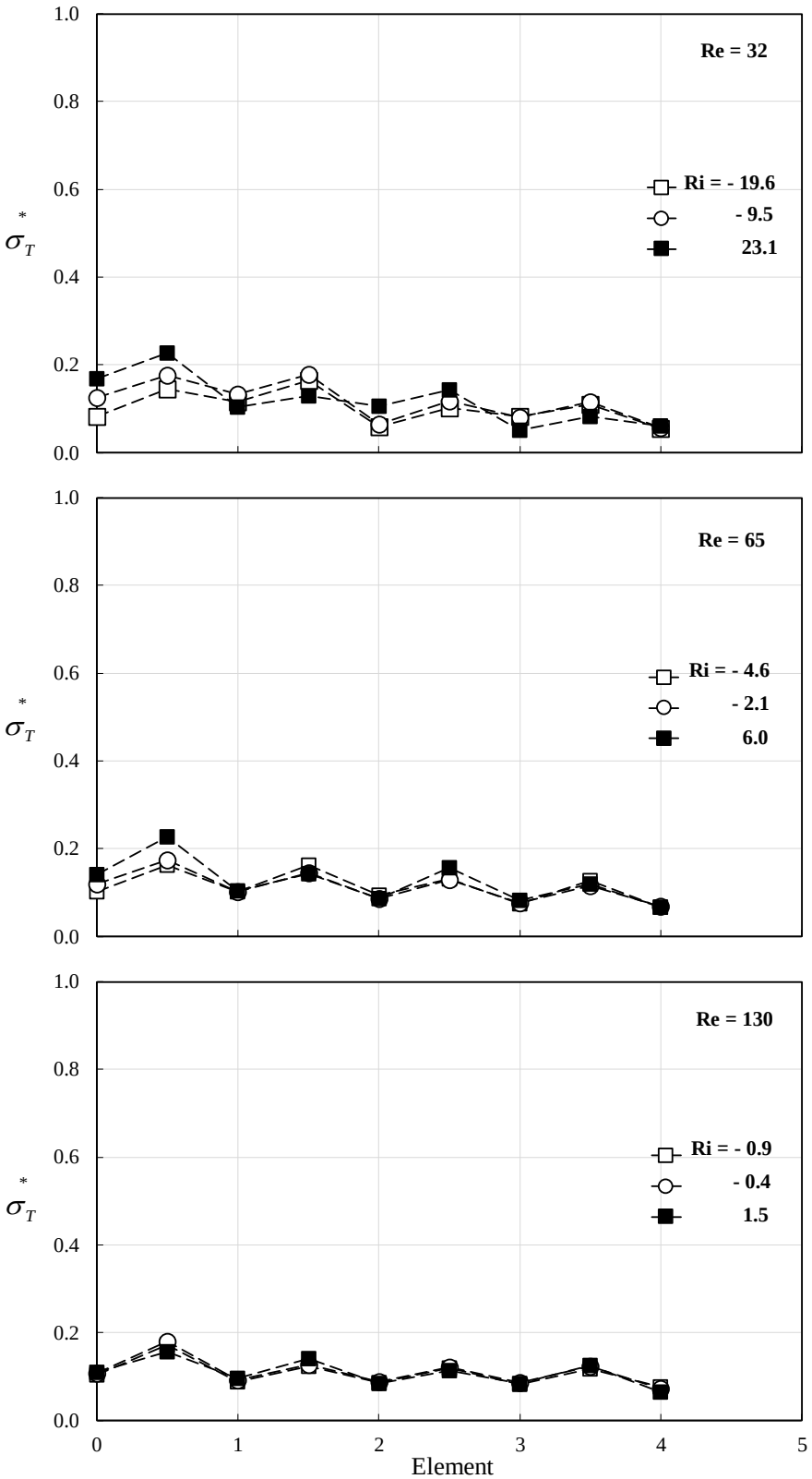

Figure 5. 30 Reactor S: computed standard deviation of temperature over the four elements along the flow passage for each of the three Reynolds number values.

5.8 Summary

This chapter described the temperature non-uniformity in the non-reacting system at a wide range of Re and Ri in the C, F and S-element Reactors. The results showed that the agreement between the experimental data and the computational results was acceptable. The results also showed that Ri has a significant effect on the temperature profile in all geometries. This effect decreased with decreasing Ri and increasing fluid flow rate (Re) due to the decrease in the effect of gravity force. This effect can be ignored at $Re \geq 130$ and at $Ri \geq 0.4$, 0.3 and 0.4 for the C, F and S element Reactors respectively. Re has an effect on the bulk temperature along the flow passage. This effect decreased with increasing Re. The velocity vectors showed that the gravity has a strong effect on the flow direction along the flow passage. This effect decreased with increasing Re. The effect of buoyancy on the flow direction, and consequently on the temperature distribution, can be ignored at $Re \geq 130$.

The temperature contours showed that gravity has a strong effect on the temperature contours along the flow passage. This effect is due to the effect of the gravity on the flow pattern. The pathlines of flow showed that the F-element reactor appears to mix slightly more effectively than the S and these two much better than the C at the low Re. The cooling system has a significant effect on the fluid temperature in all geometries. The cooling rate in the F and S element Reactors is better than in the C-element Reactor. In addition, the temperature in the F and S element Reactors is more uniform that in the C-element Reactor: this might be because the heat transfer area relative to the passage volume in the F and S element Reactors is larger than in reactor C.

Adjusting the fluid temperature to the reactor plate temperature is very poor in C-element Reactor. However, it adjusts better in the F-element Reactor compared to the C and S element Reactors. This may indicate that the fluid mixing in the F-element Reactor is better than in the C and S element Reactors. In addition, the cooling system in the F-element Reactor is more efficient due to enhanced fluid mixing. The temperature non-uniformity decreased along the flow passage in all boundary conditions used and in all geometries. The temperature non-uniformity is affected by the Ri and the inlet temperature of the reagent stream. The temperature non-uniformity for the cool reagent stream inlet is higher than the temperature non-uniformity for the hot reagent stream inlet. The temperature non-uniformity is also affected by flow rate of fluid (Re) as it decreased with increasing fluid flow rate.

These results for the non-reacting flow system may differ compared to those for the reacting flow system due to the effect of heat released. Buoyancy may still have an effect on the temperature non-uniformity at values of Ri lower than the cut-off values of Ri for non-reacting flow, as the cut-off values of Ri may be lower. In addition, the Re may still affect the flow pattern and temperature distribution at Re slightly higher than 130.

Chapter Six

6. Results of the Reacting Flow

This chapter presents the measurements and corresponding computations of the two reactions (HCl-NaOH and $NaClO_2$- $K_2S_4O_6$ reacting systems) in the F-element Reactor (details of these reacting systems are provided in Section 3.7 and Appendix B). The chapter is divided into four main sections. The first section considers the issue of electrical noise affecting temperature measurement in the reacting liquids and the wire coating method used to overcome this. The wire coating section shows the effect of noise on the temperature profile and how it could be eliminated. The second section describes how the kinetic parameters in the reaction model used in the computations were selected. In addition, this section also shows evidence of the release of heat due to the chemical reaction. The third section shows the computations in comparison with the results from the experiments of the two reacting systems in the F-element Reactor for a range of Re and Ri. These comparisons aim to show how well the computational model is able to reproduce the measured results. This comparison may indicate the possibility of using the model to reliably predict the spatial temperature distribution within the domain of the reactor. Finally, the chapter closes with the effect of the Ri, Re and the enthalpy of reaction on the temperature non-uniformity within the reactor domain. The effect of these parameters was studied based on the standard deviation of temperature from the bulk temperature along the flow passage.

6.1 The experimental conditions

Two reacting flow systems were tested at different thermal boundary conditions. The reacting systems used were HCl-NaOH and $NaClO_2$- $K_2S_4O_6$. The tests were implemented in the F-element Reactor only to measure the temperature along the rear and front paths. Tables 6.1 and 6.2 show the thermal boundary conditions used in the HCl-NaOH and $NaClO_2$- $K_2S_4O_6$ reacting systems respectively. The thermal conditions depend on the temperature of the copper preheater plates (T_P) and the temperature of the copper reactor plates (T_R). The value of the Richardson number (Ri) depends on the temperature differences (ΔT) between T_R and the inlet temperature of the reagent stream (Section 4.2.2 shows how T_I is determined). The Reynolds (Re) and Richardson numbers (Ri) were calculated according to Eq. 3.22. The reference density

(ρ_o) represents the density of the liquid at T_R. The value of T_R was selected to ensure that the phase of flow remains liquid to prevent the formation of bubbles, which could affect the accuracy of temperature measurements.

Table 6. 1 The boundary conditions used in the HCl-NaOH reacting tests

Re	T_P, °C	T_I, °C	T_R, °C	ΔT, °C	F-Element Reactor Ri
32	31	31.0	40	-9	6.7
	34	34.0	40	-6	4.6
	37	37.0	40	-3	2.4
	40	40.0	40	0	0.0
130	37	33.5	40	-3	0.3
	40	35.8	40	0	0.2
	43	38.4	40	3	0.1

Table 6. 2 The boundary conditions used in the $NaClO_2$-$K_2S_4O_6$ reaction tests.

Re	T_P, °C	T_I, °C	T_R, °C	ΔT, °C	F-Element Reactor Ri
32	25	25.0	35	-10	6.4
	30	30.0	35	-5	3.4
	35	34.0	35	1	0.7
50	25	25.0	35	-10	2.6
	30	29.1	35	-5	1.6
	35	34.5	35	0	0.2

6.2 Temperature measurement

6.2.1 Wire coating

Measuring the temperature in small-scale structured passages requires a high level of accuracy in order to show clearly the features of the temperature profile. This accuracy was obtained in the thermal mixing experiments (as shown in the results in Ch. 5), whereas in the experiments of the reacting systems, HCl-NaOH and $NaClO_2$- $K_2S_4O_6$, the features of the temperature measured were not clear: a high level of noise was observed in the temperature profile in all geometries used. Fig. 6.1 shows the noise in the temperature profile of the rear path

at Re 130 and Ri 0.3 in the F-element Reactor in the HCl-NaOH reacting system. This noise may be a consequence of the high ion concentrations used and the pattern of mixing in these reactors. The ions may be formed static electric charges along the thermocouple wire. These charges increase with time to form an electrical field around the wire. This electrical field might lead to disturbance in the transfer of the voltage along the wire. This disturbance may affect the efficiency of the wire when measuring the temperature. The noise was observed in the measurements in all of the reactors at all of the conditions used (Re = 32 and 130). The noise increased in the chlorite reaction and when using a high flow rate of reagents (Re = 130) due to the increase in the concentrations of the ions in the flow system.

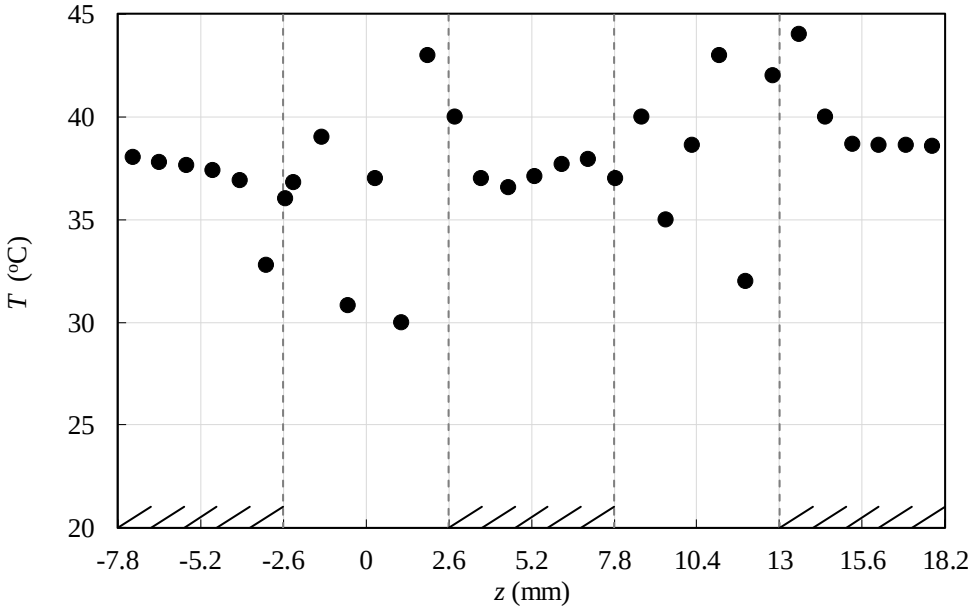

Figure 6. 1 Temperature profile using uncoated thermocouple wire at the HCl-NaOH reaction system in F-element Reactor.

To solve this problem, the wire was coated with a varnish to help insulate the wire from the ions used in the experiments. This varnish was a dilute liquid of polyethylene. The wire was coated by fingers. The wire was suspended vertically in the air using a clamp. The wire was passed between two fingers wetted with varnish from top to bottom. This process is repeated 4 times to ensure the wire surface had been completely coated. The thickness of the coating layer was about 3-9 μm. The coating layer was measured using KENNEDY Vernier. The noise was eliminated once the wire had been coated. Fig. 6.2 shows the temperature profile, after the wire had been coated, at the rear path at Re 130 and Ri 0.3 in the F-element Reactor in the HCl-NaOH reacting system. However, for the chlorite reaction at the high flow rate (Re = 130), the noise

was not successfully eliminated using this initial coating method. Therefore, the experiments for the chlorite system were implemented at a low flow regime (Re ≤ 50). Neither did this method of wire coating succeed in eliminating the noise in the C and S element Reactors. This may be due to the passage geometry, followed by the mixing pattern of these reactors: due to time restrictions, this problem has not been solved. Therefore, the tests for the reacting systems were only implemented in the F-element Reactor.

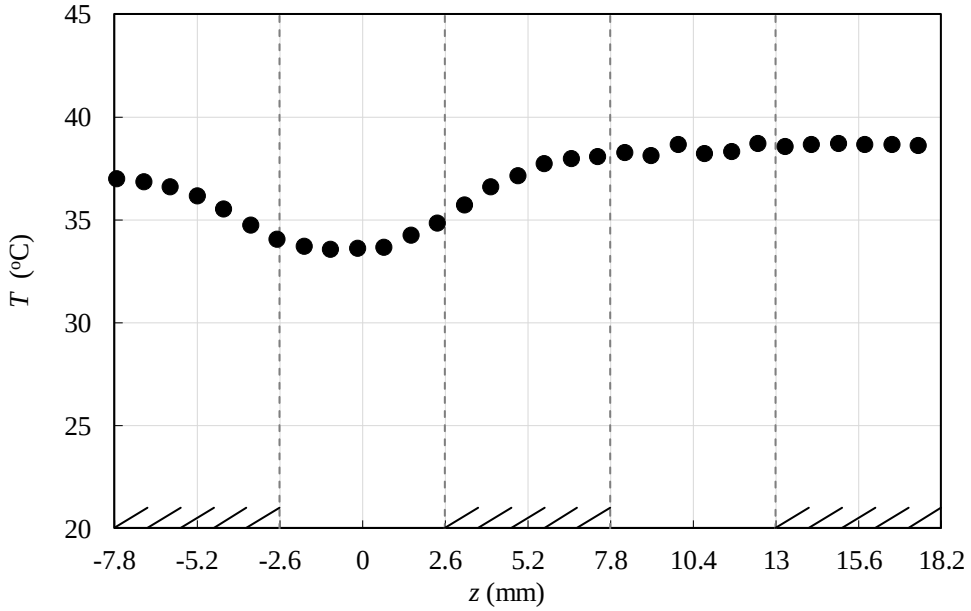

Figure 6. 2 Temperature profile using coated thermocouple wire at the HCl-NaOH reaction system in F-element Reactor.

6.3 Reaction parameters

6.3.1 Reaction kinetics

The activation energy (*E*) of a chlorite reaction is 60 kJ/mole approximately (Jakab, et al., 2002). According to this value, the value of the pre-exponential factor (*A*) is adjusted computationally to match the experimental temperature profile. A good agreement with experimental data is obtained when *A* is 10^6 $L^3.mol^{-3}.s^{-1}$. Two results were calculated at ± 10% of *A* value in order to investigate the accuracy of the value of *A*. Fig. 6.3 shows the effect of *A* values when matching the experimental temperature profile with computational results. The experimental data represents the average temperature measured along each element at Reynolds number 32 and Richardson number 3.4. The figure shows the computational results coincide

less with the experimental profile as the value of *A* increases and decreases. The figure also shows that the appropriate value of *A* to match the experimental profile is 10^6 $L^3.mol^{-3}.s^{-1}$.

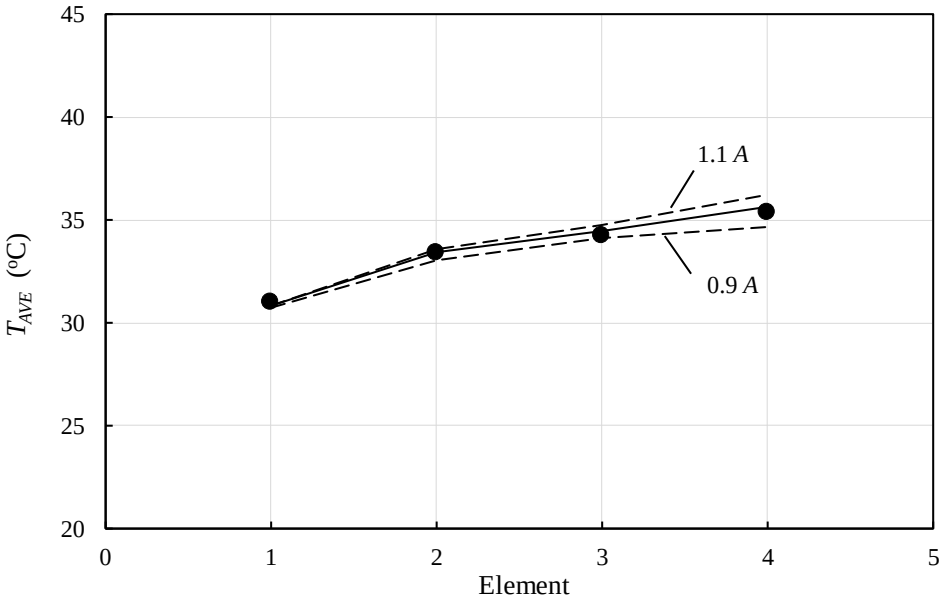

Figure 6. 3 Effect of the pre-exponential factor (A) on the profile of average temperature along each element at Re 32 and Ri 3.4.

Another investigation was carried out to investigate the accuracy of the value of the activation energy. This investigation includes the computational results at Re 32 at three different Richardson numbers (Ri), slightly higher activation energy (*E*) and specific pre-exponential factor (*A*). The Ri are 0.7, 3.4 and 6.4, while the *E* is 65 kJ/mol and *A* is 10^6 $L^3.mol^{-3}.s^{-1}$. Fig. 6.4 shows a slight divergence of the computational results from the experimental data at the *E* 65 kJ/mole, where the computational results increased at high temperature and decreased at a low temperature. This indicates the reaction rate constant (*k*) increased at high temperature and decreased at low temperature compared with the results at *E* 60 kJ/mole.

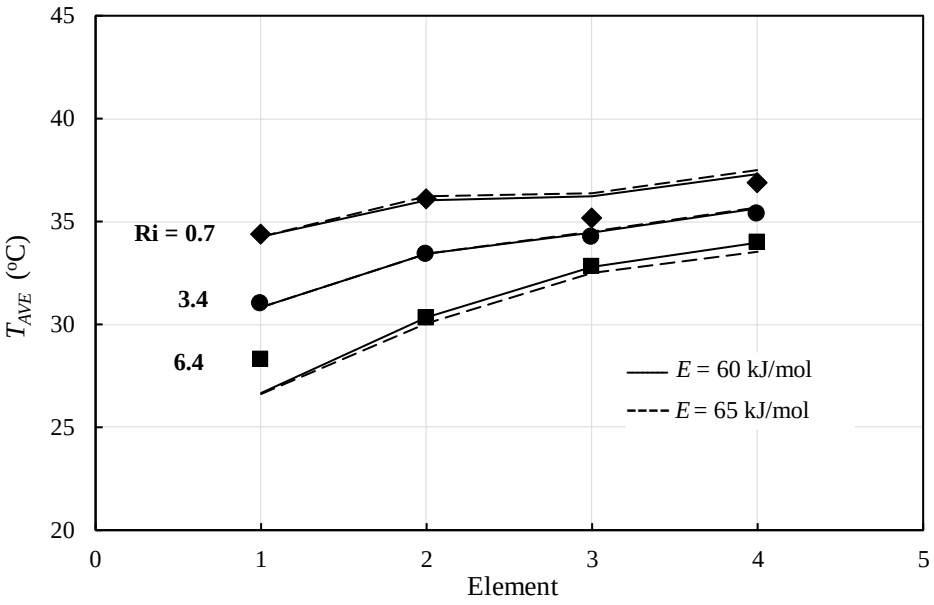

Figure 6. 4 Effect of the activation energy (E) on the average temperature along the wire path through each element computed using two different values of activation energy. Symbols are the corresponding values from the experiment.

The activation energy for the hydrochloric acid reaction was assumed to be zero (E = 0 J/mol) because the reaction is very fast since the HCl is a strong acid and NaOH is a strong base (see Section 3.7). The value of the pre-exponential factor (A) was adjusted computationally to match the experimental data. A good agreement with experimental data was obtained when A was 0.00015 $L.mol^{-1}.s^{-1}$ of the HCl-NaOH reaction.

6.3.2 Heat released indication

The temperature of the fluid could be affected by the heat released from the reaction and the cooling system. In other words, the cooling system could affect the temperature non-uniformity within the domain of the reactor by affecting the temperature of the fluid. The effect of the cooling system strongly depends on the flow rate of the fluid (Re). The heat transfer from the cooling system to the fluid increases with increasing Re due to a decrease in the thickness of the thermal boundary layer, Eq. 3.37. In spite of, the increasing of the Re could enhance the reaction rate through enhancing the mixing and diffusion of species, the heat released decreases with increasing Re due to reducing the residence time and thereby decreasing the reaction rate (Kockmann *et al.*, 2013; Plouffe, et al, 2016; Laudadio *et al.*, 2017). In other words, the increase in the fluid temperature with increasing Re could directly indicate the effect of the cooling

system. In the same time, when the fluid enters the reactor at the same temperature as the cooling system, $T_I = T_R$, the temperature rise of the fluid could indicate the releasing heat from the reaction.

The effect of the cooling system could be sensed by determining the difference between the reagent stream inlet temperature (T_I) and the maximum temperature of the profile in element 2 ($T_{2\ max.}$). The temperature difference ($\Delta T_{max.}$) between the $T_{2\ max.}$ and T_I could indicate the effect of the cooling system roughly. Table 6.3 shows the temperature differences ($\Delta T_{max.}$) for HCl-NaOH and $NaClO_2$-$K_2S_4O_6$ reacting system at different Re. Fig. 6.5 represents the temperature differences at different Re for both of the reacting systems. The figure shows there is a clear indication of increasing the temperature in element 2 in both reacting systems used. The figure shows the temperature rise increases with increasing the flow rate of fluid (Re). The figure also shows the temperature rise in the chlorite reacting system is greater than the hydrochloric acid reacting system. This may be due to the effect of the greater enthalpy of chlorite reaction.

At Re 32 in the hydrochloric acid reacting system, the temperate of the fluid is equal to the temperature of the cooling system, $T_I = T_R$. Therefore, the temperature rise in element 2 could indicate the heat released from the reaction. The temperature has raised as expected for the exothermic reaction.

Table 6. 3 The temperature difference ($\Delta T_{max.}$) between T_I and $T_{2\ max.}$ in the HCl-NaOH and $NaClO_2$-$K_2S_4O_6$ reacting system

Reacting system	Re	Ri	T_R (^oC)	Experimental data			Computational results		
				T_I (^oC)	$T_2 max.$ (^oC)	$\Delta T max.$ (^oC)	T_I (^oC)	$T_2 max.$ (^oC)	$\Delta T max.$ (^oC)
HCl-NaOH	32	0.0	40	40	40.5	0.5	40	40.51	0.51
	130	0.1	40	38.4	40.9	2.5	38.4	40.80	2.40
$NaClO_2$-$K_2S_4O_6$	32	0.7	35	34	36.3	2.3	34	36.32	2.32
	50	0.2	35	34.5	37.3	2.8	34.5	37.20	2.70

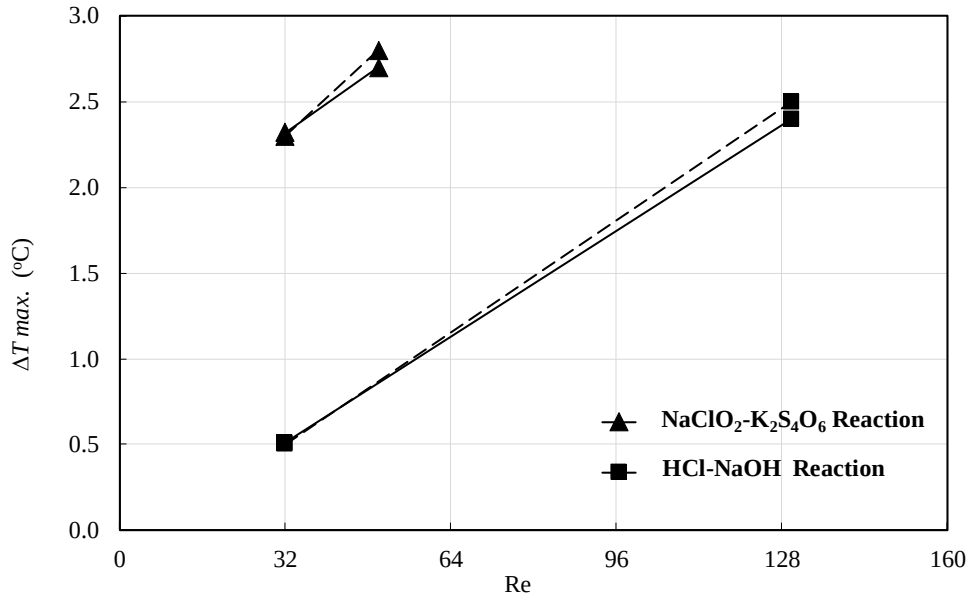

Figure 6. 5 Temperature difference (ΔT_{max}.) between T_1 and $T_{2\,max}$. in the HCl-NaOH and $NaClO_2$- $K_2S_4O_6$ reacting systems at different Re. The solid lines and dashed lines represent the computations and the experiments respectively.

6.4 Temperature profiles

6.4.1 Comparison with measured temperature profiles

This section shows the agreement between the experimental data and the computational results in the F-element Reactor in the hydrochloric acid and chlorite reacting systems. The results represented in this section include all the boundary conditions used in this chapter. The wire path includes two paths: rear and front path (see Fig. 4.6). The domain for measuring the temperature across the reactor includes solid domain and the flow passage. The shading along the top plot indicates the regions that are solid. Fig. 6.6 and 6.7 show the comparison between the computational results and the experimental data in the hydrochloric acid reacting system at Re 32 and 130 respectively. The figures show a good agreement between the computations and the experiments, with the exception of the results at the high Re value, i.e., Re = 130. The deviation between the experimental data and computational results could be reduced by the use of a very fine mesh size. The figures also show the effect of Ri on the temperature profile: there is a clear effect of Ri on the temperature profile, which could be due to the effect of the gravity force on the flow pattern and temperature distribution, equations 3.21 and 3.33.

Figs. 6.8 and 6.9 show the comparison between the computations and the experiments in the chlorite reacting system at Re 32 and 50 respectively. The figures show a good agreement between the computations and the experiments with slight deviations, especially at Re 50. The effect of the flow regime on the deviations between the computations and experiments in the chlorite reacting system is larger than in the hydrochloric acid reaction system. This may be because the enthalpy of the chlorite reacting system is larger than that in the hydrochloric acid reacting system. The figures show also that Ri has a clear effect on the temperature profile due to the effect of Ri on the flow pattern and temperature. This effect decreased with decreasing Ri. The agreement between the computations and the experiments in the F-element Reactor in non-reacting flow was better than the agreement in the reacting flow, especially at a high flow regime. This is probably due to the effect of the release of the heat from the exothermic reaction. Generally, the agreement between the experimental data and the computational results was acceptable and this allows use of the model to reliably predict the characters and features of flow pattern and the temperature within the domain of the reactor.

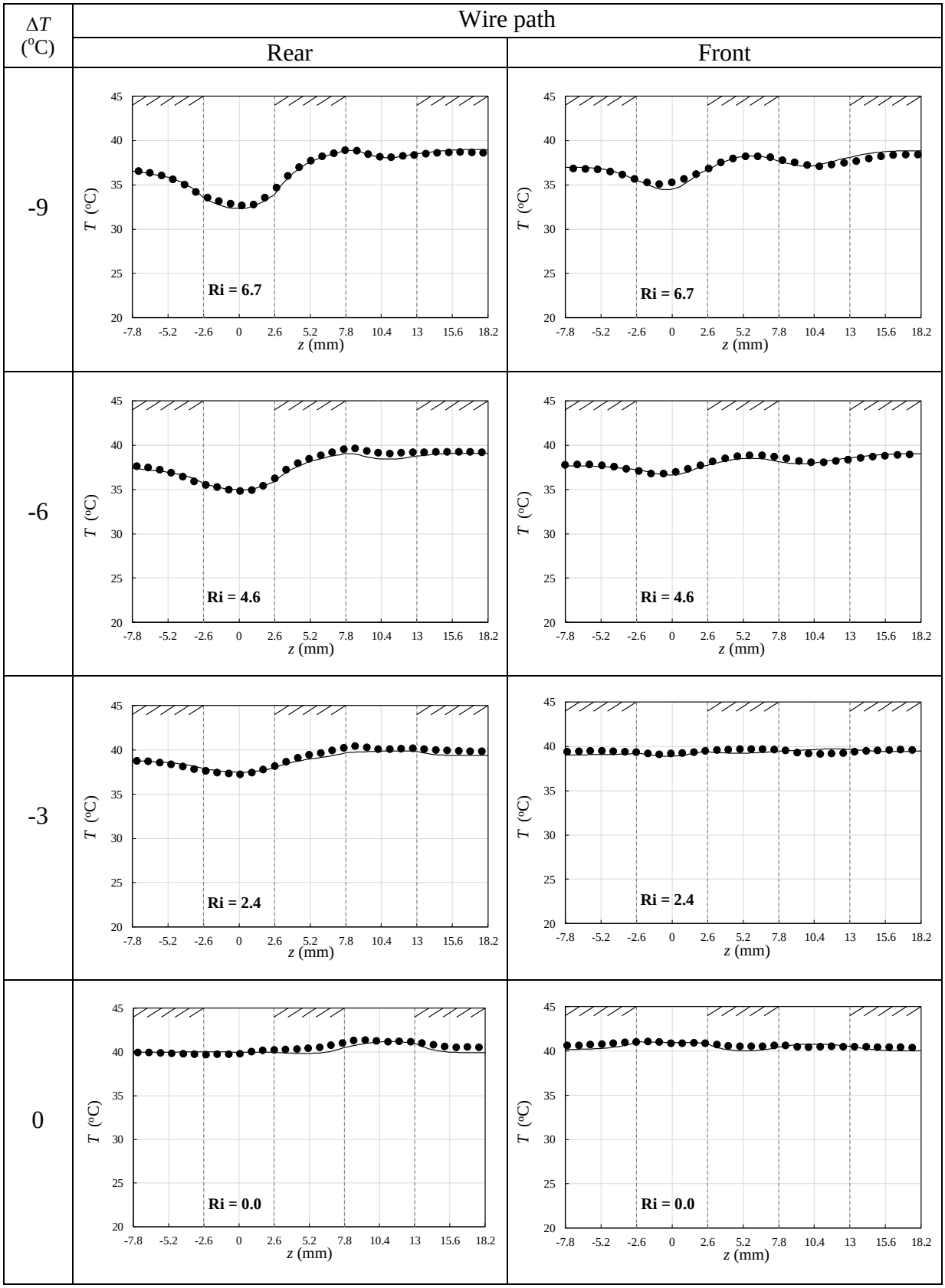

Figure 6. 6 Measured and computed temperature profiles along the rear and front path at Re 32 in HCl-NaOH reaction system. Effect of imposed temperature difference.

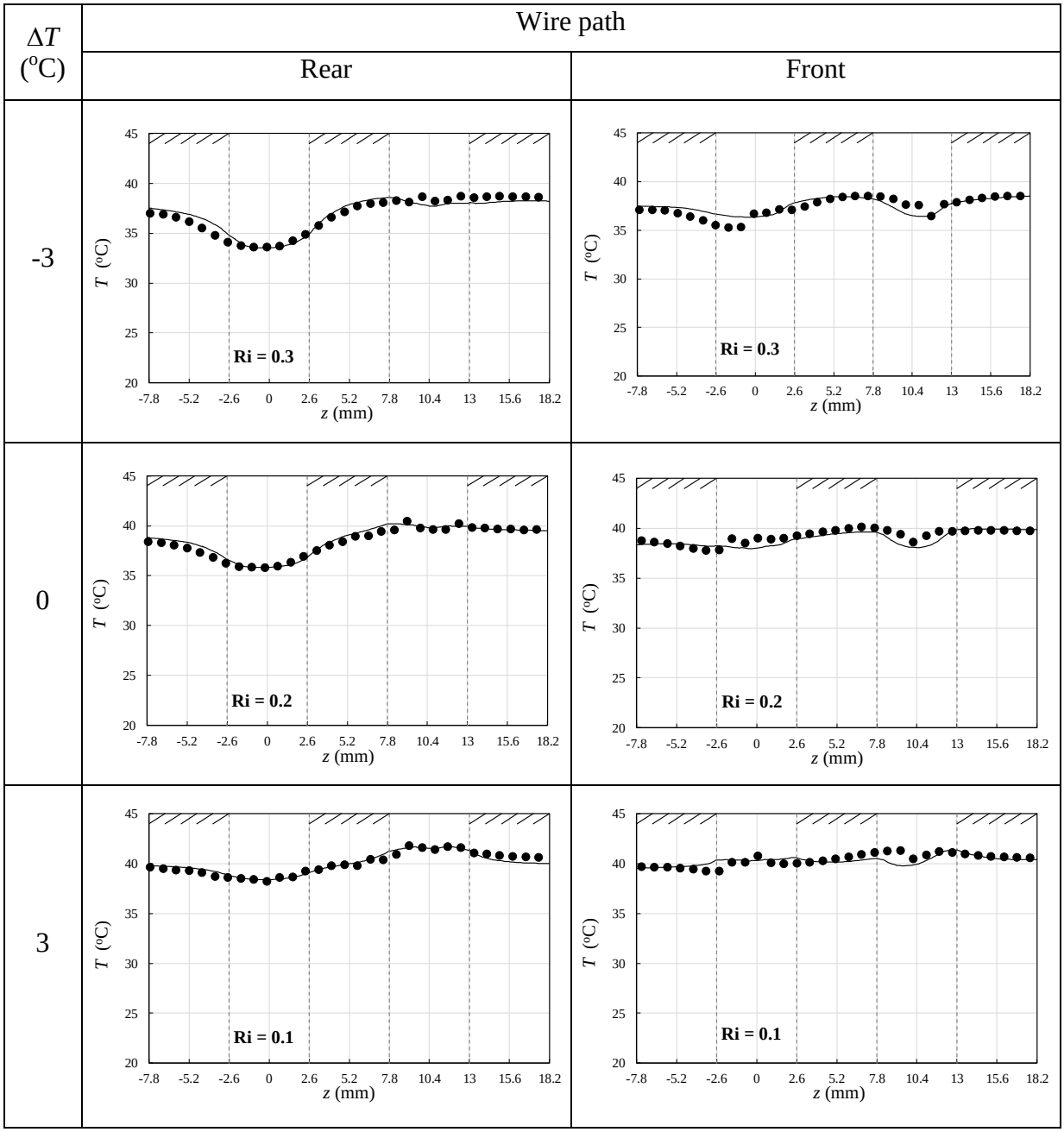

Figure 6. 7 Measured and computed temperature profiles along the rear and front path at Re 130 in HCl-NaOH reaction system. Effect of imposed temperature differences.

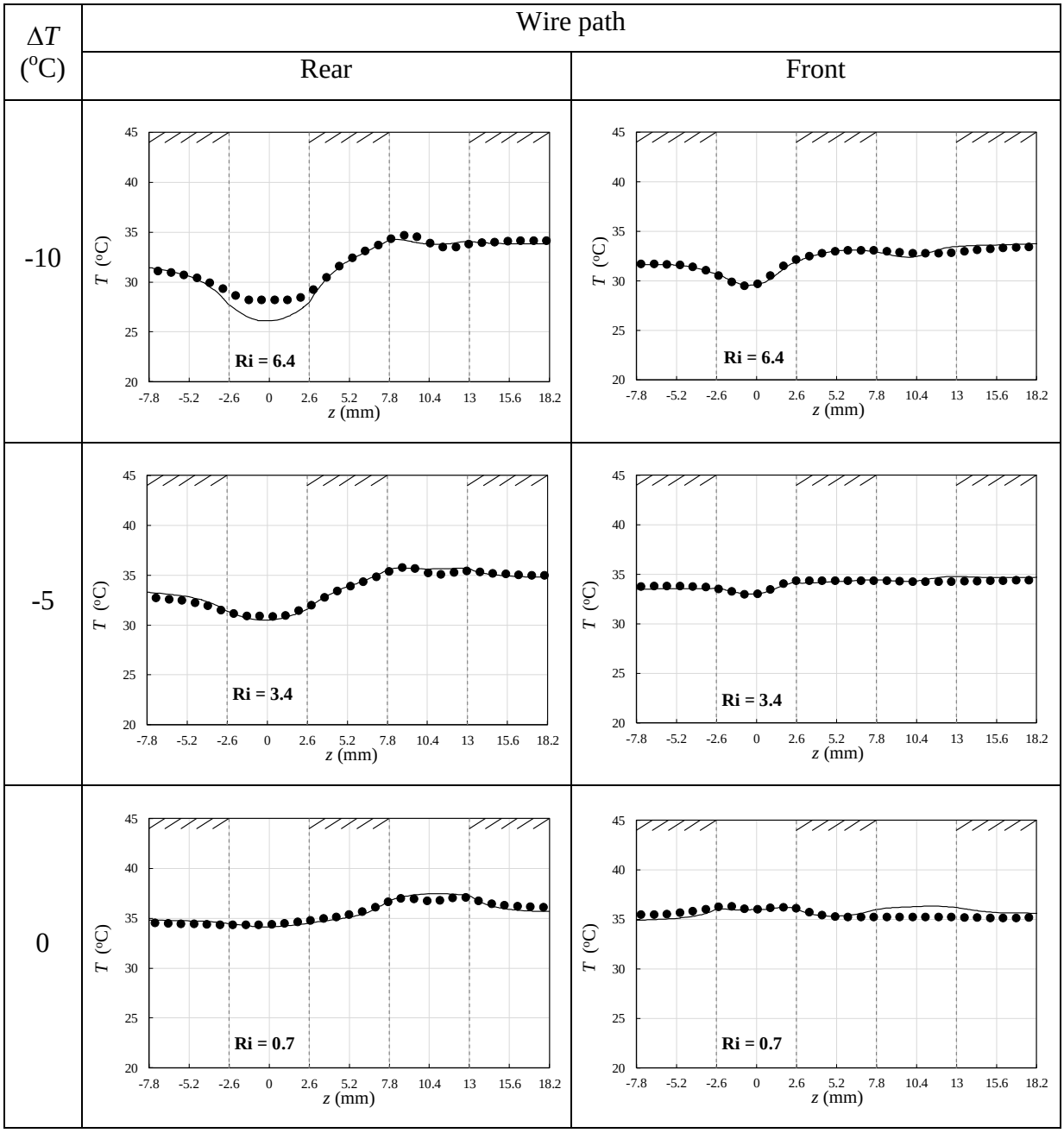

Figure 6. 8 Measured and computed temperature profiles along the rear and front path at Re 32 in the $NaClO_2$-$K_2S_4O_6$ reaction system. Effect of imposed temperature differences.

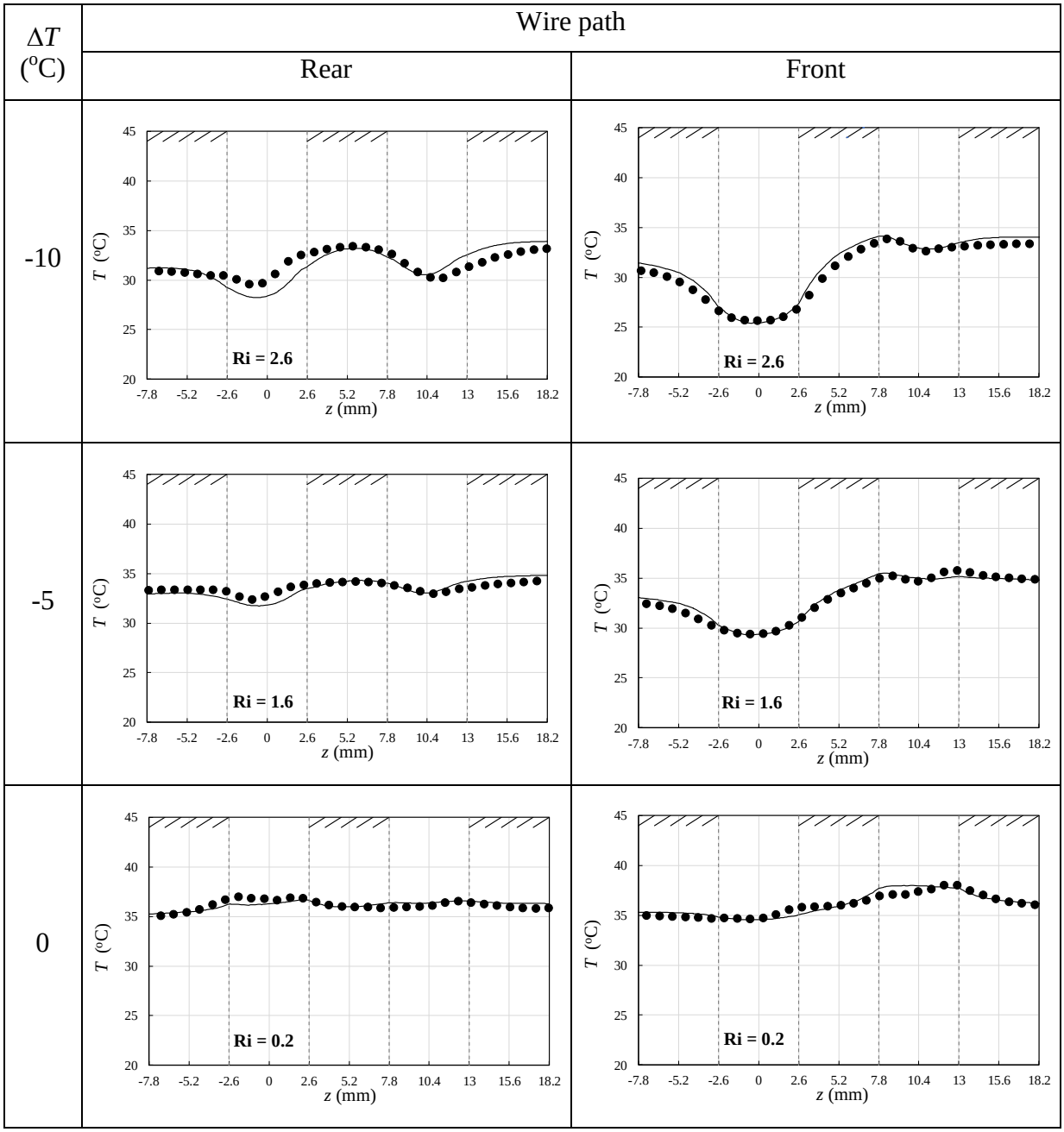

Figure 6. 9 Measured and computed temperature profiles along the rear and front path at Re 50 in the $NaClO_2$-$K_2S_4O_6$ reaction system. Effect of imposed temperature differences.

6.5 Temperature statistics

6.5.1 Mean temperature change along the passages

Figs. 6.10 and 6.11 show the effect of Ri on the bulk temperature (Eqs. 3.49 and 3.50 describe how the bulk temperature is calculated) within a domain of each element in the F-element Reactor in the HCl-NaOH and $NaClO_2$- $K_2S_4O_6$ reacting systems. In these figures, normalised temperature is plotted so the range of temperature is similarly scaled. The

normalized bulk temperature (T_B^*) is a temperature difference between the bulk temperature and the reagent stream inlet temperature ($T_B - T_I$), divided by the temperature difference between the copper reactor plate temperature and the reagent stream inlet temperature ($(T_R - T_I)$). The figures show that the bulk temperature increases along the flow passage due to an increase in the reagent inlet temperature and may be due to the heat released from the exothermic reaction. The figures also show the Richardson number (Ri) has a clear effect on the bulk temperature. The bulk temperature increases with decreasing Ri. The bulk temperature rises rapidly when the inlet temperature of the reagent and the temperature of the copper reactor plates are close, i.e., at very low Ri. This is probably due to the effect of heat released from the reaction.

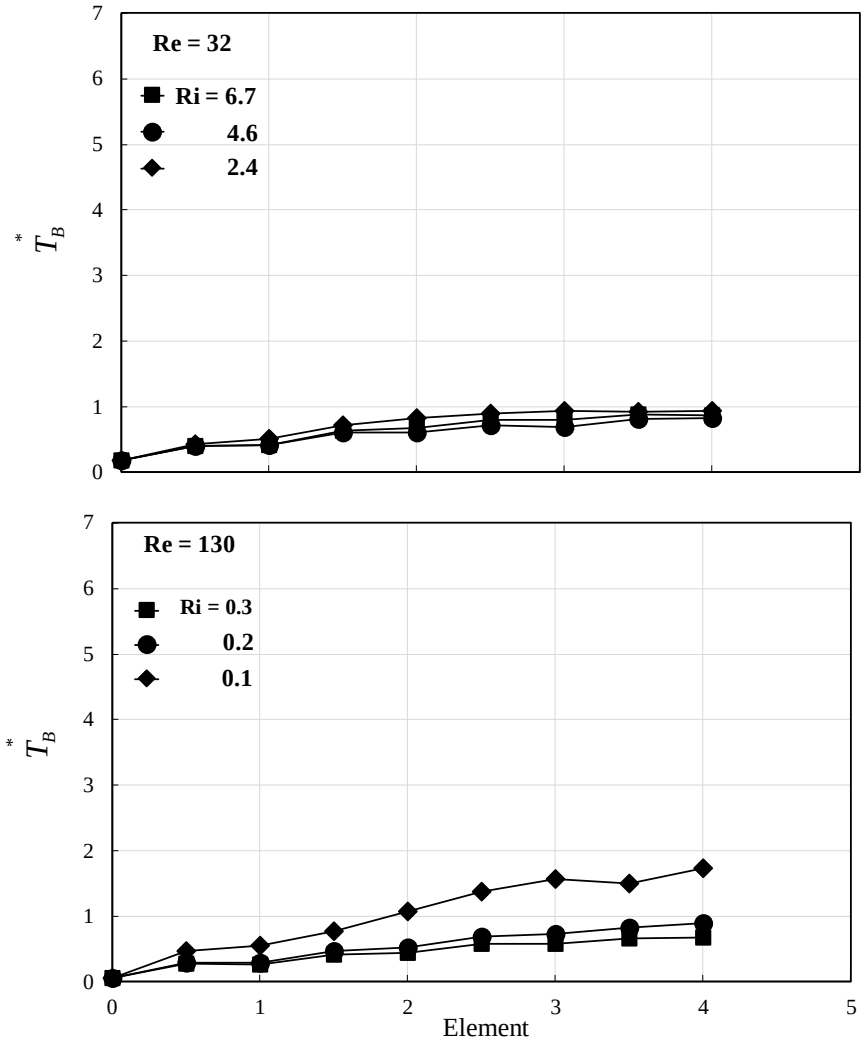

Figure 6. 10 Computed bulk temperature over the four elements along the flow passage for each of the two Reynolds number values of the HCl-NaOH reacting system.

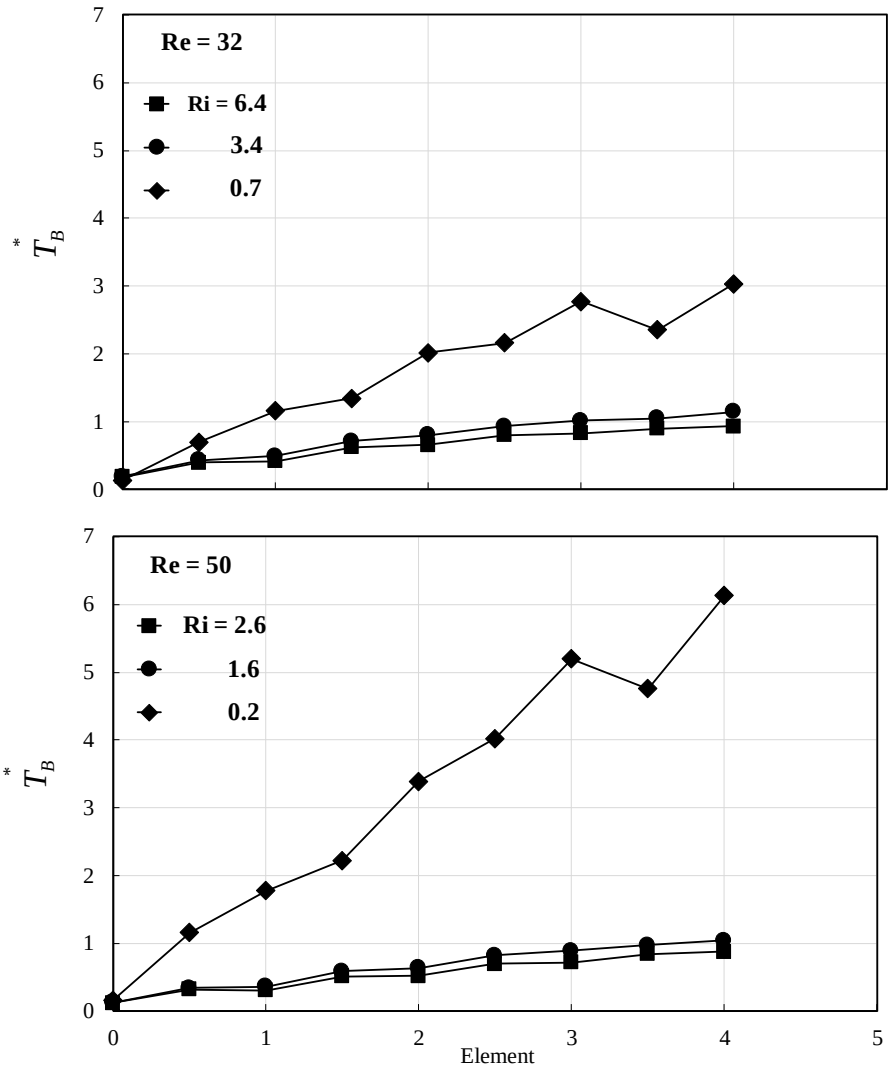

Figure 6. 11 Computed bulk temperature over the four elements along the flow passage for each of the two Reynolds number values of the $NaClO_2$- $K_2S_4O_6$ reacting system.

6.5.2 Temperature non-uniformity change along the passages

6.5.2.1 Influence of Ri on the temperature non-uniformity

Quantitative comparisons were made of the effect of Richardson number (Ri) on the temperature non-uniformity. These comparisons were made using the plots of the standard deviation of temperature from the bulk temperature. The temperature deviation from the bulk temperature was calculated, as shown in Section 3.8, along the flow passage in the HCl-NaOH and $NaClO_2$- $K_2S_4O_6$ reacting systems, at different Ri and Re in the F-element Reactor.

Figs. 6.12 - 6.15 show that the standard deviation of temperature decreases along the flow passage in both reaction systems. This could be due to enhancing the heat transfer within the domain of the reactor through effective dissipating the accumulated heat released. In other words, the small scale structured reactor can be used to reduce the temperature non-uniformity in the chemical reacting systems (Eq. 3.39).

The figures show also that the Richardson number (Ri) has a significant effect on the temperature deviation. The standard deviation of temperature increases with increasing Ri. This may be due to the increasing effect of gravity on the flow pattern (Eq. 3. 21) and temperature distribution (Eq. 3.33). This case was clearly seen at high Ri. Ri still has an effect on the temperature non-uniformity at low values, i.e., Ri $\geq$ 0.1. The effect of Ri in the reacting flow is slightly larger than in the non-reacting flow. This is may be due to the effect of the heat released from the reaction. The figures also show that the Ri has an effect on the bulk temperature along the flow passage, which increases with decreasing Ri due to the increase in the inlet temperature of the reagent stream.

The bulk temperature exceeded the copper reactor plate temperature (see Tables 6.1 and 6.2) at the lower Ri: this clearly indicates the heat released from the exothermic reaction. The maximum standard deviation of temperature ($\sigma_{T\max.}$) for the HCl-NaOH reacting system was 1.9 ^{o}C at Re = 32 and Ri = 6.7, while in the $NaClO_2$- $K_2S_4O_6$ reacting system it was 2.2 ^{o}C at Re = 32 and Ri = 6.4. This slight difference in the ($\sigma_{T\max.}$) could indicate that the effect of the heat released is bigger in the chlorite reaction than in hydrochloric reaction.

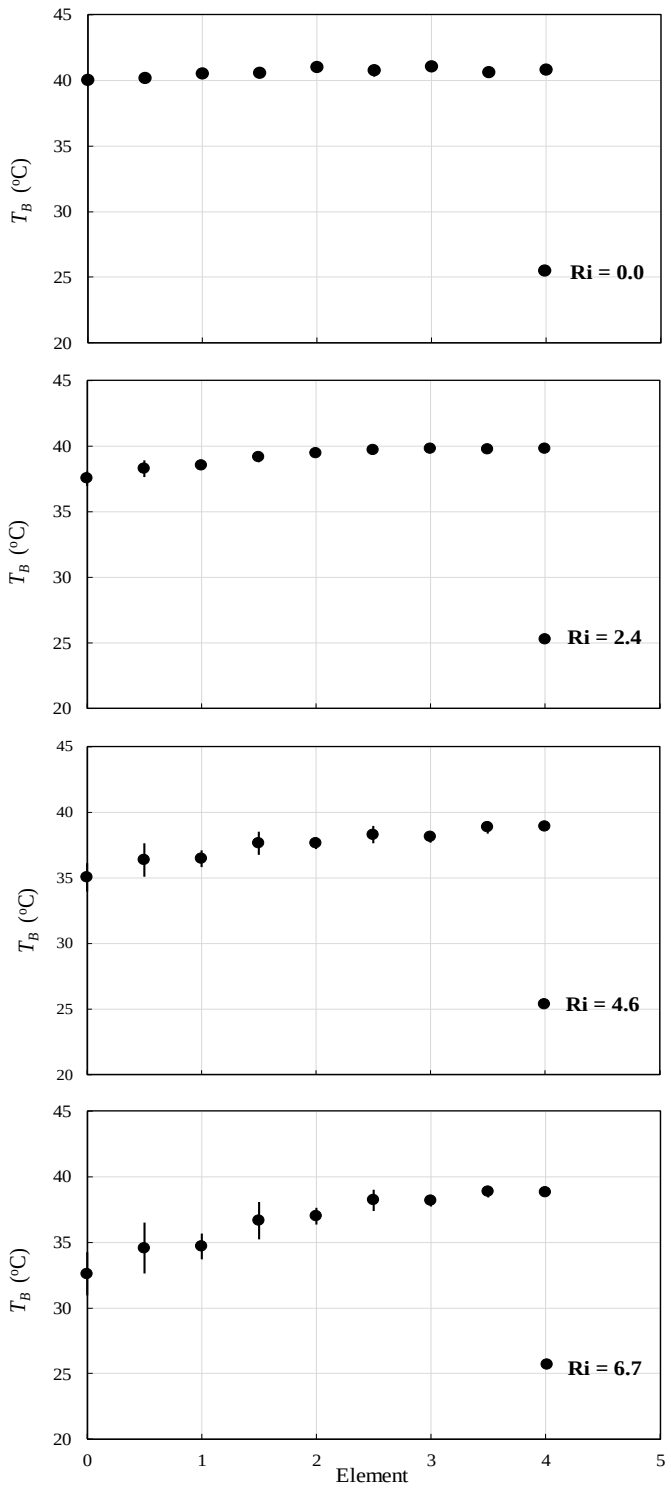

Figure 6. 12 Computed standard deviation of temperature over the four elements along the flow passage at Re 32 of the HCl-NaOH reacting system.

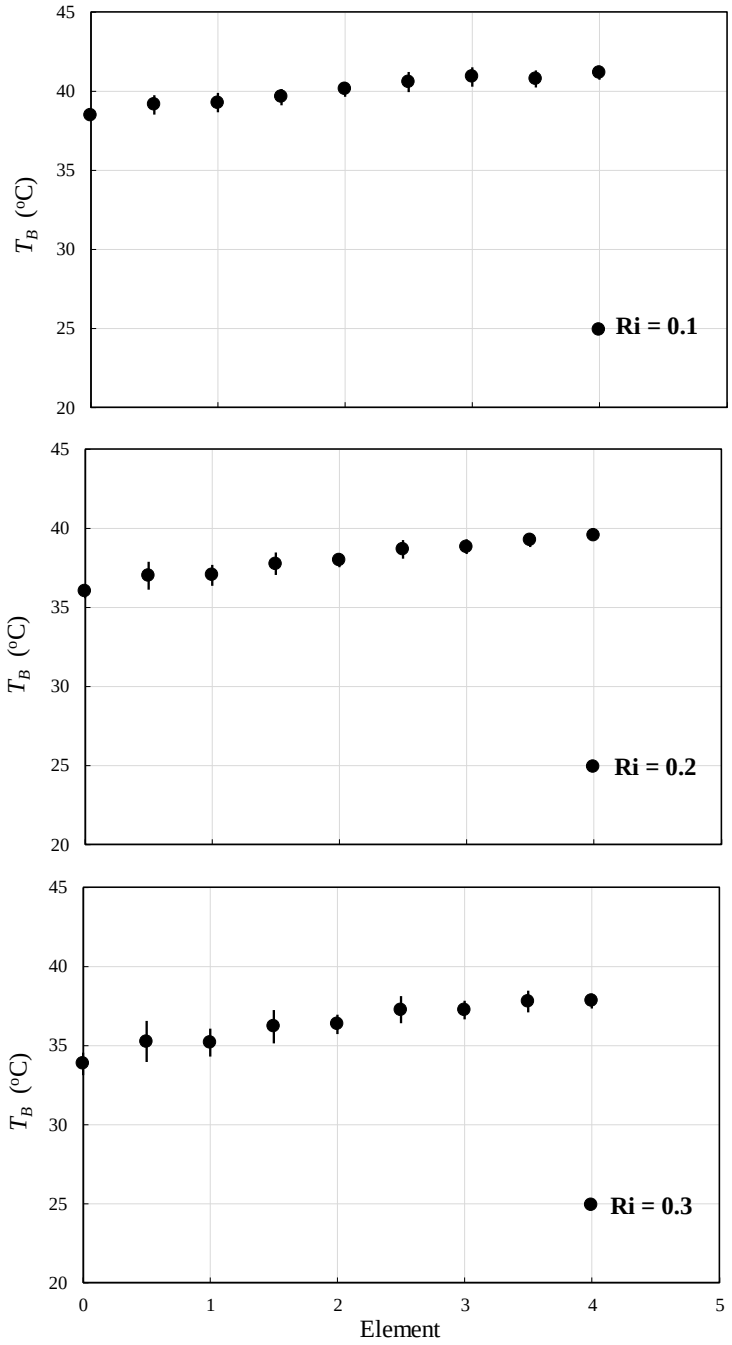

Figure 6. 13 Computed standard deviation of temperature over the four elements along the flow passage at Re 130 of the HCl-NaOH reacting system.

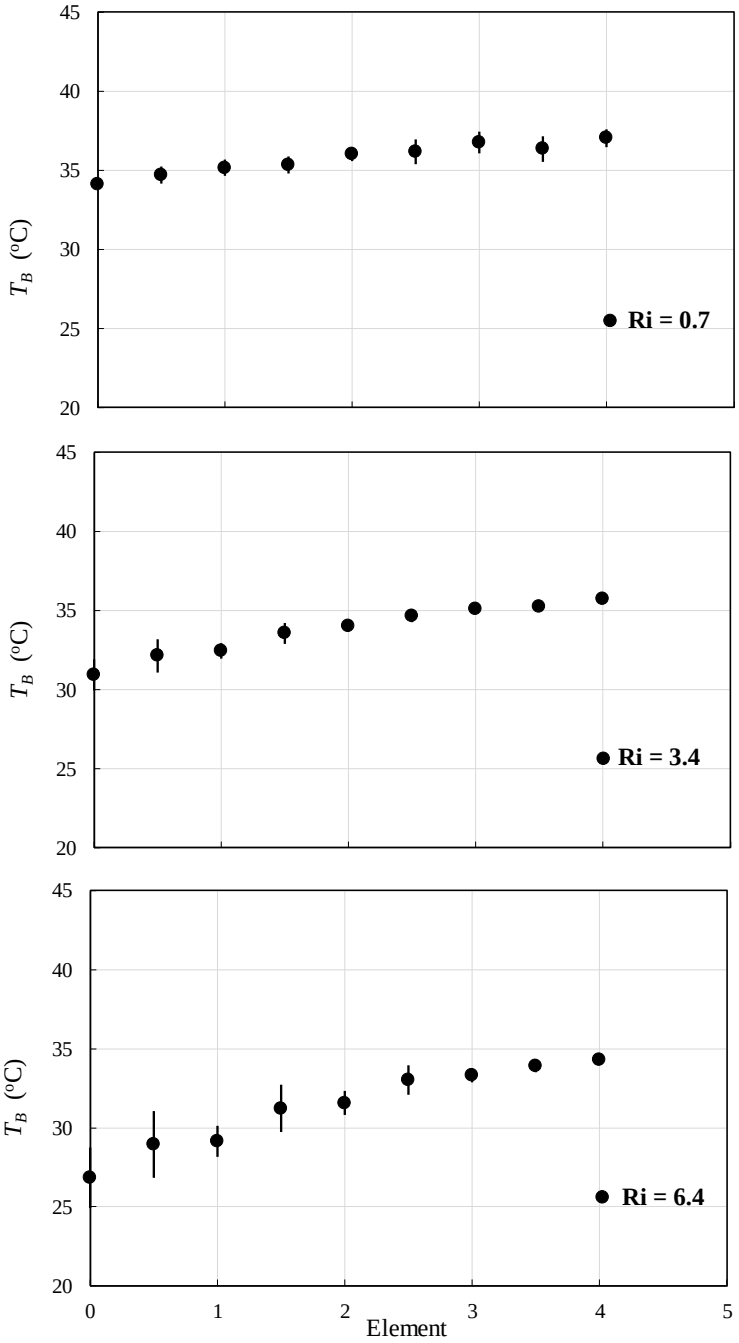

Figure 6. 14 Computed standard deviation of temperature over the four elements along the flow passage at Re 32 of the $NaClO_2$- $K_2S_4O_6$ reacting system.

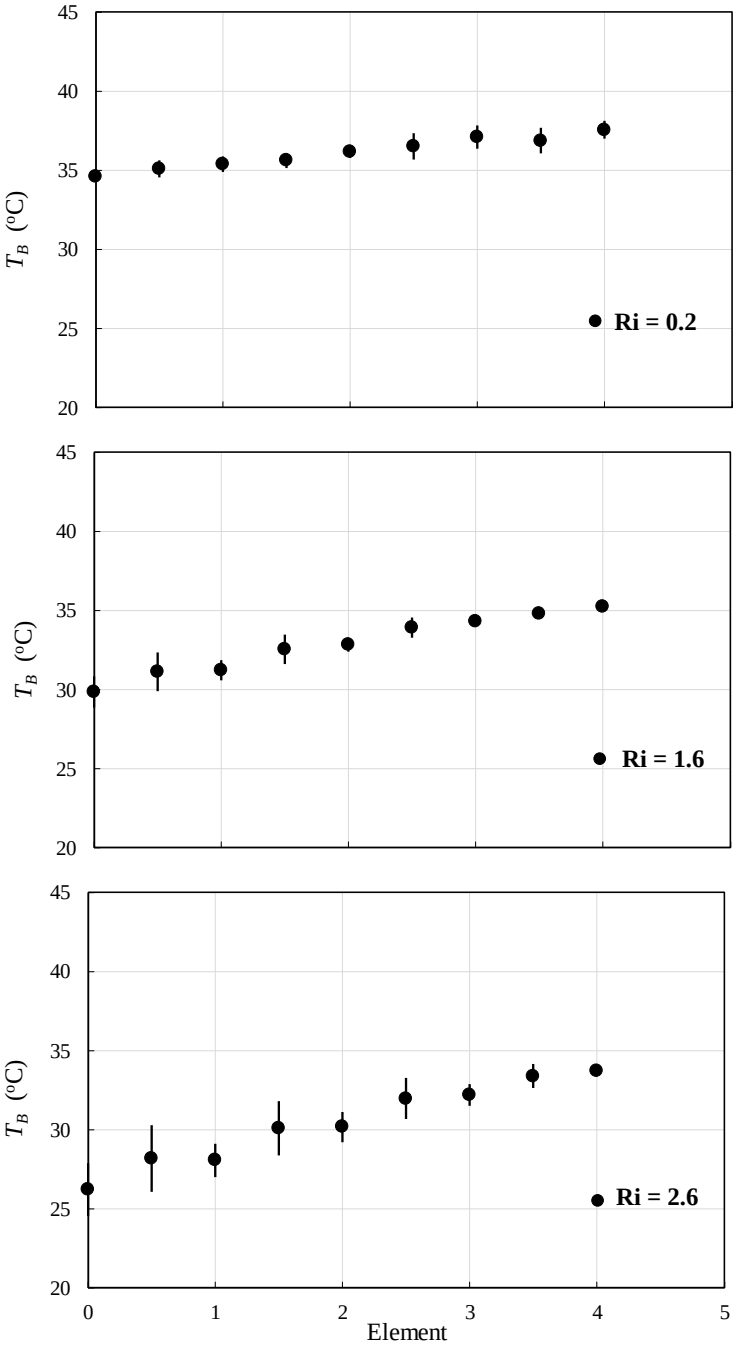

Figure 6. 15 Computed standard deviation of temperature over the four elements along the flow passage at Re 50 of the $NaClO_2$- $K_2S_4O_6$ reacting system.

6.5.2.2 Influence of enthalpy of reaction on temperature non-uniformity

The temperature non-uniformity can be affected by increasing the enthalpy of reaction by increasing the heat released. Fig. 6.18 shows the standard deviation of temperature for hydrochloric acid and chlorite reacting systems at the same Re (Re = 32) and a slight difference in Ri. Ri is 6.7 and 6.4 for the hydrochloric acid reacting system and chlorite reacting system

respectively. The maximum standard deviation of temperature ($\sigma_{T\max.}$) for the HCl-NaOH and the $NaClO_2$- $K_2S_4O_6$ reacting systems is 1.9 ^oC and 2.2 ^oC respectively. The figure shows that enthalpy of reaction has an effect on the standard deviation of temperature. The temperature non-uniformity in the chlorite reacting system was higher than the temperature non-uniformity in the hydrochloric acid reacting system (Eq. 3.39). This could be because the enthalpy of the chlorite reaction is higher than the enthalpy of the hydrochloric acid reaction (Waterkamp, 2007; Löwe 2010). The figure also shows that the temperature non-uniformity decreases along the flow passage. This may be due to the effective dissipation of heat released within the domain of the passages (Schubert et al., 2001; Schubert et al., 1998).

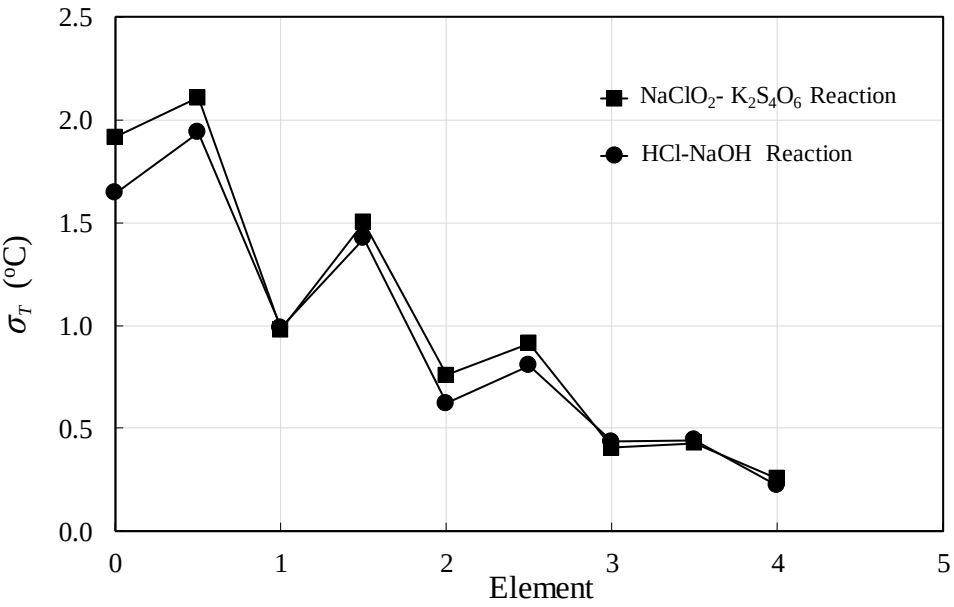

Figure 6. 16 Computed standard deviation of temperature over the four elements along the flow passage at Re = 32 in the HCl-NaOH and $NaClO_2$- $K_2S_4O_6$ reacting systems.

6.6 Summary

This chapter described the temperature non-uniformity in the F-element Reactor in the HCl-NaOH and $NaClO_2$- $K_2S_4O_6$ reacting systems at different Re and Ri. The results showed that using the movable fine-wire thermocouple method to measure the spatial temperature in the reacting flow can cause noise in the temperature profile, especially at the high flow regime. This problem was solved by coating the wire with a thin layer (3-9 μm) of varnish to insulate the wire from the ions used in the experiments. The results also showed that the value of the pre-exponential factor (*A*) of reaction could be deduced computationally by matching the

experimental temperature profile at specific activation energy. The activation energy (*E*) for the HCl-NaOH and $NaClO_2$- $K_2S_4O_6$ reactions was zero and 60 kJ/mol. According to these values, a good agreement with experimental data was obtained when A was 0.00015 $L.mol^{-1}.s^{-1}$ and 10^6 $L^3.mol^{-3}.s^{-1}$ for the HCl-NaOH and $NaClO_2$- $K_2S_4O_6$ reactions respectively. Moreover, the results showed that there is clear evidence of chemical reaction occurring at the beginning of the flow passage. In addition, the Ri has a significant effect on temperature non-uniformity in both reaction systems. Temperature non-uniformity decreased with decreasing Ri. Ri still has an effect on the temperature non-uniformity at low values, i.e., $Ri \geq 0.1$. The effect of Ri in the reacting flow is slightly larger than in the non-reacting flow. This is may be due to the effect of the heat released from the reaction. Furthermore, the results showed that the Ri has an effect of the bulk temperature along the flow passage. The bulk temperature increases with decreasing Ri due to the increasing of the inlet temperature of reagent stream. Finally, the enthalpy of reaction also has an effect on temperature non-uniformity: the latter increased with the increasing enthalpy of reaction (Eq. 3.39).

Chapter Seven

7. The Conclusion and Future work

A number of studies have identified that using small scale structured channels could enhance the control of the heat of reaction. To investigate these ideas required effective tools, such as an effective method to measure the spatial temperature in small channels and develop a computational model to predict the flow direction and temperature distribution in these channels. The current study was conducted to investigate the control of the heat of reaction in the liquid-phase reaction using structured passages.

7.1 Conclusions

The list below shows the main conclusions of the current study.

- The study suggested a mathematical model that shows the main parameters affecting temperature non-uniformity within the flow passage in a reacting flow system. The model demonstrates that temperature non-uniformity can be reduced when the flow passage size, species concentration and enthalpy of reaction are decreased, and when the flow rate of species is increased. In addition, temperature non-uniformity may also be affected by buoyancy.
- The results show that temperature non-uniformity decreased along the flow passage in all geometries and in all boundary conditions used. This could indicate that temperature non-uniformity can be minimised using small-scale structured passages.
- The results for reacting flow showed that the enthalpy of reaction also has an effect on temperature non-uniformity: the latter increased with the increasing enthalpy of reaction.
- The buoyancy (Ri) has a significant effect on the flow direction and the temperature profile in all geometries used (C, F and S element Reactors). Temperature non-uniformity was decreased by decreasing the buoyancy effect (Ri). This may be due to the decrease in the effect of gravity force on the flow pattern and temperature distribution. The buoyancy effect decreases with decreasing Ri and increasing fluid flow rate (Re). This effect can be ignored at

Re ≥ 130 at the Ri ≥ 0.4, 0.3 and 0.4 for the C, F and S element Reactors respectively in the non-reacting flow, and at the Ri ≥ 0.1 for the F-element Reactor in the reacting system. This could indicate that the effect of Ri in the reacting flow is larger than that effect in the non-reacting flow due to the heat being released from the reaction.

- The cooling system has a significant effect on the fluid temperature in all geometries. The cooling rate in the F and S element Reactors is better than in the C-element Reactor. In addition, the temperature in the F and S element Reactors is more uniform that in the C-element Reactor: this might be because the heat transfer area relative to the passage volume in the F and S element Reactors is larger than in the Reactor C. The effect of the cooling system of the reactor increased with the increasing fluid flow rate (Re), due to the increasing heat transfer into the fluid.

- The heat released from the exothermic reaction in the small-scale structured reactors can be sensed by measuring the spatial temperature across different positions along the flow passage.
- The spatial temperature in the small scale structured passages at the non-reacting flow can be measured successfully using the movable fine-wire thermocouple method. This method can cause an error in heat conduction depending on the wire size and wire velocity. The heat conduction error increased with increasing wire diameter and increasing wire velocity. Reliable temperature measurement can be obtained experimentally at wire diameter 75 μm and wire velocity 0.4 m/s or below. The temperature measurement has the largest error at peaks or troughs in the temperature profile, and these may be up to around 5%.
- Using the movable fine-wire thermocouple method to measure the spatial temperature in the reacting flow caused noise in the temperature profile, especially at the high flow regime. This noise may be a consequence of the high ion concentrations used and the pattern of mixing in these reactors. This problem was solved by coating the wire with a thin layer (3-9 μm) of varnish to insulate the wire from the ions used in the experiments. However, coating the wire with varnish only succeeded in eliminating noise in the F-element Reactor.

- Air bubbles can form at any position of the flow passages as a result of desorption of the dissolved gases in the reagent solutions inside the reactor. These bubbles could cause a significant error in the profile of the temperature measured when the bubbles are formed close to the thermocouple paths. The number of bubbles formed was reduced by pushing a surfactant at a high flow rate at the beginning of the test, using DI water in the preparation of the reagent solutions A and B and covering the reagents solutions A and B inside the pressure pots with floats; nevertheless, some bubbles still formed in the flow passages.
- The temperature profile along the reactor domain in the small scale structured passages at the laminar flow regime can be successfully simulated using CFD. This simulation can be used to predict the flow direction and temperature distribution in the flow passages.
- The value of the pre-exponential factor (*A*) of reaction was deduced computationally by matching the experimental temperature profile at a specific activation energy. The activation energy (*E*) for the HCl-NaOH and $NaClO_2$-$K_2S_4O_6$ reactions was set to zero and 60 kJ/mol. According to these values, a good agreement with experimental data was obtained when *A* was 0.00015 $L.mol^{-1}.s^{-1}$ and 10^6 $L^3.mol^{-3}.s^{-1}$ for the HCl-NaOH and $NaClO_2$- $K_2S_4O_6$ reactions respectively.

7.2 Recommendations for future work

This section includes some recommendations for future work for further investigation and development to build, systematically, upon the current study.

- Investigation of the effect of fluid flow rate (Re) at constant buoyancy effect (Ri) on temperature non-uniformity in the structured reactors in the liquid phase exothermic reaction.
- Future work could be directed at improving wire coating to eliminate the noise in reactors with a specific geometry, i.e., C and S. The coating could be improved by using a thick layer of varnish or another material.
- Investigation of the performance of the use of small scale structured passages to control the heat of reaction in the endothermic liquid phase reaction.

- An attempt to find another method to measure the spatial temperature in small scale passages, especially in the reacting flow, e.g., using a laser.
- Investigation of the effect of increasing the number of elements in the reactors on temperature non-uniformity within the flow passage.

References

Agilent Technologies, "Making good thermocouple measurements in noisy environments" Measurement Tips, Vol. 1, No. 1, Agilent Technologies, Inc., USA, Pp. 1-4, 2008.

Alépée, L. Vulpescu, P. Cousseau, P. Renaud, R. Maurer, A. Renken, IMRET 4: 4th International Conference on Microreaction Technology (Atlanta, USA, 2000), American Institute of Chemical Engineers Topical Conference Proceedings, p. 71.

Al-Rawashdeh M., F. Yue, N. G. Patil, T. A. Nijhuis, V. Hessel, and J. C. Schouten, "Designing flow and temperature uniformities in parallel microchannelS-element Reactor", AIChE Journal, 60, 5, Pp. 1941-1952, 2014.

Alwaaly A. A. Y., M. C. Paul, and P. S. Dobson, "Effects of thermocouple electrical insulation on the measurement of surface temperature" Applied Thermal Engineering, 89, Pp. 421-431, 2015.

ASTM MNL 11, "Manual on The Use of Thermocouples in Temperature Measurement," 4th edition, American Society for Testing and Materials, Philadelphia, Pennsylvania, 1993.

Bailey N.P, "Measurement of Surface Temperatures, Accuracies Obtainable With Thermocouples," Mechanical Engineering, Vol. 54, No. 8, p. 553-336, August 1932.

Bánsági T., D. Horváth, and Á. Tóth, "Multicomponent convection in the chlorite-tetrathionate reaction", Chemical Physics Letters, 384, Pp. 153-156, 2004.

Boelter L.M.K., and R.W. Lockhart, "An Investigation of Aircraft Heaters XXXV - Thermocouple Conduction Error Observed in Measuring Surface Temperatures," NACA Technical Note 2421, NACA, Washington, D.C., July 1951.

Boelter L.M.K., F.E. Romie, A.G. Guibert and M.A. Miller, "An Investigation of Aircraft Heaters XXVIII - Equations for Steady-State Temperature Distribution Caused by Thermal Sources in Flat Plates Applied to Calculation of Thermocouple Errors,

Heat-Meter Corrections, and Heat Transfer by Pin-Fin Plates," NACA Technical Note 1452, NACA, Washington, D.C., August 1948.

Boissonade, J. et al. (2001) 'Spatial bistability and waves in a reaction with acid autocatalysis', 120, pp. 353–361.

Botti, L. et al. (2018) 'Modeling hemodynamics in intracranial aneurysms: Comparing accuracy of CFD solvers based on finite element and finite volume schemes', International Journal for Numerical Methods in Biomedical Engineering, 34(9), pp. 1–13. doi: 10.1002/cnm.3111.

Branebjerg, P. Gravesen, J. P. Krog, C. R. Nielsen, IEEEMEMS'96 (San Diego, USA, 1996), p. 441.

Chen, P. et al., 2012. Simulation guided-design of a microfluidic thermal reactor for polymerase chain reaction. Chemical Engineering Research and Design, 90(5), pp. 591-599.

Chen, Z. et al., 2009. Performance analysis of a folding flow micromixer. Micro fluids and Nano fluids, 6(6), pp. 763-774.

Date A. W. (2005) Introduction to Computational Fluid Dynamics, Journal of Chemical Information and Modelling. Bombay: Cambridge university press. doi: 10.1017/CBO9781107415324.004.

David, P. L. (2004) CRC Handbook of chemistry and physics. 84th edition. Florida: CRC Press. Florida.

Druschel G. K., R. J. Hamers, G. W. Luther, and J. F. Banfield, "Kinetics and mechanism of trithionate and tetrathionate oxidation at low pH by hydroxyl radicals", Aquatic Geochemistry, 00, Pp. 1-20, 2003.

Dutta V.B., "Junction-to-Case Thermal Resistance – Still a Myth?" Fourth Annual IEEE Semiconductor Thermal and Temperature Measurement Symposium (SEMI-THERM), p. 8-11, San Diego, CA, February 10-12, 1988.

Ehrfeld, V. Hessel, H. LDwe, Microreactors, Wiley-VCH, Weinheim, 2000.

Ehrfeld, V. Hessel, V. Haverkamp, Ullmann's Encyclopedia of Industrial Chemistry, 6th ed., Wiley-VCH, Weinheim, 1999.

Gobby, D., Angeli, P. & Gavriilidis, A., 2001. Mixing Characteristics of T-type microfluidic mixers. Journal of Micromechanics and Micro engineering, 11(2), pp. 126-132.

Gravesen, J. Branjeberg, O. S. Jensen, Micro Mechanics Europe, MME'93 (Neuchatel, Switzerland, 1993), p. 143.

Hermann, S. (1970) Boundary Layer Theory. Seventh Ed. Edited by J. F. H. Frank J. Cerra. Germany: McGRAW-HILL Inc. Available at: https://www.sciencedirect.com/science/article/pii/S0997754600011018.

Hessel V., "Design and engineering of microreactor and smart-scaled flow processes", Special Ed., MDPI, Basel, Beijing, China, Pp. 1-251. 2015.

Hessel, V. et al., 2014. Designing Flow and Temperature Uniformities in Parallel Micro channelS-element Reactor. AIChE Journal, 60(5), pp. 1941-1952.

Hessel, V., Jähnsich, K., Löwe, H. & Baerns, M., 2004. Chemistry in Micro structured Reactors. Angew. Chem. Int., 43(4), pp. 406-446.

Hessel, V., Löwe, H. & Schönfeld, F., 2005. Micromixers - A review on passive and active mixing principles. Chemical Engineering Science, 60(9), pp. 2479-2501.

Horváth A. K., I. Nagypál, and I. R. Epstein, "Kinetics and mechanism of the chloride dioxide-tetrathionate reaction", J. Phys. Chem. A., 107, Pp. 10063-10068, 2003.

Incropera et al. (2013) 'Principles of Heat and Mass Transfer', in. John Wiley & Sons, Inc., pp. 458–459.

Jäckel, Microsystem Technology for Chemical and Bio- logical Microreactors, DECHEMA Monographs, Vol.132 (Ed.: W. Ehrfeld), VCH, Weinheim, 1996, p. 29.

Jakab, É., Horváth, D. and Tóth, Á. (2002) 'Temperature-controlled cellular fronts', Physical Chemistry Chemical Physics, 4(8), pp. 1307–1309. doi: 10.1039/b109263d.

Jakab, É., Horváth, D. and Tóth, Á. (2002) 'Temperature-controlled cellular fronts', Physical Chemistry Chemical Physics, 4(8), pp. 1307–1309. doi: 10.1039/b109263d.

Joiner B., B. Siegal, T. Tarter, and B. Bright, "Use of Experimental Data in Guiding Thermal Specification Development," Twelfth Annual IEEE Semiconductor Thermal Measurement and Management Symposium (SEMI-THERM), p. 65-71, Anstin, Texas, March 5-7, 1996.

Jovanovic, J. (2017) Liquid-liquid microreactors for phase transfer catalysis. Joegoslavië: geboren te Beograd. Available at: https://pure.tue.nl/ws/files/3561757/719772.

Kato K., M. Tagawa, and K. Kaifuku, "Fluctuating temperature measurement by a fine-wire thermocouple probe: influences of physical properties and insulation coating on the frequency response", Measurement Science and Technology, 18, Pp. 779-789, 2007.

Khine S. M., T. Houra, and M. Tagawa, "Heat-conduction error of temperature sensors in a fluid flow with nonuniform and unsteady temperature distribution", Review of Scientific Instruments, 84, 044902, Pp. 044902-1-12, 2013.

Klaus J_hnisch,* Volker Hessel,* Holger L_we, and Manfred Baerns. Chemistry in Microstructured Reactors, Chemistry in Microreactors, 2004.

Kockmann, N. et al. (2013) 'Liquid-liquid test reactions to characterize two-phase mixing in microchannels', Heat Transfer Engineering, 34(2–3), pp. 169–177. doi: 10.1080/01457632.2013.703508.

Kockmann, N. et al. (2013) 'Liquid-liquid test reactions to characterize two-phase mixing in microchannels', Heat Transfer Engineering, 34(2–3), pp. 169–177. doi: 10.1080/01457632.2013.703508.

Kolev, N. I. (1991) 'Multiphase Flow Dynamics 4'. 2nd Edition. Berlin: Springer.

Kozarek R.L., "Effect of Case Temperature MeasuArement Errors on the Junction-to-Case Thermal Resistance of a Ceramic PGA," Seventh Annual IEEE Semiconductor Thermal Measurement and Management Symposium (SEMI-THERM), p. 44-51, Phoenix, Arizona, February 12-14, 1991.

Kralj A. K., "Determination of a reaction's activated energy using NaOH as a reactant", Biomed. J. Sci. & Tech. Res., 6(1), Pp. 1-7, 2018.

Laudadio, G. et al. (2017) 'An environmentally benign and selective electrochemical oxidation of sulfides and thiols in a continuous-flow microreactor', Green Chemistry, 19(17), pp. 4061–4066. doi: 10.1039/c7gc01973d.

Laudadio, G. et al. (2017) 'An environmentally benign and selective electrochemical oxidation of sulfides and thiols in a continuous-flow microreactor', Green Chemistry, 19(17), pp. 4061–4066. doi: 10.1039/c7gc01973d.

Lerou, M. P. Harold, J. Ryley, J. Ashmead, T. C. O'Brien, M. Johnson, J. Perrotto, C. T. Blaisdell, T. A. Rensi, J. Nyquist, Microsystem Technology for Chemical and Biological Microreactors, DECHEMA Monographs, Vol.132 (Ed.: W. Ehrfeld), VCH, Weinheim, 1996, p. 51.

Levenspiel O. 1999. Chemical Reaction Engineering, 3rd Edition, John Wiley & Sons. New York.

Lin, Y., Gerfen, G. J., Rousseau, D. L. & Yeh, S.-R., 2003. Ultrafast Microfluidic Mixer and Freeze-Quenching Device. Analytical Chemistry, 75(20), pp. 5381-5386.

Liu Y. Z., B. J. Kim, and H. J. Sung, "Two-fluid mixing in a microchannel", International Journal of Heat and Fluid Flow, 25, Pp. 986-995, 2004.

Liu Y., X. Ren, C. Pan, T. Zheng, L. Yuan, J. Zheng, and Q. Gao, "Chlorine dioxide-induced and Congo red-inhibited Marangoni effect on the chlorite-trithionate reaction front", Chaos, 27, Pp. 104610-1-8, 2017.

Löwe, H. et al., 2010. Heat Pipe-Cooled Micro structured Reactor Concept for Highly Exothermal Ionic Liquid Syntheses. Chemical Engineering Technology, 33(7), pp. 1153-1158.

Löwe, W. Ehrfeld, V. Hessel, T. Richter, J. Schiewe, IMRET 4: 4th International Conference on Microreaction Technology (Atlanta, USA, 2000), American Institute of Chemical Engineers Topical Conference Proceedings, p. 31

MacInnes J. M., Z. Chen, R. W. K. Allen, "Investigation of alternating-flow mixing in microchannels" Chemical Engineering Science, 60, Pp. 3453-3467, 2005.

MacInnes, J. M., Vikhansky, A. & Allen, R., 2007. Numerical characterization of folding flow microchannel mixers. Chemical Engineering Science, 62(10), pp. 2718-2727.

Mengeaud, V., Josserand, J. & Girault, H. H., 2002. Mixing Processes in a Zigzag Microchannel: Finite Element Simulations and Optical Study. Analytical Chemistry, 74(16), pp. 4279-4286.

Minn Khine, S., Houra, T. and Tagawa, M. (2013) 'Heat-conduction error of temperature sensors in a fluid flow with nonuniform and unsteady temperature distribution', Review of Scientific Instruments, 84(4). doi: 10.1063/1.4801853.

Mtsambiwa R., "Local temperature measurement in a structured channel over a range of Reynolds number", M.Sc. Thesis, CBE Dept., University of Sheffield, Sheffield, UK, Pp. 1-43, 2017.

Nagypál, I. and Epstein, I. R. (1986) 'Fluctuations and stirring rate effects in the chlorite-thiosulfate reaction', Journal of Physical Chemistry, 90(23), pp. 6285–6292. doi: 10.1021/j100281a044.

Nelder, J. A. and Mead, R. (1965) 'A simplex method for function minimization', Proceedings of the IEEE International Conference on Systems, Man and Cybernetics, 7, p. 308.

Nguyen, N.-T. & Wu, Z., 2005. Micromixers - A review. Journal of Micromechanics and Micro engineering, 15(2), pp. R1-R16.

Peela N. R., I. C. Lee, and D. G. Vlachos, "Design and fabrication of a high-throughput microreactor and its evaluation for highly exothermic reactions", Ind. Eng. Chem. Res., 51, Pp. 16270-16277, 2012.

Peintler, G. et al. (2010) 'An improved chemical model for the quantitative description of the front propagation in the tetrathionate-chlorite reaction', Physical Chemistry Chemical Physics, 12(10), pp. 2356–2364. doi: 10.1039/b920618c.

Phillips R., "Computation of the temperature non-uniformity for a reaction in a structured channel", M.Sc. Thesis, CBE Dept., University of Sheffield, Sheffield, UK, Pp. 1-40, 2017.

Plouffe, P., Roberge, D. M. and Macchi, A. (2016) 'Liquid-liquid flow regimes and mass transfer in various micro-reactors', Chemical Engineering Journal. Elsevier B.V., 300, pp. 9–19. doi: 10.1016/j.cej.2016.04.072.

Ragless C. L., and B. Park, "Ceramic Coated Wires and Thermocouples" United States Patent, No. 5069726, D. Dec. 3, 1991.

Rica T., G. Schuszter, D. Horváth, and Á. Tóth, "Tuning density fingering by changing stoichiometry in the chlorite-tetrathionate reaction", Chemical Physics Letters, 585, Pp. 80-83, 2013.

Schubert, J. Brandner, M. Fichtner, G. Linder, U. Schygulla, A. Wenka, Microscale Thermophys.Eng.2001, 5, 17.

Schubert, W. Bier, J. Brandner, M. Fichtner, C. Franz, G. Linder, Process Miniaturization—IMRET 2: 2nd International Conference on Microreaction Technology (New Orleans, USA, 1998), Topical Conference Preprints (Eds. : W. Ehrfeld, I. H. Rinard, R. S. Wegeng), American Institute of Chemical Engineers, p. 88.

Shah S. I. A., L. W. Kostiuk, and S. M. Kresta, "The Effects of Mixing, Reaction Rates, and Stoichiometry on Yield for Mixing Sensitive Reactions—Part I: Model

Development", Research Article, International Journal of Chemical Engineering, Hindawi Publishing Corporation, Vol. 2012, Pp. 1-17, 2012.

Shaukatullah H., and A. Classen, "Effect of Thermocouple Wire Size and Attachment Method on Measurement of Thermal Characteristics of Electronic Packages". 19th IEEE SEMI-THERM SYMPOSIUM, 2003.

Shaukatullah, H. and Alan, C. (2003) 'Effect of thermocouple wire size and attachment method on measurement of thermal characteristics of electronic packages', IEEE Xplore. doi: 10.1109/STHERM.2003.1194345.

Soleyman A., E. Kolehmainen, and I. Turunen, "Numerical and experimental investigations of liquid mixing in T-type micromixers", Chemical Engineering Journal, 135S, S219-S228, 2008.

Sparrow E.M., "Error Estimates in Temperature Measurement," in Measurements in Heat Transfer, 2nd edition, edited by E.R.G. Eckert, and R.J. Goldstein, Chapter I, p. 1-23, Hemisphere Publishing, Washington, D.C., 1916.

Stroock, A. D. et al., 2002. Chaotic mixer for micro channels. Science, 295(5555), pp. 647-651.

Tagawa M., K. Kato, and Y. Ohta, "Response compensation of fine-wire temperature sensors" Review of Scientific Instruments, 76, 094904, Pp. 094904-1-10, 2005.

Tarnopolsky, M. and Seginer, I. (1999) 'Leaf temperature error from heat conduction along thermocouple wires', Agricultural and Forest Meteorology, 93(3), pp. 185–194. doi: 10.1016/S0168-1923(98)00123-3.

Tarnopolsky, M. and Seginer, I. (1999) 'Leaf temperature error from heat conduction along thermocouple wires', Agricultural and Forest Meteorology, 93(3), pp. 185–194. doi: 10.1016/S0168-1923(98)00123-3.

Tóth, Á., Horváth, D. and and Siska, A. (1997) 'Velocity of propagation in reaction – di † usion fronts of the chlorite – tetrathionate reaction', 93(1), pp. 73–76.

Veser, G. Friedrich, M. Freygang, R. Zengerle, Micro reaction Technology—IMRET 3: Proceedings of the 3rd International Conference on Micro reaction Technology (Ed.: W. Ehrfeld), Springer, Berlin, 2000, p. 674.

Veser, G., 2001. Experimental and theoretical investigation of H_2 oxidation in a high-temperature catalytic microreactor. Chemical Engineering Science, 56(4), pp.1265-1273.

Walker, J., Halliday, D. and Resnic, R. (2008) Fundamentals of physics. 8th edition. Hoboken, N.J. : John Wiley & Sonns, Inc.

Wang, H., Iovenitti, P., Harvey, E. & Masood, S., 2002. Optimizing layout of obstacles for enhanced mixing in micro channels. Smart Materials and Structures, 11(5), pp. 662-667.

Waterkamp, D. A. et al., 2007. Synthesis of ionic liquids in micro-reactors - a process intensification study. Green Chemistry, 9(10), pp. 1084-1090.

Waterkamp, D. A., Engelbert, M. & Thöming, J., 2009. On the Effect of Enhanced Mass Transfer on Side Reactions in Capillary Micro reactors during High-Temperature Synthesis of an Ionic Liquid. Chemical Engineering Technology, 32(11), pp. 1717-1723.

Watson G.G., "Techniques for Measuring Surface Temperature -Part 2," Instrument Practice, Vol. 20, No. 4, p. 335-341, April 1966.

Wegeng, C. J. Call, M. K. Drost, American Institute of Chemical Engineers Spring National Meeting (New Orleans, USA, 1996), p. 1.

White, F. M. (2008) "Fluid Mechanics". 6th edition.

Appendix A

Physical properties used in the computations

A.1 Determining the density and viscosity of solution

The equations for ρ and μ of the solutions used were calculated depending on the ρ and μ of water as follows:

$$\rho = \left(\frac{\rho}{\rho_w}\right)_{T_R} \rho_w \tag{A.1}$$

$$\mu = \left(\frac{\mu}{\mu_w}\right)_{T_R} \mu_w \tag{A.2}$$

where $\left(\frac{\rho}{\rho_w}\right)_{T_R}$ and $\left(\frac{\mu}{\mu_w}\right)_{T_R}$ are the relative density and viscosity of solution at the reference temperature. The relative density and viscosity of the solution were calculated according to the Poiseuille method (Walker, 2008). In this method, the density of the solution is calculated by measuring the weight of a specific volume of solution at room temperature. Also, the viscosity of the solution is determined by calculating the time required for a specific quantity of solution to pass freely through a capillary tube at room temperature (Equation A.3). The density and viscosity of solutions used were measured experimentally using a syringe needle at 20^{o}C. Table A.1 shows the relative density and viscosity of the solutions used.

$$\frac{\mu}{\mu_w} = \left(\frac{\rho}{\rho_w}\right)\left(\frac{t}{t_w}\right) \tag{A.3}$$

where μ, μ_w, ρ and ρ_w are the viscosity of the solution, viscosity of water, density of solution and density of water respectively. t and t_w are the times required for a specific volume of solution and water to individually pass through the capillary tube.

Table A.1. Relative density and viscosity of solutions used at 20 ^{o}C.

Solution	(ρ/ρ_w)	(μ/μ_w)
HCl	1.014026	1.079296
NaOH	1.042873	1.235434
$K_2S_4O_6$	1.022682	1.011588
$NaClO_2$	1.040800	1.132181

The equations for density and viscosity of the solutions used can be represented as follows:

$$\rho(T) = aT^3 - bT^2 + cT + d \quad \text{(A.4)}$$

$$\mu(T) = aT^4 - bT^3 + cT^2 - dT + e \quad \text{(A.5)}$$

where a, b, c, d and e are the equation factors. *T* is the temperature (K). Tables A.2, A.3, A.4 and A.5 show these factors for the solutions of HCl-NaOH and $NaClO_2$-$K_2S_4O_6$ reacting systems. The factors for the equations for the density and viscosity of the products of each reacting system were calculated as an average of reactant equation factors.

Table A.2. Factors for the density equation for the HCl-NaOH system.

ρ (kg/m^3)	a	b	c	d
H_2O	1.569×10^{-5}	-1.877×10^{-2}	6.759	2.342×10^{2}
HCl	1.591×10^{-5}	-1.903×10^{-2}	6.854	2.375×10^{2}
NaOH	1.636×10^{-5}	-1.957×10^{-2}	7.049	2.442×10^{2}
Product	1.614×10^{-5}	-1.930×10^{-2}	6.951	2.409×10^{2}

Table A.3. Factors for the viscosity equation for the HCl-NaOH system.

μ (kg/m·s)	a	b	c	d	e
H_2O	3.323×10^{-11}	-4.555×10^{-8}	2.345×10^{-5}	-5.379×10^{-3}	4.648×10^{-1}
HCl	3.586×10^{-11}	-4.915×10^{-8}	2.530×10^{-5}	-5.804×10^{-3}	5.015×10^{-1}
NaOH	4.104×10^{-11}	-5.625×10^{-8}	2.896×10^{-5}	-6.643×10^{-3}	5.740×10^{-1}
Product	3.845×10^{-11}	-5.270×10^{-8}	2.713×10^{-5}	-6.224×10^{-3}	5.378×10^{-1}

Table A.4. Factors for the density equation for the $NaClO_2$-$K_2S_4O_6$ system.

ρ (kg/m^3)	a	b	c	d
H_2O	1.569×10^{-5}	-1.877×10^{-2}	6.759	2.342×10^{2}
$K_2S_4O_6$	1.605×10^{-5}	-1.920×10^{-2}	6.912	2.395×10^{2}
$NaClO_2$	1.633×10^{-5}	-1.954×10^{-2}	7.035	2.438×10^{2}
Product	1.619×10^{-5}	-1.937×10^{-2}	6.974	2.416×10^{2}

Table A.5. Factors for the viscosity equation for the $NaClO_2$-$K_2S_4O_6$ system.

μ (kg/m.s)	5	4	3	2	1
H2O	3.323×10^{-11}	-4.555×10^{-8}	2.345×10^{-5}	-5.379×10^{-3}	4.648×10^{-1}
K2S4O6	3.363×10^{-11}	-4.610×10^{-8}	2.373×10^{-5}	-5.444×10^{-3}	4.704×10^{-1}
NaClO2	3.762×10^{-11}	-5.156×10^{-8}	2.655×10^{-5}	-6.089×10^{-3}	5.262×10^{-1}
Product	3.562×10^{-11}	-4.883×10^{-8}	2.514×10^{-5}	-5.766×10^{-3}	4.983×10^{-1}

Appendix B

B.1 Determining Enthalpy of a Chemical Reactions

In order to determine some of the important parameters of reaction, a preliminary study on the bench-scale was implemented for the two chemical reaction systems used in this work: the first reaction was the Hydrochloric Acid-Sodium Hydroxide (HCl-NaOH) reaction and the second reaction was the Chlorite-Tetrathionate ($NaClO_2$-$K_2S_4O_6$) reaction. These parameters are the temperature rise due to the reaction, which refers to the enthalpy of reaction, and the minimum temperature in which the reaction can happen immediately. In another words, the purpose of this study was to determine the enthalpy change of reaction and the suitable thermal conditions of the reaction. The chemical equations for the reactions are shown below.

The first reaction $HCl + NaOH \longrightarrow NaCl + H_2O$

The second reaction $7ClO_2^- + 2S_4O_6^{2-} + 6H_2O \longrightarrow 7Cl^- + 8SO_4^{2-} + 12H^+$

B.2 Testing procedure

Two solutions, A and B, of reactants were prepared initially at specific concentrations. Appendix D explains the solution preparation method. The concentrations used for the first and second reactions are shown in Table B.1. For each solution, A and B, 250 ml were placed separately and simultaneously on the magnetic hotplate stirrer for a period of time to reach the uniform temperature required. Thermocouple type K was suspended in the beaker of Solution A to record the temperature of the solution. The hotplate was placed inside a fume cupboard for the safety purposes (for the second reaction only). The data logger was connected to the laptop to record the temperature continuously. All of Solution B was quickly added to Solution A at a given temperature. This temperature was recorded as the initial temperature of the reaction. The temperature of the reaction was recorded over time to determine the maximum temperature of the reaction. The temperature rise is a difference between the maximum temperature of reaction and the initial temperature of reaction.

Table B.1. Concentrations used for the reactions.

Property	Reaction 1		Reaction 2	
	HCl	NaOH	$K_2S_4O_6$ + NaOH	$NaClO_2$
Solution A	√		√	
Solution B		√		√
Concentration, M	1	1	0.010 + 0.002	0.350

B.3 Results and discussion

B.3.1 Minimum temperature of the reaction

For the first reaction, the test shows the reaction initiated at 19 ^{o}C immediately, where the reaction was very fast. This means the reaction can be implemented successfully at this temperature and above. Figure B.1 shows the minimum temperature required to initiate the second reaction. According to this figure, the reaction can initiate immediately at 24 ^{o}C and above.

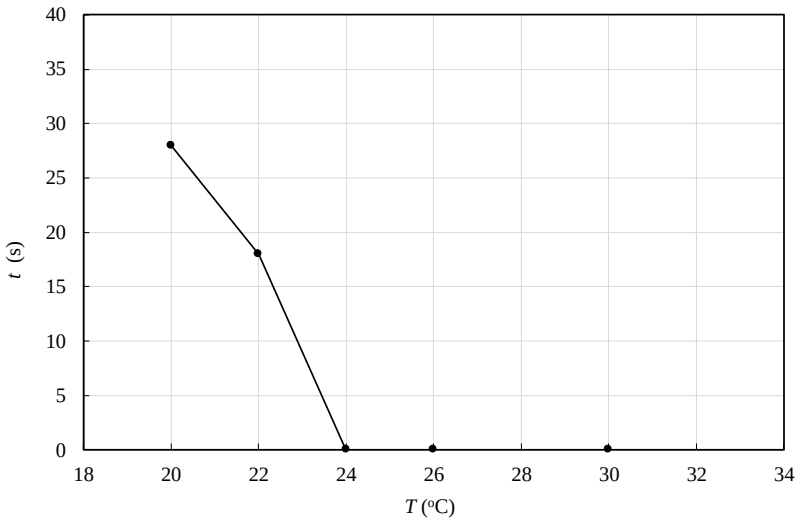

Figure B.1. Residence time of Chlorite-Tetrathionate reaction.

B.3.2 Calculating the enthalpy of reaction

The enthalpy of exothermic reaction can be calculated from the following equation:

$$\Delta h_R = -C_P \Delta T \qquad \text{(B.1)}$$

where Δh_R : the enthalpy of reaction. C_P : the heat capacity of the reaction mixture, which was assumed the heat capacity of water. ΔT is the adiabatic temperature rise of the reaction. The temperature rises of the first and second reaction were 6.8 and 18.0 ^{o}C respectively. The enthalpy of reaction was calculated according to Equation B.1 and was -28438 and -75276 J/kg for the HCl-NaOH reaction and $NaClO_2$-$K_2S_4O_6$ reaction respectively.

Appendix C

Assessment of the wire conduction error

At the initial stage of this work, an investigation study was implemented to assess the heat conduction error resulting from using the continuous thermocouple wire experimentally. This study was carried out using a small scale swirl element apparatus. This work includes the thermal mixing of cool and warm water at buoyant laminar flow under convenient non-reacting conditions. The spatial temperature was measured along the passage of an element using wire of different diameters and at different velocities.

C.1 Swirl element geometry

The passage geometry in the swirl element includes two circular chambers: upstream and downstream chamber (Fig. C. 1). The height and diameter of each chamber are 1 cm and 2.4 cm respectively. The upstream and downstream chambers are connected together by a narrow central hole. The height and diameter of a central hole are 0.5 and 1 cm. In this thermal work, the mixer was fixed with 30^{o} to the horizontal plane in order to make the movement of the thermocouple wire through the chambers flexible without interfering with the pulleys (Fig. C. 1). The two inlet streams enter the element in the upstream chamber and pass around the circumference of the chamber and then through the narrow central hole. In the central hole, the streams are mixed closely, and this mixing would activate the thermal mixing. After the narrow hole, the geometry expands to a downstream chamber and the emerging flow tends to move outward radially as a result of its angular velocity. This produces the toroidally circulating flow as the liquid travels towards the outlet.

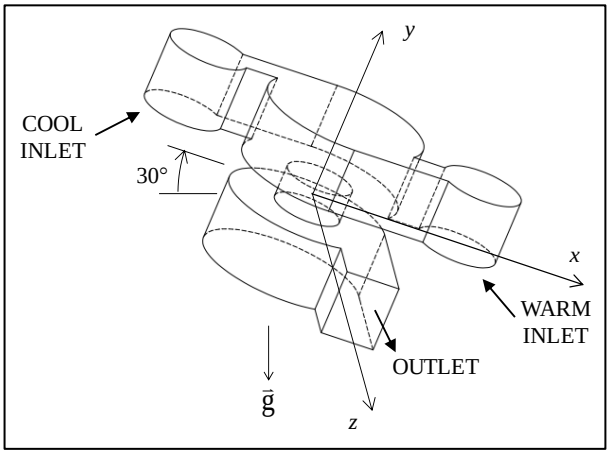

Figure C. 1. The swirl mixer fixed at 30^{o} to the horizontal plane.

The swirl mixer geometry consists of three parts (Fig. C. 2). The main part contains passage geometry is made from Poly Vinyl Chloride (PVC). The passages are closed with top and bottom covers made from transparent Lexan. The PVC layer includes seven main external holes. The fluid enters through two inlet holes and goes out through one hole. There are two small side holes in each chamber. These holes are opposite to each other and they are located on the z-axis of a coordinate system of geometry. These holes can be used to pass the thermocouple wire through them to measure the temperature spatially along the line of the upstream and downstream chamber. The points of measuring line were (0, 7.5, -12), (0, 7.5, 12) in an upstream chamber and (0, -7.5, -12), (0, -7.5, 12) in a downstream chamber according to the (x, y, z) coordinate element system. These holes allow the use of wire with a diameter up to 500 µm. A plastic sleeve is inserted between the hole and the wire to reduce liquid leakage.

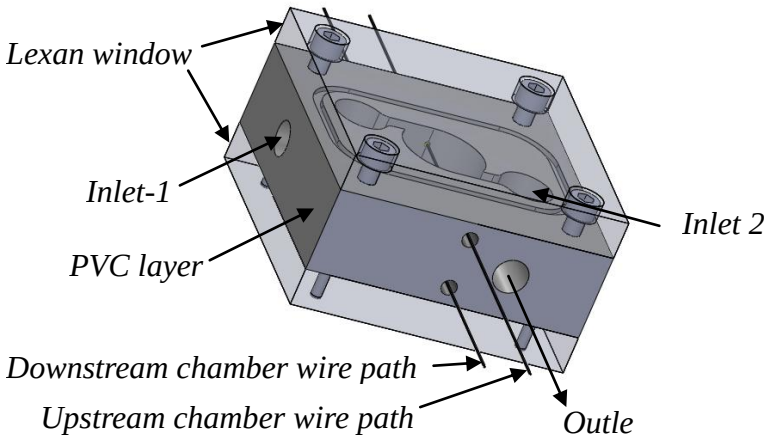

Figure C. 2. Experimental set up of swirl element.

C.2 Flow System

Deionized water was used as inlet cool and warm liquid. The water is put in pressure bottles and then it is pumped to swirl element through compressing it by air. The water flow rate is controlled through a pressure valve. Capillary tubes were used to reduce the pressure of the swirl element up to 1 bar. The water flow rate was measured manually by collecting a specific quantity of fluid that pumped into the system through a period of time. The individual flow rate of each warm and cool water stream must be the same. The flow rate was used in the laminar regime which is determined at Re < 120 according to the preliminary work. The Reynolds number value used for the study was 60. Air bubbles formed inside the mixer through pushing water due to the presence of the dissolved air in the water. The flow pattern and temperature distribution through the element were affected by these bubbles. They were eliminated by opening small vent holes leading upward from locations at the top of passage features where gas pockets may form. The power voltage supply was used to control the inlet warm temperature. Heating tape was used to convert the electrical current to heat for heating the inlet warm liquid. The warming up process took approximately 40 minutes to achieve the thermal steady-state.

C.3 Temperature measurement

Warm and cool water enter the upstream chamber through the two inlet holes to produce a temperature variation in the flow. The warm water enters through the lower inlet, while the cool water enters through the top inlet (Fig. C. 1). The mixing water stream leaves the element through one hole. The temperature was measured along the upstream chamber of the element using a movable continuous-wire thermocouple technique (details of this method in Section 4.3). The temperature of the warm and cool stream was measured using sheathed thermocouple wire Type-K. The temperature difference between the warm inlet and cool inlet was 2 ^{o}C. Different wire diameters and different wire velocities were used (Table 4. 3 shows the wire diameters used and their sleeve).

Appendix D

Chemical Materials Used

D.1 Deionized water

Deionized water used in the experiments was produced by the Milli-Q® Reference Water Purification system. The water is processed through Quantum® purification cartridges and Q-Gard® to reach a total organic compound (TOC) value below 5 ppb and a resistivity of 18.2 MΩ.cm (at 25 °C).

D.2 Solutions A and B

The tested solutions were prepared using deionized water in all experiments and one of the chemicals listed in Table A.1. The dilution law was used to prepare all the solutions.

Table A.1. The raw chemicals used in the experiments.

Name	Chemical Formula	Phase	Manufacturer	Density (g/mL)	Molecular weight (g/mol)	Concentration	
						Wt %	M
Hydrochloric Acid	HCl	liquid	fisher scientific	1.16	36.46	30	9.500
Sodium hydroxide	NaOH	liquid	fisher scientific	1.33	40.00	30	10.000
Sodium chlorite	$NaClO_2$	liquid	Sigma-Aldrich	1.20	90.44	25	3.317
Potassium tetrathionate	$K_2S_4O_6$	solid	Sigma-Aldrich	2.96	302.45	99.9	-

D.3 Preparing the Solutions

D.3.1 HCl-NaOH Reacting System

Preparation of Solution A (2000 mL of 1M HCl solution): To prepare 2000 mL of 1 M HCl solution, 210.5 mL of stock solution (9.5 M) was slowly added to 500 mL of deionized water. The final volume of the solution was adjusted to 2000 mL with

deionized water. The prepared solution was left 15 minutes to rid it of the heat of dilution before starting the experiment.

Preparation of Solution B (2000 mL of 1M NaOH solution): To prepare 2000 mL of 1 M NaOH solution, 210.0 mL of stock solution (10 M) was slowly added to 500 mL of deionized water. The final volume of the solution was adjusted to 2000 mL with deionized water. The prepared solution was left 15 minutes to rid it of the heat of dilution before starting the experiment.

D.3.2 $NaClO_2$- $K_2S_4O_6$ Reacting System

Preparation of Solution A (2000 mL of 0.35 M $NaClO_2$ solution): To prepare 2000 mL of 0.35 M $NaClO_2$ solution, 211 mL of stock solution (3.317 M) was slowly added to 500 mL of deionized water. The final volume of the solution was adjusted to 2000 mL with deionized water. The prepared solution was left 15 minutes to rid it of the heat of dilution before starting the experiment.

Preparation of Solution B (2000 mL solution of 0.1 M $K_2S_4O_6$ and 0.002 M NaOH): To prepare 2000 mL solution of 0.1 M $K_2S_4O_6$ and 0.002 M NaOH, 60.5 g of stock solution of $K_2S_4O_6$ and 0.4 mL of stock NaOH (10 M) were slowly added to 500 mL of deionized water. The final volume of the solution was adjusted to 2000 mL with deionized water. The prepared solution was left 15 minutes to rid it of the heat of dilution before starting the experiment.

To determine the quantity of $K_2S_4O_6$ needed to prepare 2000 mL of 0.1M:

$$2.0(L)*0.1(mol/L)*302.45(g/mol)=60.5g \text{ of stock } K_2S_4O_6.$$

Appendix E

Reactor Design Details

The design uses a clamped layer approach to form the reactor as shown in Fig. E.1 where the layers have been expanded for clarity. A *Reactor Insert* contains both the preheating mixer and reactor passages and is milled from PEEK to provide thermal insulation. The reactor and preheat mixer passages are closed with *Reactor Cover* plates made from stainless steel and coated with approximately 100 μm of PFA on the reactor passage side to resist acid. The stainless steel plates allow reasonable heat conduction for thermal exchange with adjacent copper *Preheat* and *Reactor Exchangers*, which are supplied with separate cooling/heating water flows to allow independent imposition of temperatures by the copper exchangers to the preheating and reactor regions. An insulating acetal spacer provides thermal insulation between the preheat and reactor exchangers (not labelled in the figure). The exchangers are supplied with sufficient water flow of regulated temperature to impose that temperature throughout the highly conducting copper exchangers. The exchanger passages are closed using acetal *Cooling Water Covers* and positive sealing of each layer is achieved using o-rings as shown.

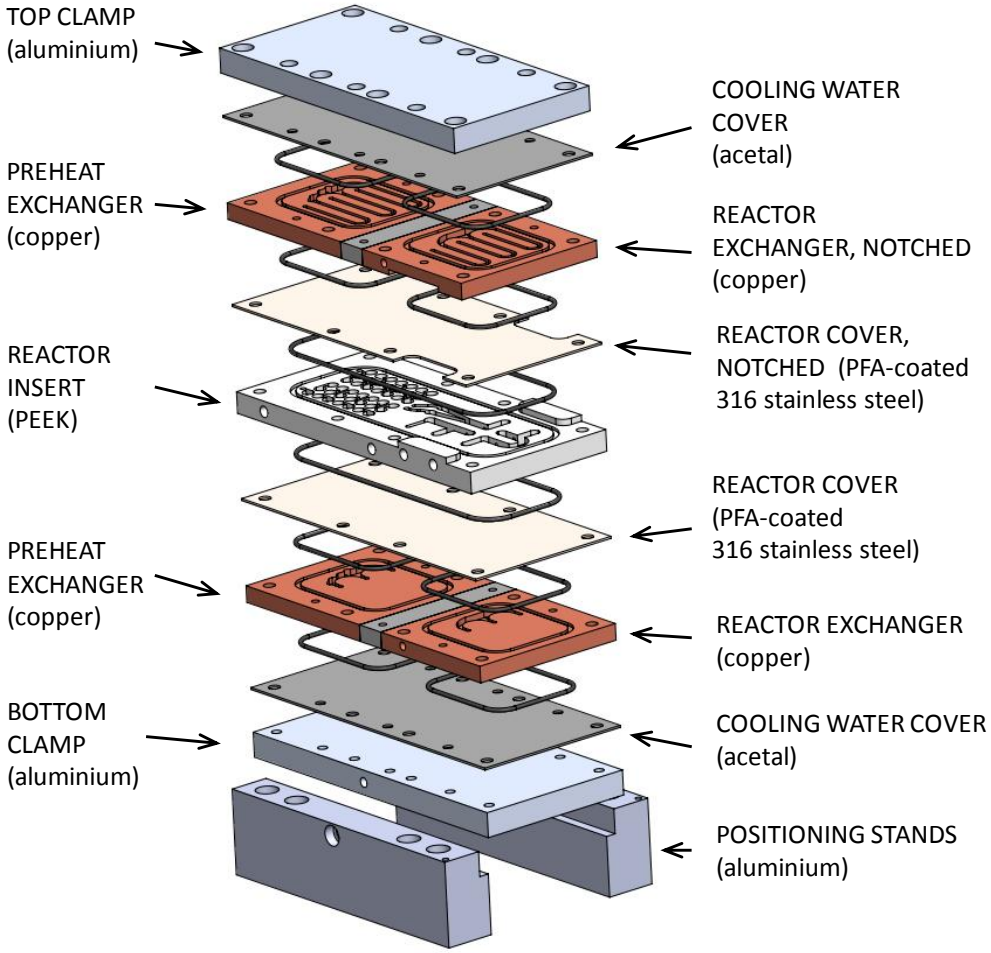

Figure E.1 Overview of reactor components. All components are common to all reactors, apart from the reactor insert itself and the mounting stands, which must position the each reactor insert so the particular thermocouple traverse paths are in line with the fixed thermocouple wire path.

Each reactor insert has a different thickness as can be seen in Fig. E .2, due to each particular passage geometry. Each reactor provides two thermocouple wire paths through the reactor passages and these are different for each of the reactor designs. Thus, for a fixed wire path relative the mounting base, a unique stand is required for each reactor insert. The figure illustrates these differences. The front and rear paths are accessed by mounting the stand using one or the other of the pairs of holes.

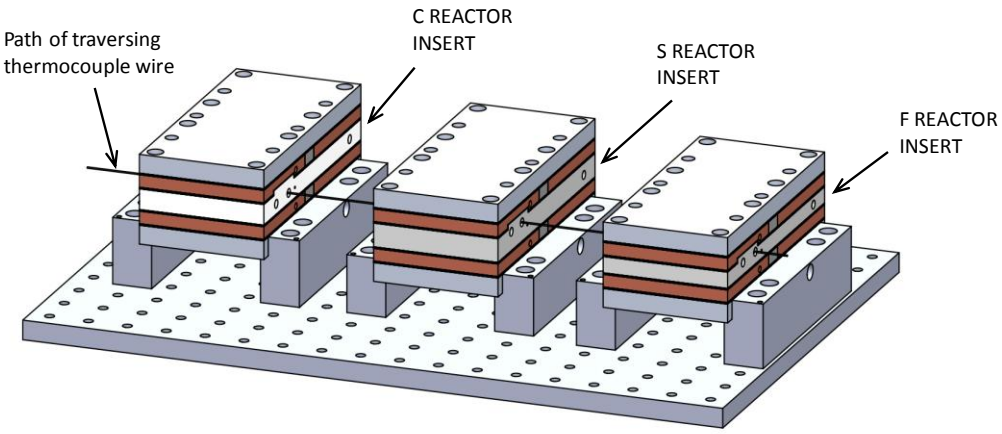

Figure E. 2 View showing the use of stands of different height and positioning on the base board to place each reactor insert in line with the thermocouple wire path. The two sets of holes in the stands allow positioning for the front and rear traversing paths through the reactors.

In the following sections, the technical drawings of the component parts that are common to all reactor inserts are presented, followed by those for each reactor. Parts are fabricated either using computer-controlled milling or by jet cutting in the case of the thin layers (i.e. the Reactor Covers and the Cooling Water Covers).

E.1 Detail drawings of components common to all reactor types

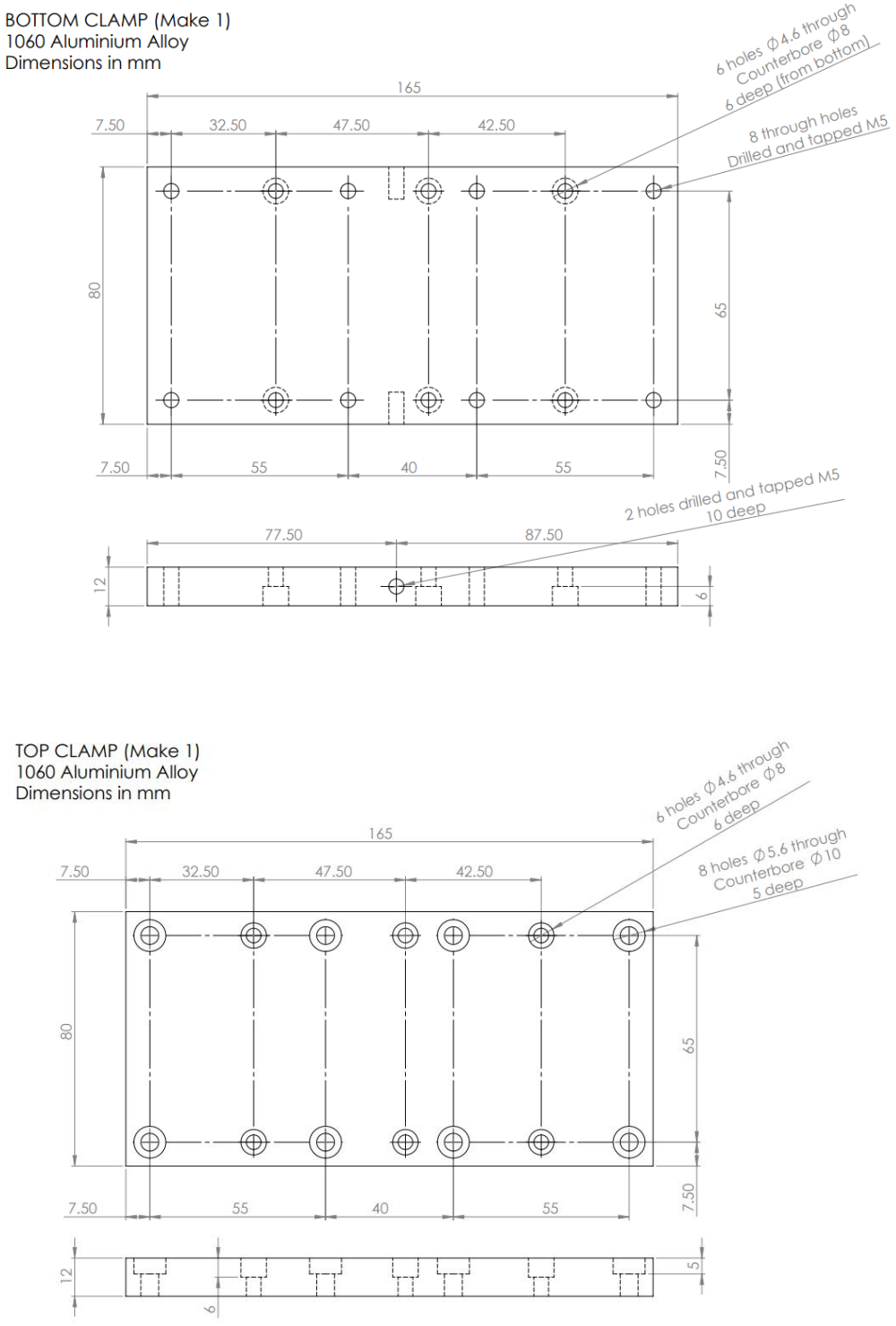

Figure E .3 Top and bottom clamps.

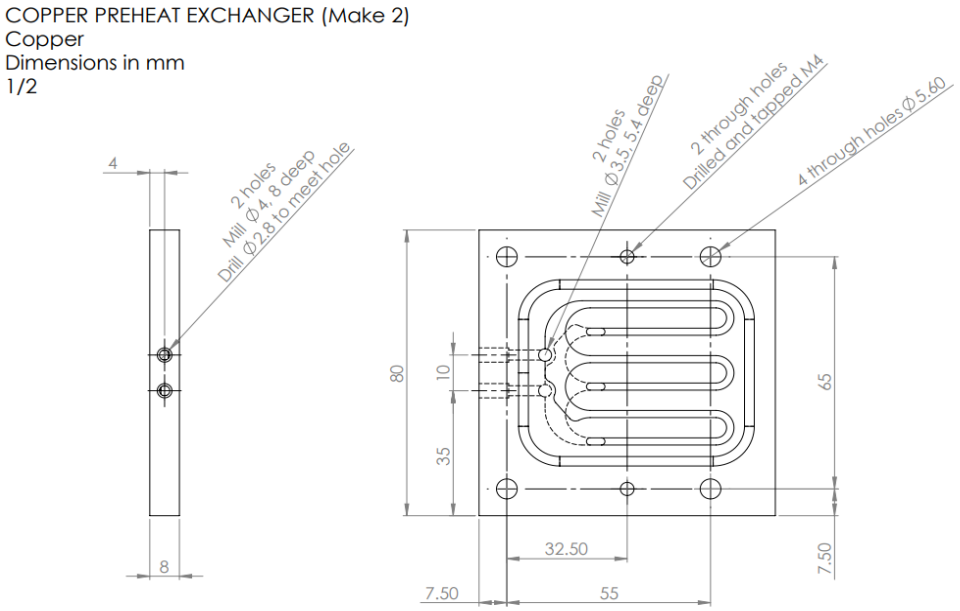

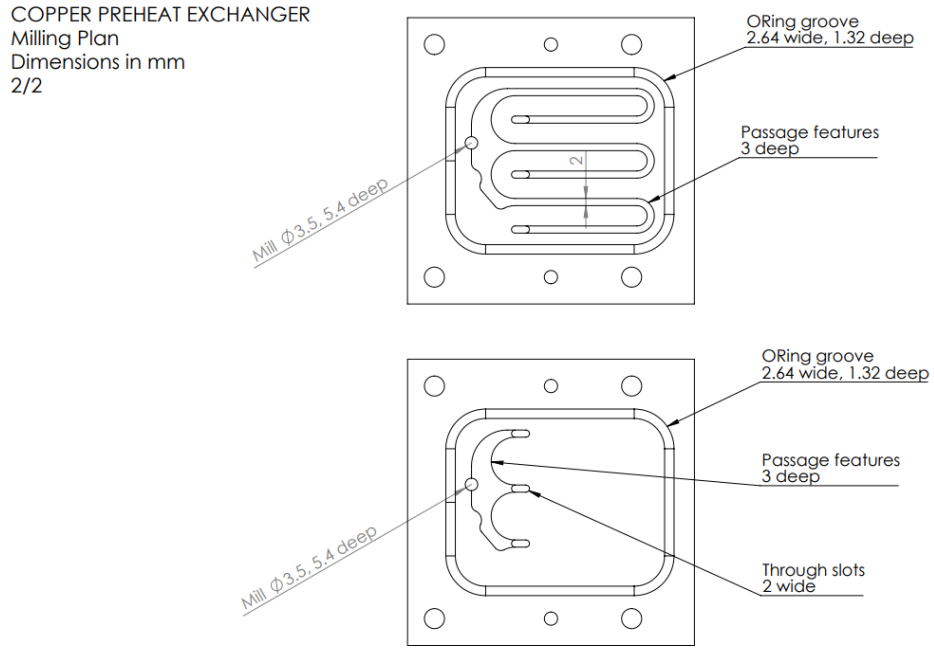

Figure E .4 Preheat exchanger.

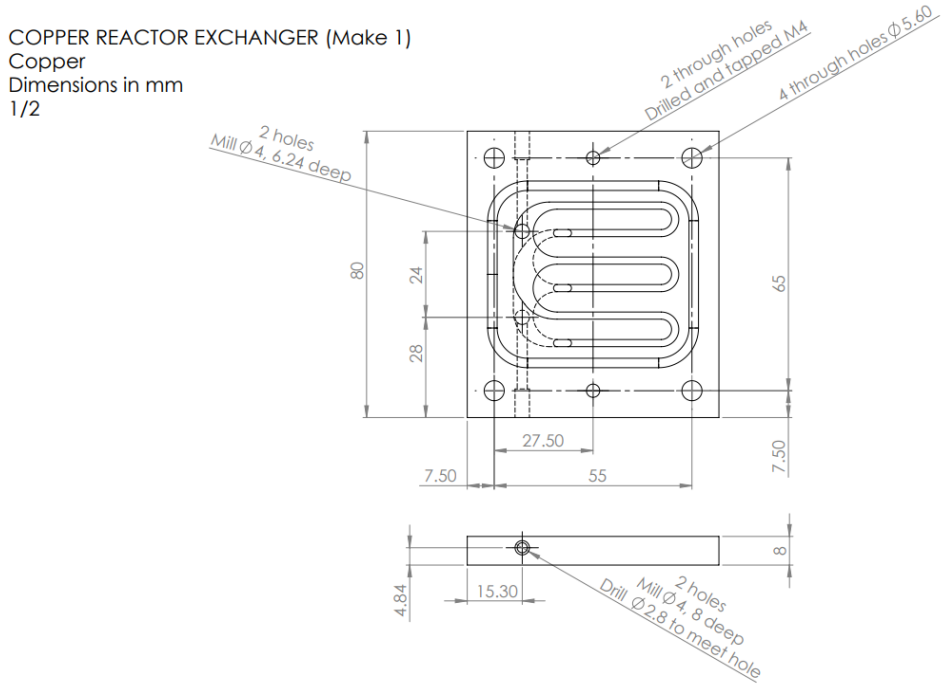

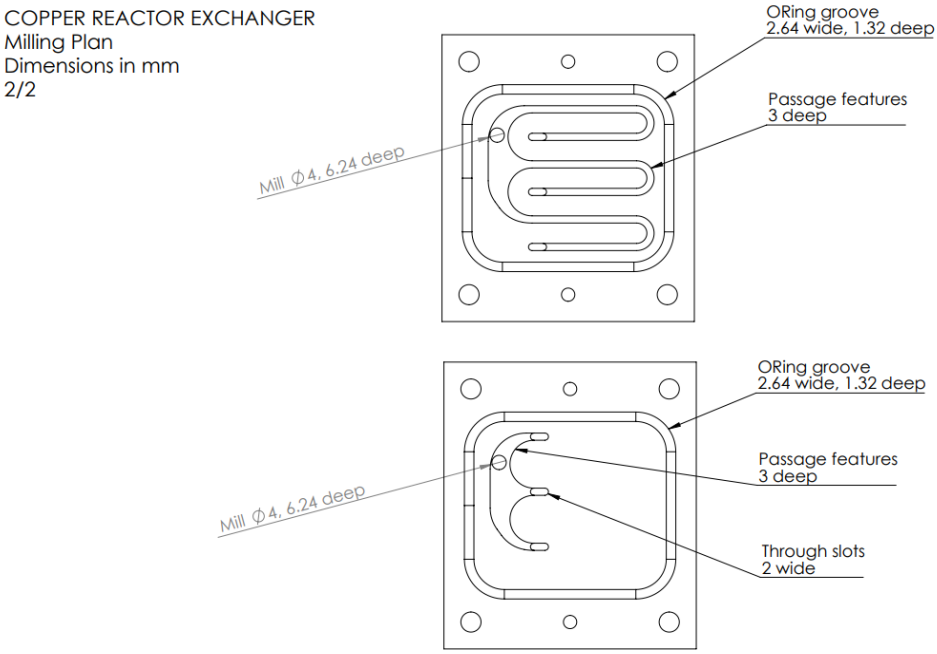

Figure E .5 Reactor exchanger

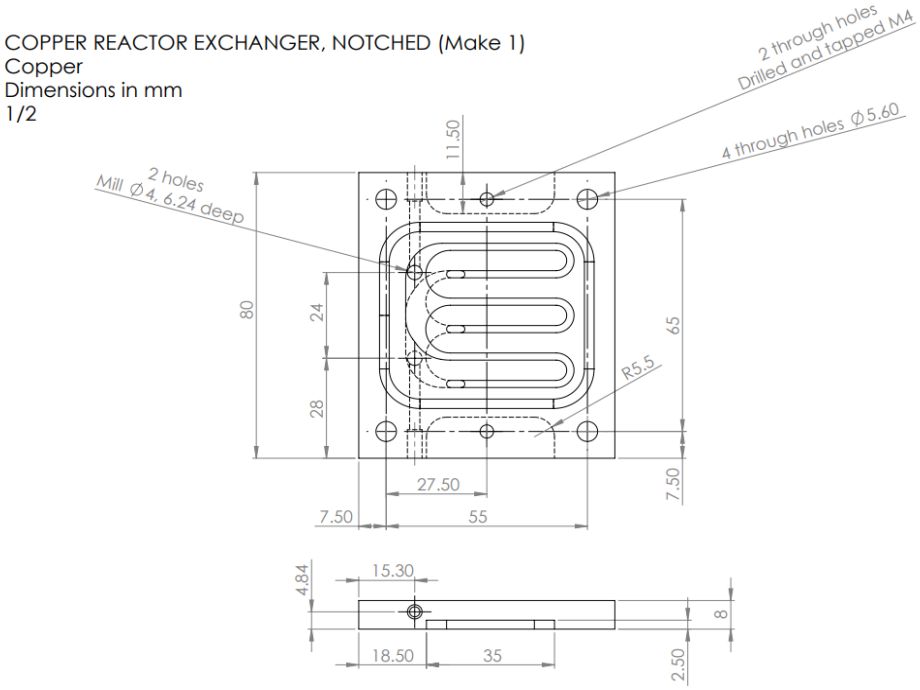

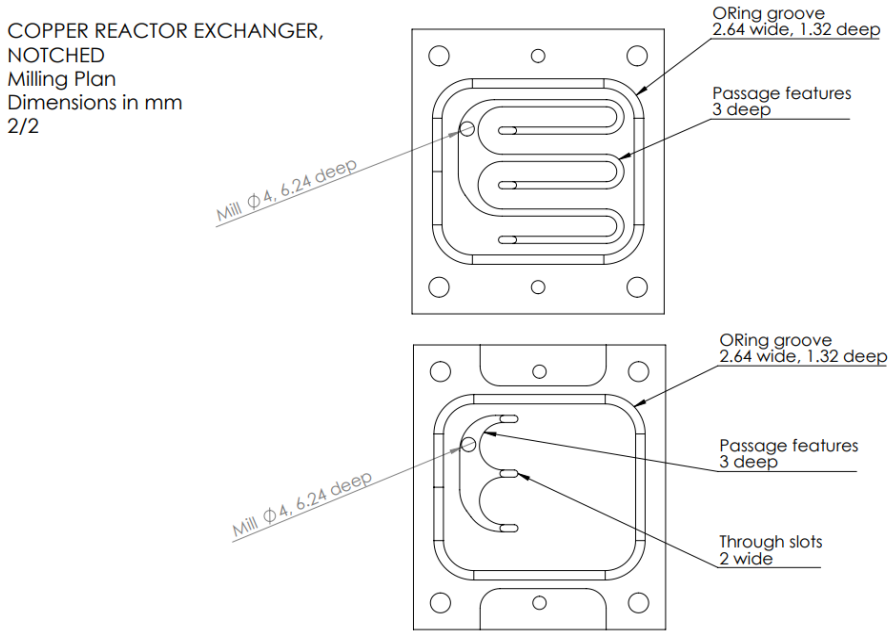

Figure E .6 Reactor exchanger with notch.

REACTOR COVER (Make 1)
316 Stainless Steel
Dimensions in mm

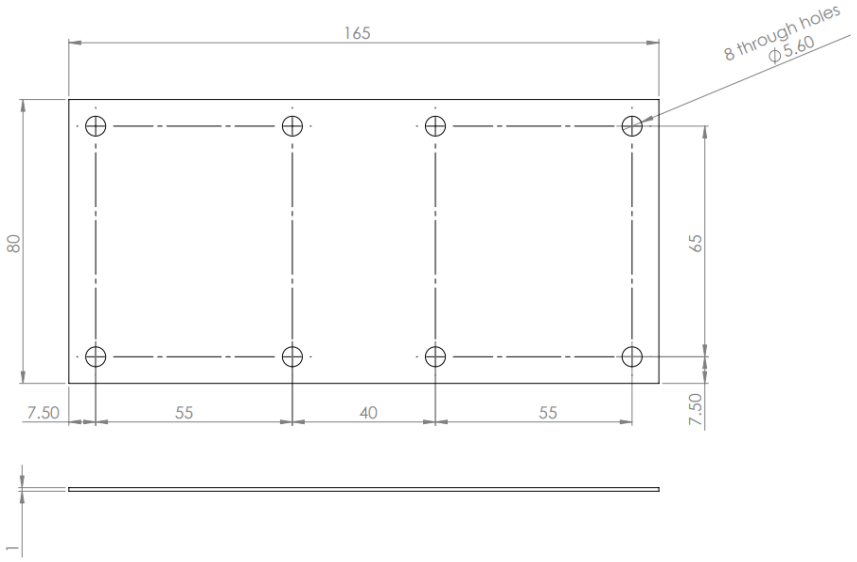

REACTOR COVER, NOTCHED (Make 1)
316 Stainless Steel
Dimensions in mm

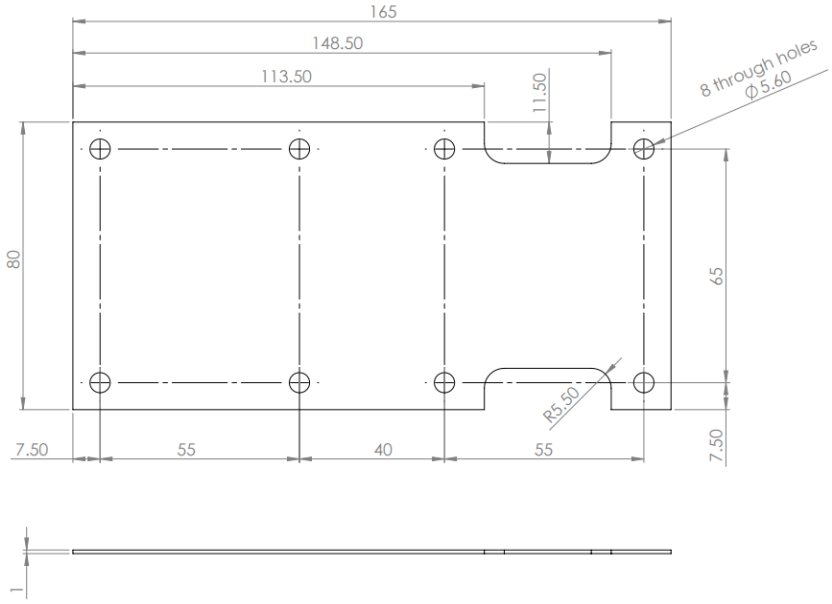

Figure E .7 Reactor covers.

COOLING WATER COVER (Make 2)
Acetal
Dimensions in mm

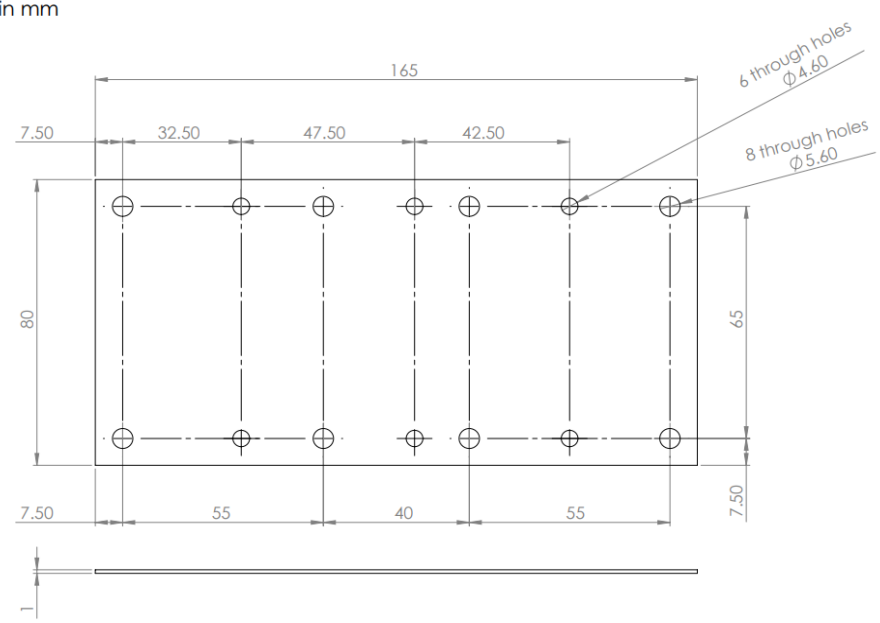

Figure E .7 Cooling water covers.

E.2 C-Element Reactor insert and stand

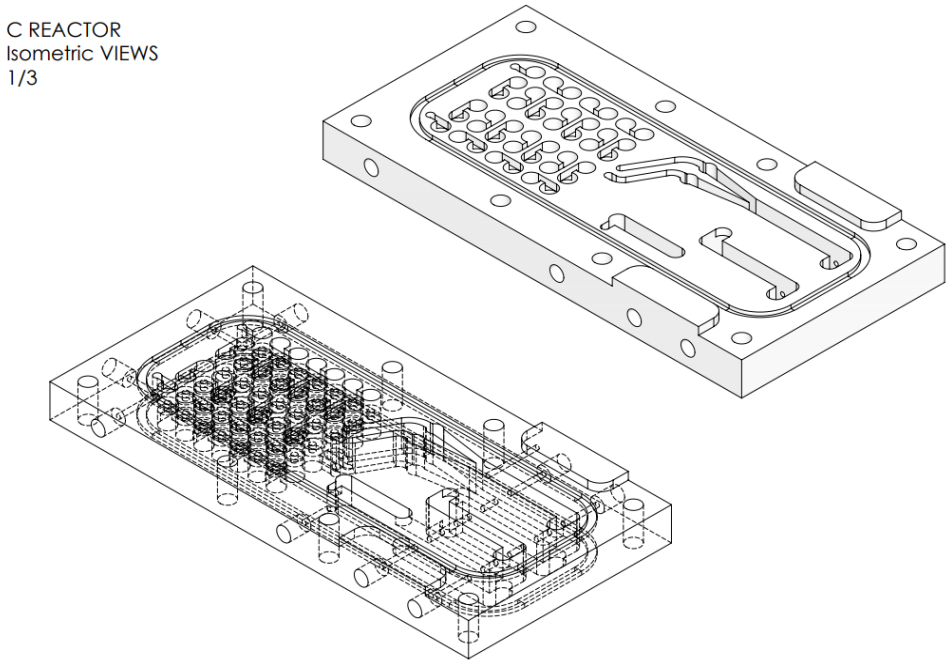

Figure E .8 Pictorial views of the C reactor insert.

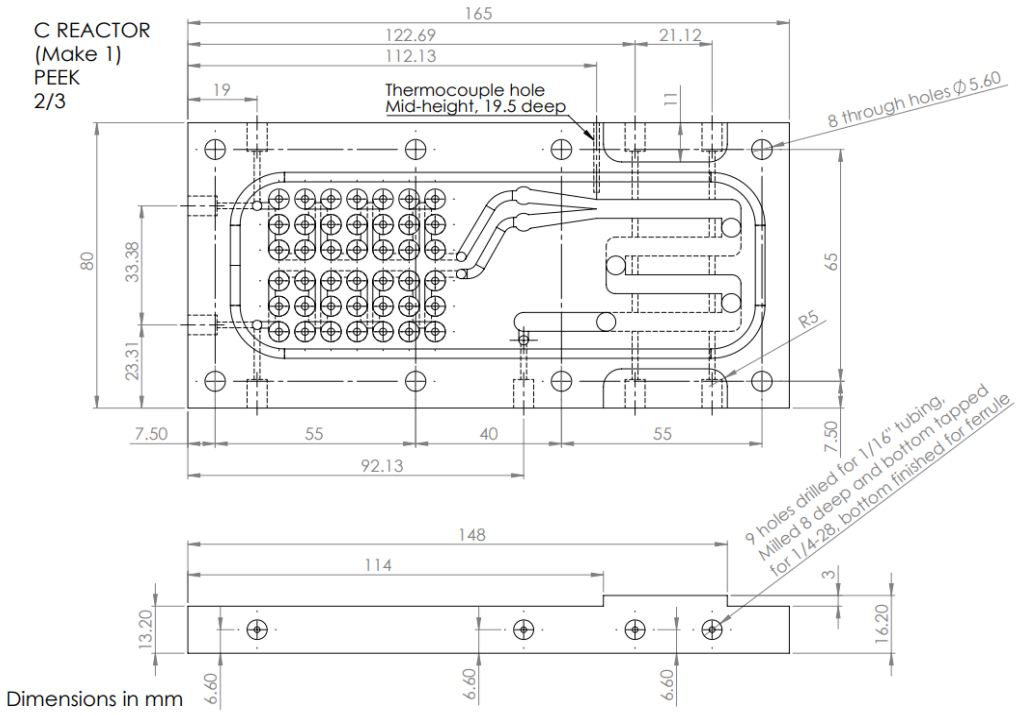

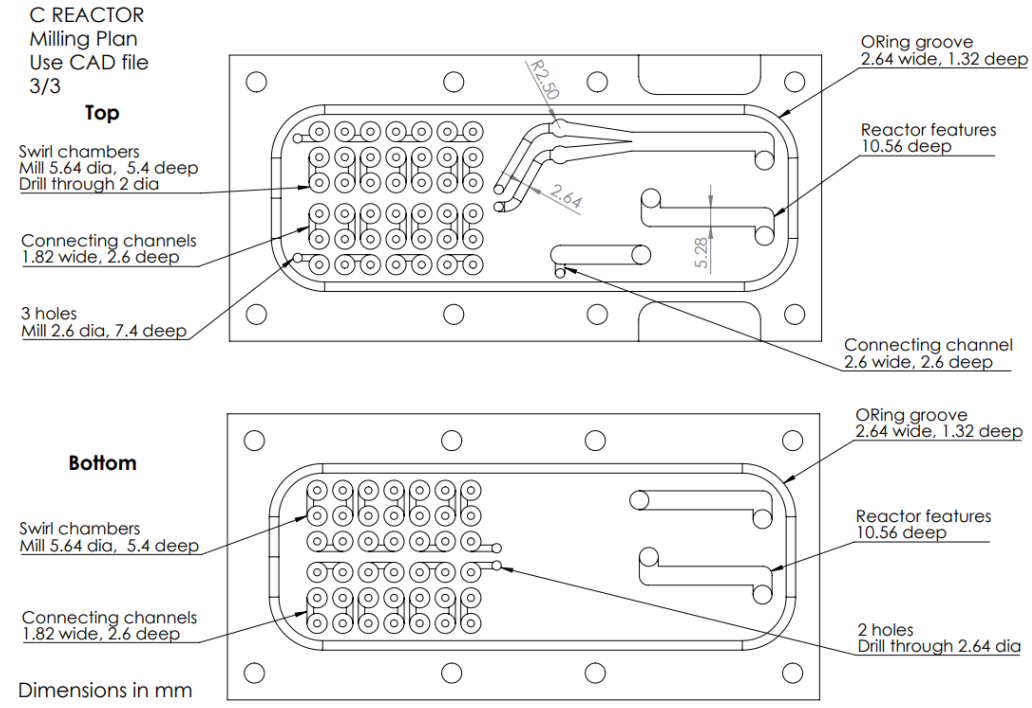

Figure E .9 Detail drawings of the C reactor insert.

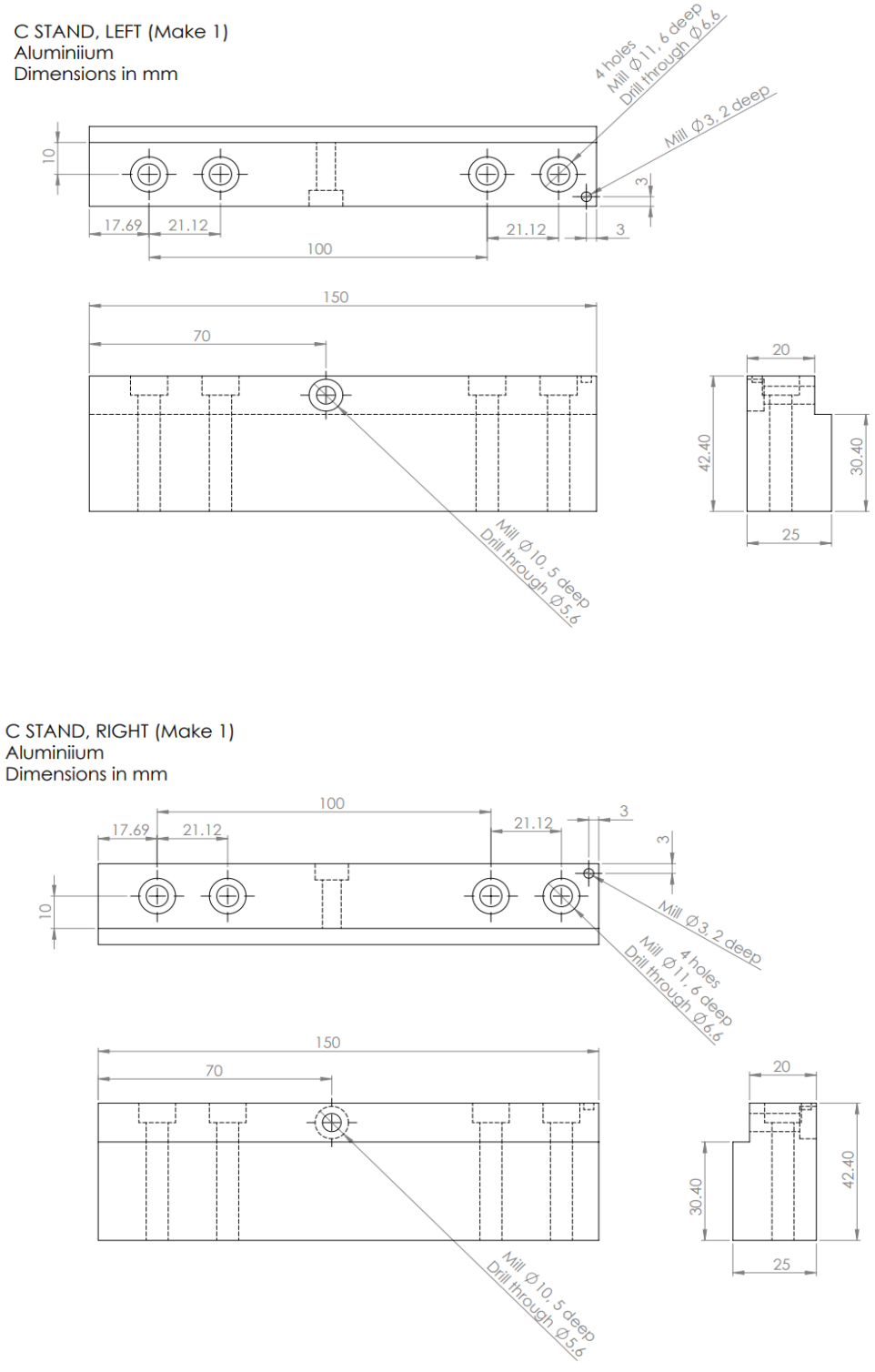

Figure E.10 Detail drawings of the left and right stands for the C reactor.

E.3 S-Element Reactor insert and stand

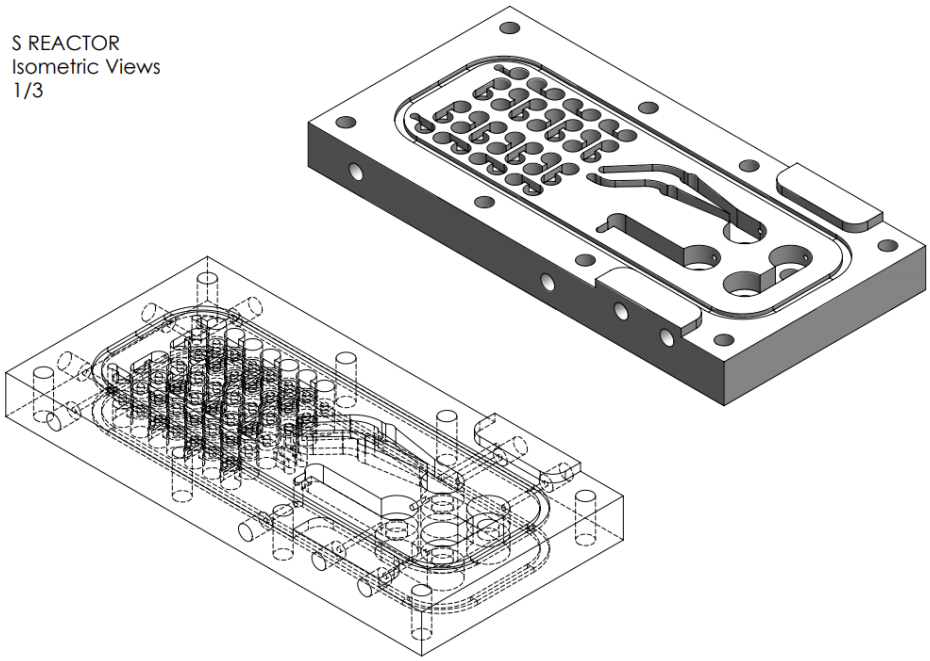

Figure E.11 Pictorial views of the S reactor insert.

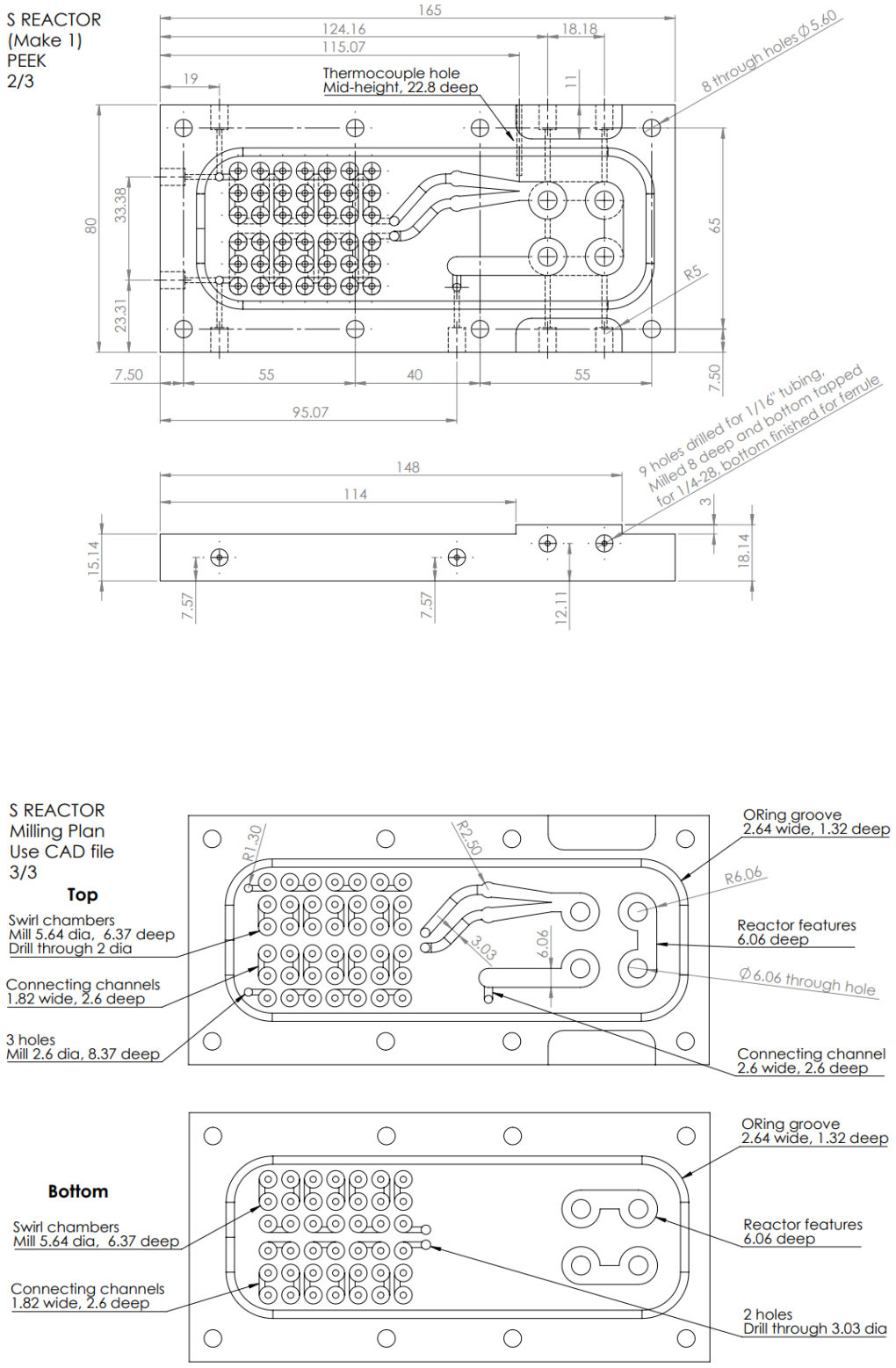

Figure E.12 Detail drawings of the S reactor insert.

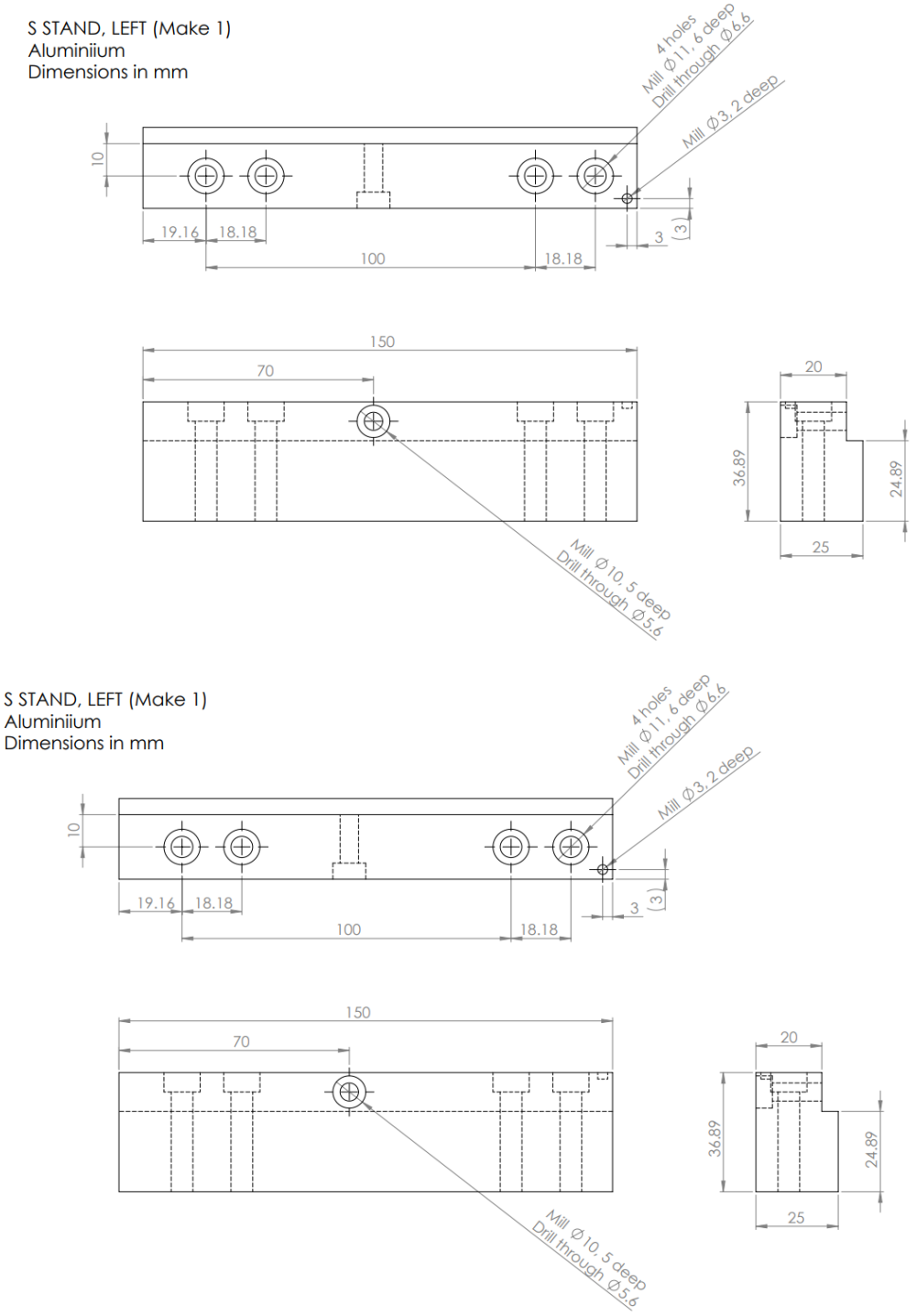

Figure E.13 Detail drawings of the left and right stands for the S reactor.

E.4 F-Element Reactor insert and stand

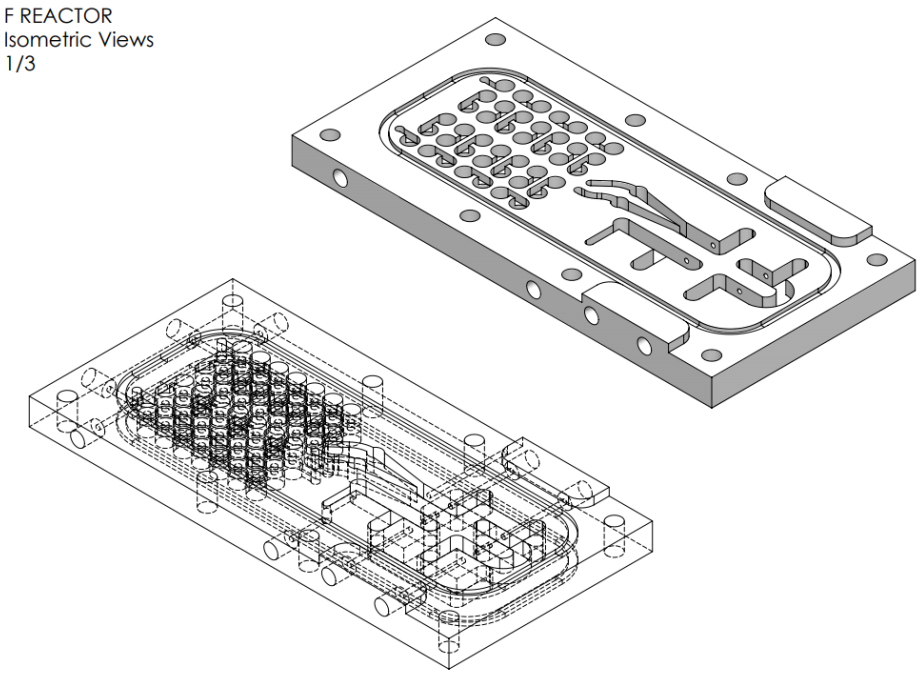

Figure E.14 Pictorial views of the F reactor insert.

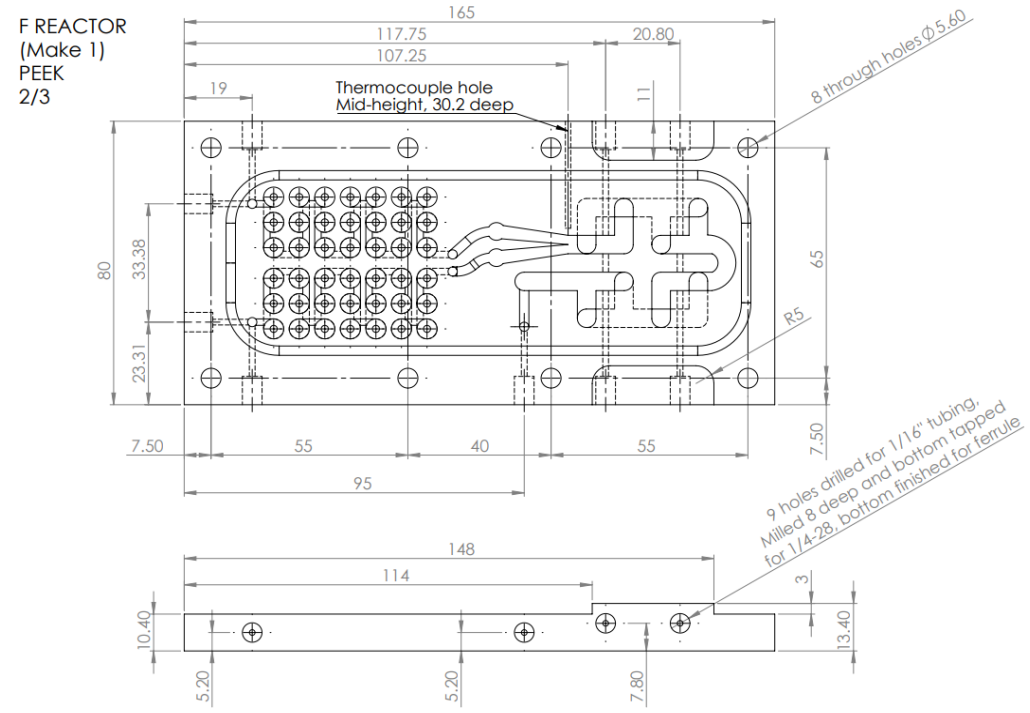

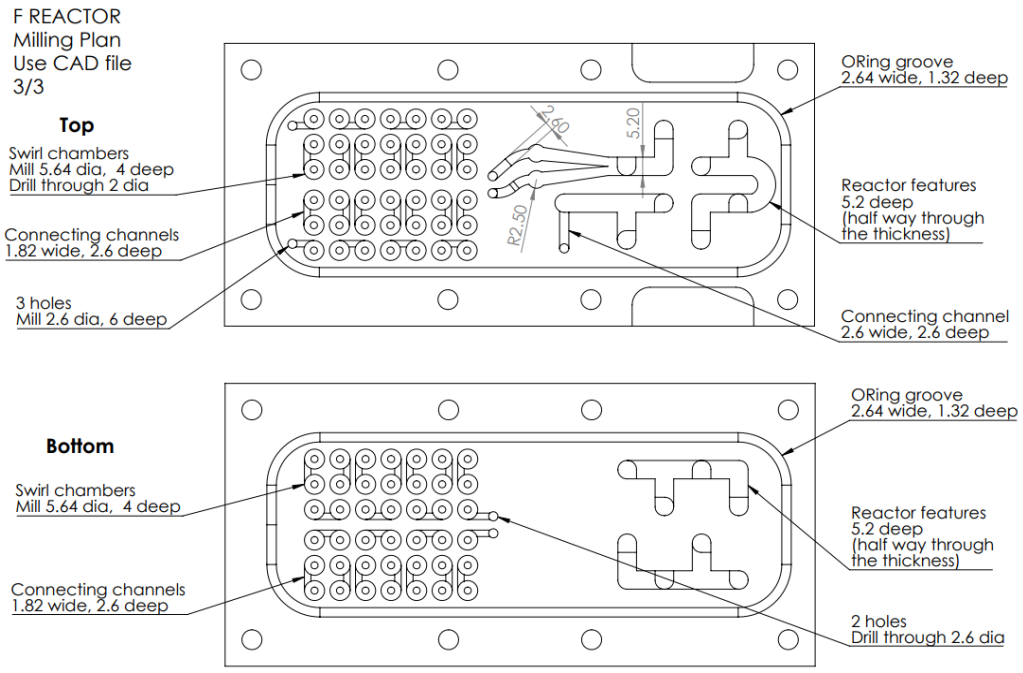

Figure E.15 Detail drawings of the F reactor insert.

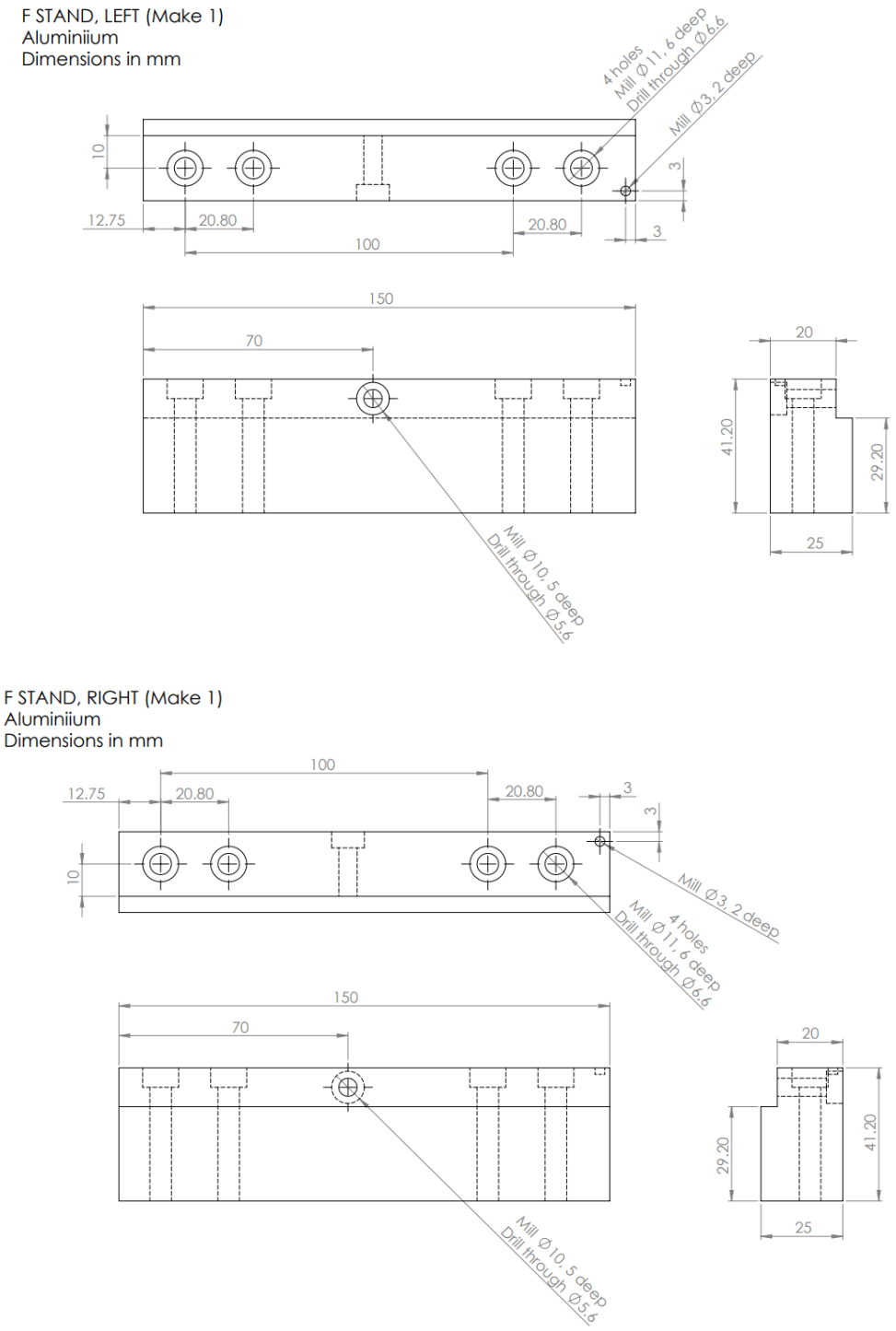

Figure E.16 Detail drawings of the left and right stands for the F reactor.

E.5 Reactor covers plates

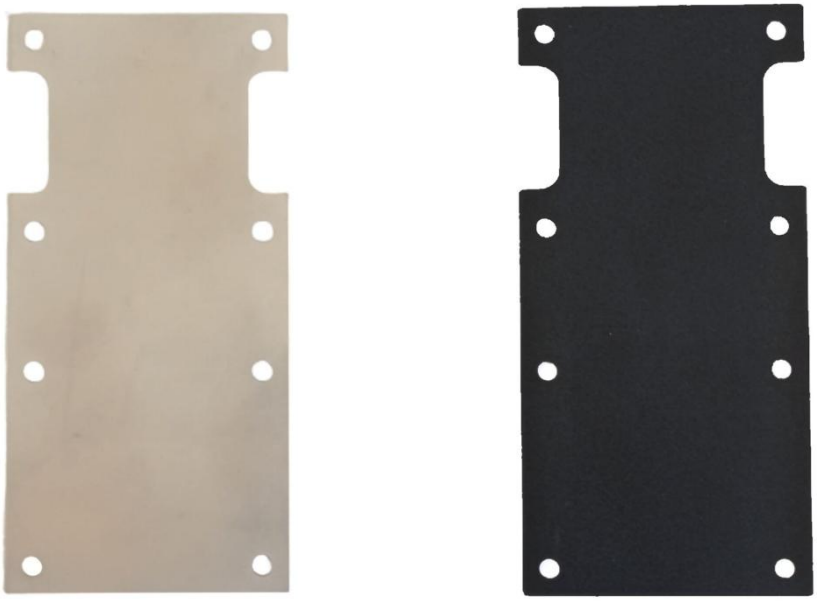

(a) Uncoated (b) PFA-Coated

Figure E.17 Reactor cover notched (316 stainless steel).

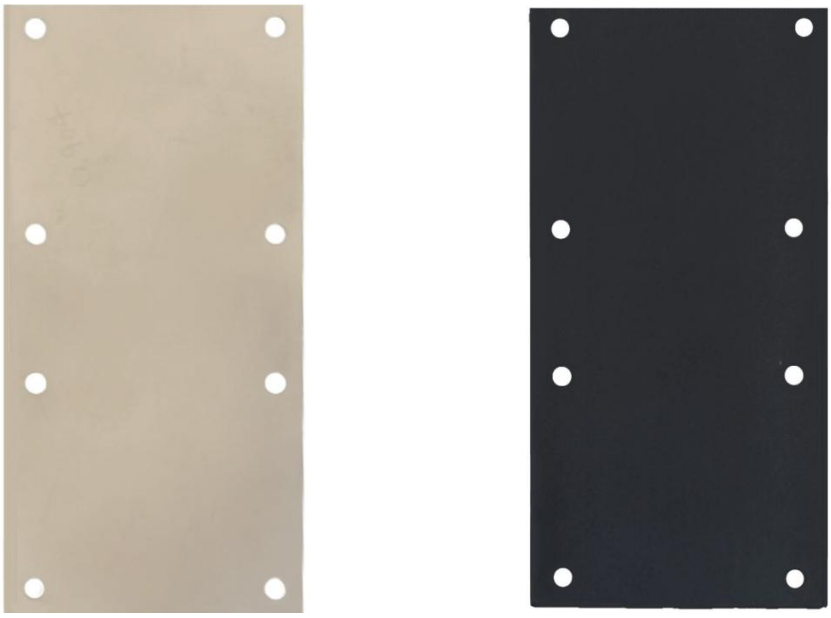

(a) Uncoated (b) PFA-Coated

Figure E.18 Reactor cover (316 stainless steel).